



**NEW APPLICATIONS OF
CHOLANGIOCARCINOMA ORGANOIDS:**

Modelling the tumor immune and
extracellular microenvironment

Ruby Lieshout

New Applications of Cholangiocarcinoma Organoids:

Modelling the tumor immune and
extracellular microenvironment

Ruby Lieshout

© Ruby Lieshout 2022.

All rights reserved. No part of this thesis may be reproduced, stored, or transmitted in any form or by any means without prior written permission of the author or, when applicable, of the publisher of the scientific paper.

Cover design: Ruby Lieshout
Layout: Ruby Lieshout
Printing: Proefschriftmaken
ISBN: 978-94-6469-125-2

The printing of this thesis has been financially supported by the Erasmus Medical Center Rotterdam and the Medical Delta.



New Applications of Cholangiocarcinoma Organoids:

Modelling the tumor immune and extracellular microenvironment

Nieuwe toepassingen van cholangiocarcinoom organoïden:

Modelleren van de tumor immuun en extracellulaire micro-omgeving

Thesis

to obtain the degree of Doctor from the

Erasmus University Rotterdam

by command of the

rector magnificus

Prof. dr. A.L. Bredenoord

and in accordance with the decision of the Doctorate Board.

The public defence shall be held on

Wednesday the 14th of December at 15.30 hrs

by

Ruby Lieshout

born in Hoorn

Doctoral Committee:

Promotors: Prof. dr. L.J.W. van der Laan
Prof. dr. J.N.M. IJzermans

Other members: Prof. dr. A. de Bruin
Prof. dr. R. Fodde
Dr. ir. W.M. van Weerden

Copromotor: Dr. ing. M.M.A. Verstegen

TABLE OF CONTENTS

Chapter 1	
General introduction & thesis outline	7
Chapter 2	
Cholangiocyte organoids from human bile retain a local phenotype and can repopulate bile ducts in vitro	23
Chapter 3	
Kinome profiling of cholangiocarcinoma organoids reveals potential druggable targets that hold promise for treatment stratification	69
Chapter 4	
Cholangiocarcinoma cell proliferation is enhanced in primary sclerosing cholangitis: A role for IL-17A	89
Chapter 5	
Modelling immune cytotoxicity for cholangiocarcinoma with tumor-derived organoids and effector T cells	111
Chapter 6	
Extracellular matrix drives tumor organoids toward desmoplastic matrix deposition and mesenchymal transition	143
Chapter 7	
General discussion & summary	185
Chapter 8	
Nederlandse samenvatting	199
Appendices	
List of publications	206
PhD portfolio	208
About the author	210
Dankwoord	211

CHAPTER

1

General introduction & Thesis outline

Partially based on:

From organoids to organs: Bioengineering liver grafts from hepatic stem cells and matrix

Ruby Lieshout*, Jorke Willemse*, Luc J.W. van der Laan, Monique M.A. Verstegen

**These authors contributed equally*

Best Pract Res Clin Gastroenterol 2017; 31(2):151-9

&

Experimental models to unravel the molecular pathogenesis, cell of origin and stem cell properties of cholangiocarcinoma

Silvestre Vicent, Ruby Lieshout, Anna Saborowski, Monique M.A. Verstegen, Chiara Raggi, Stefania Recalcati, Pietro Invernizzi, Luc J.W. van der Laan, Domenico Alvaro, Diego F. Calvisi, Vincenzo Cardinale

Liver Int 2019; 39 Suppl 1:79-97

Cholangiocarcinoma (CCA) is a malignancy arising from the biliary tree. It is divided into three subtypes based on anatomical site of origin: intrahepatic CCA (iCCA) located in or upstream of the second-order bile ducts, perihilar CCA (pCCA) in the hepatic ducts or their junction, and distal CCA (dCCA) in the common bile duct.¹ All subtypes have both shared and subtype-specific epidemiological features, molecular characteristics, tumor biology, risk factors, and management (Fig. 1). CCA is a rare cancer, with 0.5-3.4 cases per 100,000 people in Europe and Northern America.² For the majority of cases, an underlying cause of CCA is undetermined. Several diseases associated with bile stasis and chronic inflammation of the biliary epithelium have been linked to CCA, e.g. chronic fibrotic inflammatory disease primary sclerosing cholangitis.³ Mainly for iCCA, cirrhosis also provides risk, which is an end-stage of many liver diseases including viral hepatitis and alcohol-related liver disease.³ Although the incidence of CCA is generally low in developed countries, iCCA incidence seems to be on the rise over the past decades.⁴⁻⁶ It is proposed that this could be due to life style aspects related to affluence, such as alcohol consumption, obesity, and type 2 diabetes, which are known risk factors for iCCA.^{4,7} Together with the increased incidence, the number of iCCA-related deaths has also risen considerably, while mortality for pCCA and dCCA decreased slightly in most countries.^{8,9} Overall, the prognosis for CCA is dismal with 5-year survival rates reported at 7-20%.¹ This poor outcome is likely due to a late onset of symptoms, often when it has already progressed to locally advanced or metastatic disease beyond eligibility for curative (surgical)treatments. Moreover, CCA possesses marked inter- and intratumoral heterogeneity, and harbors pronounced resistance to chemotherapeutics, making it difficult to effectively treat with systemic therapies.

Thus, there is a great need to better understand the complexity of CCA, to discover new effective therapies for CCA patients, and to develop methods to stratify patients that will benefit from specific treatments.

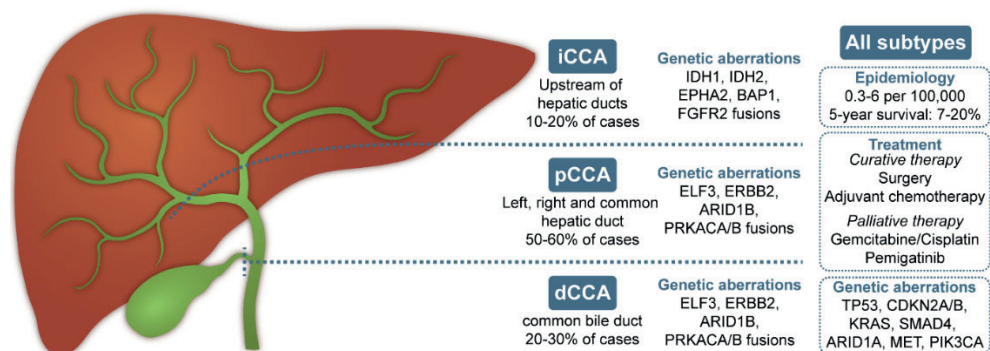


Figure 1. Anatomical subtypes and key characteristics of cholangiocarcinoma. Cholangiocarcinoma (CCA) is divided into three subtypes based on anatomical site of origin: intrahepatic CCA (iCCA), perihilar CCA (pCCA) and distal CCA (dCCA). These subtypes have both shared and subtype-specific characteristics.

The tumor microenvironment

CCA is characterized by an extensive desmoplastic stroma, a dense collagenous hypovascularized extracellular matrix (ECM), populated by cancer cells and a range of other cell types including cancer-associated fibroblasts (CAFs), immune cells and endothelial cells.¹⁰⁻¹² The ECM provides cell support and physical signals due to its stiffness, facilitates communication between cells and interacts with various cell types in the tumor microenvironment (TME).¹² Thereby, the ECM influences CCA cell invasion, progression, and metastasis.¹⁰ In return, the ECM is constantly remodeled by cells in the TME. Cancer-associated fibroblasts (CAFs) are the main modulators of the ECM, constantly depositing new matrix proteins, and excreting proteolytic enzymes to degrade other parts, shaping the ECM to support tumor progression.¹³ Furthermore, CAFs can directly promote tumor growth and metastasis, and can modulate immune cell functions, inhibiting cytotoxic T cells, dendritic cells and NK cells while activating regulatory T cells.^{12, 14, 15} Recently, single cell RNA sequencing of intrahepatic CCA revealed five different tumor CAF subtypes.¹⁶ Vascular CAFs were the most prevalent subtype, and were associated with enhanced malignancy.

The immune cell compartment of the CCA TME includes tumor-associated innate immune cells and tumor infiltrating lymphocytes (TILs).^{12, 17, 18} Tumor-associated macrophages are the best studied innate immune cell in CCA. They have an M2-like phenotype and cause T cell suppression, while stimulating tumor progression.^{12, 18} The role of tumor-associated neutrophils and myeloid-derived suppressor cells is less clear, but they are known to dampen anti-cancer immune responses effectively in other cancers.^{12, 18} TILs comprise of both effector cells, in the form of NK cells, CD8⁺ cytotoxic T cells, CD4⁺ T helper cells and B lymphocytes, and immunosuppressive CD4⁺ regulatory T cells. Cytotoxic T cells are pivotal in effective anti-tumor immune responses, and their presence in CCA is associated with a better prognosis.^{19, 20} However, regulatory T cells are accumulated in the CCA TME to counteract cytotoxic T cell function, by expression of immune checkpoint proteins TIGIT, GITR and CTLA-4.^{12, 16, 21} Hence, the CCA TME presents a cytotoxic effector cell population inhibited by an immunosuppressive environment created by immunosuppressive immune cells, CAFs and cancer cells.

Cholangiocarcinoma therapy

Treatment with curative intent

The only curative treatment option for CCA is surgical intervention in early stage disease. However, due to the silent nature of early stage CCA, only 20-30% of patients present with a resectable tumor at the time of diagnosis. Depending on the location of the tumor, surgery usually involves an (extended) hemi-hepatectomy with or without resection of the extrahepatic bile duct, or a pancreaticoduodenectomy (Whipple procedure), often combined with lymphadenectomy.²² Surgical resection in iCCA and pCCA increases 5-year survival to ~30% (5-56% range).^{22, 23} Unfortunately, CCA recurrence is common after resection, affecting 61-98% of patients within 5 years of surgery.^{22, 23} This is because it is often difficult to resect the complete tumor, especially for iCCA. CCA is also prone to metastasize and late diagnosis allows CCA cells to migrate before resection. Upon

recurrence, patients either need another resection, or more often are appointed to palliative treatment regimens.

For a carefully selected group of patients with early stage unresectable pCCA, often due to underlying liver diseases such as primary sclerosing cholangitis, liver transplantation is considered. The Mayo protocol for liver transplantation combined with neoadjuvant chemoradiotherapy demonstrated impressive 5-year survival rates of 53-56%.^{24, 25} The potential benefit of liver transplantation for unresectable iCCA has only been established recently, when a retrospective study showed that patients with a single iCCA ≤ 2 cm had a 5-year survival rate of 65% after transplantation.²⁶ However, eligibility for liver transplantation remains low, and is complicated by a shortage of donor organs.

Even with potential curative surgical intervention, CCA recurrence after treatment is common. Therefore, adjuvant therapy is investigated to reduce the risk of relapse. Adjuvant chemotherapy has been evaluated in three randomized controlled trials, comparing surgery alone to surgery followed by 6 months of different chemotherapeutics.²⁷⁻²⁹ Adjuvant treatment with capecitabine significantly improved relapse-free survival and prolonged median overall survival to 51.1 months compared to 36.4 months with surgery only.²⁹ Subsequently, the American Society of Clinical Oncology (ASCO) included adjuvant capecitabine treatment in their CCA guidelines.³⁰ Evidence for adjuvant radiotherapy is less substantial, although one trial demonstrated a promising 2-year survival rate of 65% for patients with pCCA/dCCA that received adjuvant chemoradiotherapy, which warrants larger randomized trials.³¹

Treatment of advanced disease

The large majority of CCA patients are ineligible for surgery. First-line standard-of-care for these patients is a chemotherapy regimen of gemcitabine and cisplatin, which is superior over gemcitabine alone, although median overall survival is still just under one year.³²⁻³⁴ Upon inevitable progression, second-line therapy with FOLFOX (folinic acid, 5-FU and oxaliplatin) can be considered. FOLFOX provided a modest but significantly improved median overall survival (6.2 months versus 5.3 months), and, more importantly, 6- and 12-month survival rates were improved by 15%.³⁵

Beyond these chemotherapeutics, there are no standard-of-care therapies for advanced CCA. Locoregional therapy could be considered for unresectable localized disease or locoregional recurrence. Trans-arterial (chemo)-embolization, hepatic arterial infusion of chemotherapy, radio-embolization, and radiofrequency ablation have all displayed survival benefits to some extent in retrospective or small selective studies.⁶ In addition, radiotherapy has shown local control rates in 45-100% of patients and 1-year survival rates of 58-81% in retrospective series and early studies, often in addition to chemotherapy.³⁶ However, randomized controlled trials need to be completed to definitively validate these locoregional therapies for CCA treatment.

New systemic therapies that have revolutionized cancer treatment over the last decades include targeted therapies based on molecular profiling and immunotherapy. These novel perspectives could have the potential to substantially improve CCA survival.

Targeted therapies

Molecular profiling of CCAs has elucidated a complex and heterogeneous mutational, epigenetic and transcriptomic landscape. Aberrations were found in a multitude of cellular processes, including cell cycle regulation, DNA damage and genomic instability, epigenetic regulation, kinase signaling and cell survival.¹ Molecular profiling revealed that the CCA subtypes have both a shared and a subtype-specific pattern of genetic alterations (Fig. 1).^{37, 38} iCCA and eCCA both display genetic alterations in common oncogenic driver genes TP53, CDKN2A/B, KRAS, SMAD4, ARID1A, MET and PIK3CA.^{37, 38} IDH1, IDH2, EPHA2, and BAP1 mutations and FGFR2 fusion events occur predominantly in iCCA, while ELF3, ERBB2 and ARID1B mutations and PRKACA or PRKACAB fusions occur more often in eCCA.³⁷⁻³⁹ In total, about 40% of CCAs possess potentially targetable genetic alterations with currently available therapeutics.³⁷

When targeted therapeutics came to market, clinical trials were performed in CCA patients adding the targeted drugs to palliative treatment regimens. The outcome of these clinical trials with kinase inhibitors targeting HER family, MET, KRAS-BRAF-MEK-ERK, and PI3K-AKT-mTOR, was disappointing.⁴⁰⁻⁴⁷ Addition of the kinase inhibitors did not prove more effective than current treatment protocols. These trials lacked selection of relevant targets and accurate biological stratification of patients, enrolling patients with aberrant and normal signaling pathways alike. Therefore, efforts to design targeted therapeutics for CCA shifted its focus to patients pre-selected by genetic alteration. Feasibility of this approach was supported by the biliary tract cancer subgroup analysis of the MOSCATO-01 trial.⁴⁸ 23 out of 34 patients with biliary tract cancer had druggable alterations and 18 of those were treated with molecular targeted therapeutics accordingly. Median overall survival was 17 months, compared to 5 months in patients without alteration-driven selection of treatment.⁴⁸

Targeted therapy research for CCA has been most successful for FGFR2 mutations/fusions and IDH1 mutations, both predominantly present in iCCA (13.1% IDH1 mutant, 10-15% FGFR2 fusion/alteration) and often mutually exclusive.^{37, 49-52} In clinical trials for CCA patients with FGFR2 fusions or mutations, FGFR1/2/3 inhibitor Pemigatinib demonstrated an objective response rate of 35.5%. Of the responders, 37% achieved long-term stabilization of disease of over 12 months.⁵³ In patients with advanced IDH1-mutant CCA refractory to chemotherapy, IDH1-inhibitor ivosidenib significantly improved progression-free survival (median 2.7 months versus 1.4 months in placebo group) and overall survival (10.3 months versus 5.1 months for crossover corrected-placebo group).^{54, 55} Even though the overall benefit is modest, a subgroup of patients achieved long-term stabilization of disease, with 22% of ivosidenib treated patients reaching 12 month progression free survival (versus 0% in the placebo arm).⁵⁴ Both pemigatinib and ivosidenib were subsequently approved for treatment of locally advanced or metastatic CCA with the appropriate genetic alterations.^{56, 57}

Even though described targeted therapeutics clearly show the feasibility and clinical advantage of targeted therapy in advanced CCA treatment, they only cater to a subgroup of patients that have the relevant molecular profiles. There is a plethora of targeted drugs available and thoroughly testing these in mono- and combinational therapies in clinical trials

with CCA patients that bear the appropriate molecular profile would be very expensive and time-consuming, also limited by the rarity of the disease. Moreover, it remains difficult to predict which patients respond to targeted therapeutics, even when molecular profiling is available, as only a subset of selected patients display clear benefit in performed clinical trials. Thus, there is a need for drug testing in preclinical models to identify potentially effective drugs and drug combinations at an earlier stage, and to develop a better understanding of the complexity of CCA to stratify patients to effective treatments more successfully.

Immunotherapy

The healthy immune system has the potential to effectively recognize and destroy aberrant cancer cells. However, cancer cells and the tumor microenvironment (TME) utilize a range of mechanisms to inhibit or evade anti-tumor immune responses, including expression of immune checkpoint proteins such as programmed cell death protein 1 (PD-1) and cytotoxic T-lymphocyte-associated antigen 4 (CTLA-4), downregulation of MHC expression and modulation of the TME to create immunosuppressive conditions. Immunotherapy aims to circumvent the immune evasion of cancer cells by counteracting the immunosuppression and potentiating the immune cells. Immune checkpoint inhibitors (ICIs) have vastly improved cancer treatment for a variety of tumor types, leading to durable anti-tumor responses with limited toxicity.⁵⁸⁻⁶¹ Other immunotherapy approaches are in a more developmental stage, although promising initial clinical data is available for most of them. They include agonists of co-stimulatory molecules to further activate T cells, anti-cancer vaccines, oncolytic virotherapy and adoptive cell therapies that consist of patient immune cell isolation, *ex vivo* manipulation and reinfusion.⁶²

The CCA TME contains a CD8⁺ cytotoxic T cell population inhibited by an immunosuppressive environment with regulatory T cells, indicating immunotherapy might provide effective activation of the suppressed anti-tumor immunity.^{12, 16, 21} A select number of early phase clinical trials investigating ICIs in unselected advanced CCA has been completed, while many clinical trials are ongoing.⁶³ PD-1 inhibitors pembrolizumab and nivolumab provide objective responses in a subset of 3-22% of advanced CCA patients, and importantly, the responders show prolonged effects up to several years.⁶⁴⁻⁶⁶ To increase the efficacy of immunotherapy, many trials are ongoing to examine combination therapy with other immunotherapeutics, targeted therapies, chemotherapy or locoregional therapy.⁶³ Combining ICIs with chemotherapy seems to improve the objective response rate to 36-56% in early studies, although toxicity is more prominent, potentially leading to discontinuation of treatment.^{65, 67} Combining multiple ICIs, inhibiting both PD-1 by nivolumab and CTLA-4 by ipilimumab, displayed an objective response rate of 23% in advanced iCCA patients, again with prolonged duration of response.⁶⁸

A small subset of <5% of CCA patients with high microsatellite instability or mismatch repair deficiency might be specifically sensitive to immunotherapy.^{37, 39, 69} These patients harbor a large amount of mutations that in turn provide many neo-antigens to stimulate the immune system. Pembrolizumab was shown highly effective in this patient group and was subsequently approved by the FDA.^{17, 70}

Altogether, immunotherapy for CCA is an emerging field that holds promise. PD-1 and CTLA-4 checkpoint inhibitors seem to induce durable responses, albeit only in small subgroups of CCA patients. It is important to develop a better understanding of why these tumors respond well, while others do not. This will advance the discovery of biomarkers for immunotherapy response and help to stratify patients. Preclinical models that incorporate both the tumor cell and the immune system compartments could aid in the development of new immunotherapies for CCA, either as monotherapy or combined with other drugs, and to further our understanding of tumor immunity so patient stratification will be more precise.

Modelling CCA with patient-derived organoids

Organoids

The first organoid culture system was developed over a decade ago, when a 3-dimensional (3D) long-term culture was established from murine small-intestinal stem cells which closely resembled crypt-villus units.⁷¹ These intestinal stem cells are marked by expression of the leucine-rich repeat-containing G-protein coupled receptor 5 (Lgr5). The Lgr5-positive cells were shown to be multipotent stem cells able to form all cell types of the intestinal epithelium by lineage tracing.⁷² *In vitro*, these adult stem cells were cultured in a specific mouse-derived hydrogel, Matrigel™. This hydrogel acts as a basement membrane substitute, allowing cells to organize into 3D crypt-villus units containing both self-renewing stem cells and differentiated cells of all intestinal epithelial lineages.⁷¹ Adaptations to this culture method has allowed organoid culture from many stem cell sources, including neonatal and adult tissues and pluripotent stem cells of human or other mammalian species, which were concisely reviewed earlier.⁷³ As this field of research grows rapidly, a clear-cut definition of the term organoids is essential. Marsee, Roos *et al.* defined an organoid as a “Three-dimensional structure derived from (pluripotent) stem cells, progenitor and/or differentiated cells that self-organize through cell-cell and cell-matrix interactions to recapitulate aspects of the native tissue architecture and function *in vitro*.”⁷⁴ This diverse culture system is remarkably suitable for many purposes. Because of their stem cell origin, organoids are a fitting model to study developmental biology.^{75, 76} Additionally, organoids can be used for drug screening, and tissue engineering purposes.⁷⁷⁻⁷⁹ Furthermore, organoids were used as a model system for many diseases, ranging from infectious diseases to monogenic and more complex diseases, including several types of cancer.^{76, 80-84} These disease models can be used to study disease mechanisms and discover new diagnostic, therapeutic and prognostic approaches.

Cholangiocarcinoma organoids

Over 30 years ago, the first *in vitro* CCA model was established by Yamaguchi *et al.* in the form of CCA cell line HChol-Y1.⁸⁵ In the following decades, a range of CCA cell lines was generated and applied to expand our knowledge on CCA. In more recent years, the poor clinical translational value of cell lines has encouraged researchers to explore new ways of cancer modelling. Primary cultures were established and alongside cell lines, they were employed to culture 3D spheroids to better mimic the tumor architecture and allow for intercellular and cell-matrix interactions.⁸⁶ However, the cells comprising these spheroids

are still produced in 2D culture, with its high selective pressure, and can only be obtained from a part of the subset of CCAs that is resected.

Recently, an innovative 3D patient-derived CCA organoid model system was established from resected specimens and core needle biopsies.^{87,88} CCA organoids are able to overcome several of the drawbacks of 2D cell culture and spheroids.^{87,88} They histopathologically resemble the patient tumor, both in culture and upon xenografting in immune deficient mice.⁸⁷⁻⁹⁰ Moreover, whole exome sequencing revealed that over 80% of the mutations were retained when organoids were derived from resected tissues, while mutation retention in biopsy-derived organoids varied from 20% to 90%.⁸⁷⁻⁹¹ Also, gene expression profiles partly reflected their parental tumors, even while the organoids only consist of epithelial cancer cells.^{87,89,91} Initial reports on establishment efficiency were high, documenting 75% (3/4) efficiency from resected tissue biopsies and 60% (3/5) from core needle biopsies.^{87,88} A recent international multicenter analysis demonstrated that the actual establishment efficiency is lower, demonstrating successful CCA organoid establishment for 36% (31/86) of patients.⁹² Clearly, this limited establishment efficiency currently compromises the potential for precision medicine and patient stratification.

Drug screening using a 29 compound library was performed in CCA organoids derived from two different patients and showed proof-of-concept for drug testing and personalized medicine applications, identifying ERK1/2 inhibitors as a potentially effective treatment for one CCA patient, causing growth inhibition in both organoids and organoid-derived xenografts.⁸⁷ Later, a 339 compound screen was performed in one iCCA organoid line, demonstrating high throughput application of CCA organoids that identified 22 potentially effective drugs.⁸⁹ The same study demonstrated that CCA organoids could be used to identify biomarkers for patient stratification, linking gene expression to drug sensitivity.⁸⁹ CCA organoids were also utilized to identify the role of intratumor heterogeneity in drug screening. 129 FDA-approved compounds were screened in 5-6 organoid lines per patient. Although part of the compounds were effective in all organoid lines included, a subset of compounds was only effective in part of the patient-specific organoid lines, demonstrating intratumoral heterogeneity in drug response, which was also reflected in different mutational profiles.⁹³ This advocates for the establishment of multiple organoid cultures of different tumor regions to model all facets of the patient tumors. Furthermore, CCA organoid technology was applied to demonstrate that CCA organoids have a limited capacity to differentiate towards hepatocytes using a differentiation protocol developed for healthy human liver organoids.^{94,95}

As CCA organoids are a novel source of *in vitro* cancer cells, its translational value has not yet been established. First proof of clinical predictive value of cancer organoids was demonstrated with gastrointestinal cancer organoids. They were able to predict chemotherapy and targeted therapy responses in patients with 100% sensitivity and 93% specificity.⁹⁶ The first clinical trial where the personalized effects of stereotactic body radiation therapy will be compared in patients and in patient-derived CCA organoids is currently ongoing.⁹⁷

Despite the clear benefits of the CCA organoid model, providing a long-term 3D biologically representable patient-specific tumor model, it also holds some limitations. At present, it only includes the epithelial cancer cells, which are cultured in a basement membrane substitute that does not reflect the composition of the ECM of CCAs. Thus, it lacks key components of the CCA TME, with its relevant cell types including CAFs, immune cells and endothelial cells, and the extensive desmoplastic stroma.¹² Recently, CAFs were successfully incorporated in the CCA organoid model, which resulted in increased CCA cell proliferation *in vitro* and upon xenografting *in vivo*, in accordance with previous studies.⁹⁸ CAF co-culture also decreased CCA organoid sensitivity to chemotherapeutics, highlighting the importance to add relevant components of the TME to drug screening models.⁹⁸ Organoid culture in an environment that better reflects the original ECM could improve the biological resemblance of the model and allow the study of interactions between cancer cells and the ECM. Moreover, the immune cells would be an important component to add to the CCA organoid model to be able to explore immunotherapy with CCA organoids.

Although clinical applicability is an avenue that needs to be further explored for CCA organoids, they are a promising new 3D *in vitro* model faithfully recapitulating the epithelial cancer cell component of the patient tumor. CCA organoids could provide insight into CCA cancer biology and may aid in the discovery and stratification of promising new CCA therapies, potentially complemented with components of the TME.

1 THESIS OUTLINE

The aim of my thesis is to extend the current CCA organoid model by 1) investigating bile as a new source of CCA organoids, 2) identifying therapeutic targets and providing patient stratification by applying new techniques to the model, and 3) adding the immune cell and extracellular matrix components of the tumor microenvironment to the model to facilitate research of a broader range of cancer therapeutics and provide a more faithful model of the patient tumor.

In **Chapter 2**, bile is explored as an alternative source for cholangiocyte organoids. Bile organoids are established, characterized and compared to the well-established intrahepatic and extrahepatic cholangiocyte organoids. It is known that cancer cells are present in bile of CCA patients.⁹⁹⁻¹⁰¹ In the future, bile could form a new minimally invasive source of CCA organoids. In **Chapter 3**, the novel technique of kinome profiling is applied to investigate kinase activity patterns in CCA organoids. The kinome profiles of tumor and healthy organoids are compared to determine potential druggable targets. A library of targeted therapeutics is screened in CCA organoids, and an attempt is made to identify kinases that could provide patient stratification by predicting drug responses. In **Chapter 4**, the proliferative capacity of primary sclerosing cholangitis (PSC)-related CCA as compared to sporadic CCA is studied. Specifically, the effect of PSC-associated pro-inflammatory cytokines on CCA organoid proliferation is investigated to determine the role of the chronic inflammatory environment, which identifies IL-17A as a potential therapeutic target. **Chapter 5** describes the combination of immune cells and CCA organoids as a model for immunotherapy research. Co-culture conditions are determined and effects of both direct and indirect immune cell-CCA organoid interactions are studied. In **Chapter 6**, CCA organoids are cultured with decellularized tumor and healthy liver extracellular matrix to ascertain if this model is able to better mimic the patient tumor and to study the interaction of cancer cells and the surrounding environment. Finally, in **Chapter 7**, I discuss and summarize the results of the studies included in this thesis and provide a future outlook of the use of the CCA organoid model.

REFERENCES

1. Banales JM, Marin JGG, *et al.* Cholangiocarcinoma 2020: the next horizon in mechanisms and management. *Nat Rev Gastroenterol Hepatol*, 2020. 17(9):557-88.
2. Banales JM, Cardinale V, *et al.* Expert consensus document: Cholangiocarcinoma: current knowledge and future perspectives consensus statement from the European Network for the Study of Cholangiocarcinoma (ENS-CCA). *Nat Rev Gastroenterol Hepatol*, 2016. 13(5):261-80.
3. Khan SA, Tavolari S, *et al.* Cholangiocarcinoma: Epidemiology and risk factors. *Liver Int*, 2019. 39 Suppl 1:19-31.
4. Saha SK, Zhu AX, *et al.* Forty-Year Trends in Cholangiocarcinoma Incidence in the U.S.: Intrahepatic Disease on the Rise. *Oncologist*, 2016. 21(5):594-9.
5. West J, Wood H, *et al.* Trends in the incidence of primary liver and biliary tract cancers in England and Wales 1971-2001. *Br J Cancer*, 2006. 94(11):1751-8.
6. Valle JW, Kelley RK, *et al.* Biliary tract cancer. *Lancet*, 2021. 397(10272):428-44.
7. Palmer WC, Patel T. Are common factors involved in the pathogenesis of primary liver cancers? A meta-analysis of risk factors for intrahepatic cholangiocarcinoma. *Journal of Hepatology*, 2012. 57(1):69-76.
8. Bertuccio P, Bosetti C, *et al.* A comparison of trends in mortality from primary liver cancer and intrahepatic cholangiocarcinoma in Europe. *Ann Oncol*, 2013. 24(6):1667-74.
9. Bertuccio P, Malvezzi M, *et al.* Global trends in mortality from intrahepatic and extrahepatic cholangiocarcinoma. *Journal of hepatology*, 2019. 71(1):104-14.
10. Sirica AE, Gores GJ. Desmoplastic stroma and cholangiocarcinoma: clinical implications and therapeutic targeting. *Hepatology*, 2014. 59(6):2397-402.
11. Carpino G, Overi D, *et al.* Matrisome analysis of intrahepatic cholangiocarcinoma unveils a peculiar cancer-associated extracellular matrix structure. *Clin Proteomics*, 2019. 16:37.
12. Fabris L, Sato K, *et al.* The Tumor Microenvironment in Cholangiocarcinoma Progression. *Hepatology*, 2021. 73 Suppl 1:75-85.
13. Winkler J, Abisoye-Ogunniyan A, *et al.* Concepts of extracellular matrix remodelling in tumour progression and metastasis. *Nature Communications*, 2020. 11(1):5120.
14. Sahai E, Astsaturov I, *et al.* A framework for advancing our understanding of cancer-associated fibroblasts. *Nat Rev Cancer*, 2020. 20(3):174-86.
15. Monteran L, Erez N. The Dark Side of Fibroblasts: Cancer-Associated Fibroblasts as Mediators of Immunosuppression in the Tumor Microenvironment. *Front Immunol*, 2019. 10:1835.
16. Zhang M, Yang H, *et al.* Single-cell transcriptomic architecture and intercellular crosstalk of human intrahepatic cholangiocarcinoma. *J Hepatol*, 2020. 73(5):1118-30.
17. Loeuillard E, Conboy CB, *et al.* Immunobiology of cholangiocarcinoma. *JHEP Rep*, 2019. 1(4):297-311.
18. Loeuillard E, Yang J, *et al.* Targeting tumor-associated macrophages and granulocytic myeloid-derived suppressor cells augments PD-1 blockade in cholangiocarcinoma. *The Journal of clinical investigation*, 2020. 130(10):5380-96.
19. Goepfert B, Frauenschuh L, *et al.* Prognostic impact of tumour-infiltrating immune cells on biliary tract cancer. *British journal of cancer*, 2013. 109(10):2665-74.
20. Xia T, Li K, *et al.* Immune cell atlas of cholangiocarcinomas reveals distinct tumor microenvironments and associated prognoses. *J Hematol Oncol*, 2022. 15(1):37.
21. Zhou G, Sprengers D, *et al.* Reduction of immunosuppressive tumor microenvironment in cholangiocarcinoma by ex vivo targeting immune checkpoint molecules. *J Hepatol*, 2019. 71(4):753-62.
22. Cillo U, Fondevila C, *et al.* Surgery for cholangiocarcinoma. *Liver Int*, 2019. 39 Suppl 1:143-55.
23. Mavros MN, Economopoulos KP, *et al.* Treatment and Prognosis for Patients With Intrahepatic Cholangiocarcinoma: Systematic Review and Meta-analysis. *JAMA Surg*, 2014. 149(6):565-74.

24. Rosen CB, Heimbach JK, *et al.* Liver transplantation for cholangiocarcinoma. *Transplant International*, 2010. 23(7):692-7.
25. Murad SD, Kim WR, *et al.* Efficacy of neoadjuvant chemoradiation, followed by liver transplantation, for perihilar cholangiocarcinoma at 12 US centers. *Gastroenterology*, 2012. 143(1):88-98. e3.
26. Sapisochin G, Facciuto M, *et al.* Liver transplantation for "very early" intrahepatic cholangiocarcinoma: International retrospective study supporting a prospective assessment. *Hepatology*, 2016. 64(4):1178-88.
27. Ebata T, Hirano S, *et al.* Randomized clinical trial of adjuvant gemcitabine chemotherapy versus observation in resected bile duct cancer. *Journal of British Surgery*, 2018. 105(3):192-202.
28. Edeline J, Benabdelghani M, *et al.* Gemcitabine and oxaliplatin chemotherapy or surveillance in resected biliary tract cancer (PRODIGE 12-ACCORD 18-UNICANCER G1): a randomized phase III study. *Journal of Clinical Oncology*, 2019. 37(8):658-67.
29. Primrose JN, Fox RP, *et al.* Capecitabine compared with observation in resected biliary tract cancer (BILCAP): a randomised, controlled, multicentre, phase 3 study. *The Lancet Oncology*, 2019. 20(5):663-73.
30. Shroff RT, Kennedy EB, *et al.* Adjuvant therapy for resected biliary tract cancer: ASCO clinical practice guideline. *Journal of Clinical Oncology*, 2019. 37(12):1015-27.
31. Ben-Josef E, Guthrie KA, *et al.* SWOG S0809: a phase II intergroup trial of adjuvant capecitabine and gemcitabine followed by radiotherapy and concurrent capecitabine in extrahepatic cholangiocarcinoma and gallbladder carcinoma. *Journal of Clinical Oncology*, 2015. 33(24):2617.
32. Valle J, Wasan H, *et al.* Cisplatin plus gemcitabine versus gemcitabine for biliary tract cancer. *New England Journal of Medicine*, 2010. 362(14):1273-81.
33. Okusaka T, Nakachi K, *et al.* Gemcitabine alone or in combination with cisplatin in patients with biliary tract cancer: a comparative multicentre study in Japan. *Br J Cancer*, 2010. 103(4):469-74.
34. Valle JW, Furuse J, *et al.* Cisplatin and gemcitabine for advanced biliary tract cancer: a meta-analysis of two randomised trials. *Annals of oncology*, 2014. 25(2):391-8.
35. Lamarca A, Palmer DH, *et al.* ABC-06 | A randomised phase III, multi-centre, open-label study of active symptom control (ASC) alone or ASC with oxaliplatin/5-FU chemotherapy (ASC+ mFOLFOX) for patients (pts) with locally advanced/metastatic biliary tract cancers (ABC) previously-treated with cisplatin/gemcitabine (CisGem) chemotherapy. *Journal of Clinical Oncology*, 2019. 37(15_suppl):4003.
36. Keane FK, Zhu AX, *et al.*: Radiotherapy for biliary tract cancers *Seminars in Radiation Oncology* 2018; 28:342-50.
37. Nakamura H, Arai Y, *et al.* Genomic spectra of biliary tract cancer. *Nature genetics*, 2015. 47(9):1003-10.
38. Lamarca A, Barriuso J, *et al.* Molecular targeted therapies: Ready for "prime time" in biliary tract cancer. *J Hepatol*, 2020. 73(1):170-85.
39. Weinberg BA, Xiu J, *et al.* Molecular profiling of biliary cancers reveals distinct molecular alterations and potential therapeutic targets. *J Gastrointest Oncol*, 2019. 10(4):652-62.
40. Zhu AX, Meyerhardt JA, *et al.* Efficacy and safety of gemcitabine, oxaliplatin, and bevacizumab in advanced biliary-tract cancers and correlation of changes in 18-fluorodeoxyglucose PET with clinical outcome: a phase 2 study. *The lancet oncology*, 2010. 11(1):48-54.
41. Valle JW, Wasan H, *et al.* Cediranib or placebo in combination with cisplatin and gemcitabine chemotherapy for patients with advanced biliary tract cancer (ABC-03): a randomised phase 2 trial. *The Lancet Oncology*, 2015. 16(8):967-78.
42. Malka D, Cervera P, *et al.* Gemcitabine and oxaliplatin with or without cetuximab in advanced biliary-tract cancer (BINGO): a randomised, open-label, non-comparative phase 2 trial. *The lancet oncology*, 2014. 15(8):819-28.

43. Leone F, Marino D, *et al.* Panitumumab in combination with gemcitabine and oxaliplatin does not prolong survival in wild-type KRAS advanced biliary tract cancer: A randomized phase 2 trial (Vecti-BIL study). *Cancer*, 2016. 122(4):574-81.
44. Lee J, Park SH, *et al.* Gemcitabine and oxaliplatin with or without erlotinib in advanced biliary-tract cancer: a multicentre, open-label, randomised, phase 3 study. *The lancet oncology*, 2012. 13(2):181-8.
45. Bridgewater J, Lopes A, *et al.* A phase 1b study of selumetinib in combination with cisplatin and gemcitabine in advanced or metastatic biliary tract cancer: the ABC-04 study. *BMC cancer*, 2016. 16(1):1-9.
46. Ahn DH, Li J, *et al.* Results of an abbreviated phase-II study with the Akt Inhibitor MK-2206 in Patients with Advanced Biliary Cancer. *Scientific reports*, 2015. 5(1):1-8.
47. Peck J, Wei L, *et al.* HER2/neu may not be an interesting target in biliary cancers: results of an early phase II study with lapatinib. *Oncology*, 2012. 82(3):175-9.
48. Verlingue L, Malka D, *et al.* Precision medicine for patients with advanced biliary tract cancers: An effective strategy within the prospective MOSCATO-01 trial. *European Journal of Cancer*, 2017. 87:122-30.
49. Farshidfar F, Zheng S, *et al.* Integrative Genomic Analysis of Cholangiocarcinoma Identifies Distinct IDH-Mutant Molecular Profiles. *Cell Rep*, 2017. 18(11):2780-94.
50. Rizvi S, Khan SA, *et al.* Cholangiocarcinoma—evolving concepts and therapeutic strategies. *Nature reviews Clinical oncology*, 2018. 15(2):95-111.
51. Goyal L, Kongpetch S, *et al.* Targeting FGFR inhibition in cholangiocarcinoma. *Cancer treatment reviews*, 2021. 95:102170.
52. Boscoe AN, Rolland C, *et al.* Frequency and prognostic significance of isocitrate dehydrogenase 1 mutations in cholangiocarcinoma: a systematic literature review. *Journal of gastrointestinal oncology*, 2019. 10(4):751.
53. Abou-Alfa GK, Sahai V, *et al.* Pemigatinib for previously treated, locally advanced or metastatic cholangiocarcinoma: a multicentre, open-label, phase 2 study. *The Lancet Oncology*, 2020. 21(5):671-84.
54. Abou-Alfa GK, Macarulla T, *et al.* Ivosidenib in IDH1-mutant, chemotherapy-refractory cholangiocarcinoma (ClarIDHy): a multicentre, randomised, double-blind, placebo-controlled, phase 3 study. *Lancet Oncol*, 2020. 21(6):796-807.
55. Zhu AX, Macarulla T, *et al.* Final Overall Survival Efficacy Results of Ivosidenib for Patients With Advanced Cholangiocarcinoma With IDH1 Mutation: The Phase 3 Randomized Clinical ClarIDHy Trial. *JAMA Oncol*, 2021. 7(11):1669-77.
56. FDA. FDA grants accelerated approval to pemigatinib for cholangiocarcinoma with an FGFR2 rearrangement or fusion. <https://www.fda.gov/drugs/resources-information-approved-drugs/fda-grants-accelerated-approval-pemigatinib-cholangiocarcinoma-fgfr2-rearrangement-or-fusion-2022>.
57. FDA. FDA approves ivosidenib for advanced or metastatic cholangiocarcinoma. <https://www.fda.gov/drugs/resources-information-approved-drugs/fda-approves-ivosidenib-advanced-or-metastatic-cholangiocarcinoma-2022>.
58. Schadendorf D, Hodi FS, *et al.* Pooled analysis of long-term survival data from phase II and phase III trials of ipilimumab in unresectable or metastatic melanoma. *Journal of clinical oncology*, 2015. 33(17):1889.
59. Motzer RJ, Escudier B, *et al.* Nivolumab versus everolimus in advanced renal-cell carcinoma. *New England Journal of Medicine*, 2015. 373(19):1803-13.
60. Borghaei H, Paz-Ares L, *et al.* Nivolumab versus docetaxel in advanced nonsquamous non-small-cell lung cancer. *New England Journal of Medicine*, 2015. 373(17):1627-39.
61. Rosenberg JE, Hoffman-Censits J, *et al.* Atezolizumab in patients with locally advanced and metastatic urothelial carcinoma who have progressed following treatment with platinum-based chemotherapy: a single-arm, multicentre, phase 2 trial. *The Lancet*, 2016. 387(10031):1909-20.

62. Martin-Liberal J, Ochoa de Olza M, *et al.* The expanding role of immunotherapy. *Cancer Treat Rev*, 2017. 54:74-86.
63. Charalampakis N, Papageorgiou G, *et al.* Immunotherapy for cholangiocarcinoma: a 2021 update. *Immunotherapy*, 2021. 13(13):1113-34.
64. Piha-Paul SA, Oh DY, *et al.* Efficacy and safety of pembrolizumab for the treatment of advanced biliary cancer: Results from the KEYNOTE-158 and KEYNOTE-028 studies. *Int J Cancer*, 2020. 147(8):2190-8.
65. Ueno M, Ikeda M, *et al.* Nivolumab alone or in combination with cisplatin plus gemcitabine in Japanese patients with unresectable or recurrent biliary tract cancer: a non-randomised, multicentre, open-label, phase 1 study. *The lancet Gastroenterology & hepatology*, 2019. 4(8):611-21.
66. Kim RD, Chung V, *et al.* A Phase 2 Multi-institutional Study of Nivolumab for Patients With Advanced Refractory Biliary Tract Cancer. *JAMA Oncol*, 2020. 6(6):888-94.
67. Feng K, Liu Y, *et al.* Efficacy and biomarker analysis of nivolumab plus gemcitabine and cisplatin in patients with unresectable or metastatic biliary tract cancers: Results from a phase II study. *Journal for immunotherapy of cancer*, 2020. 8(1).
68. Klein O, Kee D, *et al.* Evaluation of Combination Nivolumab and Ipilimumab Immunotherapy in Patients With Advanced Biliary Tract Cancers: Subgroup Analysis of a Phase 2 Nonrandomized Clinical Trial. *JAMA Oncol*, 2020. 6(9):1405-9.
69. Rizzo A, Ricci AD, *et al.* PD-L1, TMB, MSI, and other predictors of response to immune checkpoint inhibitors in biliary tract cancer. *Cancers*, 2021. 13(3):558.
70. Le DT, Durham JN, *et al.* Mismatch repair deficiency predicts response of solid tumors to PD-1 blockade. *Science*, 2017. 357(6349):409-13.
71. Sato T, Vries RG, *et al.* Single Lgr5 stem cells build crypt-villus structures in vitro without a mesenchymal niche. *Nature*, 2009. 459(7244):262-5.
72. Barker N, Van Es JH, *et al.* Identification of stem cells in small intestine and colon by marker gene Lgr5. *Nature*, 2007. 449(7165):1003-7.
73. Clevers H. Modeling development and disease with organoids. *Cell*, 2016. 165(7):1586-97.
74. Marsee A, Roos FJM, *et al.* Building consensus on definition and nomenclature of hepatic, pancreatic, and biliary organoids. *Cell Stem Cell*, 2021. 28(5):816-32.
75. Shyer AE, Huycke TR, *et al.* Bending gradients: how the intestinal stem cell gets its home. *Cell*, 2015. 161(3):569-80.
76. Lancaster MA, Renner M, *et al.* Cerebral organoids model human brain development and microcephaly. *Nature*, 2013. 501(7467):373-9.
77. Takasato M, Er PX, *et al.* Kidney organoids from human iPS cells contain multiple lineages and model human nephrogenesis. *Nature*, 2015. 526(7574):564-8.
78. Sampaziotis F, Muraro D, *et al.* Cholangiocyte organoids can repair bile ducts after transplantation in the human liver. *Science*, 2021. 371(6531):839-46.
79. Willemse J, Roos FJM, *et al.* Scaffolds obtained from decellularized human extrahepatic bile ducts support organoids to establish functional biliary tissue in a dish. *Biotechnol Bioeng*, 2021. 118(2):836-51.
80. Schwank G, Koo B-K, *et al.* Functional repair of CFTR by CRISPR/Cas9 in intestinal stem cell organoids of cystic fibrosis patients. *Cell stem cell*, 2013. 13(6):653-8.
81. McCracken KW, Catá EM, *et al.* Modelling human development and disease in pluripotent stem-cell-derived gastric organoids. *Nature*, 2014. 516(7531):400-4.
82. Forbester JL, Goulding D, *et al.* Interaction of Salmonella enterica serovar Typhimurium with intestinal organoids derived from human induced pluripotent stem cells. *Infection and immunity*, 2015. 83(7):2926-34.
83. Boj SF, Hwang CI, *et al.* Organoid models of human and mouse ductal pancreatic cancer. *Cell*, 2015. 160(1-2):324-38.

84. van de Wetering M, Francies HE, *et al.* Prospective derivation of a living organoid biobank of colorectal cancer patients. *Cell*, 2015. 161(4):933-45.
85. Yamaguchi N, Morioka H, *et al.* Establishment and characterization of the human cholangiocarcinoma cell line HChol-Y1 in a serum-free, chemically defined medium. *Journal of the National Cancer Institute*, 1985. 75(1):29-35.
86. Friedrich J, Seidel C, *et al.* Spheroid-based drug screen: considerations and practical approach. *Nature Protocols*, 2009. 4(3):309-24.
87. Broutier L, Mastrogianni G, *et al.* Human primary liver cancer-derived organoid cultures for disease modeling and drug screening. *Nat Med*, 2017. 23(12):1424-35.
88. Nuciforo S, Fofana I, *et al.* Organoid Models of Human Liver Cancers Derived from Tumor Needle Biopsies. *Cell Rep*, 2018. 24(5):1363-76.
89. Saito Y, Muramatsu T, *et al.* Establishment of Patient-Derived Organoids and Drug Screening for Biliary Tract Carcinoma. *Cell Rep*, 2019. 27(4):1265-76 e4.
90. Maier CF, Zhu L, *et al.* Patient-Derived Organoids of Cholangiocarcinoma. *Int J Mol Sci*, 2021. 22(16).
91. Lampis A, Carotenuto P, *et al.* MIR21 drives resistance to heat shock protein 90 inhibition in cholangiocarcinoma. *Gastroenterology*, 2018. 154(4):1066-79. e5.
92. van Tienderen GS, Li L, *et al.* Hepatobiliary tumor organoids for personalized medicine: a multicenter view on establishment, limitations, and future directions. *Cancer Cell*, 2022. 40(3):226-30.
93. Li L, Knutsdottir H, *et al.* Human primary liver cancer organoids reveal intratumor and interpatient drug response heterogeneity. *JCI insight*, 2019. 4(2).
94. Saito Y, Nakaoka T, *et al.* Induction of differentiation of intrahepatic cholangiocarcinoma cells to functional hepatocytes using an organoid culture system. *Scientific reports*, 2018. 8(1):1-15.
95. Huch M, Gehart H, *et al.* Long-term culture of genome-stable bipotent stem cells from adult human liver. *Cell*, 2015. 160(1-2):299-312.
96. Vlachogiannis G, Hedayat S, *et al.* Patient-derived organoids model treatment response of metastatic gastrointestinal cancers. *Science*, 2018. 359(6378):920-6.
97. Koedijk MS, Heijmen BJM, *et al.* Protocol for the STRONG trial: stereotactic body radiation therapy following chemotherapy for unresectable perihilar cholangiocarcinoma, a phase I feasibility study. *BMJ Open*, 2018. 8(10):e020731.
98. Liu J, Li P, *et al.* Cancer-Associated Fibroblasts Provide a Stromal Niche for Liver Cancer Organoids That Confers Trophic Effects and Therapy Resistance. *Cell Mol Gastroenterol Hepatol*, 2021. 11(2):407-31.
99. Kurzawinski TR, Deery A, *et al.* A prospective study of biliary cytology in 100 patients with bile duct strictures. *Hepatology*, 1993. 18(6):1399-403.
100. Hung LY, Chiang NJ, *et al.* A Microfluidic Chip for Detecting Cholangiocarcinoma Cells in Human Bile. *Sci Rep*, 2017. 7(1):4248.
101. Sugimoto S, Matsubayashi H, *et al.* Diagnosis of bile duct cancer by bile cytology: usefulness of post-brushing biliary lavage fluid. *Endosc Int Open*, 2015. 3(4):E323-8.

CHAPTER

2

Cholangiocyte organoids from human bile retain a local phenotype and can repopulate bile ducts *in vitro*

Floris J.M. Roos^{1*}, Haoyu Wu^{2*}, Ruby Lieshout^{1#}, Jorke Willemse^{1#}, Laura A. Muñoz Albarinos¹, Yik Yang Kan¹, Jan-Werner Poley³, Marco J. Bruno³, Jeroen de Jonge¹, Richard Bártfai², Hendrik Marks², Jan N.M. IJzermans¹, Monique M.A. Verstegen^{1x} & Luc J.W. van der Laan^{1x}

**These authors contributed equally*

#These authors contributed equally

xThese authors contributed equally

¹Erasmus MC Transplant Institute, Department of Surgery, Erasmus University Medical Center, Rotterdam, The Netherlands

²Department of Molecular Biology, Radboud University, Nijmegen, The Netherlands

³Department of Gastroenterology and Hepatology, Erasmus University Medical Center, Rotterdam, The Netherlands

ABSTRACT

The well-established 3D organoid culture method enabled efficient expansion of cholangiocyte-like cells from intrahepatic-(IHBD) and extrahepatic bile duct (EHBD) tissue biopsies. The extensive expansion capacity of these organoids enables various applications, from cholangiocyte disease modelling to bile duct tissue engineering. Recent research demonstrated feasibility of culturing cholangiocyte organoids from bile, which was minimal-invasive collected via endoscopic retrograde pancreaticography (ERCP). However, a detailed analysis of these bile-cholangiocyte organoids (BCOs) and the cellular region of origin was not yet demonstrated. In this study, we characterize BCOs and mirror them to the already established organoids initiated from IHBD- and EHBD-tissue. We demonstrate successful organoid-initiation from extrahepatic bile collected from gallbladder after resection and by ERCP or percutaneous transhepatic cholangiopathy from a variety of patients.

BCOs initiated from these three sources of bile all show features similar to *in vivo* cholangiocytes. The regional-specific characteristics of the BCOs are reflected by the exclusive expression of regional common bile duct genes (HOXB2 and HOXB3) by ERCP-derived BCOs and gallbladder-derived BCOs expressing gallbladder-specific genes. Moreover, BCOs have limited hepatocyte-fate differentiation potential compared to intrahepatic cholangiocyte organoids. These results indicate that organoid-initiating cells in bile are likely of local (extrahepatic) origin and are not of intrahepatic origin. Regarding functionality of organoid initiating cells in bile, we demonstrate that BCOs efficiently repopulate decellularized EHBD scaffolds and restore the monolayer of cholangiocyte-like cells *in vitro*.

Conclusion: Bile samples obtained through minimally-invasive procedures provide a safe and effective alternative source of cholangiocyte organoids. The shedding of (organoid-initiating) cholangiocytes in bile provides a convenient source of organoids for regenerative medicine.

INTRODUCTION

The biliary tree is a complex tubular system representing the extrahepatic bile duct (EHBD) and the intrahepatic bile ducts (IHBD).¹ In addition to the difference in anatomical location, both these ductal structures originate from distinct progenitor cells during embryogenic development.² The IHBD arises from bipotential hepatoblasts, while the EHBD develops from a shared pancreaticobiliary progenitor.^{2,3} Despite the divergent origin, a single layer of highly specialized epithelial cells, cholangiocytes, are lining the ducts of the entire biliary tree.¹ Cholangiocytes are responsible for modifying bile composition and form an important barrier between the cytotoxic bile and surrounding tissues. Defects in cholangiocytes can result in severe diseases (cholangiopathies), often developing into end-stage liver diseases, for which liver transplantation is the only curative therapy.³ The regional diversity present in cholangiocytes is also reflected in different cholangiopathies.^{4,5} For instance, Alagille Syndrome is only affecting intrahepatic cholangiocytes, in line with the underlying autosomal mutation that prevents proper hepatoblast differentiation towards intrahepatic bile ducts. Other examples are primary sclerosing cholangitis (PSC) and non-anastomotic bile duct strictures, diseases that are predominantly affecting the EHBD.⁴⁻⁶ The presence of regional diversity in the extrahepatic biliary tree was recently confirmed by Rimland *et al.*, where the authors showed distinct gene-expression profiles in cholangiocytes covering different parts of the EHBD.⁷ In this study 3D cholangiocyte organoids were cultured from both IHBD and EHBD and it is demonstrated that only intrahepatic cholangiocyte organoids (ICOs) could (partially) differentiate towards hepatocyte-like cells. This result reflects the embryogenic origin of this type of cholangiocytes.⁷ Initially, cholangiocyte organoids were initiated from liver biopsies, and described as liver-derived bipotent stem cells *in vitro*.⁸ However, elaborated studies demonstrate that mature cholangiocytes, undergoing widespread (epi)genetic remodeling into a highly proliferative state, are the organoid-initiating cell type but not adult (biliary) stem cells. Due to canonical Wnt3-integration site(WNT)-stimulating culture conditions, cholangiocyte organoids start expressing adult stem cell markers/WNT-target genes (*LGR5*) which are substantially overexpressed when compared to *in vivo* cholangiocytes.⁹⁻¹² By doing so, cholangiocyte organoids acquire a phenotype comparable to rapid proliferating cholangiocytes *in vivo* (ductal reprogramming).

As ICOs maintain patient-specific characteristics upon expansion, they provide a powerful tool to study the biology and pathophysiology of cholangiocytes.⁸ The downside of this culture platform is that ICOs are generally initiated from liver biopsies which are collected during potentially harmful interventions, or during liver transplantation. This limits the use of COs in disease modeling and studying disease progression to a limited subset of patients, that is, patients that undergo liver transplantation due to end-stage liver disease. To overcome these hurdles, an elegant and minimally invasive alternative to initiate patient-specific organoids was shown by Soroka *et al.*¹³ Here, the authors expanded bile cholangiocyte organoids (BCOs) from bile samples collected during routine clinical procedures via endoscopic retrograde cholangiopancreatography (ERCP).¹³ However, it is still unclear from which region in the biliary tree (intra- or extra-hepatic) the BCO-initiating

cells originate from. Furthermore, a recent study demonstrated that cholangiocyte organoids derived from human EHBD and cultured in non-canonical WNT-stimulating conditions, could efficiently repopulate collagen scaffolds that were successfully transplanted into mice as functional EHBDs.¹⁴ However, whether this is feasible with patient-derived COs cultured in canonical-WNT stimulating conditions obtained from *in vivo* collected bile is still unknown.

Therefore, the aim of our study is to further characterize the properties of BCOs with a focus on determining the anatomical origin of BCOs. Moreover, in addition to ERCP as a source of BCOs, we extend the sources of bile with collection via percutaneous transhepatic cholangiopathy drainage (PTCD) and directly from resected gallbladders. As a proof of principle, we show efficient repopulation of human bile duct scaffolds using BCOs collected via ERCP from patients and demonstrate that human EHBD scaffold can help sustain organoids to form a functional cholangiocyte monolayer *in vitro*. Based upon this evidence, the feasibility for the use of BCOs in personalized regenerative medicine is near.

MATERIALS AND METHODS

Bile, brush and tissue collection

Bile samples (1 mL per patient) were obtained *in vivo* from patients suffering from biliary diseases (Table 1 and Table S1) and which were undergoing ERCP (n=54) or PTCD (n=3) for regular treatment regimens at the Erasmus MC, Rotterdam, the Netherlands. An additional brush specimen (n=2) was collected from the common bile duct (CBD) via ERCP if the patient already underwent brush cytology for standard diagnostics. Bile samples collected *in vivo* were transported at 4°C and processed within 1 hour after collection. All patients gave written informed consent to use the bile collected during these procedures for research purposes. This study was approved by the local Erasmus MC Medical Ethical Committee and registered under number MEC-2016-743.

Bile (3 mL) was collected from gallbladders from donor (n=6) or explanted livers (n=8) obtained during liver transplantation procedures performed at the Erasmus MC, Rotterdam and was stored at 4°C and processed within 24 hours after collection. All patients or next of kin gave written informed consent to use the tissue for research purposes. This study was approved by the local MEC of the Erasmus MC under number MEC-2014-060.

Tissue biopsies from liver (circa 0.5-3 cm³, n=4), extrahepatic bile duct (EHBD, circa 0.5-3 cm³, n=4), and gallbladders (n=3, scraped cells) were obtained from donor livers (n=5) or explant livers (n=2) during liver transplant procedures performed at the Erasmus MC, Rotterdam, the Netherlands. For complete methodology see supplementary materials and methods.

Initiation and culture expansion of organoids

Organoids from liver- and EHBD biopsies were processed, initiated and expanded as previously published by Rimland *et al.*⁷ and Huch *et al.*^{8, 15} For detailed methodology and culture conditions see Supplementary Materials and Methods and Table S2.

Organoids from bile (BCOs) were initiated according to an adapted protocol from Soroka *et al.*¹³ for culturing BCOs from bile collected via ERCP. For detailed methodology and culture conditions see supplementary material and methods and Table S2. All experiments were performed with passage five organoids unless otherwise stated. When referred to ECO-cultures in experiments, these cultures resemble canonical-WNT stimulated ECOs (tissue obtained according to Rimland *et al.* and cultured in the Huch *et al.* conditions, Table S2)^{7,8} unless otherwise stated.

Flow Cytometry

Flow cytometry analysis was performed to evaluate the presence and frequency of EPCAM⁺ cells in the collected bile samples from ERCP patients. Bile cells were stained with antibodies against human CD326 (EpCAM) (Biolegend 324203; mouse monoclonal – FITC conjugated, 1:100) according to the manufacturer's instructions. Flow cytometry analysis was performed using a Canto flow cytometer (BD Biosciences) and cell populations were analyzed using Flowjo (version v10.6.1, BD).

RNA extraction, cDNA synthesis and RT-qPCR

Total RNA was collected after removal of the culture medium by adding 700µL of QIAzol lysis reagent (Qiagen) to a 24 well containing organoids (two 25µL BME/matrigel domes). RNA was isolated using the miRNeasy kit (Qiagen) according to the manufacturer's protocol¹⁶ and the concentration was measured using a NANOdrop 2000 (ThermoFisher). cDNA from 500ng RNA was prepared using 5x PrimeScript RT Master Mix in a 2720 thermal cycler (Applied Biosystems). RT-qPCR was performed with the primer sets provided in Table S3. RT-qPCR data are presented as mean with a 95% confidence interval or as standard error of the mean. RT-qPCR values are relative to the housekeeping gene Glyceraldehyde-3-Phosphate Dehydrogenase (*GAPDH*) or Hypoxanthine-guanine-fofosforibosyl-transferase (*HPRT*).

Immunofluorescence (IF) staining

To evaluate protein expression of the organoids, IF was performed with selected antibodies for cytokeratin (KRT)-7, KRT-19, SRY Box (SOX)9, Albumin, Mucin-1 (MUC-1), Secretin Receptor (SCTR) and cystic fibrosis transmembrane conductance regulator (CFTR) (complete list of antibodies and dilutions used are displayed in Table S4), as previously described for ICOs.⁸ For detailed methodology see supplementary materials and methods.

Ussing chamber assay

COs cultured from tissue and bile were seeded on a transwell culture plate (24 well plate 6.5mm, Corning) to grow COs in a 2D fashion. Upon forming a confluent monolayer, transwells were placed in an Ussing chamber (Physiologic instruments) set up to analyze functional cholangiocyte-specific transporter channels (CFTR and Ca²⁺-activated Cl⁻ channel) using Acquire & Analyze Software 2.3 (Physiologic Instruments, San Diego, California). For detailed methodology see supplementary materials and methods.

γ -Glutamyltransferase assay

Supernatant (10 μ L) of BCOs (n=3) and, as a positive control, of ECOs cultured in non-canonical WNT conditions (n=3), was collected. These specific ECOs were chosen since they were shown to excrete the same amount of GGT as primary cholangiocytes.¹⁴ GGT activity was determined using a colorimetric assay kit (MAK089; Sigma-Aldrich), performed according to the manufacturer's protocol.

Rhodamine-123 transport functionality

Functionality of the Multi Drug Resistance (MDR)-1 transporter was assessed using the Rhodamine-123 assay.¹⁷ Specificity was determined by blocking MDR-1 transporter with Verapamil (10 μ M, Sigma Aldrich) for 30 min at 37 $^{\circ}$ C prior to Rhodamine-123 incubation (100 μ M, Sigma Aldrich). Subsequent confocal images were acquired using a Leica SP5 confocal microscope (LEICA) equipped with a 488 nm laser and a 20x zoom dipping lens.

Cell proliferation assessment

Cell proliferation characteristics of BCOs, ICOs and ECOs were measured by PrestoBlue Metabolic Assay (Life Technologies) and 5-Ethynyl-2'-deoxyuridine (EdU)-incorporation (ThermoFisher). For detailed methodology and gating strategy see supplementary materials and methods and Figure S3A and B.

RNA sequencing data obtaining and analysis

RNA was isolated from 3 biological replicates from different types of organoids (ERCP bile, GB bile, ICO, and ECO). 500 ng of total RNA was used for library construction using KAPA RNA Hyper + RiboErase HMR kit (Roche 08098140702). RNA-sequencing (RNAseq) libraries were sequenced paired-end (2 x 38bp) on Illumina NextSeq 500 platform. After sequencing, the qualities of the reads were checked using fastqc. An average of 20 million paired-end reads were aligned to human genome (hg38) using STAR¹⁸ (2.7.0f) with default settings. BAM files were sorted and indexed using SAMtools¹⁹ (1.7). The number of mapped fragments was quantified at gene level using featurecount²⁰ (1.6.4) with the following parameters, -p -g gene_name, based on Gencode annotation (v30). The R package DESeq2²¹ (1.22.2 on R 3.5.1) was used for differential gene expression analysis and for generating principal components analysis (PCA) and heatmap plots. Genes with less than 2 fragments were removed from the differential gene expression analysis. All the differentially expressed genes are determined according to adj- $P < 0.05$. Vst normalized counts were generated using vst function from DESeq2, and transformed to Z-scores. Pheatmap package was used to generate heatmap plots using either vst normalized counts or Z-scores as input. Pathway analyses were performed by Enrichr web tool²² using the significantly differentially expressed genes as input with default settings. RNAseq data from gallbladder- and common bile duct tissue as published by Rimland *et al.*⁷ was used as a reference gene set for cholangiocytes and RNAseq data from 2D cultured primary hepatocytes was obtained from Schneeberger *et al.*²³ as a reference gene set for hepatocyte gene-expression. For comparing the transcriptome between the ERCP-BCOs cultured in 3D (hydrogel) and ERCP-BCOs that were cultured on scaffolds, RNA samples were isolated from 3 biological replicates. The

library construction was done as mentioned before, and the libraries were sequenced pair-end (2x 42bp). The analysis was performed using the same strategy as mentioned before, but using the tools with different versions (STAR version=2.7.6a, SAMtools version=1.7, featureCounts version=2.0.1, R version=3.6.1, DEseq2 version=1.26.0). In particular, before generating the count table, subsampling was applied to have the samples with comparable sequencing depths using SAMtools. Differentially expressed genes are determined based on $\text{adj-}P < 0.05$ and $|\log_2(\text{Fold change})| > 1$. The R package *fgsea*²⁴ (1.12.0) was used for gene set enrichment analysis (GSEA). Genes up-regulated in either 3D (hydrogel, BME) or scaffold culture system were used as input, and then compared to the differentially gene set published by Rimland *et al.*⁷ (Tissue vs. organoid of common bile duct). Cell cycle related genes (involved in G2M and S phases) from R package *Seurat* (3.2.3)²⁵ were used for the heatmap. RNAseq data from this study was disposed to the GEO dataset (number: GSE156519).

Upregulation of hepatocyte-related genes

BCOs, ICOs and ECOs (from the same patient, n=3 individual patients) were differentiated towards hepatocyte-faith. The hepatocyte differentiation protocol used, was adapted from Huch *et al.*⁸ with slight modifications (Helmuth *et al.* patent: WO2017149025A1). For detailed methodology see supplementary materials and methods.

Repopulation of EHBD scaffolds

Decellularized human EHBD scaffolds were reseeded with BCOs. For this, EHBD tissue (n=3, length: 4cm) was obtained from research livers that were deemed unsuitable for transplantation. EHBD scaffolds were created according to the previously published protocol by Willemse *et al.*²⁶ using a Triton-X-100 based decellularisation method. EHBD scaffolds were reseeded with single-cells derived from ERCP-BCOs (passage 5-9) and cultured for 21 days. For detailed methodology see supplementary materials and methods.

Statistical analyses

All statistical analyses were conducted using SPSS (software version 21, SSPS Inc, Chicago, IL, USA). Qualitative data were analyzed with the χ^2 or Fisher exacts tests and were presented with numbers and percentages. Continuous variables were tested using an independent T-test or Mann-Whitney-U test and presented with normal distribution as means with standard deviation and if not normally distributed, they are presented as range. In all tests, a P value of < 0.05 is considered significant.

RESULTS

Human bile harbors organoid-initiating cells

Human bile was collected using the ERCP or PTCD procedure or from gallbladders after resection (Figure 1A, B). After obtaining and washing the cell fraction from bile, organoid cultures were initiated. Furthermore, cells obtained by CBD brushes were included and cultured as organoids.

BCOs could be initiated from healthy individuals as well as from a variety of patients with different underlying biliary diseases (Table 1 and Table S1), although with mixed success rates between sources. Upon initial issues with bacterial infections, vancomycin was added to the culture medium to prevent loss of cultures without losing viable cells (Figure S1). In addition, to prevent fungal infections, which were frequently observed in patients suffering from primary sclerosing cholangitis (PSC) or cholangiocarcinoma (CCA), BCO cultures of these patients were supplemented with 1% antibiotic-antimycotic instead of vancomycin for the first three days, as previously published.¹³ As shown in Figure 1C, after addition of treatment for micro-organisms, organoid-initiation was successful in 78% (42/54) of bile samples from ERCP. The success rate for brushes was 100% (2/2) and for bile samples from PTCD 67% (2/3). Organoids collected from *ex vivo* bile (resected gallbladders, >12 hours after surgery) could be cultured with a lower 33% (2/6) success rate. This is possibly due to the longer storage time of the bile as compared to the rapidly processed ERCP and PTCD bile (cultured within 1 hour after collection). Indeed, gallbladder bile processed within 12 hours after resection had a 75% (6/8) success rate of BCO initiation (Figure 1C) and ERCP-derived bile stored for 4 hours before processing yielded no viable organoids (Figure S2). Furthermore, we could not find any difference in successful culture percentages between different underlying (biliary) conditions or between cultures derived from livers transplanted after brain death- or circulatory death donation. As shown in Figure 1B, organoids from bile and brushes have a cystic morphology, similar to previous publications of organoids cultured from IHBD or EHBD tissue.^{7, 8} BCOs could be passaged long-term (>passage 15, >5 months) and could be viably frozen at different time points (Table 1). Previous research showed for ICOs that the organoid-initiating cells are EpCAM⁺ cells and likely a subset of cholangiocytes.⁸ As shown in Figure 1D, approximately 50% (mean 44.27% ±19.74, n=3) of the cells present within bile are EpCAM⁺. These EpCAM⁺ cells in bile are the likely organoid-initiating cells; however, direct evidence is still lacking. Direct cells sorting of EpCAM⁺ or EpCAM⁻ cells from bile using flow cytometry failed to yield viable cells for organoid-initiation, thus indicating that likely due to cell-stress related difficulties we are unable to grow organoids from EpCAM⁺ cells from bile (Figure S2C). In summary, human bile samples are an effective source for cholangiocyte organoids.

Bile cholangiocyte organoids resemble functional cholangiocyte-like cells *in vitro*

All bile-cholangiocyte cultures from either ERCP (n=3) or gallbladder (n=3) were analyzed on gene-expression by RT-qPCR and by normalized read counts from RNA-seq data of BCOs compared to open access data from primary cholangiocytes and hepatocytes.^{7, 23} Overall, it is clear that the BCOs follow the transcriptomic profile of cholangiocytes and have limited expression of classical hepatocyte markers compared to primary hepatocytes (Figure S4A-C). Typical biliary markers such as KRT-7, KRT-19, sodium-dependent bile acid transporter (ASBT, also known as SLC-10A2), SOX-9, CFTR, hepatocyte nuclear factor (HNF)-1 β , and Trefoil factor (TFF)-1 and TFF-2 were detected (Figure 2A and S4A). Interestingly, ERCP-derived BCOs (bile collected from the CBD) expressed TFF2 at somewhat higher levels when analyzed by RNA-seq, while gallbladder-derived BCOs did not, but showed more expression of SOX-17 (Fig. 2A and S4A and B).

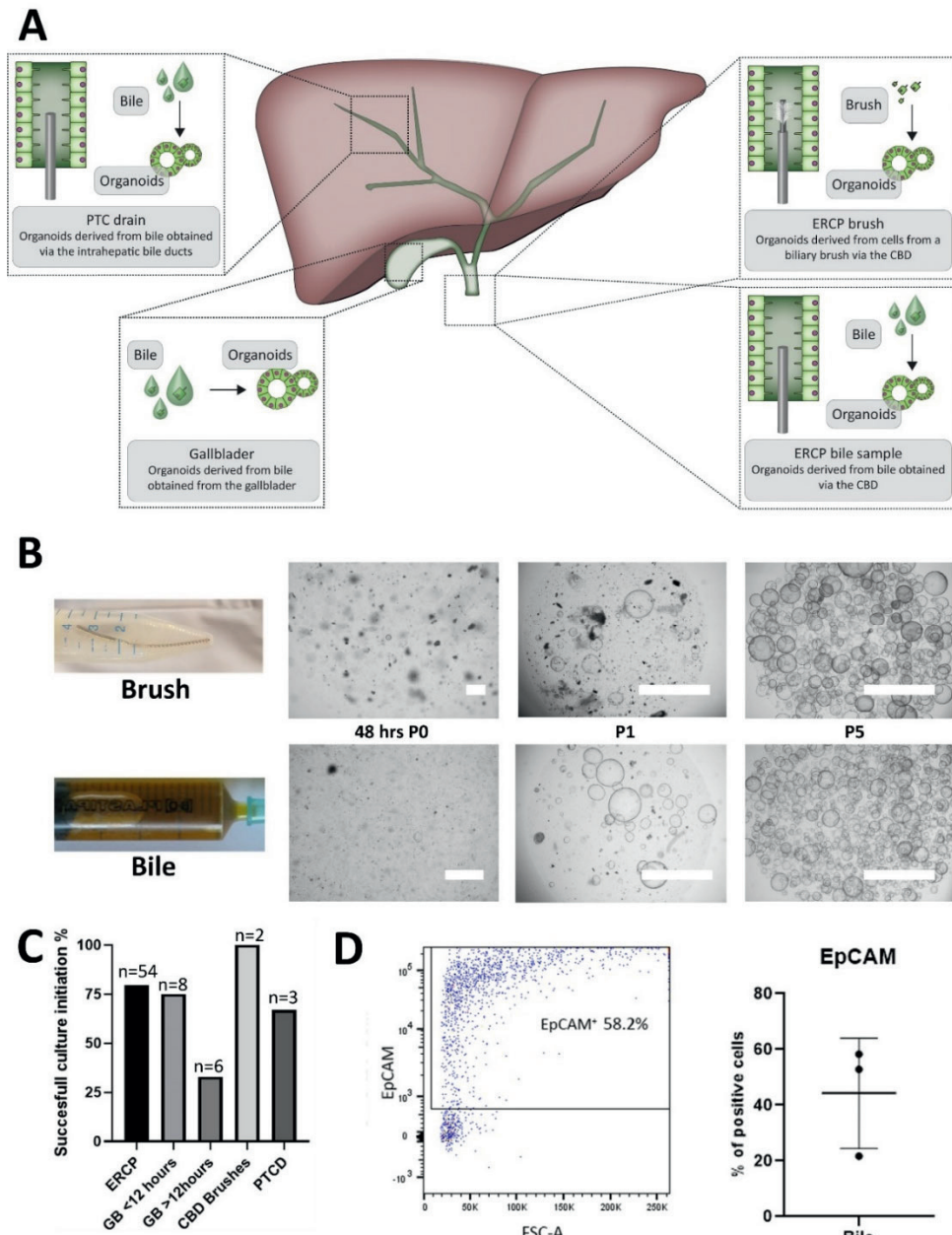


Figure 1. Culture of bile cholangiocyte organoids. (a) Schematic overview of initiation of bile cholangiocyte organoids (BCOs) from different sources of bile and from endoscopic retrograde cholangiopancreatography (ERCP)-brushes of the common bile duct (CBD). (b) Representative organoid cultures from ERCP-brushes and ERCP-derived bile at different passages. Passage 0 (48 hours after culture initiation), P1 (picture taken 72 hours after passage 1) and P5 (picture taken 120 hours after passage 5) (p), scale bars indicate 1000µm. (c) Successful culture percentage from different sources of bile and CBD brushes. (d) Flow cytometry analysis of cells within ERCP-derived bile (n=3) revealed that a mean 44.3%±19.7 is of biliary (EpCAM⁺) origin.

These results are in line with a recent publication demonstrating the local differences between cholangiocytes.²⁷ Gallbladder-BCOs had a high expression of albumin (2/3 samples) and a low expression of *CYP-3A4*, while ERCP-derived BCOs show the opposite expression profiles (Fig. 2A and S4C). Although, this high expression of albumin in GB-BCOs could not be confirmed by RNA-seq analysis, and did not reach statistical significance, a difference between ERCP- and GB-obtained BCOs still seems to be present (Fig. S4C).

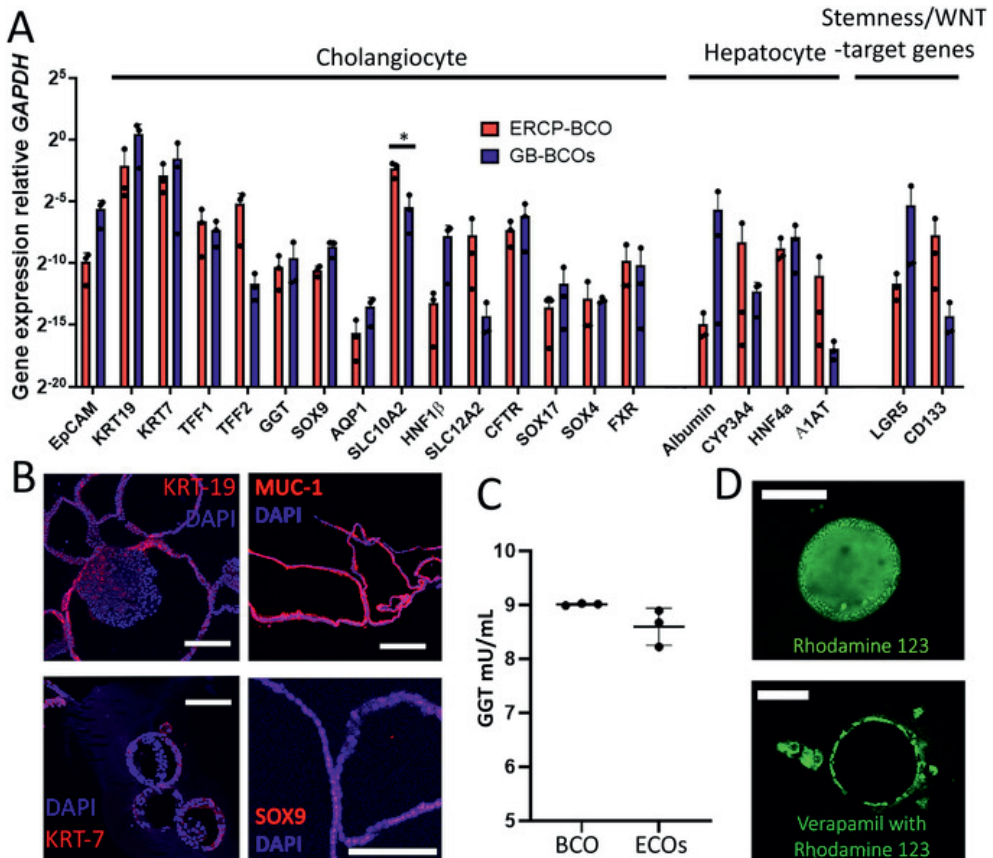


Figure 2A-D. Bile cholangiocyte organoids represent functional cholangiocyte-like cells *in vitro*. (a) Expression of typical cholangiocyte, hepatocyte and stemness/WNT-target associated genes relative to GAPDH (presented as 2^{-dct} method) analyzed using RT-qPCR in BCOs (n=6, BCO1-3 and BCO5-7). Mature cholangiocyte markers (KRT7 and KRT19, TFF1, TFF2) were expressed relatively high compared to the expression of hepatocyte and stemness/WNT-target genes. (b) Protein expression by immunofluorescence of the cholangiocyte markers: KRT-19, KRT-7, MUC-1 and SOX9 (red) and nuclei (DAPI, blue) on BCOs (n=3, BCO1, 5 and 7), scale bars indicate 100 μ m except for SOX9 where it indicates 200 μ m. Images displayed are from BCO 5 and 7. (c) Gamma-glutamyltransferase activity of BCO supernatant as measured by fluorescence is similar between BCOs (n=3, BCO5-7) and ECOs (ECO8-10, n=3) grown in non-canonical WNT stimulating conditions (Sampaziotis *et al.*¹⁴). (d) BCOs (n=3, BCO1, 5 and 7) have clear MDR-1 activity as Rhodamine 123 was actively transported out of the cells into the lumen of the organoid. Specificity was confirmed by inhibition with Verapamil, scale bars indicate 100 μ m. *indicates a significant difference (p<0.05).

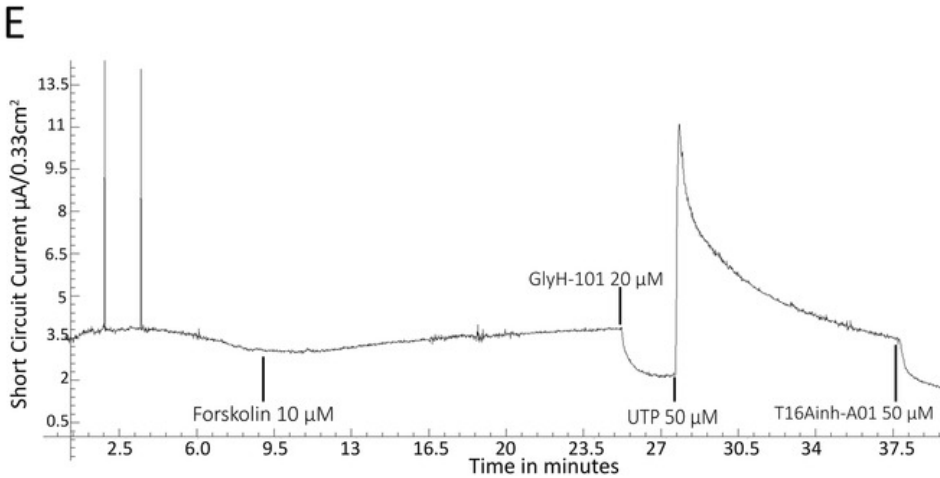


Figure 2E. Bile cholangiocyte organoids represent functional cholangiocyte-like cells *in vitro*. (e) Representative ion-channel functionality of 2D-grown BCOs (n=4, BCO1-3 and 5) in an Ussing chamber. Stimulation with cAMP-activator forskolin (both sides), resulted in an increase in short circuit current. This was completely blocked by cystic fibrosis transmembrane conductance regulator (CFTR)-inhibitor, GlyH-101, demonstrating specific CFTR-mediated activity. It also shows calcium-dependent chloride excretion ion-channel activity, specifically stimulated by UTP and inhibited by T16Ainh-A01, indicating anoctamin-1 activity.

In addition, ERCP-BCOs showed higher expression of the apical *SLC-10A2* transporter and the luminal *SLC-12A2* – also known as NKCC-1-receptor when compared to GB-BCOs (Fig. 2A and S4A). Additionally, both BCOs express the WNT-target gene leucine-rich-repeat-containing-G-protein-coupled receptor (LGR)-5 (Fig. 2A and S4A) known to be higher expressed in cholangiocyte organoids compared to primary cholangiocytes (Fig. S4C).^{9, 11} Overall, it is clear that BCOs not fully represent mature cholangiocytes, which is reflected in less expression of functional markers AQP-1, GGT and CFTR (Figure S4A), similar to previous results⁷. Immunofluorescence revealed protein expression of KRT-7, KRT1-9, CFTR, MUC-1, SCTR and SOX-9 (Figure 2B and Figure S4D), but the absence of ALB (Figure S4E) in BCOs. In addition, functionality of BCOs was assessed by determining γ -Glutamyltransferase (GGT) activity, multidrug resistance protein-1 (MDR-1) activity and ion channel activity. Figure 2C demonstrates that GGT expression levels of BCOs were similar to those found in ECOs cultured in non-canonical WNT stimulating conditions (mean $9.01 \pm SD0.2$ vs. mean $8.60 \pm SD0.13$, $P=0.1$). Previous published data showed that these specific ECOs have a similar GGT expression level when compared to primary cholangiocytes¹⁴, providing indirect evidence that GGT levels produced by BCOs might be similar to cholangiocytes. MDR-1 activity was assessed by the ability to transfer Rhodamine-123 into the lumen of the organoids. Upon incubation, Rhodamine-123 was transported into the organoid lumen (Figure 2D). By blocking the MDR-1 channel with MDR-1 antagonist verapamil, this luminal accumulation was prevented, confirming functional MDR-1 transporter channel activity in BCOs. The presence of functional cholangiocyte-specific ion channels in BCOs was analyzed on organoids grown on a 2D-monolayer, using an Ussing chamber setup. Incubation with

forskolin (cAMP-activator) caused an increase in short circuit current (Isc), which could be inhibited by GlyH-101 (CFTR-inhibitor). It is important to state that prior to forskolin stimulation, forskolin was still present in the culture medium. Therefore, upon addition Isc responses (sometimes) can be limited, however the specific inhibition by GlyH-101, undoubtedly demonstrated the presence of functional CFTR-receptors. Incubation with uridine 5'-triphosphate (UTP) resulted in an increase in Ca²⁺-dependent channel activation (via purinergic R) which could be inhibited by T16Ainh-A01 (Figure 2E). These results indicate the presence of functional cholangiocyte ion-channels CFTR and Anoctamin-1 (ANO-1). All together, these results indicate that BCOs maintain several functional characteristics of cholangiocytes *in vitro*, but do not represent a fully mature cholangiocyte.

Bile cholangiocyte organoids show similar characteristics as ECOs and ICOs

To investigate how BCOs relate to previously published cholangiocyte organoids derived from tissue^{7,8}, paired organoid cultures were initiated from extra- and intrahepatic bile duct tissues (ECOs and ICOs, respectively)²⁸ and from bile obtained from the gallbladder all from the same patients (n=3, Figure 3A). Morphologically, no obvious differences were observed between the three paired organoid types.^{7,8} The metabolic activity of the three organoid types were analyzed using PrestoBlue assay. The increase in metabolic activity over time in BCOs was similar to ECOs (fold change 2.18±SD0.73 vs. 2.08±SD0.82, day 4 activity, relative to day 1) and both had a higher fold change compared to ICOs (fold change 1.47±SD0.32, Figure 3B), although this did not reach statistical significance (p=0.1). We hypothesized that this was caused by lower numbers of proliferating cells in ICOs. However, since the Prestoblue assay only measures broad metabolic activity and not proliferation in particular, we could not rule out that other cellular processes contributed to this difference. Therefore, we quantified the percentage of proliferating cells by flow cytometry analysis of EdU incorporation. As shown in Figure 3C, the EdU-positive cell subset was similar between BCOs and ECOs (15.17%±SD3.38 vs. 15.53%±SD4.18, p=0.91, Fig. 3C), while both had a higher positive subset compared to ICOs (mean 9.1%±SD2.21, p=0.03), confirming our hypothesis. As shown in Figure 3D, ion-channel functionality of ICOs and ECOs compared to BCOs was assessed. Both ICOs, ECOs and BCOs from the same patients showed similar responses to forskolin and UTP stimulation. When all three organoid pairs were quantified, no significant differences could be found in CFTR- or ANO-1 ion-channel activity between ICOs, ECOs and BCOs (Figure 3E). These results indicate that activity of cholangiocyte ion-channels CFTR and ANO-1 is comparable between these three organoid types. To identify possible differences between ICOs, ECOs or BCOs, we performed genome-wide gene expression analyses using bulk RNA-seq. In Figure 3F, a PCA plot calculated using the top 500 variable genes is shown. Even for the most variable genes, all samples displayed no clear differences to one another and only the BCO samples seem to cluster. When looking at transcriptomic correlation between these samples using heatmap-clustering for all genes tested (Figure 3G), we do not observe any specific clusters for either source or donor. This indicates that culture conditions, in which (non-malignant) cholangiocytes are expanded as organoids, are mainly driving the general transcriptomic profile but not the source of the organoids or underlying diseases.

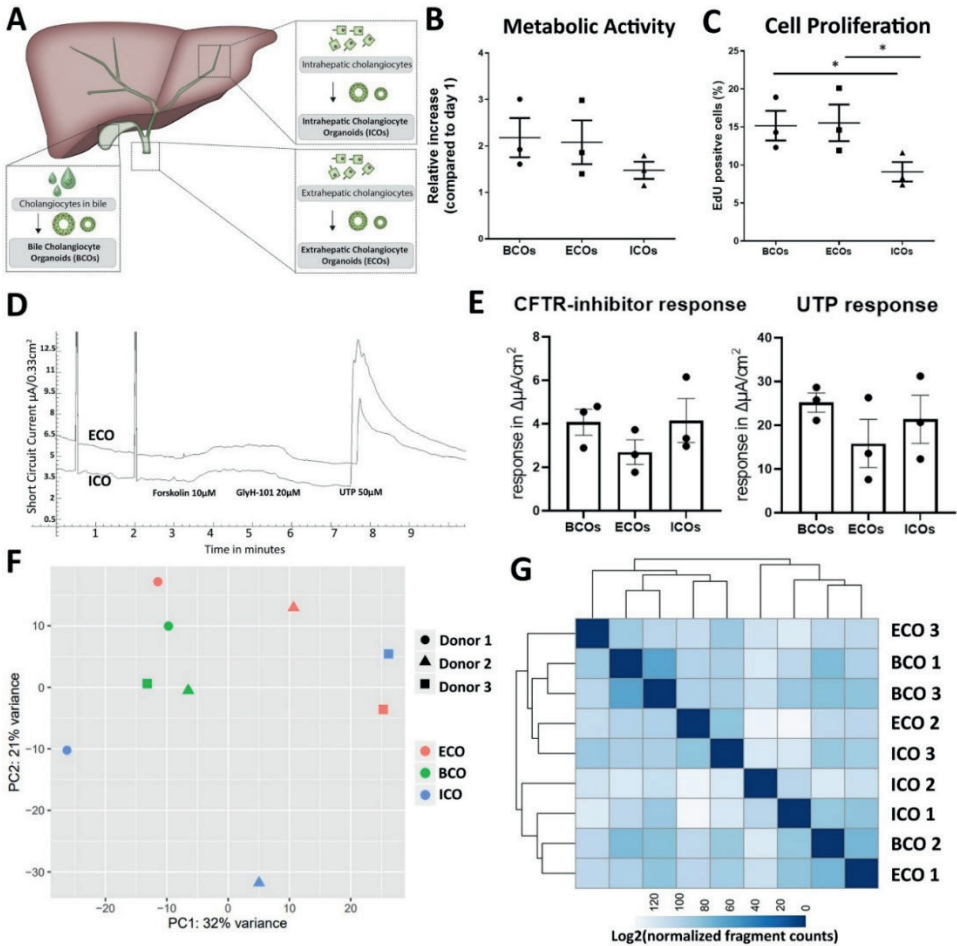


Figure 3. Paired analysis of ICOs, ECOs and BCOs from same donors reveals global similarity and specific differences in cell proliferation. (a) Schematic layout of culture of BCOs, ICOs and ECOs from the same three donors (all experiments performed with donors 1-3). (b) Metabolic activity in the three organoid types as measured by PrestoBlue at day 4 did not increase when compared to day 1 after passaging. (c) Cell proliferation as measured by EdU incorporation. Both BCOs and ECOs have a higher number of EdU positive cells compared to ICOs (15.17% \pm SD3.38 vs. 15.53% \pm SD4.18 vs. 9.1% \pm SD2.21, $p=0.03$). (d) Representative ion-channel functionality of 2D-grown ECOs (top line) and ICOs (bottom line) in an Ussing chamber. Stimulation with cAMP-activator, forskolin (addition to both sides), resulted in an increase in short circuit current. This was completely blocked by CFTR-inhibitor, GlyH-101, addition to the luminal side demonstrating CFTR-mediated activity. Also, the calcium-dependent chloride excretion ion-channel activity (anoctamin-1) could be specifically stimulated by UTP. (e) Quantification of the Ussing chamber data showed that both CFTR-activity (as defined by inhibition of the CFTR channel-activity), and anoctamin-1-activity (as defined by UTP stimulation) were similar between cholangiocyte organoids from all three sources. (f) Principal component analysis (PCA) based on top 500 most variable genes determined by RNA-seq of organoids from all three sources ($n=3$), showed no clear clustering based upon donor, however the BCO samples do seem to cluster. (g) Heatmap-clustering showing sample-to-sample distances on the same samples as used in the PCA plot. Scale bar represents the distance between samples. The lower the distance is, the more correlated the samples are. This shows no clear clustering on either source or donor.

Organoid-specific and regional gene profiles indicate BCOs are of local (extrahepatic) origin

One of the major questions considering bile organoids is whether they originate from an intrahepatic location or from cholangiocytes of the extrahepatic bile ducts. To investigate this, we compared the transcriptomes of BCOs, both ERCP or gallbladder derived, to ICOs and ECOs. As displayed in Figure S5A and B, Principal component analysis (PCA) of top 500 most variable genes between ERCP-BCOs and gallbladder BCOs does not result in specific clustering of either type of BCOs towards either ICOs or ECOs. Thus, further analysis was performed focusing on differently expressed (DE) genes between ICOs and ECOs. These ICO- and ECO- unique gene sets are shown in Figure 4A. As shown in Figure 4A and Figure S5C and D, two out of three ICOs had a unique expression profile compared to BCOs and ECOs. One ICO-line (ICO3) did had absence of ECO-specific genes, but did not show the unique ICO-regional gene-expression (Figure 4A and Figure S5E) that are mostly absent in BCOs from both sources as well (Figure S5E, F), indicating similarities between ECOs and BCOs.

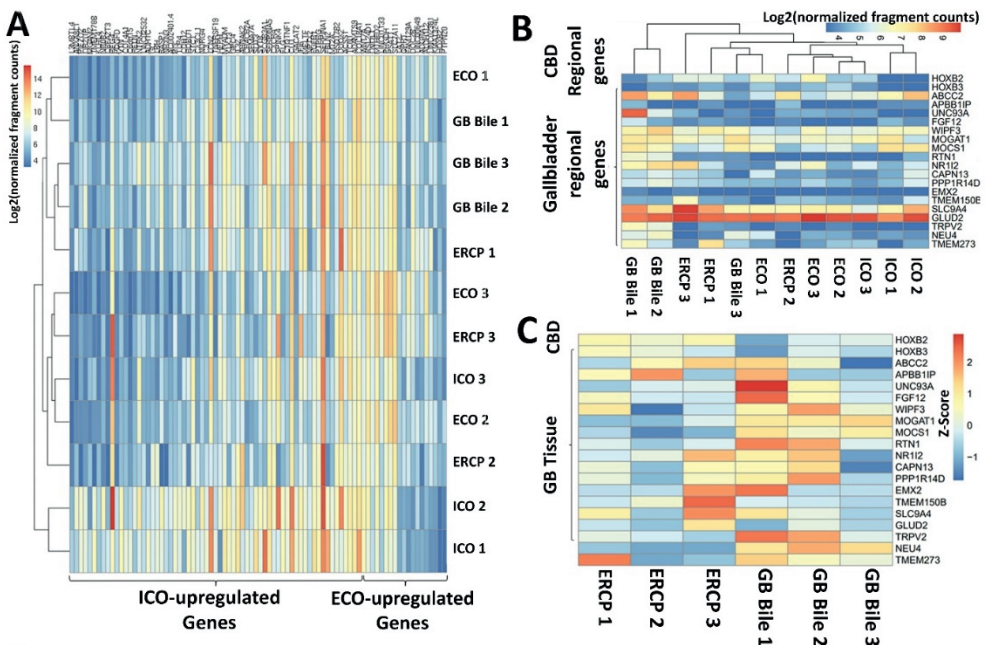


Figure 4A-C. Regional specific gene-expression suggest BCOs are of local extrahepatic originate. (a) Heatmap of the differentially expressed (DE) genes between ICOs and ECOs (n=3, for detail of genes supplementary data file 2), on all organoid samples, showing that ECOs and BCOs cluster more closely. Moreover, BCOs lack the typical ICO-specific, but do express the ECO-specific genes. **(b)** Heatmap of regional specific genes preserved in cholangiocyte organoids derived from the common bile duct and gallbladder⁷. We confirm that ICOs lack expression of HOXB2 and HOXB3 as reported⁷. Both ECOs and ERCP-derived BCOs express common bile duct genes. Moreover, it was clearly shown that in two (GB bile 1 and 2) out of three samples derived from gallbladder bile, expression of gallbladder tissue related genes was upregulated compared to other organoids. **(c)** Heatmap showing Z-score of the same gene set from b on BCOs from ERCP-bile and gallbladder-bile showing expression of either CBD-specific or gallbladder tissue-specific genes, demonstrating regional diversity between BCO sources. All experiments in figure 4 are performed with donor 1-3 and 5-7.

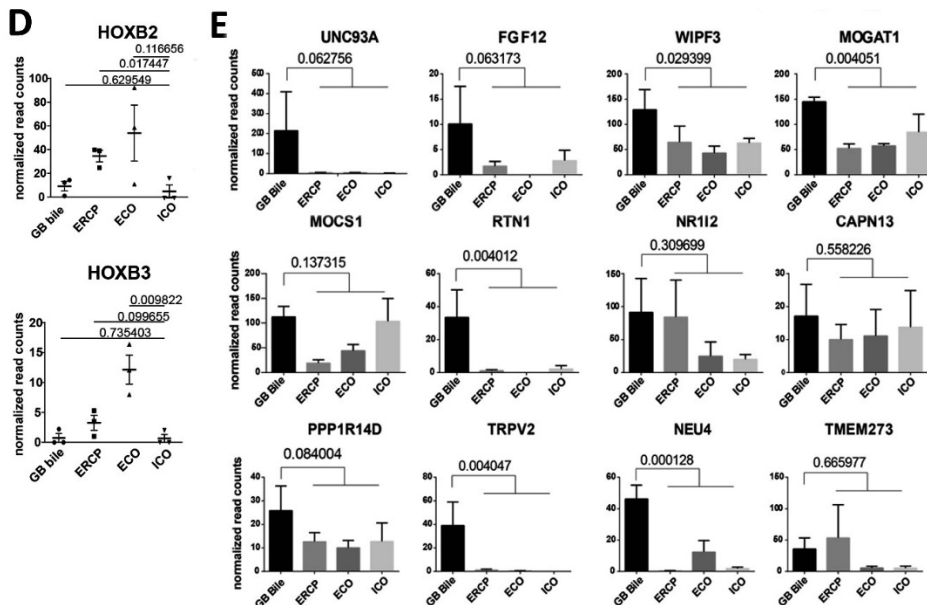


Figure 4D-E. Regional specific gene-expression suggest BCOs are of local extrahepatic originate. (d) Normalized read counts for BCOs (from either GB bile or ERCP), ICOs and ECOs for common bile duct specific markers HOXB2 and HOXB3 shows higher expression in ECOs (for HOXB3) and ERCP (HOXB2) derived samples compared to ICOs. (e) Normalized read counts for BCOs (from either GB bile or ERCP), ICOs and ECOs for 12 GB-tissue specific genes. Significantly higher expression of 5 of the 12 GB genes was observed in GB-BCOs as compared to ERCP-BCOs or ICOs and ECOs. Error bars represent the SEM from three Biological replicates. P-values displayed are calculated via t-test and corrected for multiple testing. All experiments in figure 4 are performed with donor 1-3 and 5-7.

Next, we looked at regional gene-expression profiles that are preserved in cholangiocyte organoids of different parts of the biliary tree tissue as was previously published⁷. These genes were also specifically analyzed in BCOs derived from ERCP and gallbladders. As shown in Figure 4B and C, the typical CBD regional genes HOXB-2 and HOXB-3⁷ are highly expressed in ECOs and ERCP-BCOs, but significantly lower in ICOs and GB-derived BCOs (Figure 4D). Interestingly, in GB-derived BCOs, expression of regional-preserved gallbladder specific genes⁷ were more pronounced compared to all other sources of organoids (Figure 4E). Finally, we investigated the transcriptomic difference between ERCP-derived and GB-derived BCOs. With this analysis we could identify 279 DE genes (Suppl. File 2), indicating that different sources of bile organoids have unique expression profiles and enriched pathways (Figure S6). Overall, these gene-expression analyses of organoids from different sources indicate that they are highly comparable, but BCOs resemble ECOs more closely when looked at regional-specific genes. Moreover, different regions of the extrahepatic bile duct are partially preserved in organoids cultured from bile obtained from these regions, showing a high indication that the (majority of) organoid initiating cells come from locally obtained cells, however some contamination from intrahepatic bile duct cells cannot be excluded.

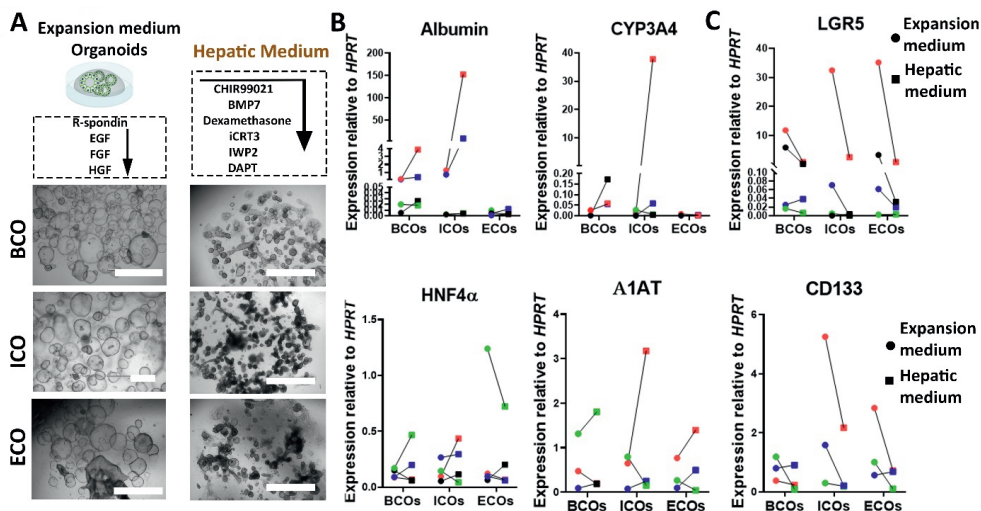


Figure 5. BCOs, similar to ECOs, lack the ability to acquire hepatocyte-like properties. (a) Schematic overview and pictures of cholangiocyte-organoids from gallbladder-derived BCO, ICOs or ECOs (all experiments in figure 5 are at least performed in three biological replicates with donors 1-4) grown in either in expansion medium containing canonical-WNT stimulatory factors (left) or after 14 days in hepatic medium (HM, right). Scale bar indicates 2mm. (b) Gene-expression by RT-qPCR for the hepatocyte-related genes (Albumin, HNF4 α , CYP3A4 and A1AT) in organoids cultured in HM (n=2). As indicated only ICOs could upregulate all four hepatocyte related genes in individual donors, whereas BCOs and ECOs do not. (c) Gene-expression by RT-qPCR relative to the housekeeper gene HPRT1 for stemness/WNT-target markers (LGR5 and CD133) from all three sources (n=2) showing downregulation of stemness/WNT-target markers for ICOs in HM compared to paired samples in expansion medium.

BCOs and ECOs both lack potential to acquire hepatocyte-related properties

Previous studies showed that ICOs but not ECOs have the potential to upregulate hepatocyte-specific genes in “Hepatic medium (HM)” conditions (Figure 5A).^{7, 28} Since the gene-expression profiling results indicate that BCOs more closely resemble ECOs, we investigate their ability to acquire hepatocyte-like potential under these conditions.^{7, 8, 28, 29} To account for inter-donor variation, we initiated BCOs, ICOs and ECOs from tissue and bile collected from the same patients (n=4). In line with previous studies^{7, 27}, big differences in the ability of ICOs to upregulate hepatocyte-related markers, albumin and CYP3A4, in HM conditions were observed between donors. Only two of the four ICO-lines showed a clear upregulation of these hepatocyte markers (Figure 5B). For the analysis of differentiation of BCOs and ECOs only the good differentiating donors were included. As shown in Figure 5B, only ICOs and not BCOs or ECOs, could upregulate all four hepatocyte markers (Albumin, CYP-3A4, HNF-4 α and A1AT) in individual donors when cultured in HM condition. Also, downregulation of stem cell/WNT-target genes LGR-5 and CD-133 was most profound in ICOs compared to BCOs (Figure 5C). Only one BCO-line showed 33-times upregulation of Albumin in HM conditions compared to the 120-times in ICOs from the same donor and is maybe due to contamination of intrahepatic cholangiocytes in this BCO line. When cultured under cholangiocyte- maturation conditions, all organoids from all sources behaved similar

(Figure S7). Overall, our results indicate that none of the ECOs could potentially acquire hepatocytes-like properties, which is in line with previous results.^{7, 27} Moreover, we demonstrate that BCOs have little to no ability to upregulate hepatocyte-markers as well, confirming that the (bulk of) organoid initiating cells for BCOs are most likely of extrahepatic origin.

BCOs can pave bile ducts scaffolds and acquire tissue-like cholangiocytes properties *in vitro*

Since most likely BCOs are of extrahepatic origin, we investigated if they could repopulate EHBD scaffold. In Figure 6A a schematic overview of the experiment is presented. The absence of cells in the EHBD scaffolds after decellularization was confirmed using hematoxylin and eosin (H&E) (Figure 6B, left panel). Repopulation of the EHBD scaffolds with ERCP-derived BCOs resulted in full coverage of the luminal side of the scaffold surface by a confluent monolayer of cholangiocyte-like cells after 21 days (Figure 6B, right panel). Cells showed columnar morphology with nuclei on the basolateral side of the cells, while cytoplasm was more prominent at the luminal side, consistent to the histology of bile ducts *in vivo* (Figure 6B, right panel).³⁰ Cross sectional imaging of immunofluorescence staining showed the presence of mature cholangiocyte proteins KRT-7, KRT-19, CFTR and SCTR (Figure 6C and S8A). No upregulation of albumin protein expression was observed (Figure S8A). Whole mount confocal imaging of reseeded EHBDs shows nearly complete paving of the bile duct lining by BCO cells. Furthermore, the ostia located in large bile ducts (peribiliary glands) were repopulated by the cells. All cells stained positive for F-actin (stained by Phalloidin) and most cells expressed cholangiocyte marker KRT-7 (Figure 6D and S8B, Video S1) and KRT-19 (Figure 6E, Video S2).

To gain more insight in cholangiocyte-like phenotype of the BCO cultured as a monolayer on a human EHBD scaffold, bulk RNA-seq was performed to look at global gene expression profiles and to compare to those of BCOs cultured in a normal BME hydrogel. As shown in Figure 6F, principal component analysis demonstrates that gene-expression profiles of BCO cells grown on scaffolds or in a hydrogel display clear differences. Similar differences were also seen using heatmap analyses (Figure S8C). Importantly, 54% of variance in gene expression (PC1) was related to the substrate (scaffold versus hydrogel), whereas 23% of variance (PC2) was related to the organoid donor (Figure 6F).

Overall, When looking in depth at specific cholangiocyte, hepatocyte- and cell cycle related genes, it is clear that there is no upregulation of hepatocyte-related genes (Figure S8E and F), but a significant downregulation of KRT19 upon repopulation of the scaffolds was observed (Figure S8E and F). This is in line with a previous study¹¹ and our own data of (Fig. S4A) that shows that KRT-19 expression in cholangiocyte organoids is higher compared to primary cholangiocytes (Fig. S4A). In addition, the WNT-target gene LGR-5 and cell-cycle related genes are severely downregulated in BCOs cultured upon scaffolds (Figure S8D-F), likely as the result of formation of a confluent monolayer and maturation of the cells due to the local environment.

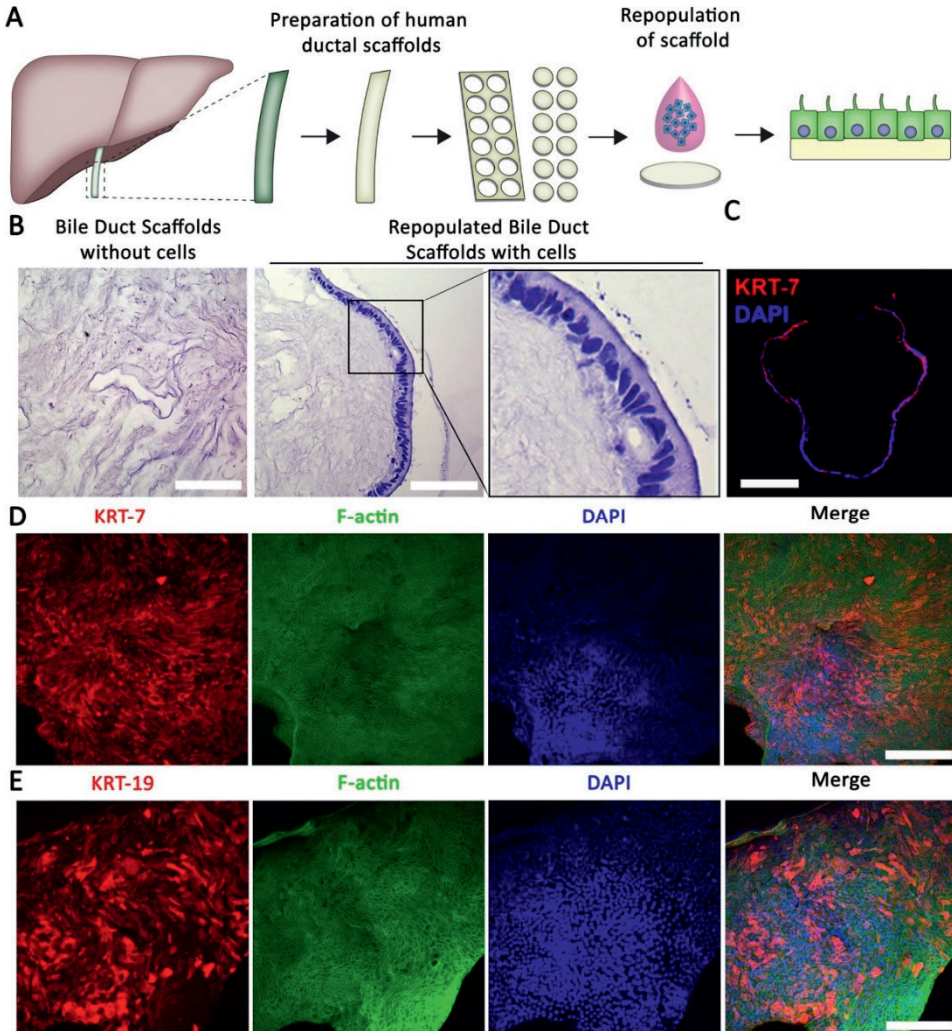


Figure 6A-E. BCOs can pave human extrahepatic bile ducts scaffolds as cholangiocyte-like cells *in vitro*. **(a)** Schematic overview of the experiment. Extrahepatic bile ducts (EHBDs) were removed from their cholangiocyte lining using a Tritox-X-100 based protocol and small punches (circular discs, \varnothing 3mm) were created which were then incubated for 21 days with a BCO cell suspension (consisting of approximately 50-103 single cells). All experiments are performed in triple (both technical and biological, BCO5-7). **(b)** H&E confirmed that all cells were efficiently removed from the EHBD scaffolds (left panel) and that single-cells derived from BCOs repopulate the luminal side of the EHBD scaffolds in a columnar manner (nuclei facing the basolateral side, right panel), scale bars indicate 200 μ m (left panel) and 50 μ m for the right panel. **(c)** The recellularized bile duct scaffolds expressed the cholangiocyte marker KRT-7 (red). Nuclei are stained with DAPI (blue) and scale bar indicates 200 μ m. **(d)** Whole mount confocal imaging of reseeded EHBDs shows nearly complete repopulation of the bile duct lining by BCOs. This included repopulation of the ostia. Most cells expressed cholangiocyte marker KRT-7 (Red) whereas all cells stained positive for Phalloidin (F-actin, green) and DAPI (nuclei, blue). Scale bars indicate 200 μ m. **(e)** Similar analysis were done by whole mount confocal imaging of cholangiocyte marker KRT-19, co-stained with Phalloidin (F-actin, green) and DAPI (nuclei, blue). A large subset of cells stained positive for KRT-19 (red) after repopulation. Scale bars indicate 100 μ m.

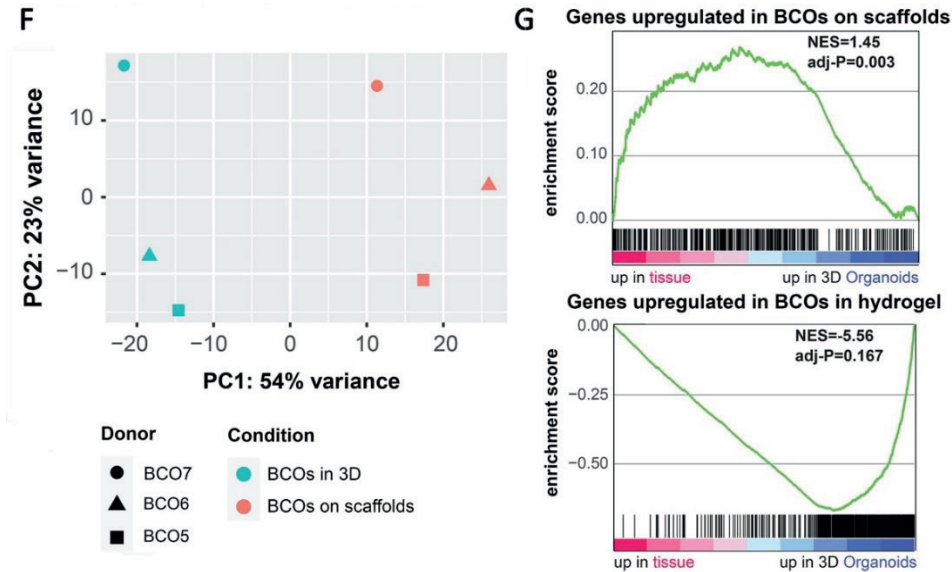


Figure 6F-G. BCOs can pave human extrahepatic bile ducts scaffolds as cholangiocyte-like cells *in vitro*. **(f)** PCA plot generated based on RNA-seq. data of BCO samples cultured on scaffolds and in 3D-hydrogel conditions (n=3 both conditions), showing that the PC1 is mainly determined by the different culture conditions and PC2 mainly by donor. **(g)** GSEA analysis of differentially expressed genes (supplementary file 3) between BCOs on scaffolds (upper panel) and BCOs grown in a hydrogel (bottom panel). This gene-set was compared to the DEgenes from primary cholangiocytes and organoids from the CBD as previously published.⁷ Clearly, BCOs on scaffolds show the highest similarity to primary cholangiocytes of the CBD ($p=0.003$), while BCOs in hydrogel show a trend towards clustering with the CBD organoid profile.

Finally, we performed GSEA of BCOs cultured on bile duct scaffolds (Figure 6G, top panel) and in a hydrogel (Figure 6G, bottom panel) comparing the DE genes between primary cholangiocytes and organoids from the common bile duct (CBD) that were described by Rimland *et al.*⁷ It is clear that the unique gene-expression profile of the repopulated scaffolds shows a significant similarity to that of cholangiocytes from the CBD ($p=0.003$), while the BCOs cultured in a hydrogel seem to overlap with organoids cultured from the CBD. Collectively, these results provide evidence that cells obtained from bile, and that are expanded as organoids, can efficiently repopulate human bile duct scaffolds without deviation from the biliary lineage and as such obtain gene-expression profiles more closely resembling primary cholangiocytes *in situ*.

DISCUSSION

In this study, we demonstrate that cholangiocyte organoids can be readily cultured from bile and brushes collected *in* and *ex vivo*. Organoids were cultured from patients and healthy donors, and could be expanded long-term (>25 weeks, >15 passages) without losing their morphological characteristics using canonical-WNT stimulating conditions. These BCOs closely resemble ECOs in their gene- and protein expression patterns, functionality and

inability to differentiate towards hepatocytes. Furthermore, we show that BCOs are capable of repairing damaged human extrahepatic bile duct scaffolds. These findings highlight the potential of BCOs as a patient-specific minimally invasive cell source for tissue engineering and regenerative medicine applications.

Progress in understanding the pathophysiology and discovering new therapies for biliary diseases have been limited by the lack of functional cholangiocyte-like cells *in vitro*. Cholangiocyte organoids, as first described by Huch *et al.*^{8,15}, have the potential to overcome this problem. Since bile is shown to be a source for cholangiocyte organoids¹³, it becomes feasible to collect patient samples in a minimally invasive manner during their routine clinical procedures rather than depending on invasive trough-cut biopsies. Thus, BCOs extend organoid-initiation beyond patients who receive a liver transplantation or undergo a risky liver biopsy procedure, to patients with rare diseases and following them over time. When cultured in canonical-WNT stimulating conditions, BCOs show a higher proliferation rate compared to ICOs, making them potentially more suitable for use in large-scale experiments. Hence, BCOs provide an attractive model to study cholangiocyte biology and (rare) cholangiopathies. Results from our study indicate that organoids obtained from bile (for the majority) have a local origin and retain characteristics of the local bile duct tissue. Two examples of this are the BCOs derived from bile samples from the common bile duct (by ERCP) and the BCOs derived from gallbladder bile. By comparing the gene expression for organoids with the regional specific signature genes that are preserved in organoids identified by Rimland *et al.*⁷, we found that ERCP-derived BCOs upregulated the common bile duct-specific genes *HOXB2* and *HOXB3*. Moreover, gallbladder bile-derived BCOs showed specific upregulation of signature genes expressed in gallbladder-tissue. Further evidence that BCOs are not derived from intrahepatic bile ducts comes from the fact that they lack the potential to acquire hepatocyte-like properties. As shown by two previous studies, only ICOs but not ECOs have this potential.^{7, 28} This difference in cell fate may be related to their embryogenic origin.⁶ In agreement with this data, we could confirm that only ICOs, but not ECOs from the same patient, are capable of upregulating hepatocyte-specific genes.^{7, 28} In contrast, one BCO line was capable of upregulating albumin expression, although to significantly lower levels compared to the ICO counterpart. Thus, it could be that some intrahepatic cholangiocytes could still end up as organoid-initiating cells in BCOs. Essentially, our results highlight the resemblance between ECOs and BCOs, suggesting that BCOs should be used to study the EHBD and EHBD-related cholangiopathies. However, a question that needs to be addressed is why these cholangiocytes are present in bile. It could be due to local turnover or due to mechanical disruption of the epithelium as a result of the procedure. But an alternative explanation would be that these cholangiocytes are harmed by the local disease and as a result detach and end up in the bile. However, this probably would not be harmful for regenerative experiments, since a recent publication showed that cholangiocyte-organoid initiation likely drives stressed cholangiocytes towards a healthier status and thereby enhancing their regenerative potential after organoid initiation.²⁷ Moreover, we demonstrate that there are no large differences between organoids from bile or from healthy donor biopsies. Interestingly, BCOs could allow scientists and clinicians to

follow patients during their inevitable disease-progression. In addition, it would be valuable to research if CCA organoids can be cultured from bile. Research indicated that tumor organoids can be cultured from tissue specimens obtained from surgical resections or biopsies, while maintaining their resemblance to the *in vivo* tumor and can be used for personalized drug screening options.³¹⁻³⁴ It is known that CCA cells are detectable in bile.³⁵⁻³⁸ Thus, it is likely that bile could provide a minimally invasive method to establish CCA organoids, with opportunities to follow CCA development over time. This could accommodate personalized treatment for a larger patient group, especially from patients suffering of CCA in the EHBD, and adjustment of therapy as the tumor progresses and changes.^{38, 39}

We are not the first group to report on BCOs, Soroka and colleagues showed that BCOs can be cultured from ERCP samples.¹³ In their publication, they provided evidence that some of the inflammatory immune profiles of PSC patients were recapitulated *in vitro*.¹³ By elaborating on their previous work, we show that BCOs can be formed from multiple sources of bile and from CBD brushes. In line with their results, we demonstrate that BCOs resemble cholangiocyte-like cells *in vitro*. In contrast, we failed to show a superiority for ECOs in function and expression of cholangiocyte-specific channels (CFTR) compared to BCO and ICOs, as was suggested.¹³ Instead, we demonstrate that the transcriptomic profile is highly comparable between organoids from different sources of the same donors (Figure 3G). Soroka *et al.* accessed expression profiles between BCOs and ICOs from different donors, thus this might explain the discrepancies found between the studies. Moreover, our research focused on the underlying biology of BCOs as well as using them for tissue-engineering purposes thus providing a valuable addition to the study by Soroka *et al.*

We are the first to demonstrate that BCOs cultured in canonical-WNT conditions can also be used for repopulation of the EHBD by seeding them on empty human scaffolds. These empty scaffolds were created as a model for bile duct damage using a method called decellularization.²⁶ We demonstrate that recellularization by BCOs results in the formation of a confluent monolayer with cholangiocyte-like cells. Importantly, BCOs are less proliferative as well as lose their *LGR5* expression when cultured upon EHBD scaffolds. Furthermore, their gene-expression profile seems to move towards tissue-like cholangiocyte as a result of interacting with these scaffolds. Thus, we are the first group that demonstrate the need for appropriate scaffolds for the recreation of EHBD-constructs. This is in line with previous studies that demonstrated the need for appropriate niches to differentiate and mature cells.⁴⁰⁻⁴⁴ Of note, a recent study indicates that cholangiocytes and cholangiocyte-organoids are plastic and can adapt their phenotype to local niches in the biliary tree.²⁷ As a proof of concept, the authors demonstrate that ECOs can successfully restore intrahepatic bile ducts as intrahepatic cholangiocytes. Similar to their study, after repopulation by BCOs there was no upregulation of hepatocyte-related markers.²⁷ Moreover, we demonstrate that BCOs are unable to upregulate these hepatocyte-related makers *in vitro*. Therefore, it is likely that no other cells from the hepatic-lineage will be formed when BCOs are used for tissue-engineering purposes. Additionally, it could be that BCOs can also be used to

regenerate the intrahepatic bile ducts *in vivo*, making BCOs a potential suitable candidate for cholangiopathy treatment.^{27,44}

Since, we recently showed that our repopulated scaffolds with BCOs are properly polarized by cilia staining and that they become functional constructs by demonstrating TEER and ion-channel functionality²⁶, the next goal would be to create a 3D construct. Cholangiocyte-organoids cultured in non-canonical WNT-stimulated conditions have previously shown feasibility to repopulate 3D constructs and function as EHBD *in vivo*.^{14,45} Thus, it is likely that BCOs can also repopulate 3D constructs. It is important to emphasize that we only decellularized and repopulated the epithelial compartment of the EHBD. For large constructs to function after transplantation a steady supply of nutrients and oxygen is required. Thus, spontaneous vascularization of the constructs would be necessary. Recent evidence emerged that this might be the case. Both Sampaziotis *et al.*¹⁴ and Struecker *et al.*⁴⁶ showed signs of spontaneous vascularization of EHBD constructs as well as long-term survival of the animals without biliary complications. Moreover, it was shown that some mesenchymal supportive cells might become spontaneously present as well.¹⁴ It would have been of great value to see if BCOs can engraft *in vivo* as well. Although previous studies showed that this is the case for mouse gallbladder-derived cholangiocyte organoids cultured in canonical-WNT stimulating conditions⁴⁷, there is still a need to demonstrate this for human BCOs as well. Our laboratory lacks the animal micro-surgery expertise and medical ethical approval to perform bile duct transplantations in mice, but in collaboration with expert labs these can hopefully be performed in the future. Furthermore, clinical applications of organoids are still (partially) limited by the use of non GMP-compliant mouse tumor ECM extracts, such as matrigel and BME. Recent studies have shown that organoids can be cultured in more clinically relevant hydrogels derived from porcine small intestine submucosa⁴⁸ or Cellulose Nanofibril.⁴⁹ Thus, in theory, patient-derived BCOs cultured in these ECM hydrogels could effectively create EHBDs *in vitro*, which might be transplanted back into the patient of which the bile is obtained.

In conclusion, our study shows that bile obtained from multiple sources from a wide range of patients can be used to culture cholangiocyte organoids from the extrahepatic bile duct. This opens new doors to study extrahepatic biliary diseases and regenerative medicine of the extrahepatic bile duct without the need of invasively collected biopsies.

REFERENCES

1. Tabibian JH, Masyuk AI, *et al.* Physiology of cholangiocytes. *Compr Physiol*, 2013. 3(1):541-65.
2. Zong Y, Stanger BZ. Molecular mechanisms of bile duct development. *Int J Biochem Cell Biol*, 2011. 43(2):257-64.
3. Banales JM, Huebert RC, *et al.* Cholangiocyte pathobiology. *Nat Rev Gastroenterol Hepatol*, 2019. 16(5):269-81.
4. Karimian N, Op den Dries S, *et al.* The origin of biliary strictures after liver transplantation: is it the amount of epithelial injury or insufficient regeneration that counts? *J Hepatol*, 2013. 58(6):1065-7.
5. Chapman R, Cullen S. Etiopathogenesis of primary sclerosing cholangitis. *World J Gastroenterol*, 2008. 14(21):3350-9.
6. Fabris L, Fiorotto R, *et al.* Pathobiology of inherited biliary diseases: a roadmap to understand acquired liver diseases. *Nat Rev Gastroenterol Hepatol*, 2019. 16(8):497-511.
7. Rimland CA, Tilson SG, *et al.* Regional Differences in Human Biliary Tissues and Corresponding In Vitro-Derived Organoids. *Hepatology*, 2021. 73(1):247-67.
8. Huch M, Gehart H, *et al.* Long-term culture of genome-stable bipotent stem cells from adult human liver. *Cell*, 2015. 160(1-2):299-312.
9. Planas-Paz L, Sun T, *et al.* YAP, but Not RSPO-LGR4/5, Signaling in Biliary Epithelial Cells Promotes a Ductular Reaction in Response to Liver Injury. *Cell Stem Cell*, 2019. 25(1):39-53 e10.
10. Pepe-Mooney BJ, Dill MT, *et al.* Single-Cell Analysis of the Liver Epithelium Reveals Dynamic Heterogeneity and an Essential Role for YAP in Homeostasis and Regeneration. *Cell Stem Cell*, 2019. 25(1):23-38 e8.
11. Aizarani N, Saviano A, *et al.* A human liver cell atlas reveals heterogeneity and epithelial progenitors. *Nature*, 2019. 572(7768):199-204.
12. Aloia L, McKie MA, *et al.* Epigenetic remodelling licences adult cholangiocytes for organoid formation and liver regeneration. *Nat Cell Biol*, 2019. 21(11):1321-33.
13. Soroka CJ, Assis DN, *et al.* Bile-Derived Organoids From Patients With Primary Sclerosing Cholangitis Recapitulate Their Inflammatory Immune Profile. *Hepatology*, 2019. 70(3):871-82.
14. Sampaziotis F, Justin AW, *et al.* Reconstruction of the mouse extrahepatic biliary tree using primary human extrahepatic cholangiocyte organoids. *Nat Med*, 2017. 23(8):954-63.
15. Broutier L, Andersson-Rolf A, *et al.* Culture and establishment of self-renewing human and mouse adult liver and pancreas 3D organoids and their genetic manipulation. *Nat Protoc*, 2016. 11(9):1724-43.
16. Roest HP, Ooms LSS, *et al.* Cell-free MicroRNA miR-505-3p in Graft Preservation Fluid Is an Independent Predictor of Delayed Graft Function After Kidney Transplantation. *Transplantation*, 2019. 103(2):329-35.
17. Sampaziotis F, de Brito MC, *et al.* Cholangiocytes derived from human induced pluripotent stem cells for disease modeling and drug validation. *Nat Biotechnol*, 2015. 33(8):845-52.
18. Dobin A, Davis CA, *et al.* STAR: ultrafast universal RNA-seq aligner. *Bioinformatics*, 2013. 29(1):15-21.
19. Li H, Handsaker B, *et al.* The Sequence Alignment/Map format and SAMtools. *Bioinformatics*, 2009. 25(16):2078-9.
20. Liao Y, Smyth GK, *et al.* featureCounts: an efficient general purpose program for assigning sequence reads to genomic features. *Bioinformatics*, 2014. 30(7):923-30.
21. Love MI, Huber W, *et al.* Moderated estimation of fold change and dispersion for RNA-seq data with DESeq2. *Genome biology*, 2014. 15(12):1-21.
22. Kuleshov MV, Jones MR, *et al.* Enrichr: a comprehensive gene set enrichment analysis web server 2016 update. *Nucleic Acids Res*, 2016. 44(W1):W90-7.
23. Schneeberger K, Sánchez-Romero N, *et al.* Large-Scale Production of LGR5-Positive Bipotential Human Liver Stem Cells. *Hepatology*, 2020. 72(1):257-70.

24. Korotkevich G, Sukhov V, *et al.* Fast gene set enrichment analysis. *bioRxiv*, 2019.060012.
25. Stuart T, Butler A, *et al.* Comprehensive Integration of Single-Cell Data. *Cell*, 2019. 177(7):1888-902 e21.
26. Willemse J, Roos FJM, *et al.* Scaffolds obtained from decellularized human extrahepatic bile ducts support organoids to establish functional biliary tissue in a dish. *Biotechnol Bioeng*, 2021. 118(2):836-51.
27. Sampaziotis F, Muraro D, *et al.* Cholangiocyte organoids can repair bile ducts after transplantation in the human liver. *Science*, 2021. 371(6531):839-46.
28. Verstegen MMA, Roos FJM, *et al.* Human extrahepatic and intrahepatic cholangiocyte organoids show region-specific differentiation potential and model cystic fibrosis-related bile duct disease. *Sci Rep*, 2020. 10(1):21900.
29. Raven A, Lu WY, *et al.* Cholangiocytes act as facultative liver stem cells during impaired hepatocyte regeneration. *Nature*, 2017. 547(7663):350-4.
30. Boyer JL. Bile formation and secretion. *Compr Physiol*, 2013. 3(3):1035-78.
31. Broutier L, Mastrogianni G, *et al.* Human primary liver cancer-derived organoid cultures for disease modeling and drug screening. *Nat Med*, 2017. 23(12):1424-35.
32. Nuciforo S, Fofana I, *et al.* Organoid Models of Human Liver Cancers Derived from Tumor Needle Biopsies. *Cell Rep*, 2018. 24(5):1363-76.
33. Saito Y, Muramatsu T, *et al.* Establishment of Patient-Derived Organoids and Drug Screening for Biliary Tract Carcinoma. *Cell Rep*, 2019. 27(4):1265-76 e4.
34. Kopper O, de Witte CJ, *et al.* An organoid platform for ovarian cancer captures intra- and interpatient heterogeneity. *Nat Med*, 2019. 25(5):838-49.
35. Macias RIR, Banales JM, *et al.* The search for novel diagnostic and prognostic biomarkers in cholangiocarcinoma. *Biochim Biophys Acta Mol Basis Dis*, 2018. 1864(4 Pt B):1468-77.
36. Shen N, Zhang D, *et al.* Bile cell-free DNA as a novel and powerful liquid biopsy for detecting somatic variants in biliary tract cancer. *Oncol Rep*, 2019. 42(2):549-60.
37. Lee SJ, Lee YS, *et al.* Triple-tissue sampling during endoscopic retrograde cholangiopancreatography increases the overall diagnostic sensitivity for cholangiocarcinoma. *Gut Liver*, 2014. 8(6):669-73.
38. Razumilava N, Gores GJ. Cholangiocarcinoma. *Lancet*, 2014. 383(9935):2168-79.
39. Rizvi S, Gores GJ. Pathogenesis, diagnosis, and management of cholangiocarcinoma. *Gastroenterology*, 2013. 145(6):1215-29.
40. Badylak SF, Freytes DO, *et al.* Extracellular matrix as a biological scaffold material: Structure and function. *Acta Biomater*, 2009. 5(1):1-13.
41. Gjorevski N, Sachs N, *et al.* Designer matrices for intestinal stem cell and organoid culture. *Nature*, 2016. 539(7630):560-4.
42. Nikolaev M, Mitrofanova O, *et al.* Homeostatic mini-intestines through scaffold-guided organoid morphogenesis. *Nature*, 2020. 585(7826):574-8.
43. Lorvellec M, Scottoni F, *et al.* Mouse decellularised liver scaffold improves human embryonic and induced pluripotent stem cells differentiation into hepatocyte-like cells. *PLoS One*, 2017. 12(12):e0189586.
44. Willemse J, Lieshout R, *et al.* From organoids to organs: Bioengineering liver grafts from hepatic stem cells and matrix. *Best Pract Res Clin Gastroenterol*, 2017. 31(2):151-9.
45. Tysoe OC, Justin AW, *et al.* Isolation and propagation of primary human cholangiocyte organoids for the generation of bioengineered biliary tissue. *Nat Protoc*, 2019. 14(6):1884-925.
46. Struecker B, Hillebrandt KH, *et al.* Implantation of a Tissue-Engineered Neo-Bile Duct in Domestic Pigs. *Eur Surg Res*, 2016. 56(1-2):61-75.
47. Lugli N, Kamileri I, *et al.* R-spondin 1 and noggin facilitate expansion of resident stem cells from non-damaged gallbladders. *EMBO Rep*, 2016. 17(5):769-79.
48. Giobbe GG, Crowley C, *et al.* Extracellular matrix hydrogel derived from decellularized tissues enables endodermal organoid culture. *Nat Commun*, 2019. 10(1):5658.

49. Krüger M, Oosterhoff LA, *et al.* Cellulose Nanofibril Hydrogel Promotes Hepatic Differentiation of Human Liver Organoids. *Adv Healthc Mater*, 2020. 9(6):e1901658.

SUPPLEMENTARY INFORMATION

SUPPLEMENTARY MATERIALS AND METHODS

Tissue collection

Biopsies were stored at 4°C in University of Wisconsin (UW, Bridge to Life Ltd. Belzer Cold Storage Solution) preservation solution during transport. For a complete overview of characteristics of patients or donors from whom (liquid) biopsies were obtained and successfully cultured as organoids, see Table 1 and Table S1. All patients or their next of kin gave written informed consent to use their tissue collected during liver transplantation for research purposes. The use of tissue biopsies and livers deemed unsuitable for transplantation was approved by the Medical Ethical Committee (MEC) of the Erasmus MC (MEC-2012-090, MEC-2014-060).

Initiation and culture expansion of tissue-derived organoids

Biopsies were digested by incubation with 4 mL collagenase digesting solution (2.5 mg/mL collagenase A1, Roche) in Earle's Balanced Salt Solution (EBSS, Hyclone, ThermoFisher) for 30 min at 37 °C. Digestion solution was diluted by adding cold Advanced (Adv)DMEM/F12 (GIBCO, supplemented with 100µg/mL penicillin/streptomycin, Life Technologies; HEPES 1M, Fisher Scientific; 1% Ultraglutamine 200mM, Fisher Scientific and 100µg/mL Primocin, Invivogen) and centrifuged for 5 minutes, 4°C at 453g. The cell suspension was filtered through a 70 µm Nylon cell strainer and centrifuged for 5 minutes, 4°C at 453g. Supernatant was removed and the cell pellet was suspended in cold (4°C) 25µL matrigel (Corning Incorporation) or 25µL Basement Membrane Extract (BME, Cultrex) diluted with 30% of AdvDMEM/F12 which was allowed to solidify for 30-45 minutes at 37°C before 250µL start-up expansion medium (SEM, table S2)¹ was added. SEM was replaced with canonical-WNT stimulating expansion medium (EM, table S2) after three days.¹ In addition to extrahepatic cholangiocyte organoids (ECOs) cultured in canonical-WNT conditions (table S2), ECOs were created from gallbladder tissue biopsies cultured in non-canonical WNT-stimulation conditions as a positive control for the γ -glutamyltranspeptidase assay. These organoids were created in a similar manner as described above, only cultured in the non-canonical WNT stimulating medium as published by Sampaziotis *et al.* (n=3).²

Initiation and culture expansion of bile-derived organoids

In short, bile was washed twice in 8 mL cold AdvDMEM/F12 and centrifugation for 5 minutes at 4°C at 453g. Subsequently, the supernatant was removed, the cell pellet was suspended in 3 mL of AdvDMEM/F12, and filtered through a 100 µm cell strainer to get a single cell suspension. After a third wash with 3 mL of AdvDMEM/F12, the cell pellet was collected and seeded either in 25µL matrigel (Corning Incorporation) or 70% BME (Cultrex) diluted with AdvDMEM/F12. SEM (250µL) was added for the first three days and then changed to EM according to the previously published protocol and table S2.^{1,3} If bile was collected via ERCP or PTC from patients having symptoms of bacterial cholangitis (either jaundice, fever or severe stomach ache), the medium was supplemented with vancomycin, (50µg/mL) during the first three days of culture. The effect of this treatment on organoid culture was evaluated

in a dose dependent manner using AlamarBlue (ThermoFisher) assay, performed according to the manufacturer's instructions, and showed no effect on cell viability (Figure S1).

Cultures initiated from PSC or cholangiocarcinoma (CCA) patient bile were supplemented with 1% Antibiotic-Antimycotic (Gibco), instead of vancomycin, during the first three days as published previously⁴ to minimize the risk of fungal infection. EM was refreshed every 3 or 4 days on all cultures and they were passaged in a 1:2-1:8 ratio according to proliferation rate. All organoid cultures described were tested and found negative for mycoplasma (data not shown).

Time window for efficient organoid initiation

To evaluate the optimal timeframe to process bile after collection, ERCP-obtained bile was divided into two aliquots of 1 mL. One aliquot was processed immediately after collection (< 1 hour), the other sample was stored for four hours at 4°C before organoid culture initiation. After 7 days of culture, the numbers of organoids larger than 100 µm in diameter were assessed (Invitrogen™ EVOS™ FL Digital Inverted Fluorescence Microscope).

Immunofluorescence (IF) staining

Organoids were fixed for 10 minutes using 4% paraformaldehyde removing the hydrogel. Samples were paraffin embedded and cut as 4 µm thick slides. Next, they were permeabilized with 0.1% Triton X-100 diluted in PBS for 15 minutes. Subsequently, they were exposed to 10% serum diluted in 1% BSA-PBS to prevent a-specific antibody binding. Primary antibodies were added to the organoids and incubated overnight at 4°C. Finally, incubation with the secondary antibody (Table S4) took place for 60 minutes at room temperature and cell nuclei were stained with DAPI (Vectashield, Vectorlabs) and analysis took place on a SP5 confocal microscope (LEICA) equipped with a 405, 488 and 561 nm laser. Images were analyzed using ImageJ (version 1.52p, supplemented with FIJI).

Ussing chamber assay

Prior to seeding of the cells, transwell inserts were coated with 5% matrigel in PBS for 2 hours. Fully expanded domes of organoids (20 fully grown domes of 25µL) were collected in AdvDMEM/F12 and centrifuged (453g, 5 min, 4°C). After removal of the supernatant, organoids were mechanically broken by vigorously up and down pipetting. The organoid suspension was spun down again and the cell pellet was made single cell by digestion in Trypsin-EDTA (TE) for 25 to 40 min at 37°C. Cells were washed in AdvDMEM/F12 and sieved through a cell 70 µm cell strainer. Approximately 3×10^5 cells were suspended in 200 µL EM and seeded on transwell inserts. Medium was changed every 3-4 days. To check confluency, the cells were examined by daily microscopy and electrophysiological analysis was performed after 4 days. Upon forming a confluence monolayer, transwells were placed in an Ussing chamber (Physiologic instruments) set up to analyze functional cholangiocyte-specific transporter channels (Cystic Fibrosis Transmembrane Conductance Regulator (CFTR)- and Ca^{2+} - activated Cl^- channel) using Acquire & Analyze Software 2.3 (Physiologic Instruments, San Diego, California). The temperature of the chambers was kept at 37°C by warm water bath circulation and chambers were gassed with 95% O_2 , 5% CO_2 . Each chamber

consisted of 3mL modified Meyler solution (128 mmol/l NaCl, 4.7 mmol/l KCl, 1.3 mmol/l CaCl₂, 1.0 mmol/l MgCl₂, 0.3 mmol/l Na₂HPO₄, 0.4 mmol/l NaH₂PO₄, 20 mmol/l NaHCO₃, 10 mmol/l HEPES, supplemented with glucose (10 mmol/l) at pH 7.3). Current was clamped and every second short circuit current (I_{sc}) was recorded. CFTR-dependent anion secretion was activated by adding Forskolin (3μL, 10mM) to both sides of the cells, and GlyH-101 (3μL, 20mM, apical). Calcium (Ca²⁺) activated chloride (Cl⁻) channels (CaCC) were stimulated by UTP (3μL, 50mM, apical) and inhibited by T16Ainhibitor-A01 (3-5 μL, 50mM, apical). The I_{sc} measurements are presented as measured (μA/0.33cm²).

Metabolic activity measurement

Metabolic activity in organoids from bile and intra- and extrahepatic bile duct biopsies (n=3 all sources) was determined using the PrestoBlue metabolic assay. In short, 400 μL of diluted PrestoBlue (10% in AdvDMEM/F12) was added per 25 μL dome (48 well plate culture suspension, Corning). After 4 hours of 37°C incubation, 100 μL of PrestoBlue solution per dome was transferred to a white walled 96 well plate (Perkin Elmer) and fluorescence intensity was measured using a plate reader (CytoFluor Series 4000, Applied Biosystems) with the excitation/emission wavelengths set to 530/590nm. BME without cells was measured to assess the background fluorescent signal. This measurement was repeated after three days of subsequent culture and the relative increase in PrestoBlue per dome was calculated.

Cell proliferation

EdU-incorporation was performed according to the manufacturer's protocol. In short: EdU (10μM) was added to the medium and incubated for 4 hours at 37°C degrees. The organoids were dissociated into single cell suspension as described earlier and suspended in 200μL of 1%BSA-PBS to be analyzed by flow cytometry (Canto flow cytometer, BD Biosciences). The gating strategy is shown in Figure S3. Subset analysis was done using Flowjo (version v10.6.1, BD) analysis software.

Upregulation of hepatocyte-specific markers/hepatocyte (trans)differentiation

In principle, upregulation of hepatocyte-specific markers/hepatocyte (trans)differentiation by the novel defined culture conditions is based upon removal of WNT/β-catenin stimulators and blocking of notch-related cholangiocyte differentiation. To achieve upregulation of hepatocyte-associated markers. Organoids were passaged once at 7 days during differentiation and the total differentiation protocol took 14 days (including pre-treatment with BMP7). Differentiation was confirmed by gene and protein expression analysis of genes associated with hepatocyte maturation (Albumin, HNF4α, CYP3A4 and alpha-1-anti trypsin (A1AT))⁵ and stemness/WNT-target genes (LGR5 and CD133)⁵ by RT-qPCR. These data are presented in fold change manner comparing them to their expansion medium controls.

Cholangiocyte maturation

Cholangiocyte-maturation medium for cholangiocyte organoids (COs) was based upon the induced-pluripotent stem cell (IPS) protocol for cholangiocyte-differentiation as established

by Sampaziotis *et al.*^{5, 6} and adapted by Verstegen MMA *et al.*⁷ for tissue-derived cholangiocyte organoid cultures. This two-step protocol largely followed the principles of differentiation hepatoblast-like IPS towards cholangiocytes. Bile-cholangiocyte organoids (BCOs), ECOs and Intrahepatic cholangiocyte organoids (ICOs) from three donors were exposed to these culture conditions and compared to their expansion culture conditions.¹ In detail, all cholangiocyte organoids were expanded for 7 days in basement membrane extract diluted in 10% Williams-E medium (WE, Gibco, Life Technologies) to near-full wells. Culture medium was then switched to maturation medium, consisting of AdvDMEM/F12 supplemented with 1:50 B27 (Gibco), 50 ng/mL FGF10 (Peprotech), 50 ng/mL Activin-A (Gibco) and 3 μ M retinoic acid (Sigma-Aldrich). After 4 days, medium was changed to WE supplemented with 10 mM nicotinamide (Sigma-Aldrich), 17 mM sodium bicarbonate (Sigma-Aldrich), 0.2 mM 2-phospho-i-ascorbic acid tri-sodium salt (Sigma-Aldrich), 6.3 mM sodium pyruvate (Invitrogen), 14 mM glucose (Sigma-Aldrich), 20 mM HEPES (Fisher Scientific), ITS+ premix (BD Biosciences), 0.1 M dexamethasone (R&D), 20 ng/mL EGF (R&D), 2 mM Ultraglutamine (Invitrogen), and penicillin (100 U/mL) & streptomycin (100g/mL). The medium was refreshed every 2 days for a total of 10 days after which the organoids were analyzed. Maturation *in vitro* was assessed by gene-expression profiles using RT-qPCR and immunofluorescence for protein-expression of mature cholangiocyte markers (cytokeratin –KRT-7, KRT19, AQP1 and CFTR) as well as looking at progenitor/stem cell/WNT-target markers (LGR5 and SOX9).⁶

Repopulation of EHBD scaffolds

EHBD scaffolds were prepared as previously published.⁸ After procurement of donor livers deemed unsuitable for transplantation, EHBD (n=3, length: 4cm) were surgically removed, stored in 0.9% saline solution and frozen at -20°C. Decellularisation was started after complete thawing of EHBD tissue. Subsequently, cells were removed by submersion in 4% Triton-X-100 + 1NH₃. The Triton solution was refreshed every 30 minutes for a total of 10 cycles. Afterwards, the EHBD segments were washed with dH₂O until all detergent was removed. This was followed by DNase type1 treatment in 0.9% NaCl + 100mM CaCl₂ + 100mM MgCl₂ treatment. Complete decellularisation was confirmed with hematoxylin and eosin (H&E) staining. H&E stained slides were imaged with Zeiss Axiokop 20 microscope and captured with a Nikon DS-U1 camera. EHBD scaffolds were prepared using a dermal biopsy punch (\varnothing 3mm). These discs were reseeded by incubation with single cell suspensions made from BCOs. This cell suspension ($5.0 \cdot 10^3$ cells/ μ L, 10 μ L) was pipetted on top of the ductal scaffolds and incubated for 4 hours at 37°C to settle. After this, 500 μ L EM supplemented with 10 μ M Y27632 was added. After 3 days, the medium was changed with 500 μ L EM without Y27632. Medium was refreshed every 2-3 days. Reseeded scaffolds were cultured for 21 days and subsequently fixed in 4% paraformaldehyde for 20 minutes. Subsequently, immunofluorescence staining with the primary antibodies, KRT-7, SCTR, CFTR and Albumin was performed on sections as previously described under the immunofluorescence section in the methods. Furthermore, repopulation efficacy was determined by whole mount confocal microscopy to assess KRT-7 and KRT-19 protein expression. For this, reseeded EHBD samples were stained with fluorescently labeled antibodies in a similar manner as described

earlier. Additional cytoskeletal staining with Phalloidin Alexa Fluor™ 488 (1:200, ThermoFisher) and nuclear staining with DAPI was performed. Samples were imaged using a Leica 20X water dipping lens on Leica DM6000 CFS microscope with a LEICA TCS SP5 II confocal system. Images were processed using ImageJ.

TABLES

Table 1. Patient and organoid culture characteristics

Culture type	Patient Age (years)	Gender	Cell source	Donor type or indication ERCP/surgery	Frozen after passage
ECO 8 ^a	13	M	GB	DBD	5
BCO 1, ICO 1, ECO 1	27	M	Liver, EHBD, GB bile	DBD	8
BCO 5	33	F	ERCP bile	Bile leakage	18
BCO 6	46	M	ERCP bile	PSC	26
ECO 9 ^a	50	M	GB	Bile stones	5
BCO 3, ICO 3, ECO 3	56	F	Liver, EHBD, GB bile	Liver explant of a cirrhotic PSC liver	10
ECO 10 ^a	59	M	GB	DBD	5
BCO 2, ICO 2, ECO 2	59	F	Liver, EHBD, GB bile	DBD	10
BCO 4, ICO 4, ECO 4	66	F	Liver, EHBD, GB bile	Liver explant of cirrhotic HCV liver with HCC	6
BCO 7	68	F	ERCP bile	Bile stones	18

Abbreviations: AS: Anastomotic bile duct Stricture, BCO: Bile Cholangiocyte Organoid, DBD: Donation after Brainstem Death, ECO: Extrahepatic Cholangiocyte Organoids, EHBD: Extrahepatic Bile Duct, ERCP: Endoscopic Retrograde Cholangiopancreatography, F: Female, GB: Gallbladder, GB Bile: Gallbladder Bile, ICO: Intrahepatic Cholangiocyte Organoids M: Male, PSC: Primary Sclerosing Cholangitis, HCV: Hepatitis C Virus, HCC: Hepatocellular Carcinoma. ^aIndicates that these organoids are cultured using the previously published protocol (Sampaziotis *et al.*²) stimulating non-canonical WNT culture conditions.

Supplementary Table S1. Characteristics of additional *in vivo* collected bile and brush samples with successful organoid initiation

Age patient (years)	Sex	Bile Source	Donor Type or Indication ERCP/surgery
48	M	ERCP	AS
63	M	ERCP	AS
66	M	ERCP	Mirizzi Syndrome
31	M	Brush	PSC
41	M	ERCP	AS
77	F	PTCD	CCA
71	M	ERCP	NAS
64	M	ERCP	AS
26	F	ERCP	AS
57	F	ERCP	AS
66	M	ERCP	AS
73	M	PTCD	NAS
79	F	ERCP	CCA
60	M	ERCP	AS
20	M	ERCP	PSC
66	F	ERCP	CCA
49	M	ERCP	AS
68	M	ERCP	AS
66	F	ERCP	CCA
48	M	ERCP	AS
52	M	ERCP and brush	CCA
58	M	ERCP	AS
57	F	ERCP	AS
57	F	PTCD	CCA
71	M	ERCP	NAS
55	M	ERCP	PSC
71	M	ERCP	Bile Stones
63	M	ERCP	CCA
73	F	ERCP	Bile Stones
61	M	ERCP	AS
59	F	ERCP	PSC
26	F	ERCP	Bile Stones
58	F	ERCP	AS
70	M	ERCP	Bile Stones
72	M	ERCP	Bile Stones
20	M	ERCP	AS
54	F	ERCP	AS
54	M	ERCP	Bile Stones
63	M	ERCP	AS
85	M	ERCP	Bile Stones
50	M	ERCP	AS
54	F	ERCP	Papiladenoma
30	M	ERCP	PSC

Abbreviations: AS: Anastomotic bile duct Stricture, CCA: Cholangiocarcinoma, ERCP: Endoscopic Retrograde Cholangiopancreatography, F: Female, M: Male, NAS: Non-Anastomotic bile duct Stricture, PSC: Primary Sclerosing Cholangitis, PTCD: Percutaneous Transhepatic Cholangiography Drainage.

Supplementary Table S2. Culture conditions used within this manuscript

Medium formulation for Start Up Medium (SEM) and Expansion Medium (EM) per ml.

Component	Concentration	Brand
Supplemented AdvDMEM/F12**		Gibco
N2	1%	Gibco
B27	2%	Gibco
N-Acetylcystein	1mM	Sigma-Aldrich
gastrin	10 nM	Sigma-Aldrich
EGF	50 ng/ml	Peprotech
FGF10	100 ng/ml	Peprotech
HGF	25 ng/ml	Peprotech
nicotinamide	10nM	Sigma-Aldrich
A83.01	5 μ M	Tocris
Forskolin	10 μ M	Tocris
R-Spondin	10%	Conditioned medium
WNT*	30% Wnt	Conditioned medium
Noggin*	25 ng/ml	Conditioned medium
Y27632*	10 μ M	Tocris
hES cell cloning recovery solution*	1:1000 dilution	Stemgent

*Components are only added to SEM.

**Supplemented AdvDMEM/F12 (Gibco) contains 1M HEPES (Invitrogen), 1x L-Ultraglutamine (Invitrogen), 500mg/mL Primocin (invivogen) and 10000U/mL penicillin and streptomycine (Invitrogen).

Medium formulation for non-canonical WNT stimulating conditions per ml.

Component	Concentration	Brand
William's-E		Gibco
EGF	20 ng/mL	Peprotech
nicotinamide	10nM	Sigma
sodium pyruvate	6.3 mM	Invitrogen
sodium bicarbonate	17 mM	Sigma
ascorbic acid	0.2 mM	Sigma
glucose	14 mM	Sigma
Ultraglutamine	2mM	Invitrogen
dexamethasone	0.1 μ M	R&D systems
DKK1	100 ng/mL	R&D systems
ITS+ premix	1x	BD Biosciences
R-Spondin	10%	Conditioned medium
penicillin and streptomycine	10000U/mL	Invitrogen
HEPES	20mM	Invitrogen

Supplementary Table S3. List of genes and primers used

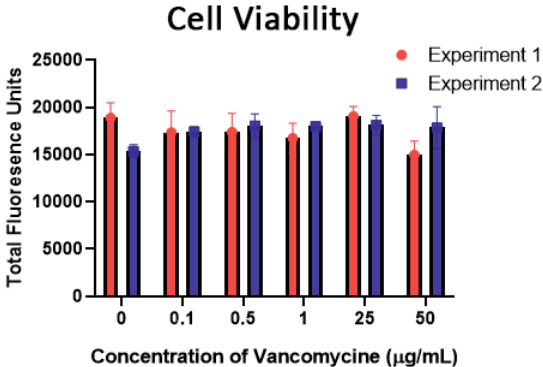
Gene	Forward sequence 5'to 3'	Reverse sequence 5'to 3'
KRT7	GGGGACGACCTCCGGAATAC	CTTGGCACGCTGGTTCTTGA
KRT19	GCACTACAGCCACTACTACACGA	CTCATGCGCAGAGCCTGTT
HNF1B	TCACAGATACCAGCAGCATCAGT	GGGCATCACCAGGCTTGTA
HPRT1	GCTATAAATTCTTTGCTGACCTGCG	CTTCGTGGGGTCTTTTTACCC
ALB	CTGCCTGCCTGTTGCCAAAGC	GGCAAGGTCCGCCCTGTATC
GAPDH	CTTTTGCCTGCCAGCCGAG	CCAGGCGCCCAATACGACCA
HNF4 α	GTA CTCTGCAGATTTAGCC	CTGTCTCATAGCTTGACCT
AQP1	GGCCAGCGAGTTCAAGAAGAA	TCACACCATCAGCCAGGTCAT
SLC12A2	ACCAAGGATGTGGTAGTAAGTGTGG	GGATTCTTTTTTCAACAGTGGTTGA
CD133	CCTGGGGCTGCTGTTTATTA	ATCACCAACAGGGAGATTGC
SOX17	ATACGCCAGTGACGACCAGA	TCCACGACTTGCCAGCATC
FXR	GGGACAGAACCTGGAAGTGG	GCCTGTATACATACATTCAGCCA
A1AT	TGAGGAGAGCAGGAAAGGACA	CTCAGCCAGGGAGACAGG
GGT	TGGTGGACATCATAGGTGGGGA	ATGACGGCAGCACCTCACTT
SLC10A2	GGTGGCCTTTGACATCCTCCC	GCATCATTCCGAGGGCAAGC
SOX9	ACCAGTACCCGCACTTGCCAC	GCGCCTTGAAGATGGCGTTG
EpCAM	GACTTTTGCCGAGCTCAGGA	AGCAGTTTACGGCCAGCTTGT
CFTR	TGGCGGTCACTCGGCAATTT	TCCAGCAACCGCCAACAACCT
LGR5	GTCACTGCTCCGAATCCC	TGAAACAGCTTGGGGGCACA
CYP3A4	AGCAAAGAGCAACACAGAGCTGAA	CAGAGGTGTGGGCCCTGGAAT
TFF1	ACAAGCTGCTGTACACGGACA	AAGTTTCCAGGGCCGGGCAAT
TFF2	TCTGTCTGCCTCCCTGATCCA	CTCTGGCACGTGAATCCCGGT
SOX4	CCCAGCAAGAAGGCGAGTTA	CCTTCCAGTTCTGTCTCTCC

Supplementary Table S4. List of antibodies used

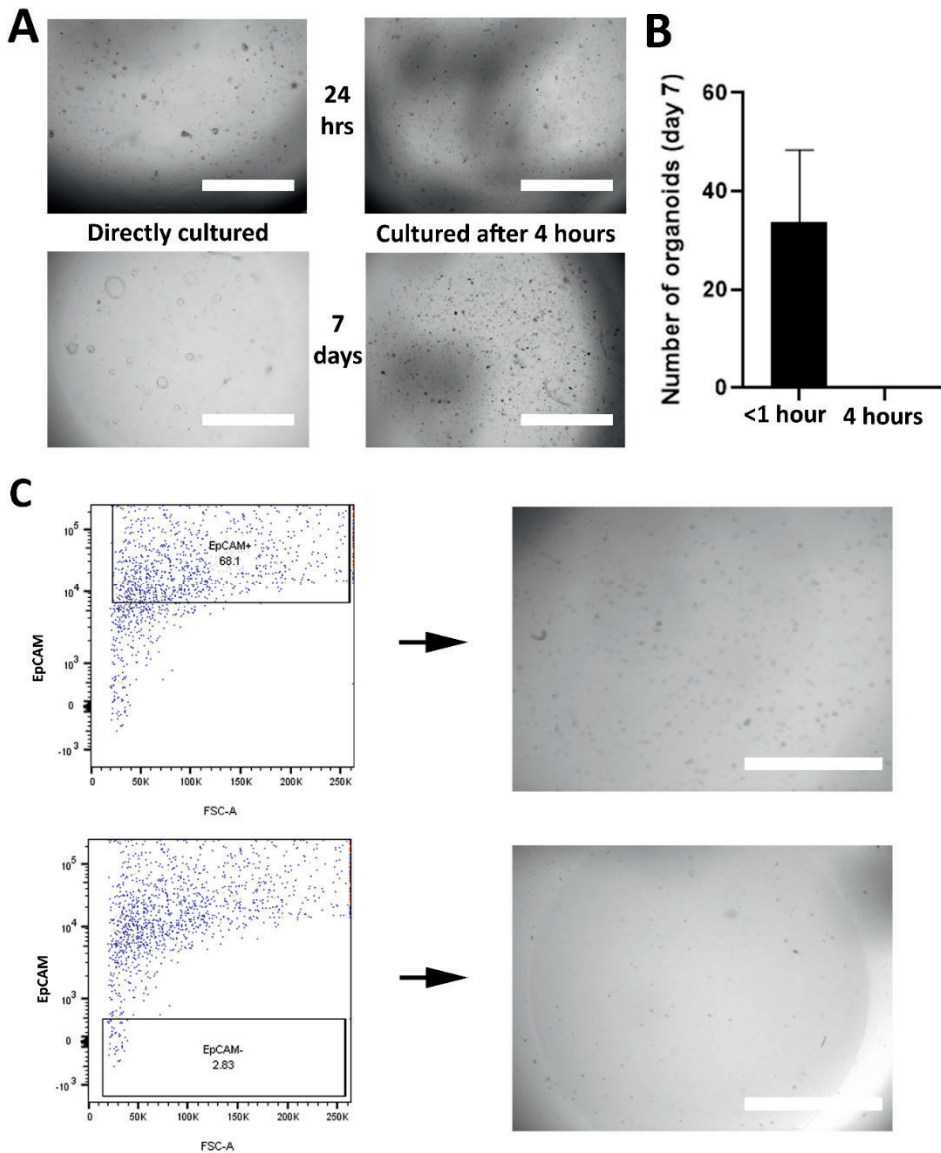
Antibody	Raised	Manufacturer-Reference	Dilution
Albumin	Mouse - monoclonal	Sigma-Aldrich: A6684	1:500
SOX9	Mouse - monoclonal	ATLAS antibodies: 02712	1:200
KRT-7	Mouse - monoclonal	DAKO: M7018	1:100
KRT-19	Mouse - monoclonal	DAKO: M0888	1:100
CFTR	Mouse - monoclonal	EMD Millipore Corp: MAB3484	1:100
MUC-1	Mouse	ThermoFisher Scientific: MA5-14077	1:500
SCTR	Rabbit	Abcam: AB234830	1:100
Alexa Fluor 555	Goat – polyclonal (anti-mouse)	ThermoFisher Scientific: A21422	1:200
Alexa Fluor 488	Goat – polyclonal (anti-rabbit)	ThermoFisher Scientific: A32731	1:200

SUPPLEMENTARY FIGURES

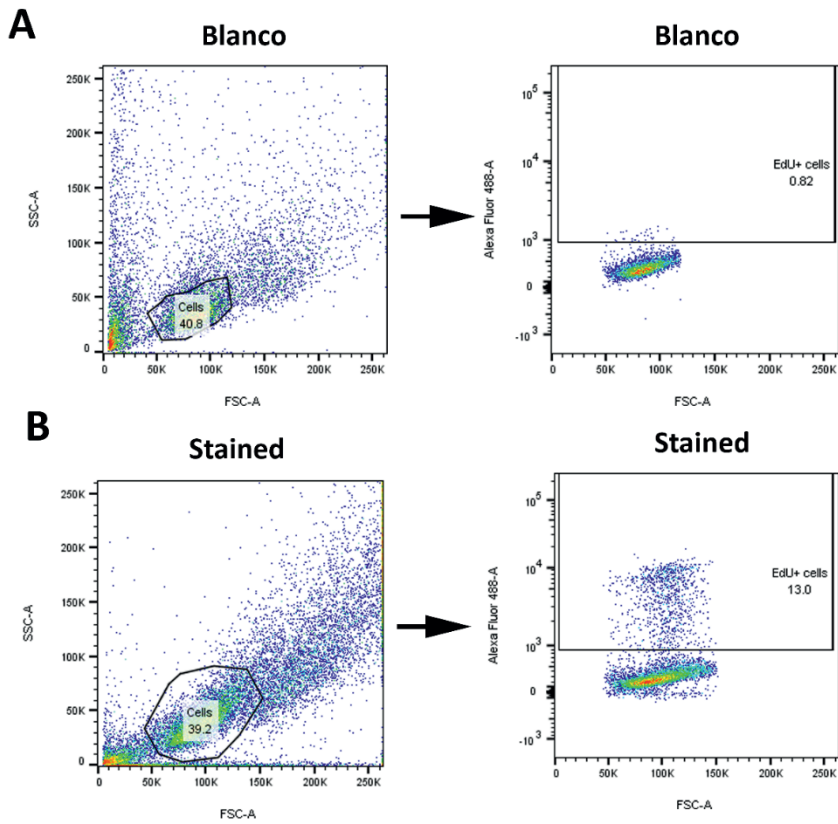
2



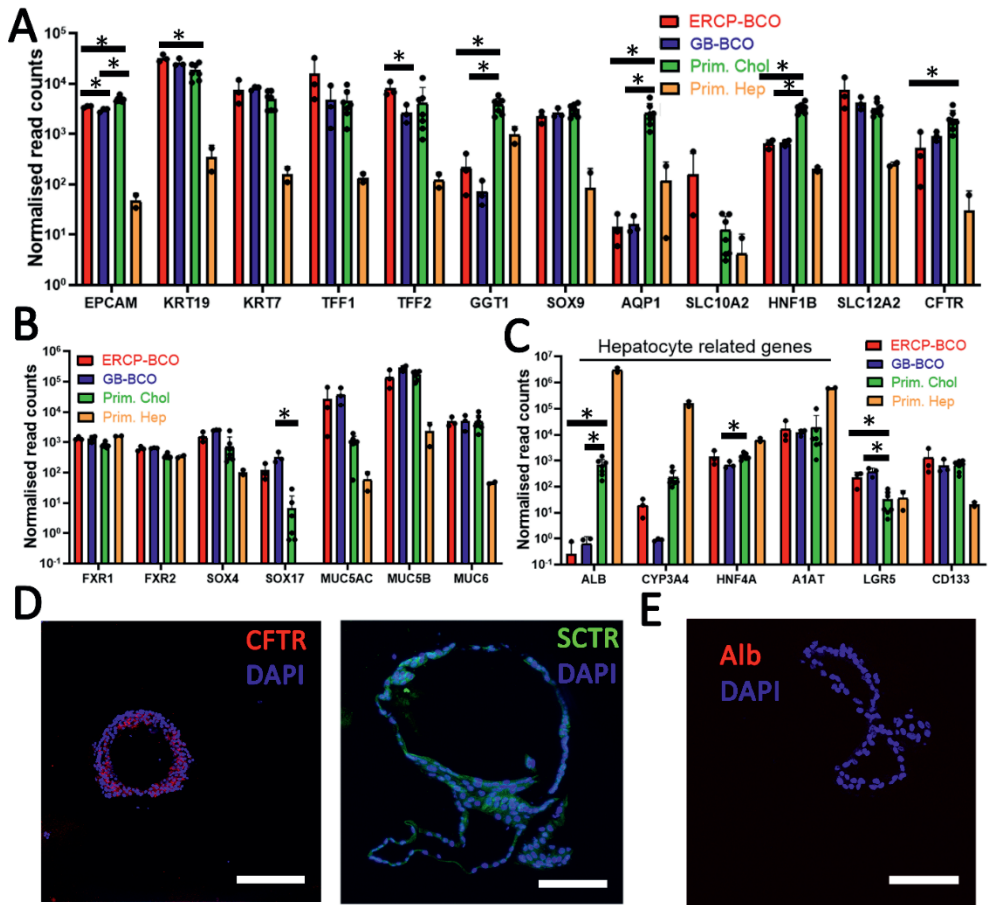
Suppl. Figure S1. Organoid Viability with vancomycin medium supplementation. AlamarBlue Fluorescence one week after initiation of bile organoid culture with different concentrations of Vancomycin (n=2 experiments, per concentration 3 technical replicates). No difference in AlamarBlue activity was observed in these experiments, indicating similar cell viability and no harm of vancomycin in BCO cultures.



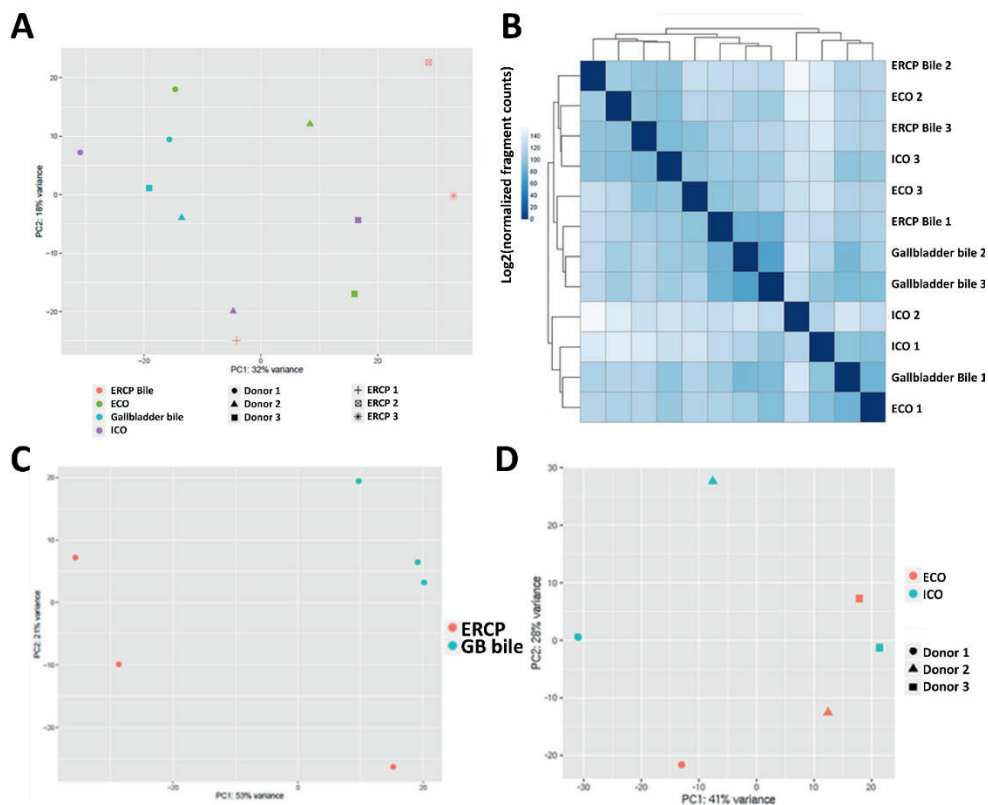
Suppl. Figure S2. Culture of ERCP-derived BCOs directly or after four hours of storage at 4°C. (a) On the left, bile samples were directly processed for organoid culture. While on the right, the bile samples were first stored at 4°C for four hours before being cultured as organoids. As shown in the bottom two pictures, bile samples directly cultured formed organoids after 7 days, while bile processed after 4 hours did not. Scale bars indicate 2mm. (b) Initiation of organoid cultures from ERCP-derived bile, cultured after < 1 hour or 4 hours of storage at 4°C, showing no outgrowth of organoids after a 4 hour storage period (n=3). * indicates a significant difference (p<0.05). (c) EpCAM+ and EpCAM- flow cytometry sorted cells from bile resulted in no viable organoids after two weeks of culture.



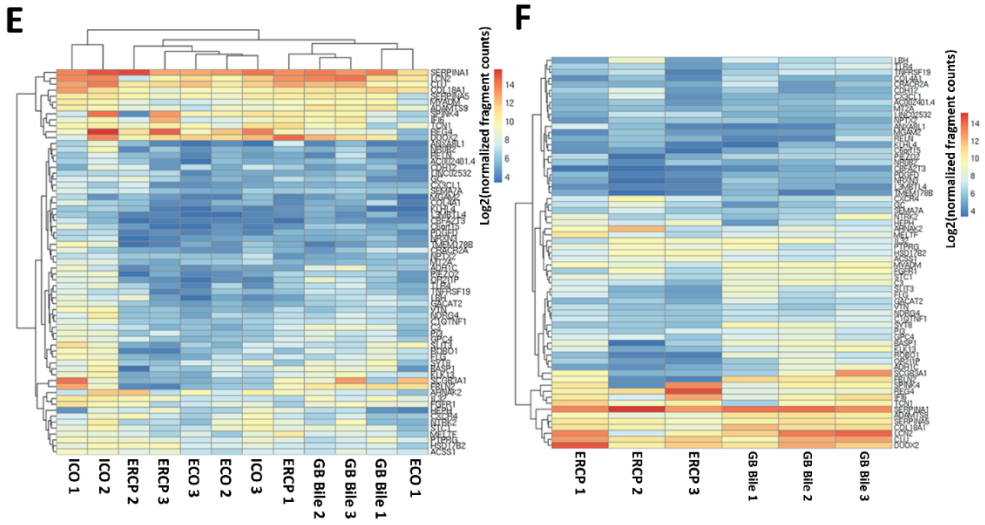
Suppl. Figure S3. Gating strategy of EdU staining in BCOs. (a) Unstimulated bile organoids ($n=3$, donors 1-3). First, cells were selected using forward-sideward scatter and next analysed on the Alexa-Fluor 488 spectrum. In (b) stained organoids are displayed.



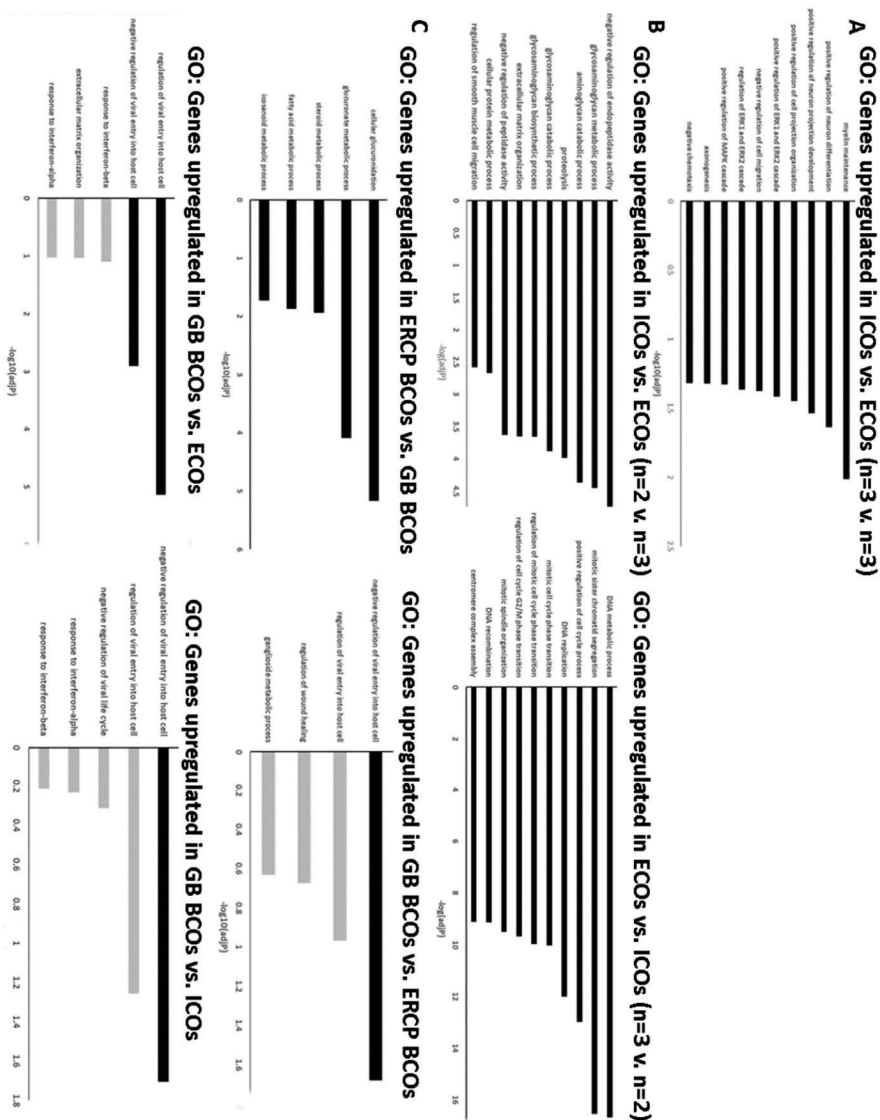
Suppl. Figure S4. Characterization of BCOs. (a-c) Normalized read counts from RNAsequencing data for BCOs obtained from gallbladder-derived bile (n=3, BCO1-3) and ERCP-derived bile (n=3, BCO5-7) compared to expression-data of primary cholangiocytes obtained from common bile duct (n=7) as published⁹ and from 2D-cultured primary hepatocytes (n=2) as published by Schneeberger *et al.*¹⁰ All genes were significantly different expressed between primary cholangiocytes and hepatocytes (not indicated), except for TFF1, TFF2, SLC10A2, LGR5, FXR2, SOX4, SOX17, MUC5AC, and MUC6. All hepatocyte related genes in panel C were significantly lower in ERCP-BCOs and GB-BCOs compared to hepatocytes (not indicated). *indicates a significant difference between ERCP-BCOs, GB-BCOs and primary cholangiocytes ($p < 0.01$). (d) Protein expression by immunofluorescence of the cholangiocyte markers: CFTR (red, left) and SCTR (green, right) with nuclei being counterstained (DAPI, blue) on BCOs (n=3, pictures displayed are from BCO5 and 7). (e) Protein expression by immunofluorescence shows absence of the hepatocyte marker: Albumin (red) in BCOs (n=3, BCO1, 5 and 7). Nuclei are counterstained with DAPI (blue). In both panels the scale bars indicate 200 μm .



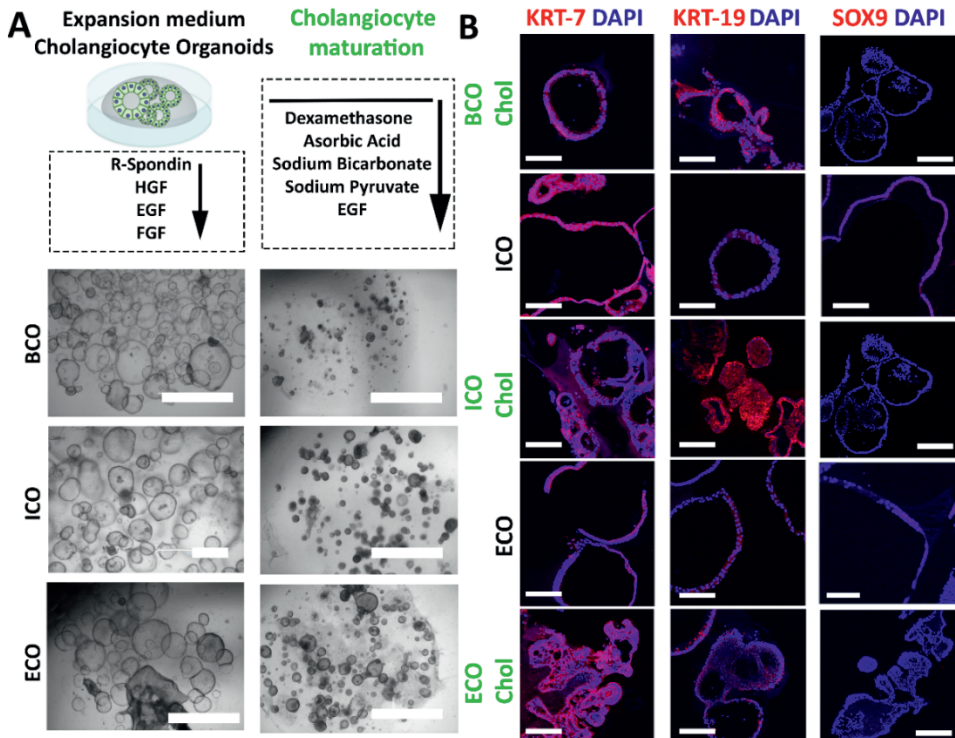
Suppl. Figure S5A-D. Expression of DE genes between ICOs and ECOs on organoid samples. (a) Principal component analysis (PCA) of top 500 most variable genes between BCOs (ERCP-derived, n=3 BCO5-7 and gallbladder-derived, n=3, BCO1-3), displayed on all organoid sample types, showing no clear clustering pattern between sources, but overall a high correlation towards each other. **(b)** Heatmap-clustering showing sample-to-sample distances on the same samples as used in the PCA plot, showing no clear clustering on either source or donor. **(c)** Principal component analysis (PCA) of ERCP-derived BCOs and gallbladder-derived BCOs. **(d)** PCA plot of ICOs vs ECOs indicating that ICO3 overlaps with ECO gene-expression profiles.



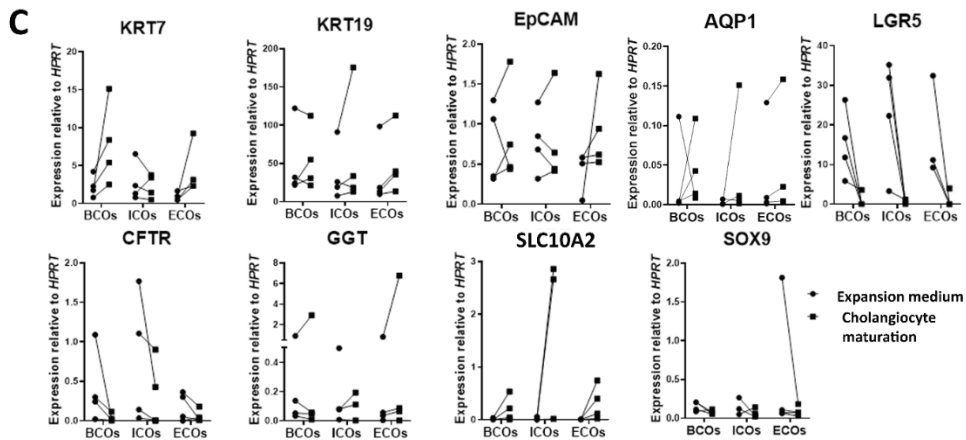
Suppl. Figure S5E-F. Expression of DEgenes between ICOs and ECOs on organoid samples. (e) Heatmap based upon ICO upregulated DEgenes on all 12 organoid samples, showing that ICO 1 and ICO 2 have an unique expression profile for ICO-specific genes compared to all other samples. **(f)** Heatmap of ICO-upregulated genes on all BCO samples, showing limited expression of these genes.



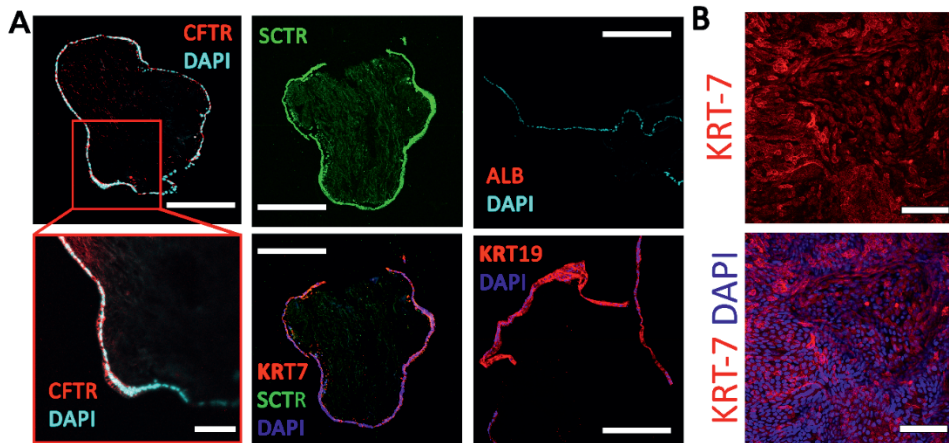
Suppl. Figure S6. Pathway analysis in cholangiocyte organoids from different sources. (a) Pathways analysis between ICOs and ECOs (n=3) revealed that certain pathways are enriched in ICOs compared to ECOs. No pathways were found to be significantly upregulated in ECOs compared to ICOs. (b) After exclusion of ICO 3, pathways analysis between ICOs (n=2) and ECOs (n=3) revealed that certain pathways are enriched in ICOs compared to ECOs. Interestingly, these analysis revealed that ECOs have significantly upregulated cell-proliferative pathways such as DNA replication and cell-cycle pathways. These results correspond to our EdU data (figure 3D) in which the two lowest proliferating ICO samples were ICO 1 and ICO 2 and ICOs were significantly less proliferative compared to ECOs. (c) Pathway analysis between different sources of BCOs showed a significant enrichment of metabolic-synthesis associated pathways in ERCP-derived BCOs compared to gallbladder-derived BCOs. No differences were found between ERCP BCOs and ICOs or ECOs. In contrast, GB-derived BCOs showed upregulation of viral-host interaction related pathways to both COs and ECOs as well as ERCP-derived BCOs. All experiments performed in Figure S6 are with donors 1-3.



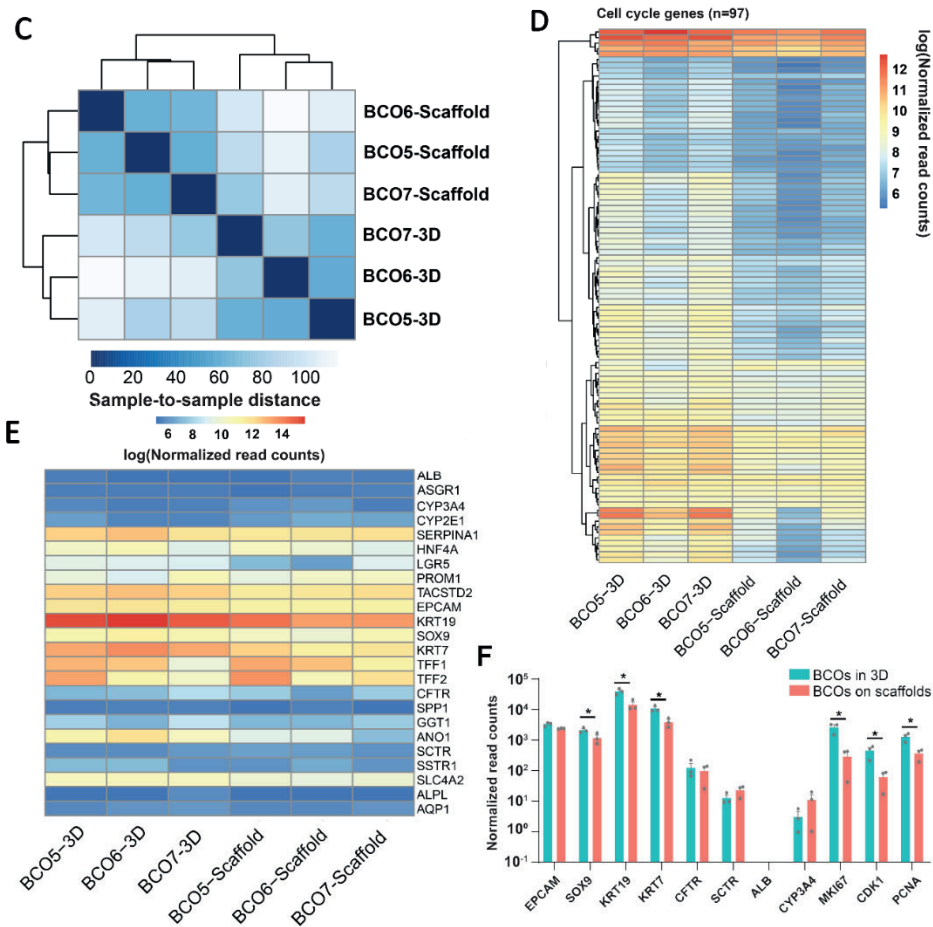
Suppl. Figure S7A-B. Cholangiocyte-organoids from all three sources can be partially matured using an established cholangiocyte-differentiation protocol. (a) Schematic overview and pictures of cholangiocyte-organoids (COs) from bile (BCO), intrahepatic biopsies (ICOs) or extrahepatic biopsies (ECOs) in either cholangiocyte maturation or in canonical-WNT stimulating conditions. Upon cholangiocyte maturation, 2D growth and smaller organoid size could be observed in multiple cultures in COs from all three sources. Scale bars indicate 2000 μ m. **(b)** Immunofluorescence images of protein expression in COs in differentiated and undifferentiated status for the cholangiocyte markers KRT-7, KRT-19 and SOX9. Images of BCOs in expansion medium for these proteins are displayed in Figure 2B. Upon cholangiocyte maturation, KRT-7 and KRT-19 expression seems more pronounced. While clear SOX9 expression could only be detected in one sample of an ICO upon cholangiocyte maturation. Scale bars indicate 100 μ m.



Suppl. Figure S7C. Cholangiocyte-organoids from all three sources can be partially matured using an established cholangiocyte-differentiation protocol. (c) Gene-expression by qRT-PCR relative to the housekeeper gene HPRT1 for cholangiocyte maturation and paired organoids cultured in canonical-WNT stimulating conditions from all three sources (n=3), for either mature cholangiocyte markers (cytokeratin-KRT-7, KRT19, CFTR, GGT, ASBT, EpCAM, AQP1 and CFTR) or stemness/cholangiocyte progenitor markers (LGR5 and SOX9). ICOs, ECOs and BCOs had higher expression of KRT7, ASBT, AQP1 and KRT19 in a similar manner after maturation, while EpCAM and GGT gene-expression remained stable. Upon cholangiocyte maturation the expression of the WNT-target gene LGR5 and the cholangiocyte progenitor marker SOX9 was lower in all cultures from all sources. In contrast, the expression of mature cholangiocyte marker CFTR was lower in the cholangiocyte maturation protocol for organoids from all three sources. As forskolin (a cAMP-activator) was removed from the cholangiocyte maturation medium, the organoids cultured in these conditions are considerably smaller (Fig. S7A) compared to organoids in expansion medium. The downregulation of CFTR could be the result of less activation by forskolin and subsequent lack of swelling, as was previously published.¹¹ However, overall our results indicate that no complete maturation is reached in vitro with this protocol, but in contrast to upregulation of hepatocyte-markers, here all organoid sources behave similar. All experiments performed in Figure S7 are with donors 1-3.



Suppl. Figure S8A-B. BCOs can successfully recellularize EHBD-scaffolds as cholangiocyte-like cells. (a) Immunofluorescence staining of sections of BCO-recellularized scaffolds demonstrating presence of the mature cholangiocyte markers CFTR (red, upper/bottom left panel), SCTR (green, upper middle panel), KRT-7 (red, bottom middle panel), KRT-19 (red, bottom right panel) and absence of the hepatocyte related marker albumin (red, upper right panel). All sections are stained with DAPI (nuclei, cyan or dark blue). Scale bars indicate 200 μm . (b) Whole mount confocal images of immunofluorescence staining KRT-7 (red, upper panel) and KRT-7 and DAPI (nuclei, blue bottom panel) of repopulated EHBD scaffolds with BCOs, scale bars indicate 100 μm .



Suppl. Figure S8C-F. BCOs can successfully recellularize EHBD-scaffolds as cholangiocyte-like cells. (c) Heatmap of sample-to-sample distances, showing a clear clustering based on the culture condition. **(d)** Heatmap showing the cell cycle gene expression from the samples in the 2 conditions. **(e)** Heatmap of the expression levels of a few selected hepatocyte and cholangiocyte markers between the 2 culture conditions. **(f)** Bar plot showing the expression of selected known cholangiocyte markers (*EPCAM*, *SOX9*, *KRT19*, *KRT7*, *CFTR*, and *SCTR*), hepatocyte markers (*ALB* and *CYP3A4*), and cell cycle related markers (*MKI67*, *PCK1*, and *PCNA*) in both conditions. *indicates a significant difference ($p < 0.05$ adjusted for multiple testing).

SUPPLEMENTARY INFORMATION REFERENCES

1. Broutier L, Andersson-Rolf A, *et al.* Culture and establishment of self-renewing human and mouse adult liver and pancreas 3D organoids and their genetic manipulation. *Nat Protoc*, 2016. 11(9):1724-43.
2. Sampaziotis F, Justin AW, *et al.* Reconstruction of the mouse extrahepatic biliary tree using primary human extrahepatic cholangiocyte organoids. *Nat Med*, 2017. 23(8):954-63.
3. Huch M, Gehart H, *et al.* Long-term culture of genome-stable bipotent stem cells from adult human liver. *Cell*, 2015. 160(1-2):299-312.
4. Soroka CJ, Assis DN, *et al.* Bile-Derived Organoids From Patients With Primary Sclerosing Cholangitis Recapitulate Their Inflammatory Immune Profile. *Hepatology*, 2019. 70(3):871-82.
5. Sampaziotis F, de Brito MC, *et al.* Directed differentiation of human induced pluripotent stem cells into functional cholangiocyte-like cells. *Nat Protoc*, 2017. 12(4):814-27.
6. Sampaziotis F, de Brito MC, *et al.* Cholangiocytes derived from human induced pluripotent stem cells for disease modeling and drug validation. *Nat Biotechnol*, 2015. 33(8):845-52.
7. Versteegen MMA, Roos FJM, *et al.* Human extrahepatic and intrahepatic cholangiocyte organoids show region-specific differentiation potential and model cystic fibrosis-related bile duct disease. *Sci Rep*, 2020. 10(1):21900.
8. Willemse J, Roos FJM, *et al.* Scaffolds obtained from decellularized human extrahepatic bile ducts support organoids to establish functional biliary tissue in a dish. *Biotechnol Bioeng*, 2021. 118(2):836-51.
9. Rimland CA, Tilson SG, *et al.* Regional Differences in Human Biliary Tissues and Corresponding In Vitro-Derived Organoids. *Hepatology*, 2021. 73(1):247-67.
10. Schneeberger K, Sánchez-Romero N, *et al.* Large-scale production of LGR5-positive bipotential human liver stem cells. *Hepatology*, 2020. 72(1):257-70.
11. Van Mourik P, van Haaren P, *et al.* R117H-CFTR function and response to VX-770 correlate with mRNA and protein expression in intestinal organoids. *J Cyst Fibros*, 2020. 19(5):728-32.

CHAPTER

3

Kinome profiling of cholangiocarcinoma organoids reveals potential druggable targets that hold promise for treatment stratification

Ruby Lieshout^{1*}, Alessandra V.S. Faria^{2,3*}, Maikel P. Peppelenbosch²,
Luc J.W. van der Laan¹, Monique M.A. Versteegen^{1#}, Gwenny M.
Fuhler^{2#}

**These authors contributed equally*

#These authors contributed equally

¹Erasmus MC Transplant Institute, Department of Surgery, Erasmus University Medical Center, Rotterdam, The Netherlands

²Department of Gastroenterology and Hepatology, Erasmus University Medical Center, Rotterdam, The Netherlands

³Department of Biochemistry and Tissue Biology, University of Campinas, UNICAMP, Campinas, SP, Brazil

ABSTRACT

Background: Cholangiocarcinoma is a rare but lethal cancer of the biliary tract. Its first-line treatment is currently restricted to chemotherapy, which provides limited clinical benefit. Kinase inhibitors targeting oncogenic intracellular signaling have changed the treatment paradigm of cancer over the last decades. However, they are yet to be widely applied in cholangiocarcinoma therapy. Cholangiocarcinoma has marked molecular heterogeneity, which complicates the discovery of new treatments and requires patient stratification. Therefore, we investigated whether a commercial kinome profiling platform could predict druggable targets in cholangiocarcinoma.

Methods: Kinase activity in patient-derived cholangiocarcinoma organoids, non-tumorous adjacent tissue-derived and healthy donor-derived intrahepatic cholangiocyte organoids was determined using the PamChip® phosphotyrosine kinase microarray platform. Kinome profiles were compared and correlated with RNA sequencing and (multi-)kinase inhibitor screening of the cholangiocarcinoma organoids.

Results: Kinase activity profiles of individual cholangiocarcinoma organoids are different and do not cluster together. However, growth factor signaling (EGFR, PDGFR β) and downstream effectors (MAPK pathway) are more active in cholangiocarcinoma organoids and could provide potential druggable targets. Screening of 31 kinase inhibitors revealed several promising pan-effective inhibitors and compounds that show patient-specific efficacy. Kinase inhibitor sensitivity correlated to the activity of its target kinases for several inhibitors, signifying them as potential predictors of response. Moreover, we identified correlations between drug response and kinases not directly targeted by those drugs.

Conclusions: In conclusion, kinome profiling is a feasible method to identify druggable targets for cholangiocarcinoma. Future studies should confirm the potential of kinase activity profiles as biomarkers for patient stratification and precision medicine.

INTRODUCTION

Peptide arrays are a cost-effective, high-throughput method to determine kinase activity in cell lysates.¹ Such kinome profiling has emerged as an effective strategy to screen activity of a large number of kinases simultaneously, and investigate how these are differentially modulated in several biological systems.² An advantage of this approach in cancer is that kinome profiling incorporates the complex additive effect of mutations, epigenetics, transcriptional regulation and posttranscriptional modification, resulting in a kinase activity profile that describes the downstream effect of these changes. Investigation of the global up- or downregulation of kinase activity in cancerous tissues may reveal which existing kinase inhibitors are potentially effective in patient treatment and could identify new potential druggable targets. In pediatric brain tumors, kinome profiling by peptide array confirmed previously reported signaling pathway activity in Epidermal growth factor receptor (EGFR or ERBB1), Hepatocyte growth factor receptor (c-MET) and Vascular endothelial growth factor receptor (VEGFR), associated these tumors with highly active Proto-oncogene tyrosine-protein kinase (Src) family kinases and demonstrated corresponding treatment responses to Src kinase inhibitors³, showing the applicability of this technique to identify potential therapeutic targets. However, to date, kinome profiling for cholangiocarcinoma (CCA) has only been performed on 2D cell lines⁴, but not primary-cancer-derived 3D organoid lines.

CCA is a relatively rare but lethal cancer originating in the biliary tract. It is the second most common form of liver cancer after hepatocellular carcinoma, representing ~15% of cases.⁵ The prognosis for CCA patients is dismal, with 5 year survival rates of 7-20%.⁵ CCA often goes undetected for an extended period of time, being discovered at an advanced stage when curative treatment by surgical removal has become impossible. The only systemic treatment for CCA is palliative and consists primarily of chemotherapeutics that provide limited benefit. Therefore, it is essential to identify more effective treatment modalities.

Treatments that have gained traction in recent years are the arsenal of (tyrosine) kinase inhibitors directed at molecular oncogenic intracellular signaling.⁶ All cellular processes depend on kinase activity, and constitutive activation of these pathways in cancerous tissues has shown to be a promising target for treatment in many cancers.⁷⁻⁹ For CCA, several clinical trials were performed where such targeted therapeutics were added to palliative treatment regimens. However, results of these clinical trials with kinase inhibitors targeting Human epidermal growth factor receptor (HER), c-MET, KRAS-BRAF-MEK-ERK (Serine/threonine-protein kinase B-raf (BRAF)-Dual specificity mitogen-activated protein kinase kinase (MAP2K or MEK)-Extracellular signal-regulated kinase (ERK)), and PI3K-AKT-mTOR (Phosphoinositide 3-kinase (PI3K)-Protein kinase B (AKT)-Serine/threonine-protein kinase mTOR (mTOR)) were disappointing, as addition of the kinase inhibitors did not prove more effective than current treatment protocols.¹⁰ A probable explanation for the failure of these trials is that there was no accurate biological stratification of patients.

Large scale studies focused on the genetic characterization of CCA have elucidated the complex and heterogeneous mutational landscape of this tumor. These studies have found

druggable mutations, amplifications or fusions of genes in about 40% of CCA patients, demonstrating notable opportunity for targeted therapies.¹¹ Recently, Fibroblast growth factor receptor (FGFR) inhibitor pemigatinib was approved for treatment of CCA patients with Fibroblast growth factor receptor 2 (FGFR2) fusions or mutations, after demonstrating an objective response rate of 35.5% and a durable response of ≥ 12 months in 37% of the responders in a phase 2 clinical trial.¹² This is one example of how genetic characterization can improve treatment stratification. However, even after selection by genetic aberration, only subgroups of included patients benefit from targeted treatment. Moreover, treatment response to signaling inhibitors is not always directly linked to mutations in the targeted pathways, as multiple mutations may accumulate in a tumor, allowing it to bypass inhibitor effects.^{6, 13, 14} Therefore, there is a pressing need for an alternative, more accurate stratification for targeted therapeutics. For CCA, correlating kinase activity to kinase inhibitor treatment response may improve personalized patient care.

As clinical trials for targeted therapies are expensive and time-consuming, a representative and scalable *in vitro* CCA model for drug screening could speed up the identification of personalized effective treatment approaches. With recent developments in organoid technology this has now become feasible for CCA. Patient-derived cholangiocarcinoma organoids (CCAOs) are 3-dimensional, self-organizing cell cultures that grow and recapitulate the genomic aberrations and gene expression patterns of the parental tumor to a large extent.¹⁵⁻¹⁸ These CCAOs can be established from both resected tumors and core needle biopsies, and are amenable to high-throughput drug screening.^{15, 16, 18}

Here, we investigated whether assessment of kinome profiles generated through a commercial platform could predict potential druggable targets in CCA. To this end, we performed phosphotyrosine kinome profiling in patient-derived CCAOs, (paired) patient-derived non-tumorous adjacent cholangiocyte organoids (HAOs), and healthy donor-derived intrahepatic cholangiocyte organoids (ICOs) to identify the differentially active kinases in CCA cells. Moreover, we screened a library of (multi-)kinase inhibitors in these CCAOs to determine if kinase activity could predict treatment response in CCA cells.

MATERIALS AND METHODS

Organoid culture

Organoids were initiated from three CCA tissue samples, two matched adjacent non-tumorous tissue samples and three healthy donor liver tissue samples. All tissue samples were collected at the Erasmus Medical Center Rotterdam after surgical resection or liver transplantation. The use of these tissue samples was approved by the medical ethics committee of Erasmus Medical Center Rotterdam (MEC-2013-143 & MEC-2014-060). All patients consented to the use of resected or transplant materials for research purposes. CCAOs and organoids from non-tumorous tissues were cultured as described previously by Broutier et al.¹⁵ and Huch et al.¹⁹ CCAO1 was derived from a perihilar CCA, while CCAO2 and CCAO3 were initiated from intrahepatic CCAs. Tumorigenicity of CCAOs was confirmed by tumor formation after subcutaneous xenografting in female NOD.Cg-Prkdc^{SCID} Il2rg^{tm1Wjl}/SzJ

(NSG) mice (Charles River) and detection of cancer-related mutations by targeted next generation sequencing for a gene panel of 63 solid cancer-related genes (Lieshout *et al.* 2022, accepted). Mutations identified related to kinase signaling were ARID1A mutation (CCAO1) and deletion (CCAO2, CCAO3), DDR2 amplification (CCAO2), ERBB2 amplification (CCAO3), FGFR1 deletion (CCAO2), IGF1R mutation (CCAO1) and amplification (CCAO2, CCAO3), KRAS mutation (CCAO1, CCAO2), MTOR deletion (CCAO3), NRAS deletion (CCAO3), PIK3R1 deletion (CCAO2), ROS1 deletion (CCAO2).

Global phosphotyrosine kinase assay

Sample preparation

Prior to kinome profile analysis, organoids were cultured for 12 hours in Advanced DMEM/F-12 (Thermo Scientific, USA) without supplements described for organoid culture, to allow full endogenous kinomic activity. After 12 hours, organoids were collected and washed with NaCl 0.9% (ice cold) to remove the Matrigel. After that, the organoids were lysed using M-PER™ Mammalian Protein Extraction Reagent (Thermo Scientific, USA) with Halt Protease Inhibitor Cocktail (Thermo Scientific, USA) and Halt Protease Inhibitor Cocktail (Thermo Scientific, USA) – organoids were incubated for 10 min on ice followed by centrifugation (14000 rpm, 10 min, 4°C). The supernatant was collected, and protein concentration was measured using Lowry method (DC protein assay, Bio-Rad, USA). Supernatants were stored at –80°C until use.

Kinase assay

Organoid lysates (1 µg/µL protein for all samples) were loaded on a PamChip tyrosine-kinase microarray (PamGene International BV, The Netherlands) as described previously.²⁰ Phosphorylation of the 144 kinase substrates on the array was detected by using FITC-labelled secondary antibody. Signal intensities of the three technical replicates for each substrate were quantified using Bionavigator software (version 6.1.42.1; PamGene International BV). The internal positive control peptide ART_003_EAI(pY)AAPFAKKKXC was not considered for further analysis and the kinase activity was normalized by the CD79A_181_193 peptide. V max values below zero were artificially set to zero. Only V max values with average above zero were considered for further analysis. A dotplot graphic was built (Lux vs time 640 sec to 1840 sec), and the area under the curve (AUC) calculated using GraphPad software (version 5.0, GraphPad Inc., USA) as a measure of peptide phosphorylation, and AUC values of zero were replaced by the lowest AUC value determined for that organoid line to allow for comparative analysis and correlation of all peptides. For upstream kinase analysis, kinases known to phosphorylate the specific peptides (target peptides) were identified by Uniprot²¹ and Ensembl²² databases. The matched peptides and upstream kinases can be found in Supplementary Table T1.

Descriptive statistics and exploratory data analysis

All exploratory data analysis were performed by R software version 4.2.1. From AUC calculated by GraphPad, data analysis was done using R 4.2.1²³ and RStudio²⁴ software, applying the packages tidyverse 1.3.0²⁵ for data manipulation, ggplot2²⁶ for data

visualization, factoextra 1.0.7²⁷ for PCA analysis and graphics, complex heatmap for heatmap visualization and clustering²⁸, and correlation 0.7.1²⁹ for correlation calculation. Upstream kinase activity and mRNA expression heatmap (Fig. 1C) is based on calculated z-scores from AUC (kinome profiling) and TMM normalized counts data (RNAseq). Clustering (Fig. 2D) is based on the distance matrix calculation (Pearson method) and followed by columns clustering.

Inferential statistics

All statistical analyses were performed by R software version 4.2.1. Statistical comparisons were performed by Kruskal-Wallis rank sum test (Stats R package, version 4.3.0) with Dunn post-test and p-values were adjusted by False discovery rate (FDR) (FSA R package, version 0.9.3).³⁰ For correlation analysis, Spearman and Pearson methods were applied and p-values were adjusted by FDR correction. Differences were determined to be statistically significant when $p < 0.05$.

RNA sequencing

Descriptive statistics and exploratory data analysis

GEO Dataset Record number GSE179601 based on the GeneChip Human Genome U133 Plus 2.0 Array (Affymetrix) was used to acquire RNA sequencing data of the three CCAO lines. All exploratory data analysis were performed by R software version 4.2.1. From TMM normalization data, data analysis was done using R 4.2.1²³ and RStudio²⁴ software, applying the packages tidyverse 1.3.0²⁵ for data manipulation, ggplot2²⁶ for data visualization, complex heatmap for heatmap visualization and clustering²⁸, and correlation 0.7.1²⁹ for correlation calculation. Clustering is based on the distance matrix calculation (Pearson method) and followed by columns clustering.

Inferential statistics

All statistical analyses were performed by R software version 4.2.1. Statistics were made by Student's t-test and p-values were adjusted by FDR correction. For correlation analysis, Pearson method was applied and p-values were adjusted by FDR correction. Differences were determined to be statistically significant when $p < 0.05$.

FDA-approved oncology drug screening

Organoid treatment

Organoids were collected and washed using ice-cold Advanced DMEM, followed by mechanical disruption into fragments. Those fragments were dissociated into single cells and small cell clumps by three cycles of three minutes incubation with Trypsin-EDTA in a 37°C water bath with mechanical disruption in between. Then, the cell suspension was filtered through a 100 μm filter, cells were plated in 5 μL droplets in white walled 96 well plates and covered with expansion medium. The FDA-approved oncology drugs library version 8 used, was kindly provided by the Developmental Therapeutics Program of the Division of Cancer Treatment and Diagnosis of the National Cancer Institute (<http://dtp.cancer.gov>). This compound library contains 37 targeted therapeutics, of which

31 are kinase inhibitors (Supplementary Table T2). Compounds were added after two days of organoid culture in 1 μM and 10 μM concentrations. After four days of exposure, organoid viability was determined.

Viability measurement

Organoid viability was determined by quantification of ATP content using the CellTiterGlo® 3D Cell Viability Assay (Promega) according to manufacturer's instructions. An ATP standard curve was included for every organoid line, using a 4x dilution series ranging from 20 μM to 4.9 nM of ATP disodium salt (Promega). Drugs were considered to effectively inhibit the organoid culture if their viability value was below the mean minus three times the standard deviation of the vehicle control treated organoids of the same organoid line.

RESULTS

Enzymatic kinase activities are not correlated to their transcriptional expression levels

RNA expression levels are known to correlate imperfectly to protein expression, let alone protein enzymatic activity. Therefore, we first investigated to what extent RNA transcription patterns in CCAOs are reflected in their kinomic activity.^{31, 32} To this end, we generated kinome profiles of three patient-derived CCAO lines to compare to established RNAseq profiles of these CCAOs (Fig. 1A). The peptide targets present on the kinome profiling array were matched to upstream kinases responsible for the phosphorylation of the target as is reported in the Uniprot and Ensemble database (Suppl. Table T1). Overall, similar gene expression levels were found in the three CCAO lines (CCAO1 to CCAO3) (Fig. 1B). However, as shown in Figure 1C, mRNA expression patterns of the individual upstream kinases included in the kinome profiling array did not always correspond to activity of these enzymes. For instance, for kinases like FES and HCK clear activity was detected but no clear gene expression. Correlation analyses, which were performed using linear regression (Pearson method, unsupervised), confirmed that kinome profiles and RNAseq data poorly correlate in each CCAO line, as shown by R^2 values below 0.01 (Fig. 1D). These data highlight that there is a poorly correlation between RNA expression profiles in cancer cells and the actual kinase enzymatic activity. Thus, kinome activity profiling may arguably provide a better proxy to predict kinase inhibitor response in cancer than transcriptional profiles.

Kinome profiles are heterogeneous

We further explored the kinome profiles of the three CCAOs, and included two patient-matched non-tumorous adjacent tissue-derived cholangiocyte organoid lines (CCAO1, CCAO2 with matched HAO2, and CCAO3 matched with HAO3) and three healthy donor-derived intrahepatic cholangiocyte organoid lines (ICO1, ICO2 and ICO3) (Fig. 2A).³³ Violin plots of the overall kinase activity levels show that activities were distributed similarly in all organoid cultures, except HAO3, which was significantly different from all samples except CCAO3 and ICO3 (FDR adjusted $p < 0.05$ for HAO3 vs. CCAO1, ICO2; $p < 0.01$ for HAO3 vs. CCAO2, HAO2, ICO3) (Fig. 2B).

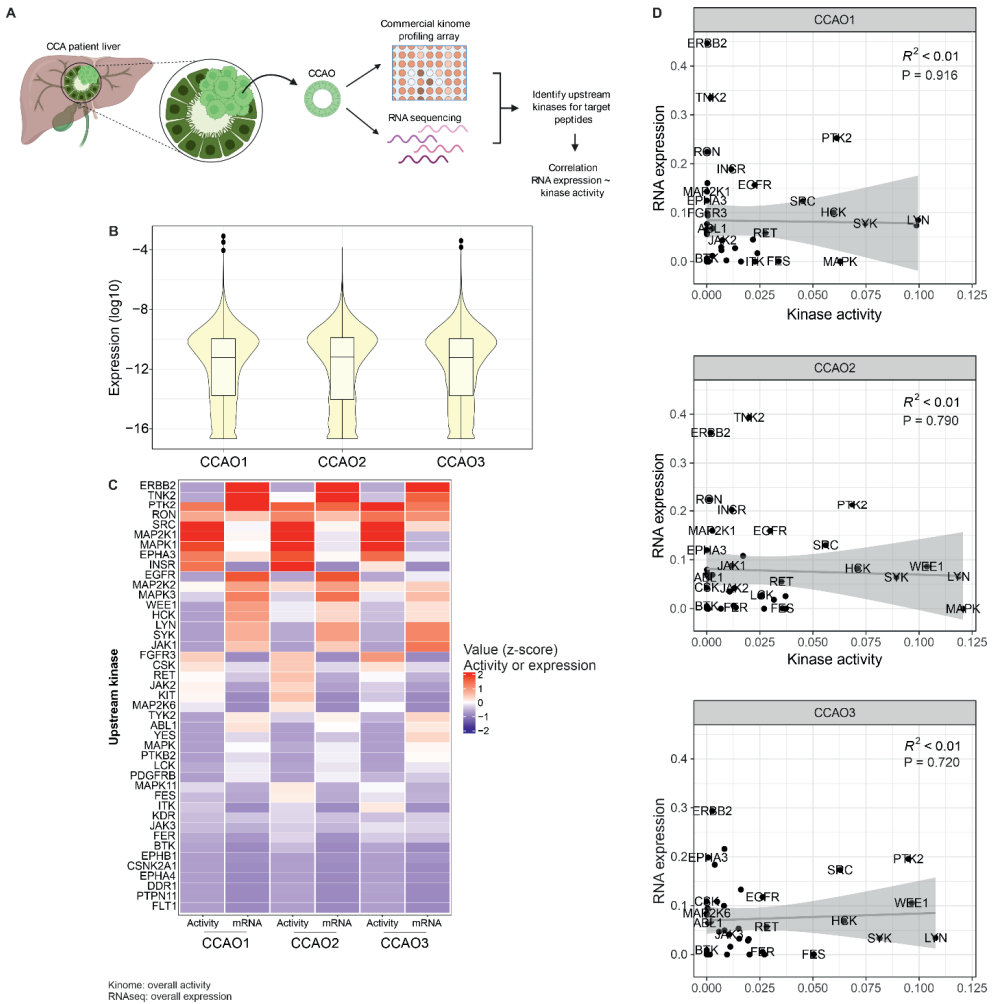


Figure 1. mRNA expression of kinases does not correlate to kinase activity. (a) Schematic representation of the workflow. Kinome profiles were established, and RNA sequencing data were acquired for patient-derived CCA organoids (CCAOs). Upstream kinases were identified from the Uniprot and Ensemble databases for the peptides included in the kinome profiling array. Correlation analysis was performed to investigate the relationship between mRNA expression levels and kinase activity. Schematic created with BioRender.com. (b) Violin plots with box plots of the RNA expression levels show a similar overall distribution of genes in the three CCAO lines. (c) Heatmap of the activity (AUC of the activity plots) and mRNA expression (normalized counts) of the 37 upstream kinases included in the kinome profiling array in the three CCAO lines. Data is shown by calculated z-score. (d) Scatter plots demonstrate there is no correlation between the kinase activity and RNA expression level of the upstream kinases in the three CCAOs.

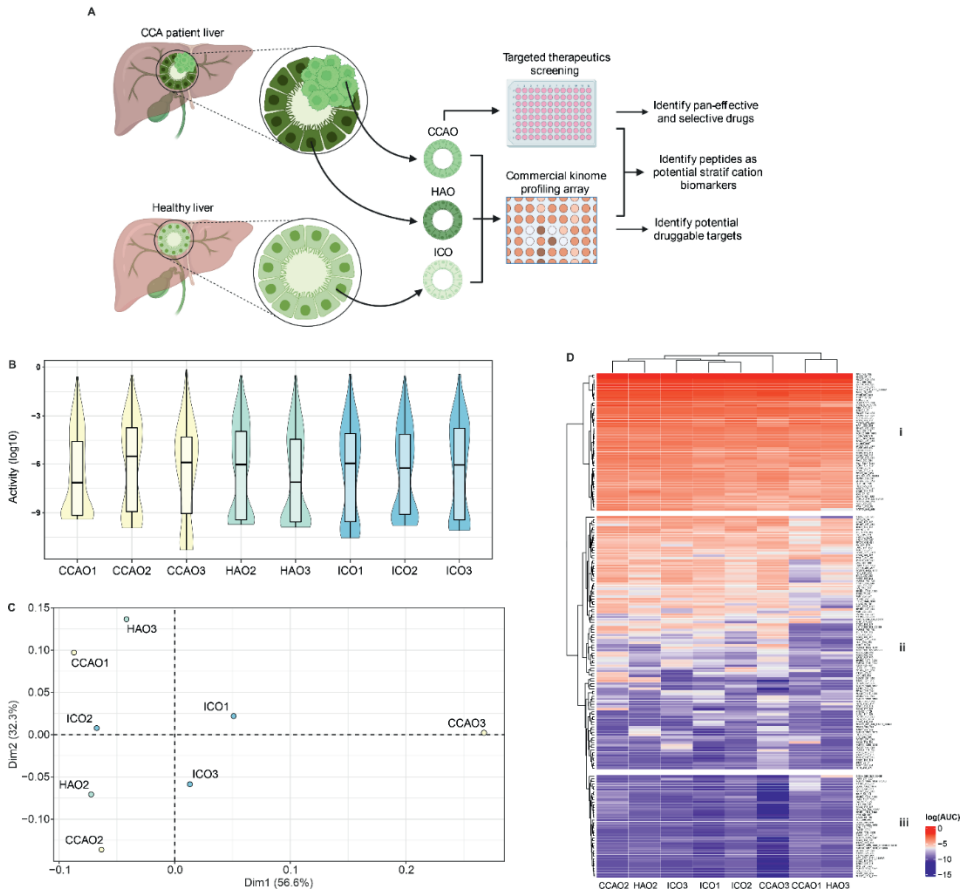


Figure 2. Exploratory kinome analysis demonstrates individual kinase activity profiles of CCAOs. (a) Schematic representation of the experimental setup. Kinase activity profiles were established for three CCAO lines with two matched non-tumorous adjacent tissue-derived organoid lines (CCAO1, CCAO2 with matched HAO2, and CCAO3 matched with HAO3) and three healthy donor-derived intrahepatic cholangiocyte organoid lines (ICO1, ICO2 and ICO3). Comparison of these profiles leads to the identification of potential druggable targets. CCAOs were also subjected to a screening of targeted therapeutics to identify pan-effective and selective compounds. Correlation between drug response and kinase activity leads to the discovery of potential biomarkers for treatment stratification. Schematic created with BioRender.com. (b) Violin plots with box plots showing that the overall kinase activity data density distribution is similar for all samples. Colors represent sample types (CCAO in yellow, HAO in green, ICO in blue). There was a significant difference in values among samples (p -value = $1.488e-03$), with HAO3 being significantly different from all samples except CCAO3 and ICO3 (FDR adjusted $p < 0.05$ for HAO3 vs. CCAO1, ICO2; $p < 0.01$ for HAO3 vs. CCAO2, HAO2, ICO3). (c) Principle component analysis (PCA) plot of kinome activity of all peptides included in the kinome profiling array based on principle component 1 and 2. Each sample is represented by one dot (CCAO in yellow, HAO in green, ICO in blue). CCAO3 is the most distinct sample in the dataset. CCAOs are positioned far apart. (d) Heatmap of all kinase target peptides on the array analyzed by unsupervised clustering for samples and for kinase target peptides. Data is shown by $\log_{10}(\text{AUC target peptide})$. Three peptide clusters are emphasized: (i) peptides highly phosphorylated in all samples, (ii) peptides with heterogeneous phosphorylation patterns between samples, and (iii) peptides lowly/not phosphorylated in all samples.

Unsupervised cluster analysis of kinase activity in organoid samples as visualised in a principle component analysis (PCA) plot (Fig. 2C) and heatmap (Fig. 2D) demonstrated that CCAO3 expressed the most distinct kinome profile. The kinome profile of CCAO2 shows the highest similarity to its adjacent tissue counterpart HAO2, suggesting a patient-specific kinome profile for this donor (Fig. 2C, D). However, this was not observed for CCAO3 and HAO3. The healthy donor-derived ICO1 and ICO2 showed the highest similarity to each other, secondary to ICO3, demonstrating that while these lines have a diverse kinomic profile, they share more features with each other as compared to the other organoid lines tested (Fig. 2D). Aside from clustering based on samples, kinome profiles were also clustered based on peptides (Fig. 2D, Suppl Table T3). Three peptide clusters were identified that embodied highly phosphorylated peptides in all samples (Fig. 2D, cluster i), lowly/not phosphorylated peptides in all samples (Fig. 2D, cluster iii), and peptides that demonstrated heterogeneous activity of kinases (Fig. 2D, cluster ii). Cluster iii peptides were excluded from further analyses as it is unlikely that kinases with very low activity could provide meaningful druggable targets. Cluster ii contains the highest number of target peptides and is likely to contain the most patient-specific information for development of CCAO-specific therapeutic targets. These findings demonstrate that there is no common kinome profile signature for CCAOs, suggesting that personalized kinase activity profiling is indeed beneficial to assess individual responses to treatment.

Identification of shared and patient-specific therapeutic targets in CCAO

We next investigated whether the CCA-derived organoids are marked by selective activity of individual kinases. To this end, we compared phosphorylation of individual peptides with known upstream kinases between the samples. Due to the low power (most comparisons are between technical triplicates of two samples to identify sample-specific patterns), no statistical analyses could be performed. Therefore, Figure 3 displays upstream kinases responsible for phosphorylation of the array peptides with an average fold change > 2 (full dataset in Suppl. Table T4). The comparison between all healthy donor-derived organoids (ICO1, ICO2, ICO3) and CCAOs (CCAO1, CCAO2 and CCAO3) revealed 10 kinases with a fold change > 2 in CCAOs, while 2 kinases were more active in ICOs (Fig. 3A). MAPK family kinases (MAPK11, 4.2 fold higher and MAP2K6, 11.0 fold higher) demonstrated the highest fold change, indicating that they were more active in CCAOs (Fig. 3A). The comparison of kinase activity of matched patient samples CCAO2 and HAO2 disclosed similar findings (Fig. 3B). Eleven kinases showed at least 2 fold higher activity in CCAO2, while one kinase was more active in HAO2. MAPK family kinases demonstrated the largest difference in activity (MAP2K6 70.3 fold higher in CCAO2; MAPK1 and MAP2K1 both 4.7 fold higher in CCAO2), followed by RON (13.3 fold) and RET (13.2 fold) (Fig. 3B). The kinome profile of CCAO3 was very different from its adjacent counterpart, displaying 29 upstream kinases with a fold change over 2 (Fig. 3C). JAK kinase family (JAK1 67.9, JAK2 3.2 and JAK3 4.7 fold higher), growth factor signaling (PDGFR β 23.1 fold, FGFR3 17.4 fold, ERBB2 25.8 fold and EGFR 8.9 fold) and MAPK (MAP2K1 19.5, MAP2K2 3.2, MAPK11 3.9 and MAPK3 3.2 fold) kinases displayed higher activity in the cancer organoids of this patient (Fig. 3C).

Comparison of the individual CCAO lines showed that the different CCAO pairs have 19, 15, and 24 upstream kinases with differential activity (fold change > 2) (Fig. 3D-E). This demonstrates that each of these CCAO lines modulates distinct kinomic pathways leading to marked diversity in kinase activity, confirming the notion that a ‘one treatment for all’ approach is not likely to be successful.

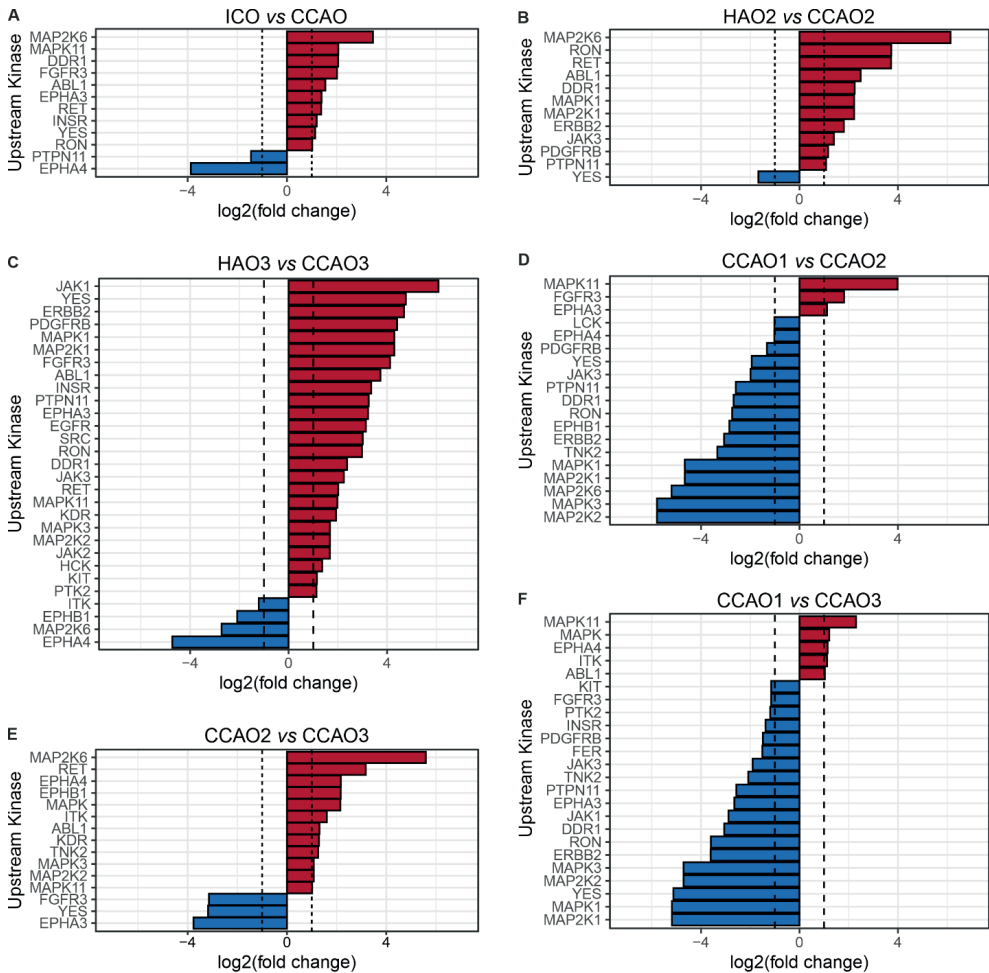


Figure 3. CCAOs demonstrate activity of diverse kinase pathways. Bar graphs displaying upstream kinases that have an average fold change > 2. **(a)** ICO (blue = higher activity) vs CCAO (red = higher activity). **(b)** HAO2 (blue = higher activity) vs CCAO2 (red = higher activity). **(c)** HAO3 (blue = higher activity) vs CCAO3 (red = higher activity). **(d)** CCAO2 (blue = higher activity) vs CCAO1 (red = higher activity). **(e)** CCAO3 (blue = higher activity) vs CCAO2 (red = higher activity). **(f)** CCAO3 (blue = higher activity) vs CCAO1 (red = higher activity).

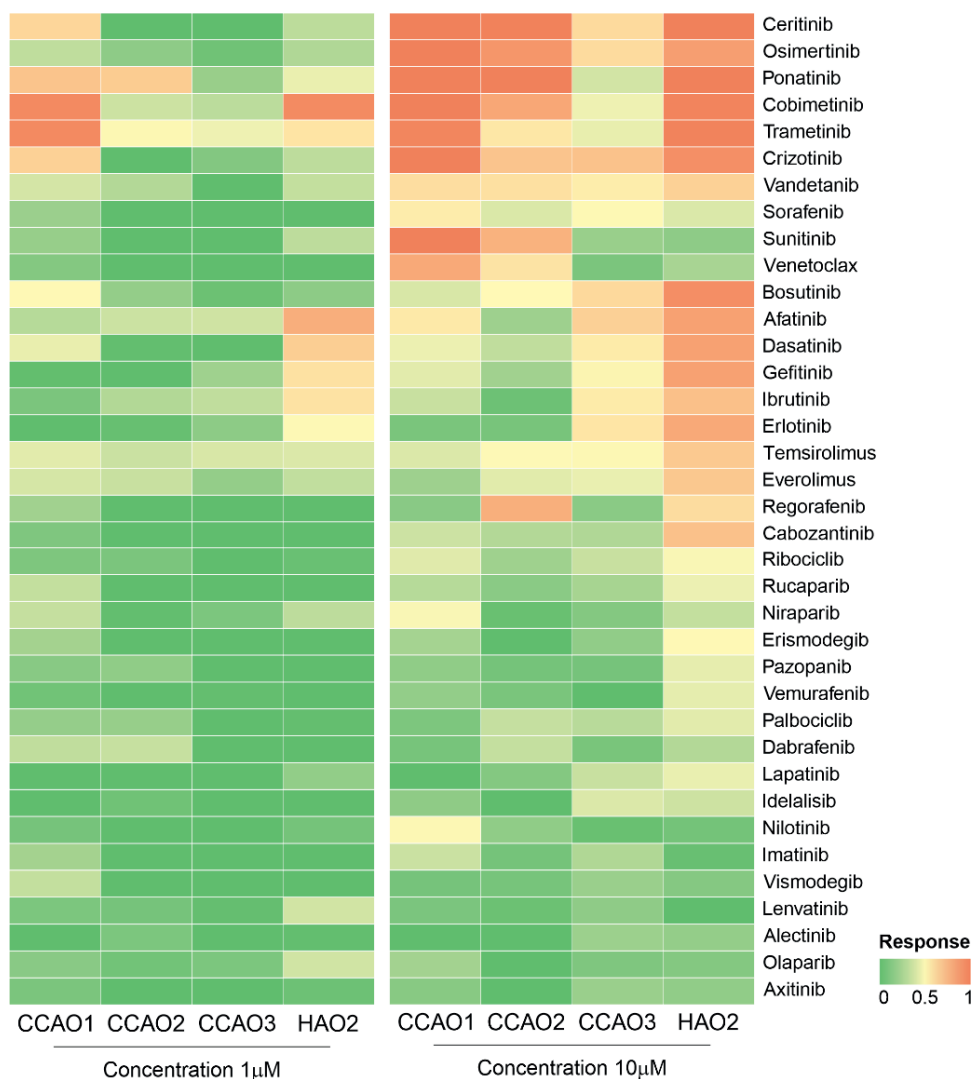


Figure 4. Drug screening reveals pan-effective and patient-specific drug efficacy. CCAOs and HAOs were treated with 37 FDA-approved targeted therapeutics (Suppl. Table T2) at 1 μM and 10 μM concentrations for four days. Drug efficacy is visualized in a heatmap of viability relative to vehicle-treated control organoids. Drug response ranges from 0, indicating that organoids are unaffected by the compound, to 1, indicating complete absence of surviving organoid cells.

Screening of targeted therapeutics in CCAOs reveals promising pan-effective and selective inhibitors

We investigated the sensitivity of the three CCAO lines to 37 FDA-approved targeted therapies, of which 31 are kinase inhibitors (Suppl. Table T2). These include multi-tyrosine kinase inhibitors (e.g. Axitinib, Sorafenib) as well as specific cytosolic kinase inhibitors (e.g. mTOR – Temsirolimus, MEK1/MEK2 – Trametinib). Organoids were subjected to treatments for four days, after which viability was determined by ATP quantification. CCAOs proved

resistant to most targeted therapeutics at 1 μM (Fig. 4). Therefore, further analyses were performed with data derived from organoids treated with 10 μM of these compounds. At this concentration, eight drugs were pan-effective in CCAOs: multi-tyrosine kinase inhibitors Crizotinib, Sorafenib, Vandetanib, and Ponatinib, MEK1/MEK2 inhibitors Cobimetinib and Trametinib, EGFR inhibitor Osimertinib and ALK inhibitor Ceritinib effectively reduced viability in all three organoid lines (Fig. 4). Of these, Ponatinib and Trametinib were also effective at the lower dose of 1 μM . These pan-effective compounds could provide interesting leads for CCA treatment. In contrast, thirteen compounds demonstrated more selective drug responsiveness in one or two CCAO lines (Fig. 4). Of these, multi-tyrosine kinase inhibitor Sunitinib and BCL-2 inhibitor Venetoclax had a selective effect for cancer organoids, inhibiting two of the CCAO lines, but leaving the third CCAO line unharmed. For these more selective inhibitors, it is important to identify stratification criteria to predict drug sensitivity. In CCAO3, activity of EGFR was higher compared to HAO3 (Fig. 3C). Interestingly, this was reflected in EGFR (ERBB1) inhibitor sensitivity, with 5 out of 5 ERBB inhibitors (Afatinib, Erlotinib, Gefitinib, Lapatinib, Osimertinib) effectively inhibiting CCAO3, while only 2/5 (CCAO1) or 1/5 (CCAO2) were effective in the other CCAO lines (Fig. 4). This promising finding encouraged a more thorough examination of the correlations between kinase activity and drug sensitivity.

Exploring kinase activity as a drug sensitivity predictor

To investigate if kinase activity could potentially provide stratification criteria for response to targeted therapeutics, we applied Spearman correlation analysis to the kinome profiling array targets and drug sensitivity data. Significantly correlated target peptides were selected for each drug, and their R^2 values were determined by linear regression (Suppl. Table T5). From the compounds that showed selective effects, efficiently inhibiting some organoid lines, but not others (Fig. 4), we selected Afatinib, Dasatinib and Sunitinib to include in Figure 5. They were chosen based on their drug target or drug response pattern (Fig. 4). Afatinib targets EGFR and serves as an example of a kinase inhibitor with a more specific target, while Dasatinib serves as an example of a multi-kinase inhibitor. Sunitinib was included because it is the drug that specifically affected tumor organoids (CCAOs) and not the non-tumorous HAOs.

Afatinib is a selective inhibitor of all members of the ERBB receptor family: EGFR, ERBB2, ERBB3 and ERBB4. It was effective in 2/3 CCAO lines (Fig. 4), and spearman correlation identified 5 target peptides of which phosphorylation was significantly correlated to Afatinib sensitivity (Fig. 5A). Three of these peptides displayed a positive correlation in linear regression: GAB1_622_632 (GAB1), VEGFR3_1061_1073 (VEGFR), and PLCG1_777_789 (PLC- γ 1), and two displayed a negative correlation: ERBB4_1277_1289 (ERBB4) and MK14_177_187 (p38 α /SAPK2). PLC- γ 1 (Tyr 783) showed the strongest correlation with an R^2 of 0.99. This peptide is phosphorylated by several kinases, including EGFR³⁴, one of the receptors that is specifically inhibited by Afatinib, which could explain the correlation between Afatinib sensitivity and PLC- γ 1 (Tyr 783) phosphorylation. Counter-intuitively, ERBB4 (Tyr1284) is inversely correlated to Afatinib sensitivity (Fig. 5A). The ERBB receptor family members form homo- and heterodimers that are capable of autocatalytic

phosphorylation.^{34,35} Therefore, one might expect that activity of ERBB family kinases would correlate to Afatinib response, but this was not detected in this study.

Dasatinib is a multi-tyrosine kinase inhibitor known to inhibit the mutant BCR-ABL kinase (a product from the genetic abnormality known as the Philadelphia chromosome³⁶) as its primary target, with Src family kinases (Lck, Yes, Fyn, Src), c-KIT, and PDGFR β as secondary targets. BCR-ABL fusions have not been described in CCA, so efficacy of Dasatinib is likely through inhibition of endogenously expressed ABL³⁷ or secondary target inhibition. Src family kinases were strongly inhibited in intrahepatic CCA cell lines treated with Dasatinib, indicating they are a critical target of Dasatinib in CCA.³⁸ Drug screening in CCAOs showed that it effectively inhibits 2/3 CCAO lines (Fig. 4) and drug response correlates to the same peptides as Afatinib (Fig. 5A, B). Of these, PLCG1_777_789 (PLC- γ 1) phosphorylation displayed a strong positive correlation to Dasatinib sensitivity ($R^2 = 0.79$). The PLC- γ 1 (Tyr 783) peptide is also a downstream target of several Src family kinases (Src, HCK, Lyn), which could provide the link between Dasatinib sensitivity and PLC- γ 1 phosphorylation. The VEGFR3 (Tyr1063, 1068) peptide also showed a strong positive correlation to Dasatinib ($R^2 = 0.91$). This peptide is phosphorylated by VEGFR3 autocatalysis.³⁹ A potential relationship between Dasatinib and VEGFR3 activity could be further explored.

For Sunitinib, the only kinase inhibitor that selectively inhibits cell viability of 2/3 CCAOs without affecting HAOs, 9 peptides displayed significant correlations with drug sensitivity (Fig. 5C): CD28_185_197, CD3E_182_194, DYR1A_312_324, EGFR_1190_1202, IRS1_890_902, LCK_387_399, MBP_259_271, PTN11_541_551, TYK2_1048_1060, of which CD28_185_197 (CD28) and PTN11_541_551 (SHP2) showed a strong positive correlation ($R^2 = 0.99$ and 1.00 respectively) (Fig. 5C). While the upstream kinase responsible for phosphorylation of CD28 (Tyr188) is unknown, making its relationship to Sunitinib sensitivity difficult to determine, the SHP2 (Tyr546/551) peptide is a target of the kinase PDGFR α . Sunitinib has a broad spectrum of molecular targets, including growth factor receptors PDGFR α , PDGFR β , VEGFR1, VEGFR2, and VEGFR3, c-KIT, FLT3, CSF1R, and proto-oncogene RET.⁴⁰ The correlation to PDGFR α -mediated phosphorylation of SHP2 (Tyr546/551) could indicate that PDGFR inhibition is potentially the most relevant mechanism through which Sunitinib affects CCAO viability.

These examples demonstrate that kinase activity of both expected and unexpected kinases can correlate to drug sensitivity, which warrants further investigation as stratification markers for kinase inhibitor therapy.

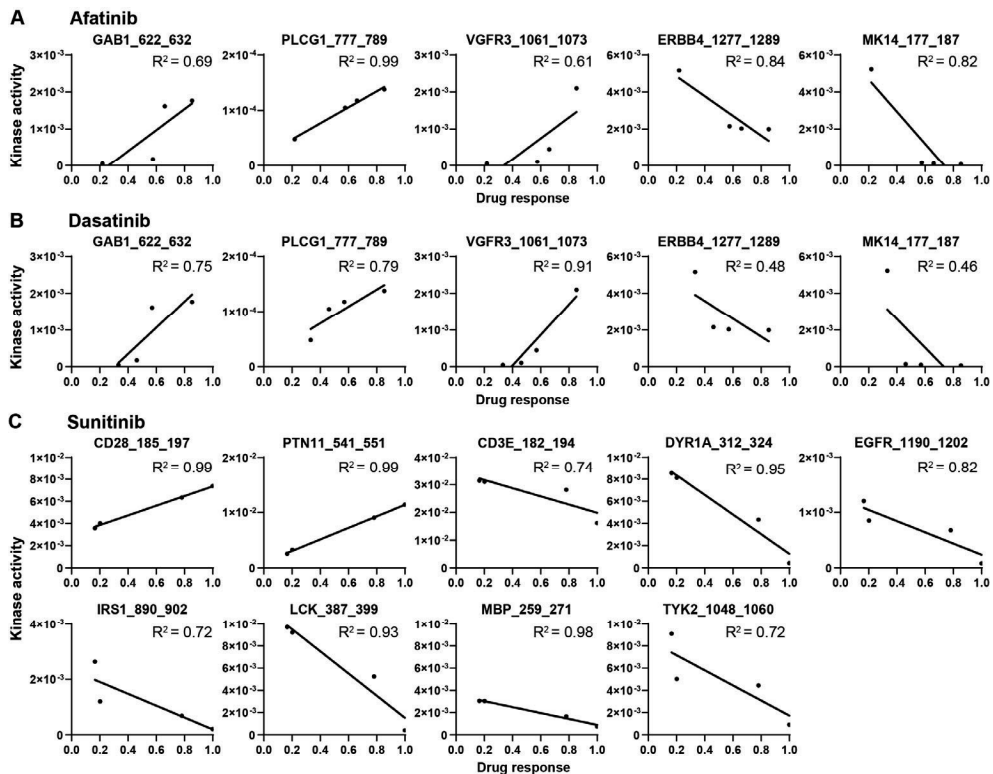


Figure 5. Exploratory correlation analysis of drug sensitivity and kinase activity. Spearman correlation analysis revealed which array peptides correlated with Afatinib (a), Dasatinib (b) and Sunitinib (c) treatment sensitivity. Drug response ranges from 0, indicating that organoids are unaffected by the compound, to 1, indicating there no surviving organoid cells. Significantly correlated peptides are portrayed as scatter plots with linear regression and R^2 values.

DISCUSSION

In this study, we explored whether kinase profiles obtained through commercial platforms can predict druggable targets in CCA. First, we found that tumor-derived organoids have individual kinase activity profiles, highlighting the need for personalized treatment approaches. Second, we demonstrated that CCAO kinase activity profiles do not correlate with the RNA expression patterns of those kinases, suggesting that RNA profiles do not reflect overall kinomic outcomes. Furthermore, despite the individual patterns, CCAOs showed common increased activity of several kinases compared to their healthy counterparts, indicating these as potential druggable targets in CCAO. These include EGFR, MAPK, and Src, well-known to coordinate proliferation and progression in several cancers.^{41, 42} Drug screening of targeted therapies revealed several pan-active compounds that show promise as CCA therapeutics. In addition, a number of kinase inhibitors showed more selective efficacy. Correlation analysis between kinase activity and drug response to these selective inhibitors demonstrated that correlations could be identified between drug

sensitivity and their known drug targets for some drugs, but not all, while correlations were also found with unexpected kinases.

Kinome profiles of CCAOs were specific to the individual patients, not clustering together when compared to healthy organoid profiles. This indicates that kinase activity is highly variable between patients and highlights the need for stratification. CCA is characterized by extensive genomic heterogeneity, so it is not unexpected that this heterogeneity is also reflected in kinase activity profiles.⁵ Of the differentially activated kinases, MAPK kinases have been intensively studied for their role in cell proliferation, differentiation, apoptosis and migration in cancer.⁴² They are activated by growth factor receptor signaling (e.g. EGFR, PDGFR), cytokines, and environmental stress signals, through, amongst others, activation of the GTPase Ras. Interestingly, we found that MEK1/MEK2 (also named MAP2K1/MAP2K2) inhibitors Cobimetinib and Trametinib effectively reduced organoid viability in all CCAO lines, correspondent with the overactive MAPK kinases. These findings agree with earlier preclinical studies where MEK inhibitors reduced growth and induced cell death in CCA cell lines, with KRAS mutations as a sensitizing factor.^{43, 44} However, in both KRAS mutant and KRAS wild type CCA mouse models, MEK inhibitors were able to repress tumor growth, again suggesting that upstream activating mutations do not always predict treatment outcomes.^{43, 44}

In line with enhanced MEK1/MEK2 signaling, EGFR and PDGFR activity were also higher in CCAOs compared to HAOs. While EGFR mutations are uncommon, occurring in ~5% of CCA patients, EGFR overexpression is reported regularly and has been associated with poor prognostic factors.⁴⁵ Based on our EGFR data, we have demonstrated that unbalanced EGFR signaling was an individual trait. High EGFR activity was mainly identified in CCAO3 organoids compared to its adjacent tissue counterparts. Correspondingly, CCAO3 organoids were more susceptible to ERBB (EGFR, ERBB2, ERBB3, ERBB4) family inhibitors than the other CCAOs.

A subset of targeted therapeutics displayed CCAO line-specific efficacy. An exploratory correlation analysis between kinase activity and kinase inhibitor efficacy was applied to identify potential stratification biomarkers. This led to both expected and unexpected correlations. For Afatinib, an ERBB family inhibitor, and Dasatinib, a multi-tyrosine kinase inhibitor, we found a positive correlation with PLC- γ 1 (Tyr783) and VEGFR3 (Tyr1063,1068) peptides. While the upstream kinases of PLC- γ 1 (Tyr783) were direct targets of these inhibitors, the relationship with VEGFR3 phosphorylation is more difficult to explain. Not every inhibitor was correlated to one of their target kinases. For example, MEK1/MEK2 inhibitor Trametinib did not correlate to MEK/ERK pathway kinase activity, and multi-kinase inhibitor Pazopanib did not correlate with its main targets c-KIT, FGFR, PDGFR, and VEGFR. There are several factors that could explain this discrepancy. First, there are several peptides on the kinome profiling array for which the upstream kinase remains unidentified, or which are phosphorylated by more than one kinase, complicating the analysis of the kinome profiles. Second, most kinase inhibitors are multi-kinase inhibitors with a broad spectrum of targets with different affinity and different efficacy per target. It is difficult to determine the impact of the activity of each kinase substrate related to an inhibitor on the kinase inhibitor sensitivity. Moreover, kinase signaling is a complex system with crosstalk between pathways

and shared downstream effectors. Negative effects of inhibition of a specific kinase could be circumvented by the cancer cell via other pathways. However, every inhibitor correlated to at least one peptide. The correlations to unexpected array peptides could be identified by chance, or could potentially indicate new targets of the (multi-)kinase inhibitors, downstream effectors of the drug targets, activity of upstream kinases not yet associated with the peptide, or kinases involved via more intricate pathways. Nevertheless, mechanistic understanding of the correlation is not an absolute requirement for a kinome profiling target to become a potentially valuable biomarker for treatment stratification.

We acknowledge several limitations in our study. First, we were able to include a limited number of organoid cultures, limiting the statistical power of our analyses. Thus, we tried to avoid over-interpretation of our data by reporting fold changes rather than statistical significance levels. Second, while we included HAO2 for our drug screening analysis, normal adjacent tissue may have already been influenced by its cancerous environment. Indeed, HAO2 showed a high overlap with CCAO2 in terms of kinomic profile, suggesting that its phenotype is already affected. Drug screening further revealed that the HAOs were efficiently killed by many of the targeted therapeutics. This is perhaps unsurprising, as HAOs do not possess the genetic alterations that CCAOs do, which provides the CCAOs with resistance to certain inhibitors, but may also reflect a somewhat transformed nature of 'normal' cholangiocytes in cancer patients. Nevertheless, although one might worry about side effects due to damage to healthy cholangiocytes in patients treated with these inhibitors, clinical studies describe skin disease, gastrointestinal complaints and hematological disorders as common side effects, rather than biliary tree toxicity.⁴⁶⁻⁴⁹ Thus, HAO death likely does not reflect patient risk.

Future studies in larger patient/control organoid cohorts which are subjected to kinome profiling and kinase inhibitor screening are needed to confirm the correlations we identified, and determine their predictive value. Some of these targets could turn out to be new biomarkers to allocate patients to specific kinase inhibitors. Furthermore, once these correlations are confirmed, future studies could attempt to discover how these kinases relate to the kinase inhibitors investigated. One approach could be to apply kinome profiling before and after treatment, to identify which kinases are affected by the compound.

In conclusion, kinome profiling demonstrated individual kinase activity patterns for each organoid culture, confirming CCA heterogeneity on a kinase activity level. EGFR, PDGFR β , and MAPK are potential druggable targets for CCA, as they seem more active in CCAOs compared to their healthy counterparts. Drug screening identified several promising pan-effective drugs, and inhibitors that portrayed a more selective effect for specific CCAOs. Explorative correlation analysis between these compounds and kinase activity identified correlations to expected and unexpected kinase targets, which could be further investigated as potential stratification biomarkers for kinase inhibitor sensitivity.

REFERENCES

1. Arsenault R, Griebel P, *et al.* Peptide arrays for kinome analysis: new opportunities and remaining challenges. *Proteomics*, 2011. 11(24):4595-609.
2. Peppelenbosch MP, Frijns N, *et al.* Systems medicine approaches for peptide array-based protein kinase profiling: progress and prospects. *Expert Review of Proteomics*, 2016. 13(6):571-8.
3. Sikkema AH, Diks SH, *et al.* Kinome profiling in pediatric brain tumors as a new approach for target discovery. *Cancer Res*, 2009. 69(14):5987-95.
4. Saha SK, Gordan JD, *et al.* Isocitrate dehydrogenase mutations confer dasatinib hypersensitivity and SRC dependence in intrahepatic cholangiocarcinoma. *Cancer discovery*, 2016. 6(7):727-39.
5. Banales JM, Marin JGG, *et al.* Cholangiocarcinoma 2020: the next horizon in mechanisms and management. *Nat Rev Gastroenterol Hepatol*, 2020. 17(9):557-88.
6. Uitdehaag JCM, Kooijman JJ, *et al.* Combined Cellular and Biochemical Profiling to Identify Predictive Drug Response Biomarkers for Kinase Inhibitors Approved for Clinical Use between 2013 and 2017. *Mol Cancer Ther*, 2019. 18(2):470-81.
7. Yau NK, Fong AY, *et al.* A Pan-Cancer Review of ALK Mutations: Implications for Carcinogenesis and Therapy. *Curr Cancer Drug Targets*, 2015. 15(4):327-36.
8. Khan PS, Rajesh P, *et al.* Recent advances in B-RAF inhibitors as anticancer agents. *Bioorg Chem*, 2022. 120:105597.
9. Friedlaender A, Subbiah V, *et al.* EGFR and HER2 exon 20 insertions in solid tumours: from biology to treatment. *Nat Rev Clin Oncol*, 2022. 19(1):51-69.
10. Lamarca A, Barriuso J, *et al.* Molecular targeted therapies: Ready for "prime time" in biliary tract cancer. *J Hepatol*, 2020. 73(1):170-85.
11. Nakamura H, Arai Y, *et al.* Genomic spectra of biliary tract cancer. *Nat Genet*, 2015. 47(9):1003-10.
12. Abou-Alfa GK, Sahai V, *et al.* Pemigatinib for previously treated, locally advanced or metastatic cholangiocarcinoma: a multicentre, open-label, phase 2 study. *Lancet Oncol*, 2020. 21(5):671-84.
13. Uitdehaag JC, de Roos JA, *et al.* Comparison of the cancer gene targeting and biochemical selectivities of all targeted kinase inhibitors approved for clinical use. *PLoS One*, 2014. 9(3):e92146.
14. Tatli O, Dinler Doganay G. Recent Developments in Targeting RAS Downstream Effectors for RAS-Driven Cancer Therapy. *Molecules*, 2021. 26(24).
15. Broutier L, Mastrogianni G, *et al.* Human primary liver cancer-derived organoid cultures for disease modeling and drug screening. *Nat Med*, 2017. 23(12):1424-35.
16. Saito Y, Muramatsu T, *et al.* Establishment of Patient-Derived Organoids and Drug Screening for Biliary Tract Carcinoma. *Cell Rep*, 2019. 27(4):1265-76 e4.
17. Maier CF, Zhu L, *et al.* Patient-Derived Organoids of Cholangiocarcinoma. *Int J Mol Sci*, 2021. 22(16).
18. Nuciforo S, Fofana I, *et al.* Organoid Models of Human Liver Cancers Derived from Tumor Needle Biopsies. *Cell Rep*, 2018. 24(5):1363-76.
19. Huch M, Gehart H, *et al.* Long-term culture of genome-stable bipotent stem cells from adult human liver. *Cell*, 2015. 160(1-2):299-312.
20. Baroncelli M, Fuhler GM, *et al.* Human mesenchymal stromal cells in adhesion to cell-derived extracellular matrix and titanium: Comparative kinome profile analysis. *J Cell Physiol*, 2019. 234(3):2984-96.
21. The UniProt C. UniProt: the universal protein knowledgebase in 2021. *Nucleic Acids Research*, 2020. 49(D1):D480-D9.
22. Howe KL, Achuthan P, *et al.* Ensembl 2021. *Nucleic Acids Res*, 2021. 49(D1):D884-D91.
23. Team RC. A language and environment for statistical computing. Vienna, Austria: R Foundation for Statistical Computing, 2020.
24. Team R. RStudio: Integrated Development for R. Boston, USA: RStudio Inc., 2020.

25. Wickham H, Averick M, *et al.* Welcome to the Tidyverse. *Journal of open source software*, 2019. 4(43):1686.
26. Wickham H. *ggplot2: elegant graphics for data analysis*.: springer, 2016.
27. Kassambara A, Mundt F. Package 'factoextra'. *Extract and visualize the results of multivariate data analyses*, 2017. 76.
28. Gu Z, Eils R, *et al.* Complex heatmaps reveal patterns and correlations in multidimensional genomic data. *Bioinformatics*, 2016. 32(18):2847-9.
29. Makowski D, Ben-Shachar MS, *et al.* Methods and algorithms for correlation analysis in R. *Journal of Open Source Software*, 2020. 5(51):2306.
30. Ogle DH DJ, Wheeler P, Dinno A. FSA: Fisheries Stock Analysis. R package version 0.9.3, 2022.
31. Schwanhäusser B, Busse D, *et al.* Global quantification of mammalian gene expression control. *Nature*, 2011. 473(7347):337-42.
32. Liu Y, Beyer A, *et al.* On the Dependency of Cellular Protein Levels on mRNA Abundance. *Cell*, 2016. 165(3):535-50.
33. Marsee A, Roos FJM, *et al.* Building consensus on definition and nomenclature of hepatic, pancreatic, and biliary organoids. *Cell Stem Cell*, 2021. 28(5):816-32.
34. Roskoski R. The ErbB/HER family of protein-tyrosine kinases and cancer. *Pharmacological Research*, 2014. 79:34-74.
35. Kaushansky A, Gordus A, *et al.* System-wide investigation of ErbB4 reveals 19 sites of Tyr phosphorylation that are unusually selective in their recruitment properties. *Chem Biol*, 2008. 15(8):808-17.
36. Ren R. Mechanisms of BCR-ABL in the pathogenesis of chronic myelogenous leukaemia. *Nat Rev Cancer*, 2005. 5(3):172-83.
37. Wang F, Hou W, *et al.* ABL1, Overexpressed in Hepatocellular Carcinomas, Regulates Expression of NOTCH1 and Promotes Development of Liver Tumors in Mice. *Gastroenterology*, 2020. 159(1):289-305 e16.
38. Saha SK, Gordan JD, *et al.* Isocitrate Dehydrogenase Mutations Confer Dasatinib Hypersensitivity and SRC Dependence in Intrahepatic Cholangiocarcinoma. *Cancer Discov*, 2016. 6(7):727-39.
39. Salameh A, Galvagni F, *et al.* Direct recruitment of CRK and GRB2 to VEGFR-3 induces proliferation, migration, and survival of endothelial cells through the activation of ERK, AKT, and JNK pathways. *Blood*, 2005. 106(10):3423-31.
40. Faivre S, Demetri G, *et al.* Molecular basis for sunitinib efficacy and future clinical development. *Nature reviews Drug discovery*, 2007. 6(9):734-45.
41. Kim LC, Song L, *et al.* Src kinases as therapeutic targets for cancer. *Nature Reviews Clinical Oncology*, 2009. 6(10):587-95.
42. Wagner EF, Nebreda AR. Signal integration by JNK and p38 MAPK pathways in cancer development. *Nat Rev Cancer*, 2009. 9(8):537-49.
43. Dong M, Liu X, *et al.* Efficacy of MEK inhibition in a K-Ras-driven cholangiocarcinoma preclinical model. *Cell Death Dis*, 2018. 9(2):31.
44. Wang P, Song X, *et al.* MEK inhibition suppresses K-Ras wild-type cholangiocarcinoma in vitro and in vivo via inhibiting cell proliferation and modulating tumor microenvironment. *Cell Death Dis*, 2019. 10(2):120.
45. Pellat A, Vaquero J, *et al.* Role of ErbB/HER family of receptor tyrosine kinases in cholangiocyte biology. *Hepatology*, 2018. 67(2):762-73.
46. Dunto RT, Keating GM. Afatinib: first global approval. *Drugs*, 2013. 73(13):1503-15.
47. Aparicio-Gallego G, Blanco M, *et al.* New insights into molecular mechanisms of sunitinib-associated side effects. *Molecular cancer therapeutics*, 2011. 10(12):2215-23.
48. Wright CJM, McCormack PL. Trametinib: first global approval. *Drugs*, 2013. 73(11):1245-54.
49. Wells Jr SA, Robinson BG, *et al.* Vandetanib in patients with locally advanced or metastatic medullary thyroid cancer: a randomized, double-blind phase III trial. *Journal of clinical oncology*, 2012. 30(2):134.

CHAPTER

4

Cholangiocarcinoma cell proliferation is enhanced in primary sclerosing cholangitis: A role for IL-17A

Ruby Lieshout^{1*}, Eline J.C.A. Kamp^{2*}, Monique M.A. Versteegen¹, Michael Doukas³, Winand N.M. Dinjens³, Kübra Köten¹, Jan N.M. IJzermans¹, Marco J. Bruno², Maikel P. Peppelenbosch², Luc J.W. van der Laan^{1#}, Annemarie C. de Vries^{2#}

**These authors contributed equally*

#These authors contributed equally

¹Erasmus MC Transplant Institute, Department of Surgery, Erasmus University Medical Center, Rotterdam, The Netherlands

²Department of Gastroenterology and Hepatology, Erasmus University Medical Center, Rotterdam, The Netherlands

³Department of Pathology, Erasmus MC Cancer Institute, Erasmus University Medical Center, Rotterdam, The Netherlands

ABSTRACT

Primary sclerosing cholangitis (PSC) is a chronic inflammatory disease of the biliary tree and a risk factor for development of cholangiocarcinoma (CCA). The pathogenesis of PSC-related CCA is largely unclear, although it is assumed that chronic inflammatory environment plays a pivotal role. We aimed to investigate the effect of inflammation-related cytokines in PSC on the proliferation rate of cancer cells. For this, the proliferation index in PSC-CCA and sporadic CCA was determined by Ki-67 immunohistochemistry. The percentage of Ki-67 positivity in cancer cells was significantly higher in PSC-CCA than in sporadic CCA ($41.3\% \pm 5.7\%$ vs $25.8\% \pm 4.1\%$; $p=0.038$). To assess which cytokines in the inflammatory environment have the potential to stimulate cancer cell proliferation, patient-derived CCA organoids (CCAOs) were exposed to five cytokines related to PSC (Interleukin (IL)- 1β , IL-6, IL-17A, interferon gamma, and tumor necrosis factor alpha). Only IL-17A showed a significant stimulatory effect on cell proliferation in CCAOs, increasing organoid size by $45.9\% \pm 16.4\%$ ($p < 0.01$) and proliferation rate by $38\% \pm 16\%$ ($p < 0.05$). IL-17A immunohistochemistry demonstrated that PSC-CCA might express more IL-17A than sporadic CCA. Moreover, correlation analysis in sporadic CCA and PSC-CCA found a significant correlation between IL-17A expression and proliferation.

In conclusion, tumor cell proliferation is increased in PSC-CCA cells compared to sporadic CCA cells. IL-17A increases CCA cell proliferation *in vitro* and may contribute to the high proliferation rate in PSC-CCA *in situ*. Therefore, IL-17A represents a new potential therapeutic target in (PSC-)CCA, to be tested in future trials.

INTRODUCTION

Primary sclerosing cholangitis (PSC) is a rare chronic disease of the biliary tree. It is characterized by progressive fibrous strictures of the bile ducts in an inflammatory environment.¹ PSC patients have a lifetime risk of 9-20% to develop cholangiocarcinoma (CCA), a severe type of cancer in the biliary tract.² CCA is the most common type of malignancy in PSC patients and the leading cause of death, accounting for 24–58% of deaths.^{3,4} Once CCA has developed, curative treatment is limited to surgical removal which is only feasible in a minority of patients due to late diagnosis. Five-year survival of PSC-related CCA (PSC-CCA) is only 10%.^{5,6} Compared to sporadic CCA, PSC-CCA occurs at a significantly younger age of 48 years old versus 65 in sporadic CCA.⁵

Biological differences between PSC-CCA and sporadic CCA and related consequences for cancer management have only recently gained attention. The developmental process of PSC-CCA is poorly understood and is presumably a combination of genetic aberrations and a dysregulated immune system, causing a chronic inflammatory environment.⁵ Genomic characterization of PSC-CCA demonstrated a heterogeneous mutational landscape containing similar mutations to sporadic CCA, with mutations in *TP53*, *KRAS*, *CDKN2A*, and *SMAD4* being the most frequent. However, in contrast with sporadic CCA, the PSC-CCA mutational landscape is independent of their anatomical location along the biliary tree.⁷ Of note, the key difference between PSC-CCA and sporadic CCA is the chronic inflammatory environment. PSC patients have massive biliary immune cell infiltration, characterized by a high number of neutrophils and T cells, of which the biliary resident CD103⁺CD69⁺CD8⁺ effector memory T cells are the most abundant.⁸ These immune cells produce pro-inflammatory and pro-fibrogenic cytokines that sustain inflammation and cause fibrous strictures of the bile ducts.^{8,9} For instance, it is known that pro-inflammatory cytokine IL-17A is increased in the periductal area of PSC livers.¹⁰ This cytokine contributed to hepatobiliary injury progression in a microbial PSC mouse model and inhibition of IL-17A producing T helper 17 (T_H17) cells efficiently ameliorated the induced damage.¹¹ IL-17A also induced an immune-reactive phenotype in bile-derived organoids from PSC patients.¹² IL-17A, together with other cytokines and immune cells, creates a chronic inflammatory environment which has been shown to be a fertile ground for cancer development and is able to promote cell proliferation in several types of cancer.¹³ Therefore, we wondered whether PSC-related inflammation has a stimulating effect on the progression of CCA, particularly on the proliferation of CCA cells.

In this study, we aim to investigate the proliferation rate in PSC-CCA in comparison with sporadic CCA by Ki-67 immunohistochemistry, and to analyze the effect of PSC-related pro-inflammatory cytokines on the proliferation of patient-derived CCA organoids (CCAOs).

MATERIALS AND METHODS

Tissue samples

Formalin-fixed paraffin-embedded (FFPE) tissue blocks of hepatobiliary resection specimens of PSC-CCA patients (n=19) were collected as a part of standard clinical care. These specimens were obtained in the Erasmus MC, University Medical Center Rotterdam, the Netherlands, between 1996 and 2019. The PSC-CCA samples were matched to sporadic CCA samples (n=19) for year of resection, tumor location (distal, perihilar or intrahepatic), and tumor differentiation grade, if possible. Patient characteristics are reported in Supplementary Table S1. 4 μ m sections were cut and stained with hematoxylin & eosin (H&E) according to standard procedures. These sections were reviewed by an expert hepatobiliary pathologist, who indicated the tumor region with the highest tumor cell percentage.

Ki-67 scoring

A second 4 μ m section of the selected FFPE tissue blocks was used for Ki-67 immunohistochemistry. The sections were incubated with a monoclonal antibody for Ki-67 according to standard protocols (Supplementary Materials and Methods). The specificity of the reaction was confirmed by positive controls, which was tonsil tissue. Expression of Ki-67 was scored according to a consensus of two investigators (EK and MD), which were both blinded for all samples. The scoring systems are described in Supplementary Materials and Methods and are based on the analytical validation of Ki-67 scoring in breast cancer.¹⁴

Cytokine receptor gene expression analysis

Gene expression data of CCA tissue (n=36) was obtained from The Cancer Genome Atlas Research Network (<https://www.cancer.gov/tcga>). In parallel, gene expression data of CCAO (n=3) was obtained from the Gene Expression Omnibus (GEO) repository with accession number GSE84073 (CCAO1) and GEO repository with accession number GSE179601 (CCAO2 and CCAO3). Normalized counts were obtained from all datasets for receptors of PSC-related cytokines interleukin (IL)-1 β , IL-2, IL-6, IL-17A, interferon gamma (IFN γ) and tumor necrosis factor alpha (TNF α).

Organoid culture

CCAOs were initiated from patient tumor samples (n=4) collected at Erasmus MC Rotterdam. Collection and use of patient material in this study was approved by the medical ethics committee of the Erasmus MC (MEC-2013-143). Patients consented to donate resected materials for research purposes. Organoids were cultured as described previously.¹⁵ Confirmation that the organoids were composed of neoplastic cells was obtained by tumor formation after subcutaneous xenografting in female NOD.Cg-Prkdc^{SCID} Il2rg^{tm1Wjl}/SzJ (NSG) mice (Charles River) and by detection of DNA aberrations by targeted next generation sequencing.

Targeted next generation sequencing

Next generation sequencing (NGS) was performed in all CCAOs (n=4) to confirm their tumor cell composition. DNA of organoid cultures was isolated according to standard procedures with 5% Chelex 100 resin and proteinase K. Both mutations and copy number variants were analyzed by using a tailor-made gene panel. Details are further described in the Supplementary Materials and Methods and in Supplementary Table S2. The sequencing coverage and quality statistics for each sample are summarized in Supplementary Table S3.

Cytokine exposure

On day 0, organoids were split 1:3-1:12 and replated in fresh basement membrane extract (Cultrex™). They were covered in organoid expansion medium supplemented with 2, 10, 50 or 200 ng/ml of cytokines IL-1 β (Bio-Techne), IL-6 (Life Technologies Europe BV), IL-17A (Merck Life Science NV), IFN γ (Life Technologies Europe BV) and TNF α (Peprotech). A vehicle control (IL-1 β , IL-6, IFN γ : PBS with 0.1% BSA; IL-17A: distilled water; TNF α : DMSO; diluted 500 times in culture medium) was included in every experiment. Medium with fresh cytokines was added at day 3. Readouts were performed at day 5.

Quantification of proliferation

Organoid proliferation was quantified using the Click-it® EdU flow cytometry assay kit (Invitrogen) according to manufacturer's guidelines. Organoid cultures were incubated with 10 μ M EdU for 4 hours. Consecutively, organoids were dissociated to single cells using Trypsin-EDTA (15-60 minutes at 37°C), fixed, permeabilised and stained with Alexa Fluor 488. Flow cytometry was performed with FACSCanto II flow cytometer (BD Biosciences) and analyzed using FlowJo software (version 10.7, LLC). Gating strategy is displayed in Supplementary Figure S1.

Bright field and Live/dead immunofluorescent imaging

Bright field and fluorescence imaging was performed with an EVOS FL Cell Imaging System equipped with RFP, GFP and DAPI light cubes. Live/dead staining mix consisted of 12.5 μ g/ml Propidium Iodide (PI, Sigma-Aldrich), 10 μ g/ml Hoechst 33342 (Thermo Fisher Scientific) and 0.5 μ M Calcein AM (Thermo Fisher Scientific). Cytokine treated organoids were stained for 1 hour before imaging. Organoid diameter measurement is described in Supplementary Materials and Methods.

IL-17A immunohistochemistry

A third section of the selected FFPE tissue blocks was used for IL-17A immunohistochemistry. The sections were incubated with monoclonal antibodies of IL-17A according to standard protocols. The IL-17A scoring was performed by an expert hepatobiliary pathologist (MD) and was based on his experience and previously published literature.¹⁶ Details of the staining and scoring method are described in the Supplementary Materials and Methods.

Statistical analysis

Statistical analyses were performed using GraphPad Prism software (v. 8.0.2). Values are portrayed as mean \pm standard error of mean (SEM). Comparisons between two matched groups were analyzed by a two-tailed paired t test or a Wilcoxon test. Comparisons between two unmatched groups were analyzed by a two-tailed unpaired t test or a Mann-Whitney test. P values below 0.05 were deemed statistically significant.

RESULTS & DISCUSSION

Increased proliferation in PSC-CCA compared to sporadic CCA

A total of 19 PSC patients with CCA were included, and matched to 19 patients with sporadic CCA (Supplementary Table S1). Each group of patients contained 11 perihilar, 4 intrahepatic, and 4 distal CCA. The age of CCA diagnosis was significantly lower in PSC-CCA compared with sporadic CCA ($p=0.000$). There was no statistically significant difference between the two used scoring systems for Ki-67 positivity, global and hotspot, in both PSC-CCA and sporadic CCA. The mean of pathological estimation and these scoring systems resulted in a significantly higher percentage of Ki-67 positive tumor cells in PSC-CCA when compared to sporadic CCA ($41.3\% \pm 5.7\%$ vs $25.8\% \pm 4.1\%$; mean \pm SEM, $p=0.038$) (Fig. 1a, b), indicating PSC-CCA tumor cells proliferate faster than their sporadic CCA counterparts.

Few other studies have performed Ki-67 immunohistochemistry in PSC-CCA. Obviously, Ki-67 positivity was significantly higher in CCA than in non-neoplastic bile ducts.^{17, 18} Ishii *et al* have analyzed Ki-67 in both PSC-CCA and sporadic CCA before, and found a similar trend with 46% Ki-67 positivity in PSC-CCA compared to 33% in sporadic CCA.¹⁹ However, their analysis did not reach significance, most likely due to the low sample size (7 PSC-CCAs vs. 15 sporadic CCAs).

Despite the fact that our study identified an increased proliferation in PSC-CCA compared to sporadic CCA, a multi-center study recently found no difference in survival after resection between perihilar PSC-CCA and sporadic CCA.²⁰ Various factors could be involved, including the younger age of PSC-CCA patients, which means they are probably physically more fit with less comorbidity than older patients. The median age of diagnosis of CCA in PSC patients is about 20 years earlier than patients with CCA without PSC.² The younger PSC-CCA patients are more likely to undergo additional treatments than older CCA patients, like chemotherapy. In addition, the intensive follow-up of PSC patients might result in an earlier detection of CCA.

Testing cell proliferation in a CCA organoid (CCAO) model

As the number of proliferating cancer cells is higher in PSC-CCA compared to sporadic CCA, we aimed to identify the direct effect of PSC-related inflammatory cytokines on CCA cell proliferation. In order to investigate this, we established CCAOs that provide an epithelial cancer cell model and confirmed their tumorigenicity by xenografting and targeted NGS. The cancer diagnostic NGS panel described in Supplementary Table S2 revealed CCAO copy

number variations and mutations in *ARID1A*, *IGF1R*, *KRAS*, *TP53*, and *BAP1* (Supplementary Fig. S2a, b). *TP53*, *KRAS*, and *ARID1A* mutations were also regularly identified in PSC-CCA.⁷

Next, we performed a literature search into PSC-related inflammatory cytokines that identified IL-1 β , IL-2, IL-6, IL-8, IL-17A, IFN γ , and TNF α .^{8,21,22} These cytokines could only exert their effects on CCA cells if their receptors are present. Therefore, we analyzed cytokine receptor gene expression in CCA tumor tissue and CCAOs. CCA transcriptomic data extracted from The Cancer Genome Atlas (n=36) shows that receptors of all cytokines are expressed in CCA bulk tumor samples, except for IL2RA (Fig. 2a). In CCAOs, which only consist of epithelial tumor cells, receptors are expressed for IL-1 β , IL-6, IL-17A, IFN γ , and TNF α (Fig. 2b). Therefore, these five cytokines were selected to analyze in organoid exposure experiments.

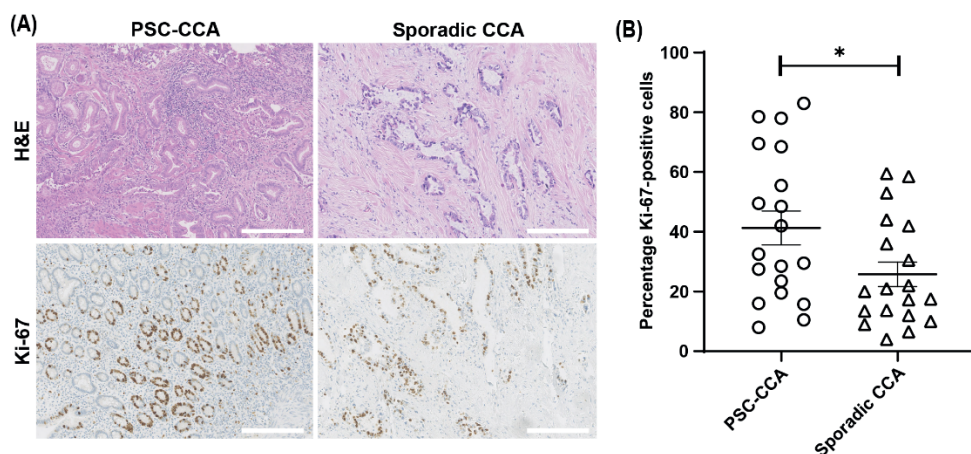


Figure 1. Proliferation rate in PSC-CCA is higher than sporadic CCA. Ki-67 immunohistochemistry in 19 PSC-CCA samples and 19 sporadic CCA samples. **(a)** Representative images of Ki-67 staining in a matched sample of PSC-CCA (left) and sporadic CCA (right). Original magnification, $\times 10$. Scalebar = 250 μm . **(b)** Quantification of Ki-67 staining in tumor cells as determined by two independent observers (* = $p < 0.05$). All values with error bars display mean \pm SEM.

IL17-A stimulates CCA cell proliferation

To assess which of the selected cytokines are able to stimulate proliferation, the cytokines were added to CCAOs. CCAOs were exposed to IL-1 β , IL-6, IL-17A, IFN γ , and TNF α for 5 days. Of these, IL-1 β , IL-6, IFN γ , and TNF α did not increase the CCAO proliferation rate (data not shown). However, incubation with IL-17A showed an increase in organoid diameter. CCAOs treated with IL-17A were $45.9\% \pm 16.4\%$ (mean \pm SEM, $p < 0.01$) bigger compared to vehicle treated organoids (Fig. 3b). Also, IL-17A treatment significantly increased the CCAO cell proliferation by $38\% \pm 16\%$ (mean \pm SEM) compared to the proliferation in vehicle treated CCAOs (Fig. 3c). IL-17A had no further impact on organoid morphology (Fig. 3a), nor did it induce cell death (Supplementary Fig. S3). These findings indicate that IL-17A is able to boost CCA cell proliferation directly.

The direct proliferation inducing effect of IL-17A has never been studied in CCA, but it has been described in colorectal cancer models. IL-17A increased the growth rate of premalignant enterocytes in colorectal cancer mouse models and murine organoids, which coincided with increased activity of ERK, p38 MAPK and NF- κ B signaling.²³ Furthermore, in colon cancer cell line CT26, IL-17A overexpression enhanced cell cycle progression.²⁴ Clinically, intra- and peritumoral IL-17A tissue expression are poor prognostic factors in sporadic CCA patients.²⁵⁻²⁷ Faster cancer cell proliferation induced by IL-17A could potentially play a role in the poor survival of these patients.

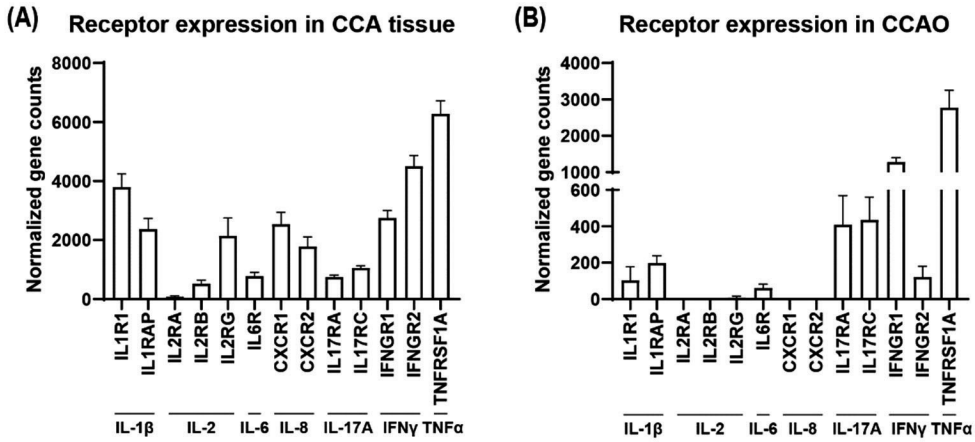


Figure 2. Gene expression of cytokine receptors in CCA tissue and CCAOs. PSC- and PSC-CCA related cytokines were selected from literature. (a) Gene expression of selected cytokine receptors in CCA tissue sections (n=36) as obtained from The Cancer Genome Atlas Research Network. (b) Gene expression of selected cytokine receptors in CCAOs (n=3). All values with error bars display mean \pm SEM.

IL-17A is expressed in PSC-CCA tissue

Next, we examined if proliferation and IL-17A expression were related in PSC-CCA patients. In PSC without malignancy, it is known that IL-17A and its producers T helper 17 (Th17) cells are overrepresented and overactive. Blood of PSC patients contains more Th17 cells compared to healthy individuals,²⁸ and has a stronger Th17 response upon pathogen stimulation.¹⁰ Single cell RNA sequencing of the intrahepatic T cells in PSC livers identified a naïve-like CD4⁺ T cell population with a predisposition to Th17 cell polarization.²⁹ Furthermore, immunohistochemistry detected a higher number of IL-17A positive cells in the periductal area of PSC patients.¹⁰ However, little is known about the expression of IL-17A in PSC-CCA. Therefore, IL-17A immunohistochemistry was performed on PSC-CCA and sporadic CCA tumor tissue samples (Fig. 3d). The percentage of IL-17A positive cells was higher in PSC-CCA (13.7% \pm 4.3%) compared to sporadic CCA (6.5% \pm 1.7%), although this did not reach statistical significance (p = 0.08).

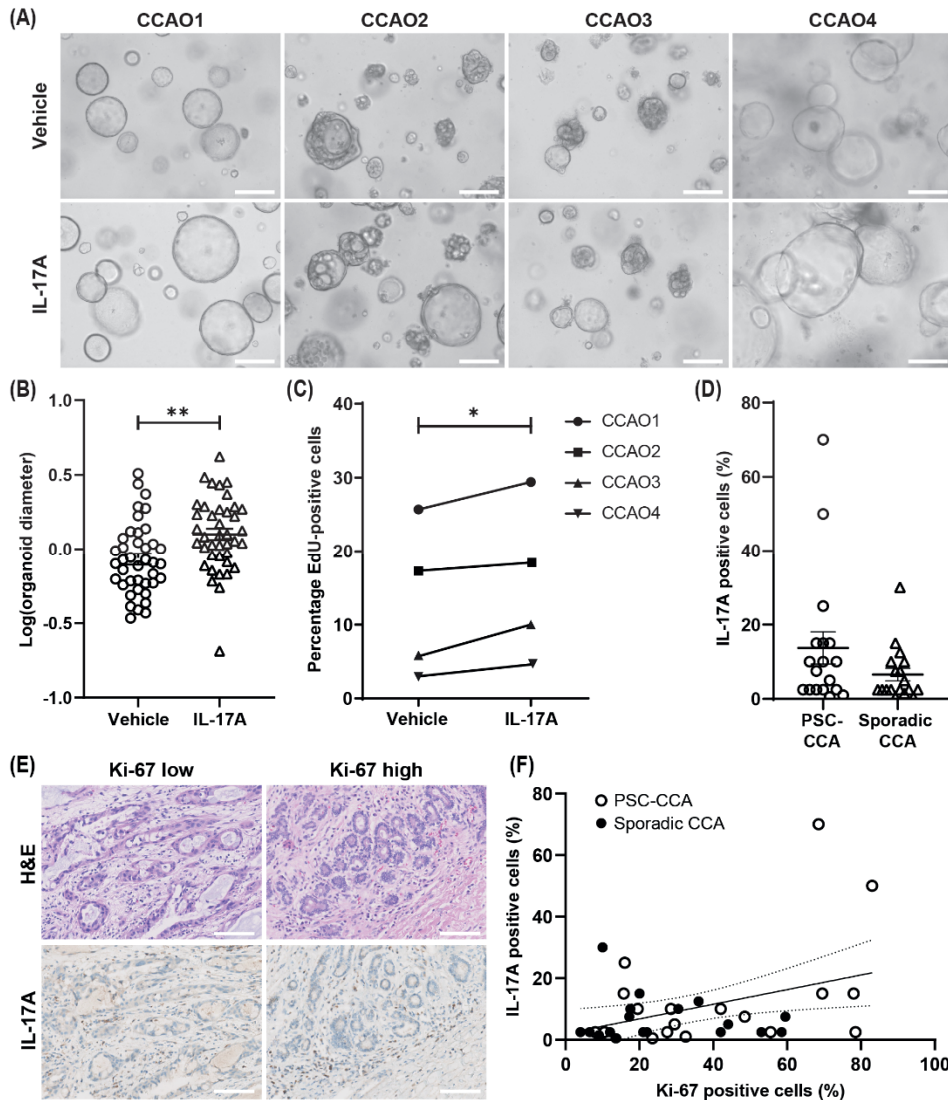


Figure 3. IL-17A stimulates proliferation of CCAOs. CCAOs were cultured for five days with 200 ng/ml IL-17A or with vehicle added to the medium. **(a)** Bright field images demonstrate morphology is not affected by 200 ng/ml IL-17A treatment. Scalebar = 200 μ m. **(b)** Log transformed organoid diameters as measured from bright field images relative to the mean of vehicle treated organoids (n=10 organoids per CCAO line per condition; n=4 organoid lines). Organoid diameter is significantly larger when treated with 200 ng/ml IL-17A (** = $p < 0.01$). **(c)** Percentage of EdU-positive cells in each CCAO line treated with 200 ng/ml IL-17A. The percentage of EdU-positive cells is significantly higher in CCAOs treated with IL-17A compared to the vehicle treated ones (* = $p < 0.05$). **(d)** Quantification of IL-17A staining in 18 PSC-CCA and 18 sporadic CCA samples as determined by an experienced GI-pathologist. **(e)** Hematoxylin and Eosin (H&E) staining and IL-17A immunohistochemistry performed in PSC-CCA with a low Ki-67 positivity score (left) and PSC-CCA with a high Ki-67 positivity score (right). The IL-17A score was determined by the percentage of all positive cells. Original magnification, x20. Scalebar = 100 μ m. **(f)** Correlation plot of the number of IL-17A positive cells and the Ki-67 positive cells in PSC-CCA and sporadic CCA samples (n=18 each). All values with error bars display mean \pm SEM.

To further investigate the specific relationship between proliferation and IL-17A, correlation analysis was performed between the number of IL-17A positive cells and the number of Ki-67 positive cells in both PSC-CCA and sporadic CCA (Fig. 3e, f). Linear regression demonstrated a significant correlation ($p = 0.018$), although the correlation coefficient was relatively low ($R^2 = 0.14$), likely due to a high degree of variation. Combined with the demonstrated proliferation-inducing effect of IL-17A on CCA cancer cells, these findings suggest that IL-17A might be higher expressed in PSC-CCA compared to sporadic CCA and could be a contributing factor to the high proliferation of PSC-CCA tumors.

CONCLUSION

In this study, we investigated the effect that a PSC background has on CCA cell proliferation and studied the role of inflammatory cytokines therein. We found that the proliferative index of cancer cells in PSC-CCA is higher than that found in sporadic CCA. Moreover, we found that cytokine IL-17A is locally expressed in tumor tissue and stimulates cell proliferation *in vitro* in CCAOs. This indicates IL-17A might be a contributing factor to the higher proliferative index in PSC-CCA. Future studies could focus on the potential of IL-17A targeted therapies in (PSC-)CCA treatment, especially in patients with highly proliferative tumors.

REFERENCES

1. Karlsten TH, Folseraas T, *et al.* Primary sclerosing cholangitis - a comprehensive review. *J Hepatol*, 2017. 67(6):1298-323.
2. Song J, Li Y, *et al.* Cholangiocarcinoma in Patients with Primary Sclerosing Cholangitis (PSC): a Comprehensive Review. *Clin Rev Allergy Immunol*, 2020. 58(1):134-49.
3. Claessen MM, Vleggaar FP, *et al.* High lifetime risk of cancer in primary sclerosing cholangitis. *J Hepatol*, 2009. 50(1):158-64.
4. Chapman MH, Webster GJ, *et al.* Cholangiocarcinoma and dominant strictures in patients with primary sclerosing cholangitis: a 25-year single-centre experience. *Eur J Gastroenterol Hepatol*, 2012. 24(9):1051-8.
5. Saffioti F, Mavroidis VK. Review of incidence and outcomes of treatment of cholangiocarcinoma in patients with primary sclerosing cholangitis. *World J Gastrointest Oncol*, 2021. 13(10):1336-66.
6. Bergquist A, Ekbohm A, *et al.* Hepatic and extrahepatic malignancies in primary sclerosing cholangitis. *J Hepatol*, 2002. 36(3):321-7.
7. Goeppert B, Folseraas T, *et al.* Genomic Characterization of Cholangiocarcinoma in Primary Sclerosing Cholangitis Reveals Therapeutic Opportunities. *Hepatology*, 2020. 72(4):1253-66.
8. Zimmer CL, von Seth E, *et al.* A biliary immune landscape map of primary sclerosing cholangitis reveals a dominant network of neutrophils and tissue-resident T cells. *Sci Transl Med*, 2021. 13(599).
9. Dyson JK, Beuers U, *et al.* Primary sclerosing cholangitis. *Lancet*, 2018. 391(10139):2547-59.
10. Katt J, Schwinge D, *et al.* Increased T helper type 17 response to pathogen stimulation in patients with primary sclerosing cholangitis. *Hepatology*, 2013. 58(3):1084-93.
11. Nakamoto N, Sasaki N, *et al.* Gut pathobionts underlie intestinal barrier dysfunction and liver T helper 17 cell immune response in primary sclerosing cholangitis. *Nat Microbiol*, 2019. 4(3):492-503.
12. Soroka CJ, Assis DN, *et al.* Bile-Derived Organoids From Patients With Primary Sclerosing Cholangitis Recapitulate Their Inflammatory Immune Profile. *Hepatology*, 2019. 70(3):871-82.
13. Elinav E, Nowarski R, *et al.* Inflammation-induced cancer: crosstalk between tumours, immune cells and microorganisms. *Nat Rev Cancer*, 2013. 13(11):759-71.
14. Leung SCY, Nielsen TO, *et al.* Analytical validation of a standardized scoring protocol for Ki67: phase 3 of an international multicenter collaboration. *NPJ Breast Cancer*, 2016. 2:16014.
15. Broutier L, Mastrogianni G, *et al.* Human primary liver cancer-derived organoid cultures for disease modeling and drug screening. *Nat Med*, 2017. 23(12):1424-35.
16. Ali ET, Masri MAM, *et al.* Immunohistochemical expression of interleukin-17 and hormonal receptors in benign and malignant breast lesions. *BMC Res Notes*, 2020. 13(1):300.
17. Boberg KM, Schruppf E, *et al.* Cholangiocarcinoma in primary sclerosing cholangitis: K-ras mutations and Tp53 dysfunction are implicated in the neoplastic development. *J Hepatol*, 2000. 32(3):374-80.
18. Bergquist A, Glaumann H, *et al.* Biliary dysplasia, cell proliferation and nuclear DNA-fragmentation in primary sclerosing cholangitis with and without cholangiocarcinoma. *J Intern Med*, 2001. 249(1):69-75.
19. Ishii Y, Sasaki T, *et al.* Elevated expression of cyclooxygenase-2 and microsomal prostaglandin H synthase-1 in primary sclerosing cholangitis: implications for cholangiocarcinogenesis. *Int J Oncol*, 2013. 43(4):1073-9.
20. Jansson H, Olthof PB, *et al.* Outcome after resection for perihilar cholangiocarcinoma in patients with primary sclerosing cholangitis: an international multicentre study. *HPB (Oxford)*, 2021. 23(11):1751-8.
21. Carpino G, Cardinale V, *et al.* Neoplastic Transformation of the Peribiliary Stem Cell Niche in Cholangiocarcinoma Arisen in Primary Sclerosing Cholangitis. *Hepatology*, 2019. 69(2):622-38.

22. Eaton JE, Talwalkar JA, *et al.* Pathogenesis of primary sclerosing cholangitis and advances in diagnosis and management. *Gastroenterology*, 2013. 145(3):521-36.
23. Wang K, Kim MK, *et al.* Interleukin-17 receptor a signaling in transformed enterocytes promotes early colorectal tumorigenesis. *Immunity*, 2014. 41(6):1052-63.
24. Do Thi VA, Park SM, *et al.* The Membrane-Bound Form of IL-17A Promotes the Growth and Tumorigenicity of Colon Cancer Cells. *Mol Cells*, 2016. 39(7):536-42.
25. Gu FM, Gao Q, *et al.* Intratumoral IL-17(+) cells and neutrophils show strong prognostic significance in intrahepatic cholangiocarcinoma. *Ann Surg Oncol*, 2012. 19(8):2506-14.
26. Asukai K, Kawamoto K, *et al.* Prognostic Impact of Peritumoral IL-17-Positive Cells and IL-17 Axis in Patients with Intrahepatic Cholangiocarcinoma. *Ann Surg Oncol*, 2015. 22 Suppl 3:S1524-31.
27. Kinoshita M, Kobayashi S, *et al.* Heterogeneity of Treg/Th17 According to Cancer Progression and Modification in Biliary Tract Cancers via Self-Producing Cytokines. *Dig Dis Sci*, 2020. 65(10):2937-48.
28. Kunzmann LK, Schoknecht T, *et al.* Monocytes as Potential Mediators of Pathogen-Induced T-Helper 17 Differentiation in Patients With Primary Sclerosing Cholangitis (PSC). *Hepatology*, 2020. 72(4):1310-26.
29. Poch T, Krause J, *et al.* Single-cell atlas of hepatic T cells reveals expansion of liver-resident naive-like CD4(+) T cells in primary sclerosing cholangitis. *J Hepatol*, 2021. 75(2):414-23.

SUPPLEMENTARY INFORMATION

SUPPLEMENTARY MATERIALS AND METHODS

Immunohistochemical stainings

Immunohistochemistry of Ki-67 (anti-rabbit; clone 90-9; dilution 2.0ug/mL; Ventana) and IL-17A (anti-goat; polyclonal; dilution 1/10; R&D) was performed with an automated, validated and accredited staining system (Ventana Benchmark ULTRA, Ventana Medical Systems, Tucson, AZ, USA) using ultraview or optiview universal DAB detection Kit. In brief, following deparaffinization and heat-induced antigen retrieval the tissue samples were incubated according to their optimized time (Ki-67 32 minutes; IL-17A 120 minutes) with the antibody of interest. Incubation was followed by hematoxylin II counter stain for 12 minutes and then a blue colouring reagent for 8 minutes according to the manufactures instructions (Ventana).

Ki-67 scoring

The Ki-67 score is referred to as the percentage of positive stained tumor cells in the investigated regions. Two investigators (EK and MD) scored the Ki-67 positive cells, independently, and were both blinded for all samples. The mean of both scores was used for analysis. Scoring of the Ki-67 positive cells was performed by an expert in hepatobiliary pathology (MD) by estimating. Second, EK used two different strategies: global and hotspot. With the global method, an average score across the neoplastic region is obtained, counting 4 fields of 100 tumor nuclei. The hotspot method included counting of 500 tumor nuclei in a field containing a high percentage of positive cells. If a heterogeneous Ki-67 pattern was observed in the tumor, the regions with the highest expression were selected for scoring, assuming that this is the most important clone of the tumor, responsible for the prognosis.

The immunohistochemical scoring system of IL17-A in the tumor tissue sections was based on the overall staining intensity, performed by a pathologist (MD). The overall percentages of stained cells were scored in each sample.

Targeted next generation sequencing

Multiregional-targeted sequencing was performed on the CCAO (n=4). Ion semiconductor sequencing on the Ion GeneStudio S5XL Prime System (Life Technologies) was done according to standard and ISO 15189 accredited operational procedures. In short, libraries were made using the Ion AmpliSeq Library Preparation plus kit, template preparation on Ion Chef, and sequencing on the Ion GeneStudio S5XL Prime System on 540 chips with the Ion 540 Chef kit. Data were analyzed with the Variant Caller v5.10.0.18. Sequence Pilot (JSI medical systems) was used to make a selection of potentially reliable variants. Total coverage per amplicon had to be above 100 reads and the following alterations were included: nonsynonymous somatic point mutations, splice site alterations, and insertions and deletions changing the protein amino acid sequence. In addition, variants reported in the ESP6500si or 1000genomes databases in more than 1% were excluded, assuming that these were single nucleotide polymorphisms (SNPs). Variants were considered potentially reliable if they were present in at least 20% of the called reads.

To determine the copy number variations (CNVs), the reads of all amplicons were selected. The amplicons used in the gene panel were in the coding regions as well as around the genes. The number of reads of each amplicon reflects the presence of gain or loss of the DNA.

Organoid diameter measurement

Diameters of single organoids (n=10 per condition per CCAO line) were determined from bright field images of CCAO cultures exposed to vehicle (0.2% distilled water) or 200 ng/ml IL-17A, using FIJI software version 2.1.0/1.53j. 10 organoids per image were selected by a random dot placement macro. Diameters of one organoid were determined in three directions. The mean diameter of each organoid is analyzed relative to the mean diameter of the vehicle treated organoids of the specific CCAO line.

TABLES

Supplementary Table S1. Patient characteristics

Patient characteristics of PSC-CCA and sporadic CCA patients whose samples were used in Ki-67 staining.

Characteristic	PSC-CCA (n=19)	Sporadic CCA (n=19)	
Male	14 (74%)	9 (47%)	
Age at CCA diagnosis	47 [SD=14]	64 [SD=12]	P=0.000
<i>Location CCA</i>			
Distal	3	3	
Perihilar	12	12	
Intrahepatic	4	4	
<i>Surgical resection</i>			
Liver transplantation	5	0	
Hemihepatectomy	8	16	
Pancreaticoduodenectomy	3	2	
Autopsy	1	1	
Liver transplantation and pancreaticoduodenectomy	1	0	
Hemihepatectomy and pancreaticoduodenectomy	1	0	

Abbreviations: PSC: primary sclerosing cholangitis, CCA: cholangiocarcinoma.

Supplementary Table S2. Targeted NGS-panel

An overview of the gene panel used for targeted next generation sequencing, containing 63 genes. Of these, 11 genes were covered for 99-100%, 1 promoter was included and of the remaining 51 genes hot spots were included in the gene panel.

	Gene	Coverage
Coding sequence	<i>ARID1A</i>	100%
	<i>BAP1</i>	100%
	<i>CDH1</i>	100%
	<i>CDKN2A</i>	100%
	<i>KEAP1</i>	100%
	<i>PIK3R1</i>	100%
	<i>PTEN</i>	100%
	<i>RB1</i>	99%
	<i>STK11</i>	100%
	<i>TP53</i>	100%
	<i>VHL</i>	100%
		Exon
Mutation hotspots	<i>AKT1</i>	3
	<i>AKT2</i>	3
	<i>ALK</i>	20, 22-25
	<i>APC</i>	16
	<i>BRAF</i>	11, 12, 14, 15
	<i>CDK4</i>	2, 4, 7, 8
	<i>CTNNB1</i>	3, 7, 8
	<i>DDR2</i>	14-19
	<i>EGFR</i>	12, 18-21
	<i>EIF1AX</i>	1, 2
	<i>HER2</i>	8, 17-21
	<i>ERBB3</i>	3, 6-10, 21, 23
	<i>ESR1</i>	4, 5, 7, 8
	<i>EZH2</i>	16
	<i>FBWX7</i>	9, 10
	<i>FGFR1</i>	4, 7, 12-14
	<i>FGFR2</i>	7, 9, 12
	<i>FGFR3</i>	7, 9, 14, 15
	<i>FOXL2</i>	1
	<i>GNA11</i>	4, 5
	<i>GNAQ</i>	4, 5
	<i>GNAS</i>	8, 9
	<i>HRAS</i>	2-4
	<i>IDH1</i>	4
	<i>IDH2</i>	4

<i>JAK2</i>	14
<i>JAK3</i>	4, 16
<i>KIT</i>	8, 9, 11, 13-18
<i>KNSTRN</i>	1
<i>KRAS</i>	2-4
<i>MAP2K1</i>	1-6
<i>MET</i>	2, 14, 19, 20
<i>MTOR</i>	30, 39, 40, 43, 47, 53, 56, 57
<i>MYD88</i>	5
<i>NFE2L2</i>	2
<i>NOTCH1</i>	26, 27
<i>NRAS</i>	2-4
<i>OXA1L</i>	1
<i>PDGFRA</i>	12, 14, 18
<i>PIK3CA</i>	2, 5, 8, 10, 14, 21
<i>POLD1</i>	6, 8, 12, 15-17, 24
<i>POLE</i>	9-14, 21, 25
<i>RAC1</i>	2
<i>RAF1</i>	7
<i>RET</i>	11, 16
<i>RHOA</i>	2
<i>RIT1</i>	4, 5
<i>RNF43</i>	2-10
<i>ROS1</i>	36-41
<i>SF3B1</i>	14, 15
<i>SMAD4</i>	3, 9, 12

Non-coding sequence

TERT

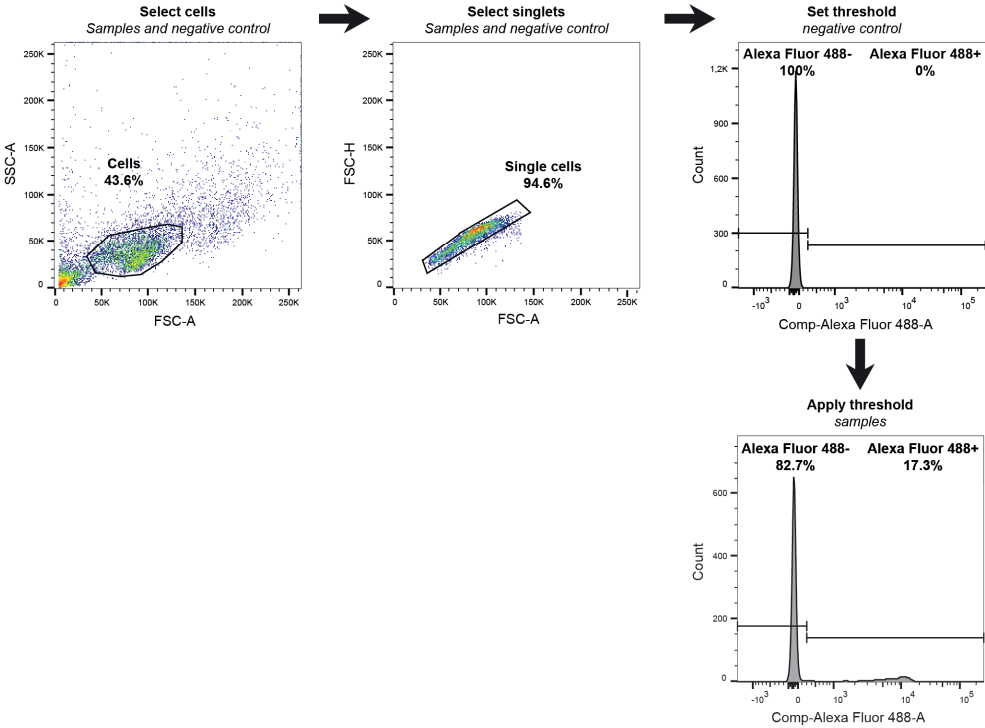
Promoter

Supplementary Table S3. Next generation sequencing details

The sequencing coverage and quality statistics of each cholangiocarcinoma organoid sample.

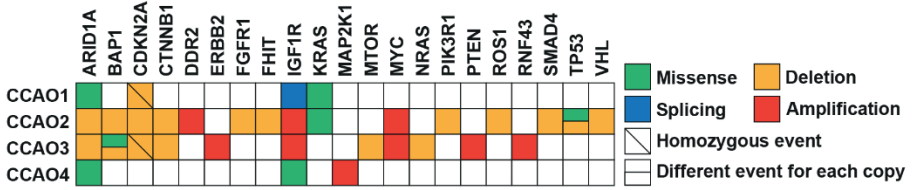
	CCAO1	CCAO2	CCAO3	CCAO4
Sample ID	CCA-010119-9_bc47	CCA-120619-10_bc48	CCA-231020-12_bc49	CCA-031120-13_bc50
Total number of sequenced reads	2,233,436	1,973,937	2,301,462	2,217,048
Total number of uniquely mapped reads	2,228,676	1,968,548	2,293,866	2,211,782
Total number of covered targeted bases	108,514	108,350	108,471	108,504
Median coverage and range per targeted base	2217 (0-8709)	1923 (0-7786)	2068 (0-7562)	2181 (0-8109)
Percentage of targeted bases with coverage >200	95.47%	94.50%	94.63%	94.65%

SUPPLEMENTARY FIGURES

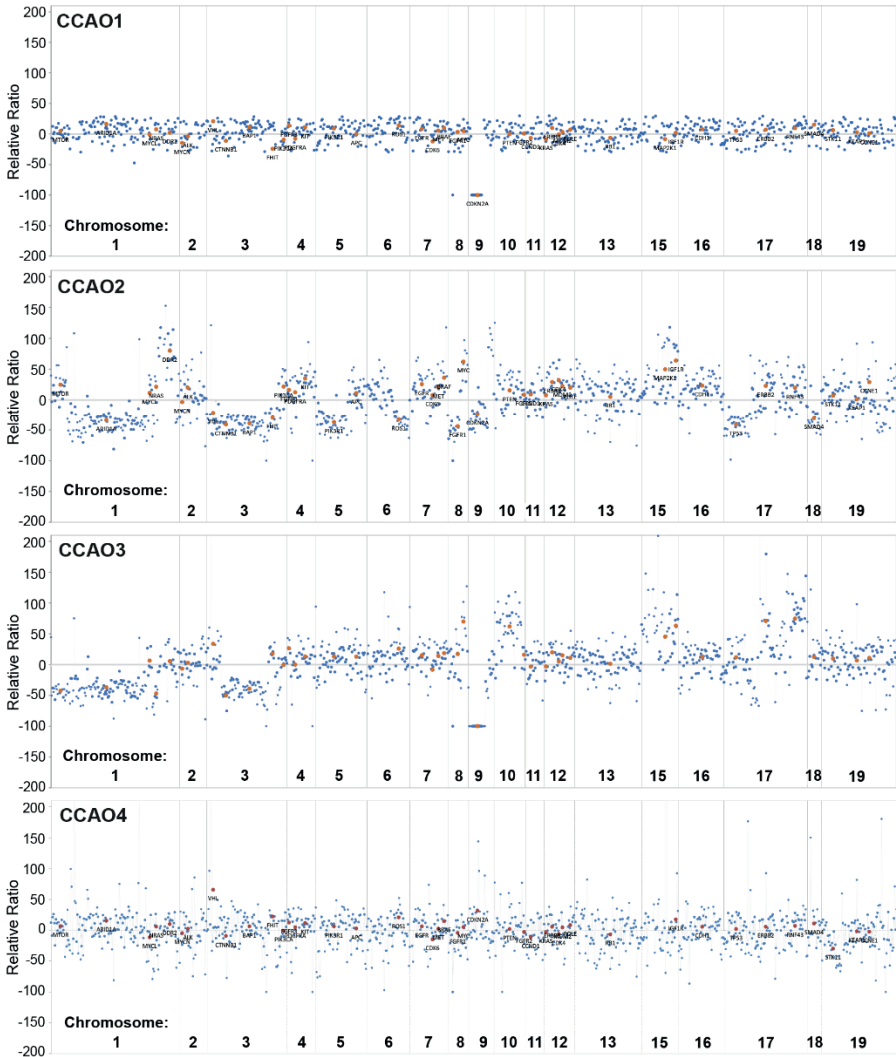


Suppl. Figure S1. Gating strategy for flow cytometry EdU data. FSC and SSC dot plots were used to select singlets in both samples and negative control. Threshold for EdU-positivity (Alexa Fluor 488+) was set based on the histogram of the negative control for each experiment. This threshold was applied to all samples in the experiment.

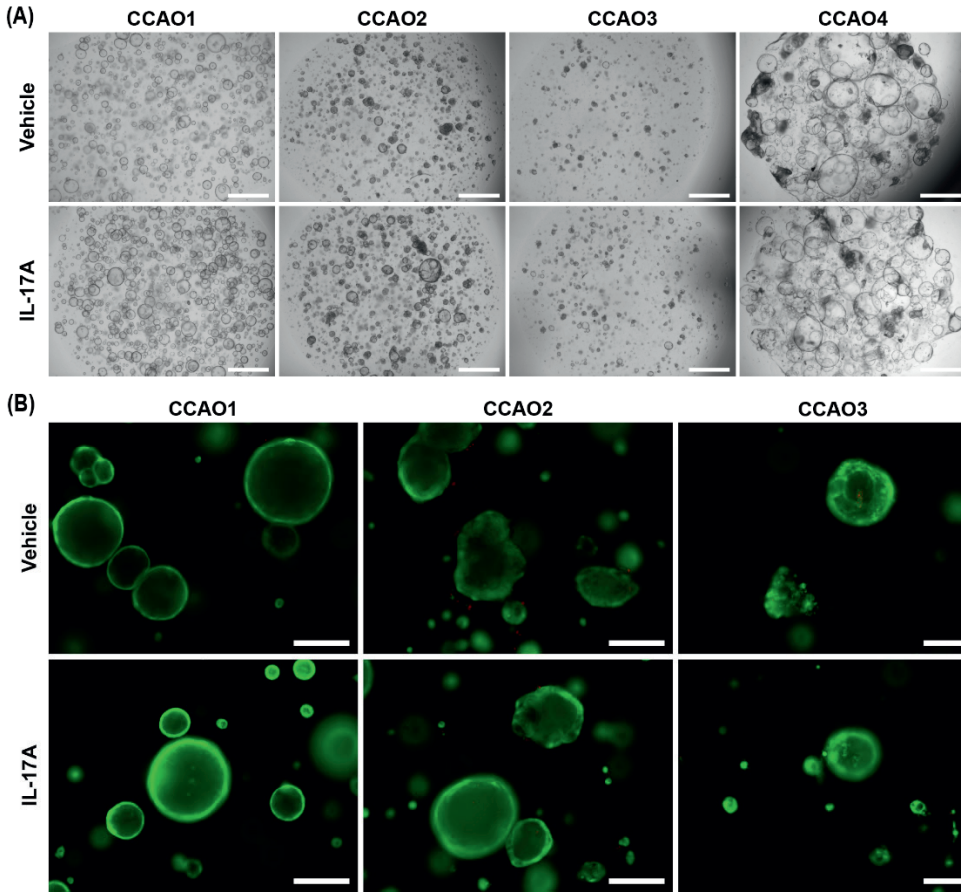
(A)



(B)



Suppl. Figure S2. Genomic aberrations in CCAOs. (a) Mutations and copy number variations in the CCAO lines, as identified by targeted next generation sequencing for a diagnostic solid cancer panel of 63 genes which can be found in Suppl. Table S2. (b) Chromosomal imbalance in the CCAO lines.



Suppl. Figure S3. CCAO cell death is not affected by IL-17A treatment. CCAOs were cultured for five days with 200 ng/ml IL-17A or with vehicle added to the medium. **(a)** Bright field images show organoids treated with IL-17A are larger. Scalebar = 1000 μ m. **(b)** Live/dead staining consisting of propidium iodide (red, dead cells) and calcein AM (green, live cells) shows no increase in CCAO cell death by IL-17A treatment. Scalebar = 200 μ m.

CHAPTER

5

Modelling immune cytotoxicity for cholangiocarcinoma with tumor-derived organoids and effector T cells

Ruby Lieshout^{1*}, Guoying Zhou^{2*}, Gilles S. van Tienderen¹, Valeska de Ruiter², Martin E. van Royen³, Patrick P.C. Boor², Luc Magré², Jyaysi Desai², Kübra Köten¹, Yik Yang Kan¹, Zhouhong Ge², Lucia Campos Carrascosa², Cecile Geuijen⁴, Dave Sprengers², Luc J.W. van der Laan¹, Monique M.A. Verstegen¹, Jaap Kwekkeboom²

**These authors contributed equally*

¹Erasmus MC Transplant Institute, Department of Surgery, Erasmus University Medical Center, Rotterdam, The Netherlands

²Department of Gastroenterology and Hepatology, Erasmus University Medical Center, Rotterdam, The Netherlands

³Department of Pathology, Erasmus MC Cancer Institute, Erasmus University Medical Center, Rotterdam, The Netherlands

⁴Merus N.V., Utrecht, The Netherlands

ABSTRACT

Background: Immunotherapy with immune checkpoint inhibitors (ICI) is being explored to improve cholangiocarcinoma (CCA) therapy. However, it remains difficult to predict which ICI will be effective for individual patients. Therefore, the aim of this study is to develop a co-culture method with patient-derived CCA organoids and immune cells, that could represent anti-cancer immunity *in vitro*.

Methods: CCA organoids were co-cultured with peripheral blood mononuclear cells or T cells. Flow cytometry, time-lapse confocal imaging for apoptosis, and quantification of cytokeratin 19 fragment (CYFRA) release were applied to analyze organoid and immune cell behavior. CCA organoids were also cultured in immune cell-conditioned media to analyze the effect of soluble factors.

Results: The co-culture system demonstrated an effective anti-tumor organoid immune response by a decrease in live organoid cells and an increase in apoptosis and CYFRA release. Interpatient heterogeneity was observed. The cytotoxic effects could be mediated by direct cell-cell contact and by release of soluble factors, although soluble factors only decreased viability in one organoid line.

Conclusions: In this proof-of-concept study, a novel CCA organoid and immune cell co-culture method was established. This can be the first step towards personalized immunotherapy for CCA by predicting which ICI are most effective for individual patients.

INTRODUCTION

Cholangiocarcinoma (CCA) is the second most prevalent type of primary liver cancer. It is an aggressive malignancy that originates from the biliary tract.¹⁻³ As CCA is often asymptomatic until late stages, at the time of diagnosis, 70-80% of the patients have non-curable disease and receive a palliative treatment regimen consisting of chemotherapeutics. Marked heterogeneity makes CCA difficult to treat successfully and the prognosis for CCA patients is poor, with five-year survival rates of 7-20%.^{4,5} Immunotherapy is one of the avenues that is being explored to improve CCA treatment. Immune checkpoint inhibitors (ICI) have been shown to be highly effective in activating pre-existing anti-cancer T-cell responses in patient subsets with several types of advanced malignancies.^{6,7} Clinical data on the efficacy of these inhibitors in CCA is limited. In phase 2 studies, anti-PD-1 antibody nivolumab demonstrated complete or partial remission (objective response) in 22% of biliary tract cancer patients⁸, and nivolumab combined with anti-CTLA-4 antibody ipilimumab induced an objective response in 31% of patients with intrahepatic CCA.⁹ Nevertheless, the majority of CCA patients do not respond well to these antibody treatments and it has proven difficult to predict which patients will benefit. Therefore, it would be of great benefit to develop an *in vitro* model that predicts a patient's response to specific ICI in order to provide optimal immunotherapy.

The establishment of cancer organoids has had a significant impact on the cancer research field by providing a patient-specific 3D-model designed to better represent the tumor than conventional 2D cell cultures.¹⁰⁻¹⁶ However, cancer organoids only represent the epithelial compartment of the tumor, limiting their utility in several fields of cancer research, including immunotherapy. Therefore, combining tumor organoids with immune cells has become an important objective to create an *in vitro* model suitable to study their interactions and for the evaluation of immunotherapies. Co-cultures of organoids and immune cells have already been reported for several types of cancer, including gastric cancer organoids co-cultured with autologous CD8⁺ T cells and dendritic cells¹⁷, pancreatic cancer with allogeneic T cells¹⁸, autologous peripheral blood mononuclear cells (PBMC)¹⁹, and autologous CD8⁺ T cells and dendritic cells²⁰, rectal cancer with autologous tumor-infiltrating lymphocytes (TIL)²¹, and non-small cell lung cancer and colorectal cancer co-cultured with T cells²².

Patient-derived CCA organoids were established from resected tissue specimens^{11, 23-25} and from needle biopsies^{26, 27}. Both were shown to largely recapitulate gene expression and mutational patterns of the patient tumor^{11, 23, 25-27}, and were suitable for high-throughput compound screens which identified several potential treatment options for CCA patients^{11, 23, 27}. However, even though CCA organoids have been in use for several years, no co-culture method combining CCA organoids with immune cells has been reported so far.

Therefore, the aim of the current study is to establish and optimize an *in vitro* 3D co-culture model of patient-derived CCA tumor organoids with PBMC and purified T cells, and to study growth inhibition and induction of organoid cell death by these cells. We performed several readouts for cytotoxicity, including flow cytometry, injury marker release in supernatant and time-lapse confocal imaging. Furthermore, we investigated the mechanism of cell death

induced by T cells, and described patient-specific differences in sensitivity to immune cell cytotoxicity. Applications of this novel culture system for screening of new immunotherapeutic antibodies and precision medicine will be discussed.

MATERIALS AND METHODS

Human subjects

Fresh tumor tissue samples were collected from seven liver cancer patients after surgical tumor resection at the Erasmus Medical Center Rotterdam. None of the patients received chemotherapy or immunosuppressive therapy at least three months prior to the surgery. The use of tumor tissue samples for research purposes was approved by the Erasmus MC medical ethics committee (MEC-2012-331; MEC-2013-143; MEC-2016-375). All patients consented to donate resected materials for research purposes. Peripheral blood buffy coat was obtained from four healthy donors (provided by Sanquin, Amsterdam, the Netherlands). PBMC were isolated by Ficoll density gradient centrifugation (600G, 20 minutes, 20°C) as described previously²⁸ and frozen at -150°C for later use.

Organoid culture

Organoids were initiated and cultured from three cholangiocarcinoma patients (Suppl. Table S1) as described previously.¹¹ A brief description can be found in Supplementary Materials. Tumorigenicity of CCA organoids was confirmed by tumor formation after subcutaneous injection in mice. Animal experiments were done in accordance to the Dutch law on laboratory animal use and performed under license number AVD101002017867 – protocol 17-867-19. Organoid fragments were injected into the flanks of female NOD.Cg-Prkd^{SCID} Il2rg^{tm1Wjl}/SzJ (NSG) mice (Charles River). Mice were checked weekly for tumor growth and tumors were harvested when tumor volume was > 2 cm³ or organoid fragments were injected > 6 months ago. CCA1 tumor formation was found in 3/3 injection sites, CCA2 tumor formation in 4/4 injection sites and CCA3 in 4/5 injection sites. Tumors were harvested and histology was assessed to confirm CCA-like tissue morphology. Moreover, mutation analysis was performed by targeted next generation sequencing for 65 cancer-related genes.

Optimization of BME concentration in co-culture assay

PBMC or purified CD3⁺ T cells were thawed 1-2 days in advance and pre-activated with anti-human CD3/CD28 dynabeads at a 1:100 bead:cell ratio in T cell medium (TM: RPMI 1640 (Lonza, Breda, The Netherlands) supplemented with 2mM L-glutamine/ Ultraglutamine (Invitrogen, Waltham, MA, USA), 50 mM Hepes Buffer (Lonza), 1% penicillin-streptomycin (Life Technologies), 5mM Sodium Pyruvate (Gibco), 1% minimum essential medium non-essential amino acids (Gibco, Waltham, MA, USA) and 10% human AB serum (Invitrogen)). One well of organoids was dissociated into single cells and counted to determine the effector:target cell ratio. Organoids used for co-culture were harvested, washed, and mechanically fragmented. For co-culture without BME, organoid fragments were plated in a flat-bottom 96-well plate. PBMC were added at a 5:1 effector:target cell ratio. For co-culture with BME domes, organoid fragments were plated in a 75% BME dome in a flat-bottom 96-

well plate, T cells were resuspended in the medium and were added 1-2 hours later around the BME dome at a 20:1 effector:target cell ratio. For co-culture in 10% BME suspension, organoid fragments and PBMC were resuspended in medium with 10% BME and plated in a flat bottom 96-well plate.

Bright field and fluorescence imaging

Bright field and fluorescence imaging was performed using an EVOS FL Cell Imaging System outfitted with RFP and DAPI light cubes. To analyze cell death, organoids and co-cultures were stained before imaging by adding 12.5 µg/ml propidium iodide (PI, Sigma-Aldrich, Saint Louis, MO, USA) and 100 µg/ml Hoechst 33342 to the culture medium for one hour.

ATP quantification cell viability assay

ATP quantification was performed to determine the effect of medium composition adjustments on the organoids. Therefore, organoids were mechanically disrupted and split into 5 µl droplets plated in a white-wall 96-well plate. Organoids were maintained in organoid expansion medium, either supplemented with 0, 2.5, 5, 7.5 or 10% human serum, supplemented with 0, 20 IU/ml (4 ng/ml) or 100 IU/ml (20 ng/ml) IL-2 or deprived of nicotinamide and/or forskolin for 6-7 days. CellTiter-Glo® 3D Cell Viability Assay (Promega, Madison, WI, USA) was used to quantify ATP content in accordance with the manufacturer's instructions.

PBMC proliferation and activity measurement

PBMC from healthy donors were cultured in TM, OM with 10% human serum, or OM with 10% human serum without one of the following reagents: A8301, recombinant human [Leu15]-Gastrin I, recombinant human EGF, recombinant human HGF, forskolin, recombinant human FGF10, N2 supplement, n-Acetyl-L-cysteine, B27 supplement, nicotinamide, Rspo-1 conditioned medium. Anti-human CD3/CD28 dynabeads (Gibco) were added in all conditions except 'TM' and 'OM' at a bead:cell ratio of 1:100. Cells were cultured in 96-well round-bottom culture plates at 37°C.

After four, seven and ten days, respectively, PBMC were harvested and stained with fixable viability dye eFluor 506 (1:500 in PBS, eBioscience, Waltham, MA, USA). Cell surface staining was then performed in the dark at 4°C for 20 minutes with anti-CD45, anti-CD8, anti-CD4, anti-CD3, anti-HLA-DR, and anti-CD137 antibodies (Suppl. Table S3). Cells were washed and resuspended in FACS buffer (PBS with 0.1% EDTA, 0.5% NaN₃, and 1% FCS). For Ki-67 staining, cells were fixed and permeabilized using the Foxp3 staining buffer set (eBioscience). PBMC were measured using a FACSCanto II flow cytometer (BD Biosciences, Franklin Lakes, NJ, USA) and analyzed using FlowJo software (version 10.0, LLC).

HepG2 killing assay

The HepG2 killing assay was performed as described previously.²⁹ PBMC were activated with anti-human CD3/CD28 dynabeads at a 1:100 bead:cell ratio for three days. PBMC and HepG2-RFPs were combined at a 30:1 PBMC:HepG2-RFP ratio. They were resuspended in either TM or OM without nicotinamide and co-cultured for seven days.

Co-culture assay

Organoid preparation

Seven days before co-culture, organoids were harvested, mechanically broken, and dissociated into small, 1-4 cell sized fragments by Trypsin-EDTA (Gibco) dissociation alternated with mechanical disruption (3 cycles of 3 minutes Trypsin-EDTA at 37°C). After, they were plated in 25 μ l droplets of 75% BME, and maintained in organoid expansion medium, which was refreshed on day 3-4.

Immune cell preparation

The CCA organoid cultures used were typed for HLA-A, -B, -C, -DRB1, -DRB345, and DQB1. PBMC were isolated from donors that were selected based on HLA mismatching with the CCA organoids. In case of PBMC co-culture, PBMC were thawed 2-3 days in advance at 37°C, then resuspended and cultured in TM with anti-human CD3/CD28 dynabeads (Gibco-Life Technologies) at a 1:100 bead:cell ratio. In case of T cell co-culture, HLA-mismatched PBMC were thawed 2-3 days in advance at 37°C, then T cells were isolated by CD3 positive selection by microbeads according to manufacturer's instructions (Miltenyi, Bergisch Gladbach, Germany). Live T cell purity was \geq 95%. T cells were cultured for 2-3 days in TM with anti-human CD3/CD28 dynabeads at a 1:20 bead:cell ratio and 20 IU/ml (4 ng/ml) IL-2.

Co-culture

On the day of co-culture, one well of organoids was harvested, mechanically broken, and dissociated into single cells by Trypsin-EDTA incubation (15 minutes at 37°C). Quantification of single cells from this well was used to determine effector:target cell ratio between immune cells and organoid cells. Immune cells were harvested, counted, and combined with organoids at 20-30:1 (PBMC) or 25-50:1 (T cells) ratios. Together, they were resuspended in 200 μ l organoid expansion medium without nicotinamide (OM-nic) with 10% BME (suspension coating) and 10% human serum and plated in a 96-well flat-bottom suspension plate. In some conditions, 25 IU/ml (5 ng/ml) IL-2, 50 IU/ml (10 ng/ml) IL-2 or 100 IU/ml (20 ng/ml) IL-2 was added. On day 3-4, 100 μ l of pre-warmed OM-nic with 10% human serum was carefully added. Readouts were performed on day seven of co-culture.

Live cell quantification by flow cytometry

Organoids and immune cells were harvested, washed, and dissociated into single cells by incubation with TrypLE Express (ThermoFisher, 3-5 cycles of 5 minutes at 37°C), combined with regular resuspension and vortexing. An aliquot was checked microscopically after cycle 3, 4 and 5 to determine when the organoids were fully dissociated. Cells were washed first in PBS and then in Annexin V binding buffer (eBioscience Annexin V apoptosis detection kit), and stained with anti-EpCAM, anti-CD45, anti-CD3, anti-CD8, anti-CD56, anti-CD14 and Annexin V (Suppl. Table S3) for 10-15 minutes at room temperature in the dark. Cells were washed and resuspended in Annexin V binding buffer and stained with DAPI to mark dead cells. Counting beads (Invitrogen, 123count eBeads) were added to each well prior to flow cytometric recording (MACSQuant, Miltenyi). A strict gating strategy was made to

distinguish live CD45⁺ immune cells and live EpCAM⁺ organoid cells (Suppl. Fig. 3A). The analysis was done using FlowJo software (version 10.0, LLC).

CYFRA (Cytokeratin Subunit 19 Fragment) quantification

Culture supernatants were collected on day seven of the co-culture assay and stored frozen at -20°C. CYFRA concentration was measured by the Lumipulse® G1200 (Fujirebio, Tokyo, Japan) automated immunoassay analyzer using the Lumipulse® G CYFRA immunoreaction cartridges (Fujirebio) according to manufacturer's instructions.

Confocal time-lapse imaging and analysis

T cells were isolated and pre-activated as described above for co-culture assays. On the day of co-culture, they were stained with 1 μM of CellTrace Far Red (Invitrogen) in PBS for 15 minutes at 37°C. Organoids were pre-stained with 0.1 μg/ml Hoechst 33342 (ThermoFisher) for 3.5 hours. Co-cultures were prepared as described above, with addition of 1:1000 caspase 3/7 detection reagent (Invitrogen) and 0.1 μg/ml Hoechst 33342 to the medium. Co-cultures were imaged in time using a Perkin Elmer confocal Opera Phenix High Content screening system equipped with a 10x air objective (NA 0.3). Imaging settings and analysis details can be found in Supplementary Materials.

Conditioned medium assay

TIL isolation and preparation of conditioned media from PBMC and TIL is described in Supplementary Materials. Organoids were harvested, mechanically broken, and dissociated into small, 1-4 cell sized fragments by Trypsin-EDTA dissociation alternated with mechanical disruption (3 cycles of 3 minutes Trypsin-EDTA at 37°C). 5 μl droplets of 75% BME (diluted in organoid base medium) with 1500 organoid fragments were plated in a 96-well flat-bottom plate. Each droplet was covered with 100 μl of OM-nic supplemented with 0%, 2.5%, 5%, 7.5% or 10% concentrated control medium, concentrated conditioned medium from stimulated PBMC or TIL, or concentrated conditioned medium from unstimulated TIL. Medium was refreshed on day four. ATP quantification by CellTiter-Glo® 3D Cell Viability Assay (Promega) was performed on day seven.

Analysis of co-stimulatory and co-inhibitory molecules by flow cytometry

Organoids were harvested and dissociated into single cells with TrypLE Express (3 cycles of 5 minutes at 37°C), combined with regular resuspension and vortexing. A half of organoid cells were stimulated with 100 ng/mL IFN-γ for two days, while the other half without stimulation. The culture was in organoid medium in 96-well round-bottom plates at 37°C. After two days, cells were harvested and stained with fluorochrome-conjugated antibodies against different immune molecules in the presence of Fc receptor block (Suppl. Table S3). DAPI was used to mark dead cells, and minus controls were used for gating purposes.

RNA sequencing analysis

Sample preparation, RNA sequencing details and data preparation can be found in Supplementary Materials. Data is stored in the GEO repository under accession number

GSE179601. Differentially expressed genes were determined by R package Limma (version 3.46.0) comparing CCA1 against CCA2 and CCA3. Gene set enrichment analysis was performed for the 1000 genes with the highest $^2\log(\text{fold change})$ using the publicly available online analysis tool DAVID^{30, 31} with the Gene Ontology: Biological Processes database. Processes with false discovery rate (FDR)-adjusted p value < 0.25 were deemed significantly enriched.

Statistical analysis

Differences among multiple matched groups of data were analyzed by either One-Way ANOVA or Mixed-effects analysis according to if there are missing values. Differences between two matched groups of data were analyzed by two-tailed paired t test. Differences between two unmatched groups of data were analyzed by two-tailed unpaired t test. The statistical analyses were performed using GraphPad Prism 9 (GraphPad Software). P values less than 0.05 were considered statistically significant (* p < 0.05; ** p < 0.01; *** p < 0.001).

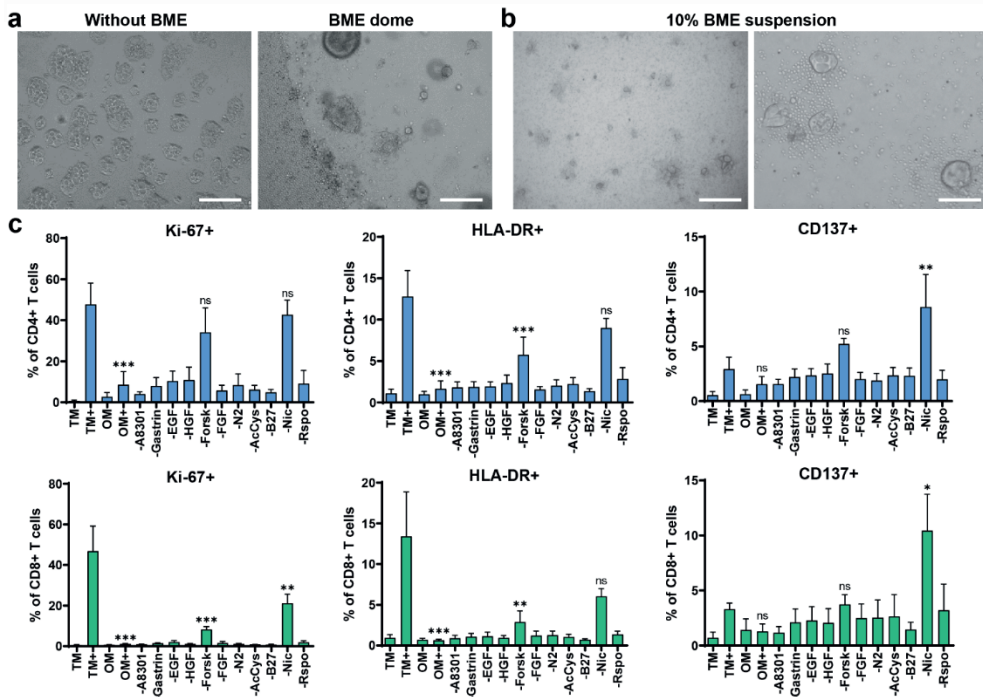
RESULTS

Establishment and optimization of 3D co-culture conditions

To set up a 3D co-culture model, we used established patient CCA organoid lines and PBMC from healthy donors to establish co-culture conditions in which both could survive and function. First, we compared co-culture of organoid fragments and PBMC without BME to co-culture in which organoid fragments were cultured in BME domes while PBMC were in the medium around the dome (Fig. 1A). Without BME, organoids adhered to the plastic did not propagate well and could not retain their 3D morphology. Loss of the 3D self-organization of organoids limits cellular interactions and changes cellular behavior. Therefore, co-culture without BME was not feasible. Culture in BME domes limited interaction between organoids and PBMC, as only a small part of the PBMC could infiltrate into the BME dome over a short distance in this setting. To overcome this, we suspended the organoid fragments and PBMC in medium with 10% BME (Fig. 1B). This way, CCA organoids kept their 3D morphology and PBMC gathered around the organoids.

Consecutively, we examined the influence of T cell medium on organoid morphology and that of organoid medium on T cell proliferation and activation. CCA organoids were not able to retain their 3D morphology in T cell medium (Suppl. Fig. S1A), while CD4⁺ and CD8⁺ T cells displayed reduced proliferation (Ki-67⁺ cells) and activation (HLA-DR⁺ cells) when cultured in organoid medium (CD4⁺ Ki-67⁺ 8.6% in OM+ vs 47.7% in TM+, p < 0.001 and HLA-DR⁺ 1.7% vs 12.8%, p < 0.001; CD8⁺ Ki-67⁺ 1.1% vs 46.8%, p < 0.001 and HLA-DR⁺ 0.6% vs 13.4%, p < 0.001) (Fig. 1C). So, we eliminated components of the organoid medium to identify their contribution to the observed suppression of T cell activity. Of all components investigated, removal of forskolin partially, and removal of nicotinamide almost completely abolished the suppressive effect of organoid medium on T cells and removal of nicotinamide even increased the number of CD137⁺ cells (CD4⁺ CD137⁺ 10.4% in OM-nic vs 3.3% in TM+, p < 0.01; CD8⁺ CD137⁺ 8.6% vs 2.9%, p < 0.05) (Fig. 1C, Suppl. Fig. S2).

The morphology and viability of all three CCA organoid lines were not affected by removing either nicotinamide or forskolin from the medium (Fig. 1E, Suppl. Fig. S1B), but removal of both reduced organoid viability as expressed by ATP quantification (fold decrease CCA1: 0.23, CCA2: 0.43, CCA3: 0.80; Fig. 1D). The other factor new to T cell culture is BME. 10% BME did not increase expression of activation markers HLA-DR, CD137 and proliferation marker Ki-67 in both CD4⁺ and CD8⁺ T cells, thereby not leading to unwanted T cell reactivity (Fig. S1C). As human serum is a key component in T cell medium, we investigated if addition to organoid culture would have harmful effects. Human serum did not suppress growth or viability of CCA organoids as shown by stable ATP content at concentrations up to 10% (Fig. 1E).



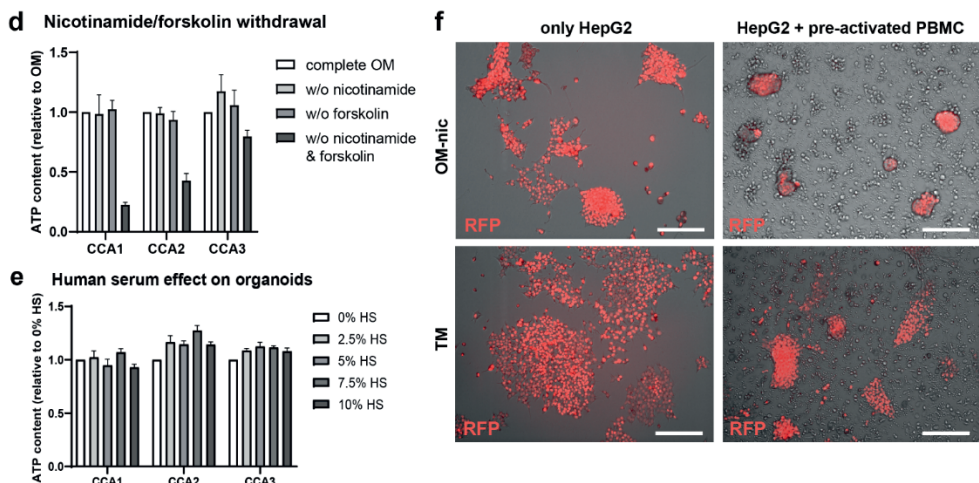


Figure 1D-F. Optimization of the co-culture setup for CCA organoids and immune cells. (d) ATP quantification shows CCA organoid survivability is not affected by removal of forskolin or nicotinamide from the organoid medium, but removal of both decreases viability (n=3 technical replicates). (e) CCA viability was not affected by the addition of human serum to organoid medium as determined by ATP quantification assay (n=3 technical replicates). (f) Overlay of bright field (gray scale) and RFP (red) demonstrates the killing potency of anti-CD3/CD28 bead pre-activated PBMC in both T cell medium (TM) and organoid medium without nicotinamide (OM-nic) is comparable. Scalebar: 200 μ m (f). All values with error bars represent mean with SEM.

We tested the cytotoxic properties of PBMC in organoid medium without the addition of nicotinamide in our previously established model of immune cell-mediated killing of tumor cell line HepG2.²⁹ PBMC were pre-activated with anti-CD3/CD28-coated beads, then co-cultured for seven days with HepG2 cells that were genetically labeled with red fluorescent protein (RFP). Figure 1F shows that HepG2 cell number was decreased in PBMC co-culture compared to HepG2 alone in both organoid medium without nicotinamide and T cell medium, indicating similar killing efficiency. All together, we determined that culture conditions for the 3D co-culture of CCA organoids and PBMC should consist of organoid medium without nicotinamide, supplemented with 10% human serum, in a 10% BME suspension.

CCA organoids show interpatient variation in PBMC-mediated cytotoxicity

Next, CCA organoids were co-cultured with HLA-mismatched anti-CD3/CD28 bead pre-activated PBMC for seven days. IL-2 is known to stimulate T cell proliferation and activation, so we investigated if the addition of three concentrations of IL-2 could enhance the effect of immune cells in co-culture, as IL-2 alone did not affect the viability of CCA organoids (Suppl. Fig. S3B). In co-culture, morphological changes in CCA2 like loss of 3D structural integrity indicated cytotoxicity of PBMC, which seems to aggravate upon addition of 5 and 10 ng/ml IL-2 (Fig. 2A). Flow cytometry (Fig. 2B) shows that co-culture with PBMC seemed to lower the number of live organoid cells (EpcAM⁺ DAPI⁻ cells) in CCA2 (fold decrease 0.89, p > 0.05), although not significantly. Addition of 10 or 20 ng/ml IL-2 significantly lowered the

number of live organoid cells (fold decrease 0.50, $p < 0.05$ and 0.51, $p < 0.01$). The number of live cells in CCA1 and CCA3 was not significantly reduced by co-culture with PBMC alone (Fig. 2C, D). While IL-2 also potentiated PBMC cytotoxicity in these organoid lines, their decrease in live cells was not significant. IL-2 increased the live cell count of CD4⁺ T cells, CD8⁺ T cells and CD56⁺ NK cells in both the co-culture and the single PBMC culture (Fig. 2E). The number of CD8⁺ T cells was over 100-fold higher and the number of CD4⁺ T cells was about 200-fold higher than the NK cell counts. After pre-activation with anti-CD3/CD28 beads, CD4⁺ and CD8⁺ T cells clearly produced IFN- γ and TNF- α compared to non-pre-activated T cells (Fig. 2F). Co-culture with CCA organoids for 19 hours seemed to already further enhance the production of these effector cytokines by CD4⁺ and CD8⁺ T cells, although at a low level. Greater effects might be observed if the timeline of the co-culture is prolonged before IFN- γ and TNF- α measurement. These data suggest that this optimized co-culture system allows for studying the interaction between CCA organoids and PBMC and for quantification of immune cell cytotoxicity of the cancerous organoid cells.

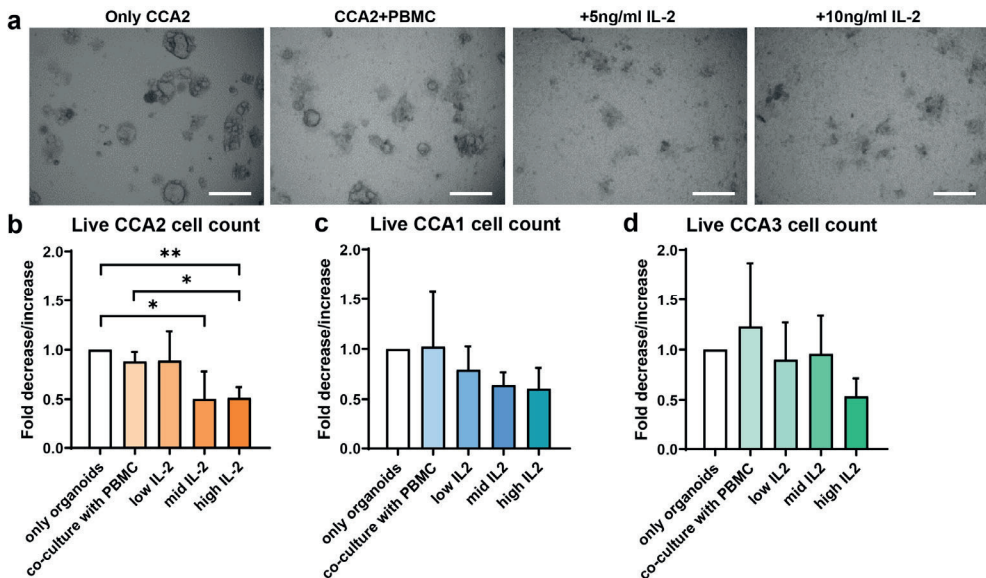


Figure 2A-D. Pre-activated PBMC co-cultured with CCA organoids and IL-2 show patient-specific killing. CCA2 organoids were co-cultured with anti-CD3/CD28 pre-activated PBMC for seven days. **(a)** Bright field imaging shows CCA2 organoids lose their regular morphology and become fragmented, especially upon addition of IL-2. **(b)** Flow cytometry cell count for EpCAM-positive, CD45- and DAPI-negative cells demonstrates CCA2 organoids sustain significant cell death in the presence of 50 IU/ml (10 ng/ml, mid) or 100 IU/ml (20 ng/ml, high) IL-2, but not with 25 IU/ml (5 ng/ml, low) IL-2. **(c, d)** CCA1 (c) and CCA3 (d) organoids do not show a significant decrease in live cells in the same co-culture setting ($n \geq 3$ biological replicates for each organoid line; $n = 2$ different PBMC batches). Scalebar: 200 μm (a). All values with error bars represent mean with SEM. * $p < 0.05$, ** $p < 0.01$.

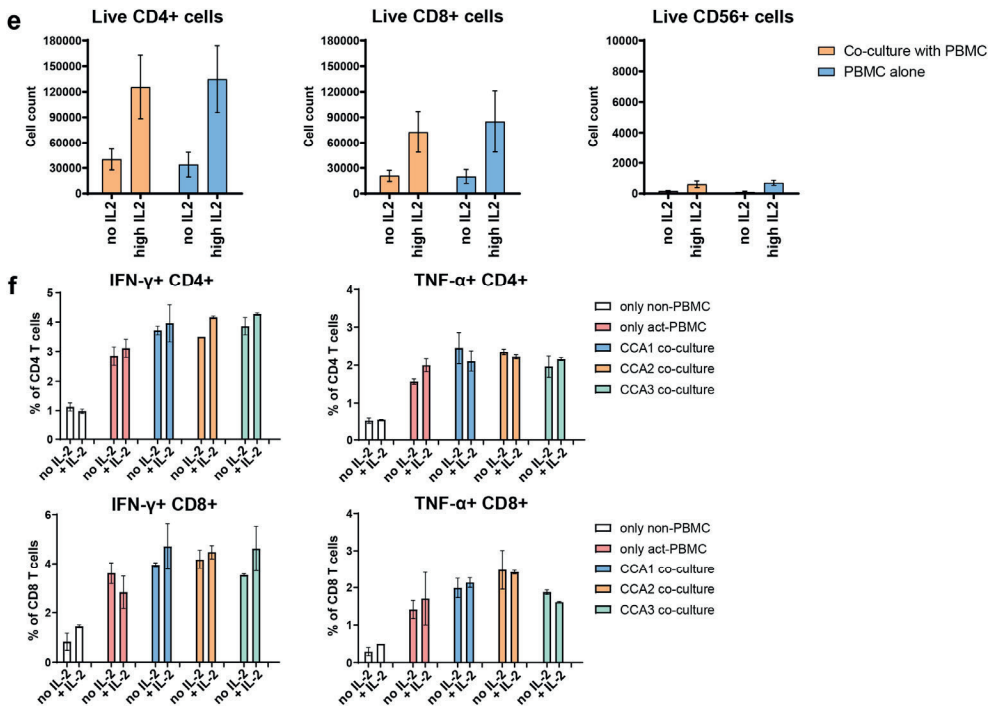


Figure 2E-F. Pre-activated PBMC co-cultured with CCA organoids and IL-2 show patient-specific killing. CCA2 organoids were co-cultured with anti-CD3/CD28 pre-activated PBMC for seven days. **(e)** Flow cytometry cell count for live (DAPI-negative) CD4⁺ and CD8⁺ T cells and CD56⁺ NK cells demonstrates that the number of live cells is comparable between solo culture and co-culture and addition of 100 IU/ml IL-2 increases the number of live cells. **(f)** Flow cytometry for intra-cellular staining of IFN-γ and TNF-α in non-pre-activated and 3-day pre-activated PBMC cultures, and co-cultures of CCA organoids with pre-activated PBMC, either with or without 100 IU/ml IL-2. The percentage of cytokine positive CD4⁺ and CD8⁺ T cells was determined after 19 hours of (co-)culture in the presence of brefeldin and monensin (n=3 technical replicates). All values with error bars represent mean with SEM. * p < 0.05, ** p < 0.01.

Purified T cells recapitulate the PBMC-mediated cytotoxicity

As PBMC are a mixed population of cells, we subsequently investigated whether purified T cells were able to kill CCA organoids. CD3⁺ T cells (purity ≥ 95%) were isolated from HLA-mismatched PBMC, pre-activated with anti-CD3/CD28 coated beads and co-cultured with CCA organoids. After seven days of co-culture, CCA1 organoids were not affected morphologically, while CCA2 and CCA3 organoids were smaller and partially disintegrated (Fig. 3A), suggesting cell death. Quantification of live cells showed significant CCA organoid cell death in co-culture with T cells in both CCA2 (fold decrease 0.30, p < 0.001) and CCA3 (fold decrease 0.39, p < 0.01) co-cultures, whereas CCA1 organoid live cell counts were not affected (Fig. 3B). Co-culture with CCA organoids did not reduce the live cell count of cytotoxic (CD8⁺) and CD8⁻ T cells compared to their single culture (Fig. 3C). CYFRA is a cytokeratin 19 fragment that is usually determined in serum or plasma as a (potential)

biomarker for a range of different solid tumors, including CCA.^{32, 33} It is released from apoptotic and necrotic cholangiocytes, while it's not released by immune cells.³⁴ Hence, we hypothesized it might serve as a simple and scalable readout in our co-culture system. CYFRA concentration was higher in the culture supernatant of CCA2 co-culture than in the culture supernatant of only organoids (fold increase 1.56, $p < 0.05$), while it was not significantly increased in CCA1 and CCA3 co-cultures (Fig. 3D & Suppl. Fig. S3C). Confocal time-lapse imaging showed that more CCA2 organoid cells were caspase 3/7-probe positive in the co-culture with T cells compared to the culture of only organoids (Fig. 3E and Suppl. Video S1 versus S2), indicating increased apoptotic cell death in co-cultured organoids. T cell only culture also showed that a large number of T cells is caspase 3/7-probe positive (Fig. 3E and Suppl. Video S3), which could be due to apoptosis, but is also seen upon T cell activation with anti-CD3.³⁵

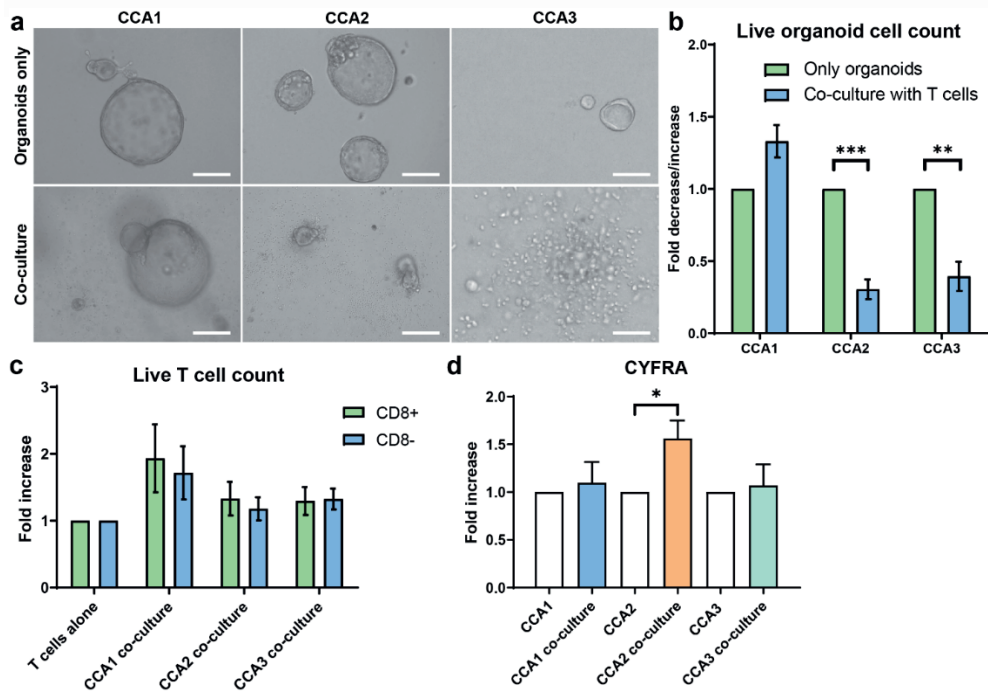


Figure 3A-D. Pre-activated T cells also kill CCA organoids in a patient-specific manner. (a) Bright field images of CCA organoids cultured with and without T cells for seven days demonstrate CCA1 organoids are not inhibited by T cells while CCA2 and CCA3 organoids are smaller and disintegrated, indicating cell death. (b) Flow cytometry cell count for EpCAM-positive, CD45-negative and DAPI-negative cells shows CCA2 and CCA3 organoids sustain significant cell death after seven days of co-culture with anti-CD3/CD28 bead pre-activated T cells, while CCA1 organoids are not affected ($n \geq 3$ biological replicates for each organoid line; $n = 2$ different PBMC batches). (c) Flow cytometry cell count for live (DAPI-negative) CD8⁺ and CD8⁻ T cells. (d) Relative difference in CYFRA concentration in supernatant after seven days of CCA organoid and T cell co-culture demonstrates a significant increase in CCA2 ($n \geq 3$ biological replicates for each organoid line). Scalebar: 200 μm (left and middle panel of a), 50 μm (right panel of a). All values with error bars represent mean with SEM. * $p < 0.05$, ** $p < 0.01$, *** $p < 0.001$.

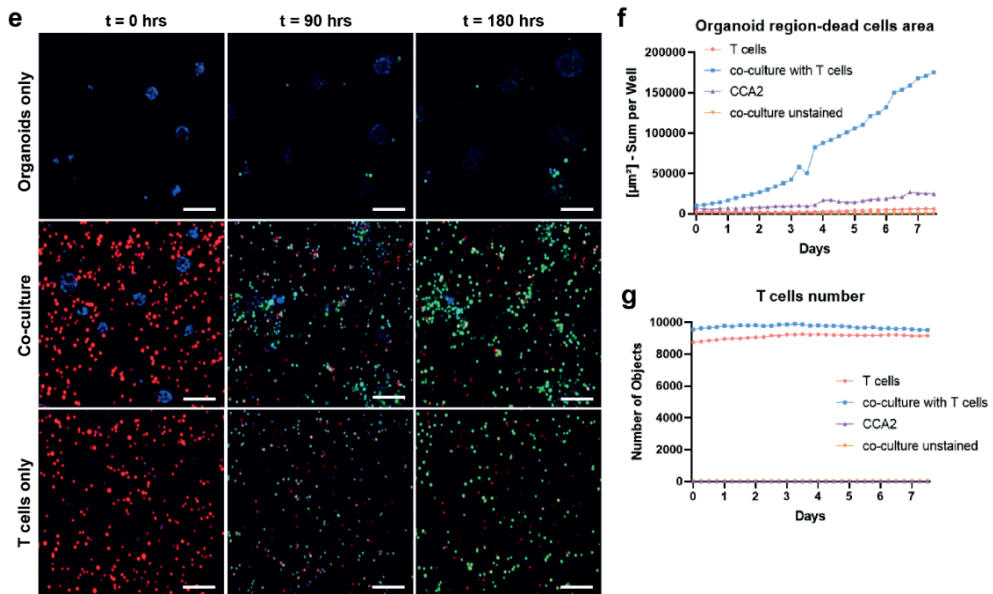


Figure 3E-F. Pre-activated T cells also kill CCA organoids in a patient-specific manner. (e) Representative confocal images of Cell Trace Far Red-stained T cells (red), Hoechst 33342-stained CCA2 organoids (blue) and co-cultures in the presence of a Caspase 3/7-probe (green) at timepoints 0, 90 and 180 hours. **(f, g)** Quantification of dead cell surface (Caspase 3/7 probe-positivity) in organoid area (Hoechst 33342 labelled) **(f)** and number of T cells **(g)** in nine fields of view of confocal time-lapse imaging every six hours for 180 hours. Organoid death is higher in co-cultures with T cells compared to CCA2 organoids alone. The number of T cells (Cell Trace Far Red labelled) is comparable between solo culture and co-culture. Scalebar: 100 μm **(e)**.

Quantitative analysis of the confocal images confirmed that the apoptotic cell area in the organoid region was increased about seven-fold after seven days of co-culture with T cells compared to the single culture of organoids (Fig. 3F). The number of T cells was similar in the co-culture and in single culture (Fig. 3G). Together, these data indicate that strong killing of CCA organoids mediated by T cells is possible in our co-culture system and the degree of cytotoxicity is different between CCA organoid lines.

Soluble immune cell-mediated factors exert pleiotropic effects on CCA organoids

In the co-culture experiments in which organoids were cultured in BME domes, while T cells were added in the medium around the dome, T cells were hardly able to infiltrate. Still, CCA2 organoids were killed after seven days of co-culture in this setting (Fig. 4A). This suggests that T cells might be able to kill CCA organoids without direct contact, possibly mediated by soluble factors produced by T cells. Therefore, we also studied the indirect effect of soluble factors produced by immune cells on CCA organoids. For this, supernatant was collected from stimulated PBMC (stimulated PBMC-conditioned medium) and control medium (OM-nic with 10% human serum), and concentrated 10 times by centrifugal filtration before adding to the culture. CCA organoids were cultured in BME domes surrounded by medium supplemented with different amounts (2.5%, 5%, 7.5% and 10%) of concentrated

conditioned medium or control medium. The viability of CCA2 organoids was significantly suppressed by stimulated PBMC-conditioned medium compared to control medium (fold decrease 0.33 vs. 1.22 at 10%, $p < 0.05$) after seven days (Fig. 4B). Yet, CCA1 and CCA3 organoids did not show growth inhibition.

Next, specific TIL-derived soluble factors were tested by adding concentrated conditioned media from unstimulated and stimulated TIL to CCA organoid cultures. Similarly, stimulated TIL-conditioned medium suppressed the viability of CCA2 organoids compared to both unstimulated TIL-conditioned medium and control medium (fold decrease stim. TIL: 0.60 vs. unstim. TIL: 1.05 vs. control: 1.22 at 10%, $p < 0.01$) (Fig. 4C). Interestingly, both unstimulated and stimulated TIL-conditioned media increased the viability and/or proliferation of CCA1 (fold increase stim. TIL: 1.54 vs. unstim. TIL: 1.44 vs. control: 0.60 at 10%, $p < 0.01$) and CCA3 (fold increase stim TIL: 2.74 vs. unstim. TIL: 1.84 vs. control: 1.38 at 10%, $p < 0.05$) organoids. These data reveal that the soluble factors secreted by stimulated TIL and PBMC show CCA organoid line-specific effects, ranging from the induction of cell death in CCA2, through TIL-specific stimulation in CCA1 and CCA3.

Variation in immune checkpoint expression in CCA organoids

The described results demonstrate clear distinctions in the response of different patient-derived organoid lines to direct and indirect contact with immune cells. CCA1 organoids were resistant to inhibitory effects in both direct co-culture and indirect conditioned media experiments. In contrast, CCA2 organoids were sensitive to killing in both assays. CCA3 organoids were sensitive to T cell-mediated cytotoxicity in co-culture, but were in fact stimulated by TIL-conditioned media. In order to understand the marked variation in CCA organoid response to direct and indirect immune cell contact, the heterogeneity of expression of co-inhibitory and co-stimulatory immune molecules and RNA expression patterns were assessed.

The three CCA organoid lines express similar levels of checkpoint molecule B7-H3 (CD276) and CD155 (possible therapeutic immunological target), which was expressed on almost every cell (B7-H3: 94.2-99.9%, CD155: 94.3-98.1%), while MHC class 2 molecules (2.6-5.0%), B7-H5 (0.5-1.4%) and co-stimulatory molecule CD80 (0.1-2.2%) were hardly present on CCA organoids (Fig. 5A, B; Suppl. Fig. 4). Co-stimulatory MHC class 1 molecules (5.9%) and CD86 (42.1%) expression was lower in CCA2 organoids than in CCA1 and CCA3. Almost 40% of CCA3 organoid cells are CD112-positive, while CCA1 and CCA2 cells hardly express it (0-3.8%). Co-inhibitory PD-L1 (13.8%) and PD-L2 (6.0%) showed lower expression on CCA3 organoids than in CCA1 and CCA2. Galectin 9 was most present in CCA1 organoids (25.4%), followed by CCA2 (16.6%). After IFN- γ stimulation (Fig. 5A, B; Suppl. Fig. 4), CCA2 and CCA3 organoids upregulated multiple co-stimulatory and co-inhibitory molecules, including PD-L1, PD-L2, MHC class 2 molecules and galectin 9, and CCA2 organoids also upregulated MHC class 1 molecules and CD86. In turn, CCA1 organoids did not respond to IFN- γ stimulation with upregulation of any of these molecules.

To identify differences in the transcriptome of CCA1 which could potentially explain its resistance to immune-mediated cell death compared to the other CCA organoid lines, we

performed gene set enrichment analysis for the 1000 most differentially expressed genes when compared to CCA2 and CCA3. As shown in Figure 5C, three cell adhesion-related processes were significantly enriched in the gene set, with enrichment scores of 4.2 (GO:0007156, FDR < 0.001), 2.0 (GO:0007155, FDR < 0.01) and 7.1 (GO:0016339, FDR < 0.01). The main type of cell adhesion-related genes found was (proto)cadherins (Suppl. Table S4). Together, these data demonstrate the marked heterogeneity among different patients' liver tumor organoids in expression of co-stimulatory and co-inhibitory molecules and RNA expression patterns.

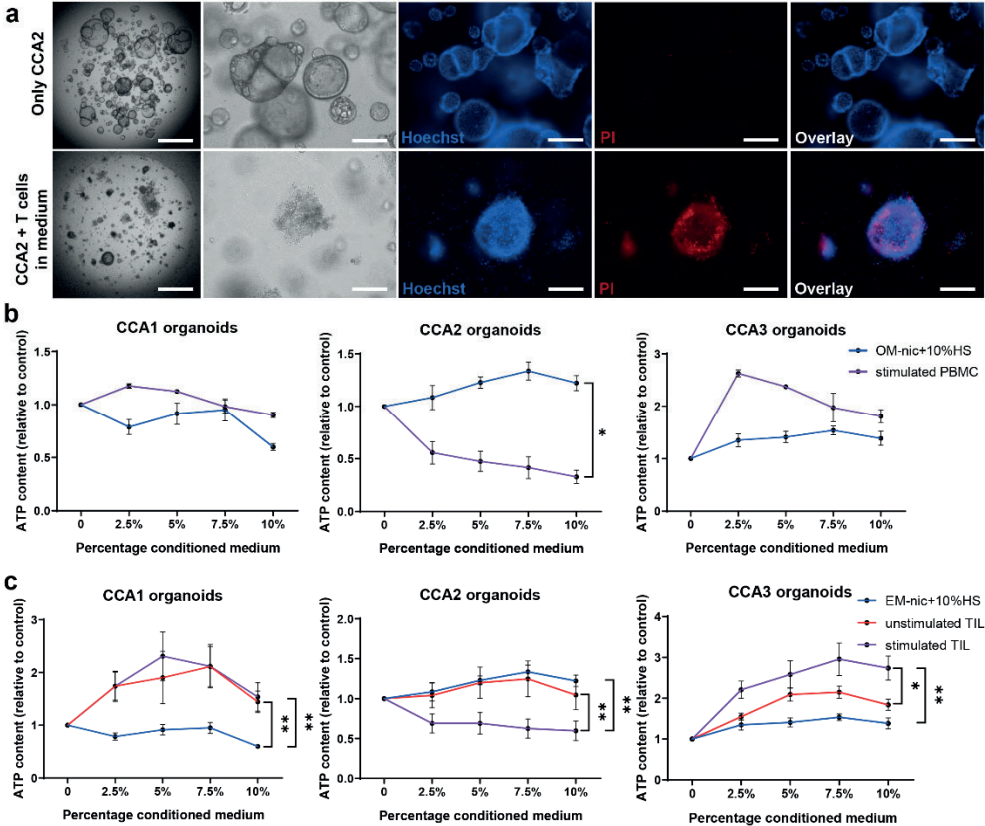


Figure 4. PBMC and TIL have patient-specific indirect CCA organoid killing capacity. (a) Representative bright field images (first two panels) and immunofluorescent staining with Hoechst 33342 (blue) and propidium iodide (red) of CCA organoids alone (top row) and co-culture of CCA organoids inside the BME dome with T cells surrounding the dome (bottom row) demonstrate CCA organoid death is increased in the co-culture setting. (b, c) Viability measurements show the effect of vehicle medium (OM –nic +10% human serum), stimulated PBMC (b), unstimulated and stimulated TIL (c) conditioned medium on CCA organoids after seven days ($n \geq 3$ biological replicates with different PBMC donor cultures or TIL patient cultures to produce conditioned media). The conditioned media and vehicle medium were concentrated 10-fold using 3KDa centrifugal filters. CCA2 organoid viability is lowered by both conditioned media, while CCA1 and CCA3 are not inhibited by PBMC conditioned medium and stimulated by TIL conditioned media. Scalebar: 1000 μ m (first panel of a), 200 μ m (other panels of a). All values with error bars represent mean with SEM.

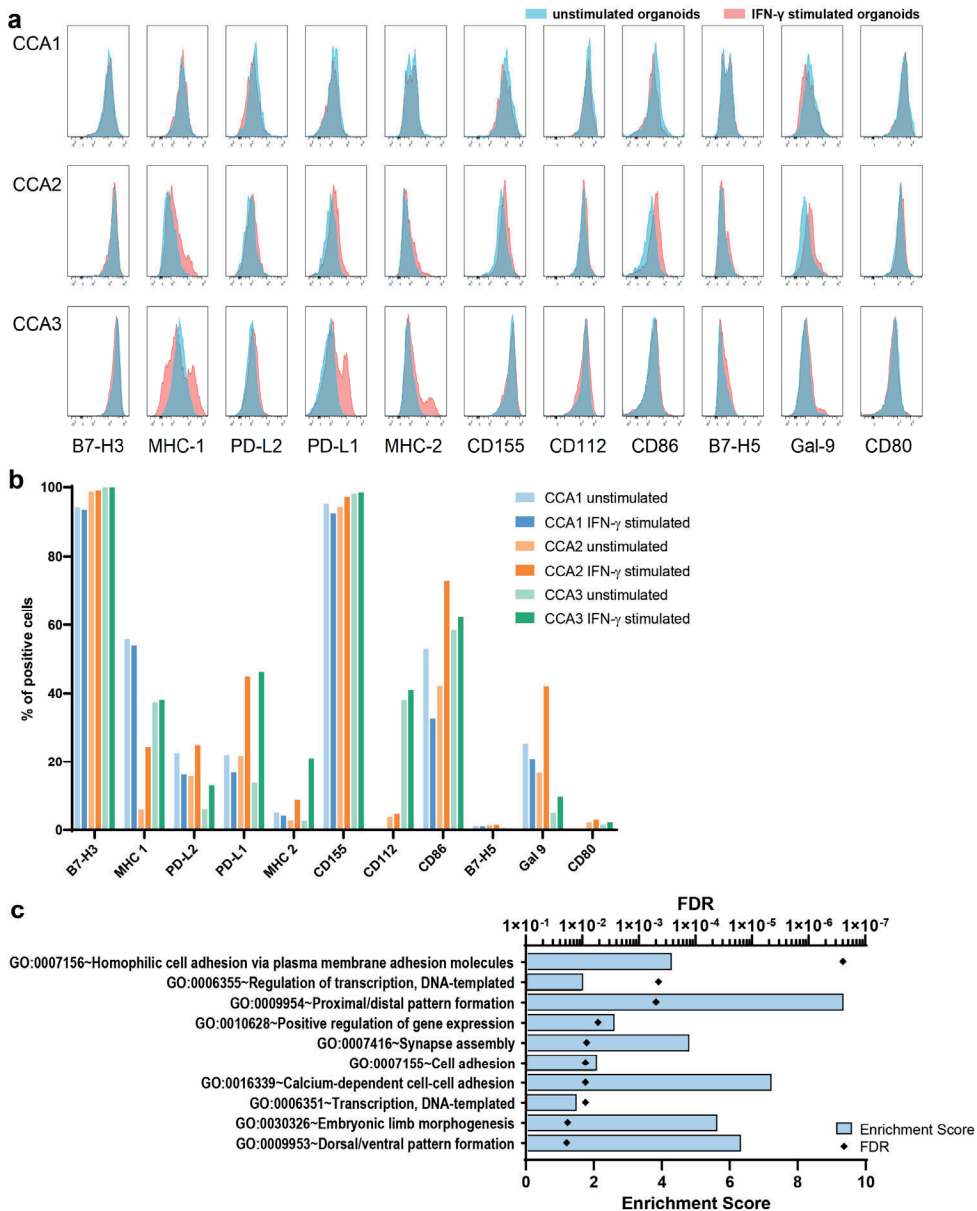


Figure 5. Identifying heterogeneity in immune checkpoint molecule expression and transcriptomics in CCA organoids. Flow cytometry was performed to determine the expression of co-inhibitory and co-stimulatory immune molecules in CCA organoid lines. **(a)** Histograms show expression on three CCA organoid lines without (blue) or with (red) IFN- γ stimulation. **(b)** Results depicted as percentage of cells expressing the proteins in organoids without and with IFN- γ stimulation. **(c)** RNA sequencing data of CCA1 was compared to CCA2 and CCA3 to determine differentially expressed genes. Top 1000 genes with the highest $^2\log$ (fold change) were inserted into the DAVID tool to perform gene set enrichment analysis using the Gene Ontology: Biological Processes (GO:BP) database. The 10 GO:BP with the lowest FDR are displayed. Blue bars represent enrichment scores, black diamonds represent FDR values.

DISCUSSION

CCA is a heterogeneous cancer with a poor prognosis and limited treatment options. Immune therapy is a promising new strategy, and the limited number of clinical trials performed suggest that a subpopulation of CCA patients could benefit from ICI treatment. However, stratification of these patients is challenging. Here, we are the first to establish a co-culture model of CCA organoids and immune cells which could potentially serve as an *in vitro* personalized model to test ICI. This novel 3D co-culture system allows for 1) maintaining the morphology and growth of CCA organoids, 2) survival and function of immune cells, 3) interaction between organoids and immune cells, and 4) quantifiable patient-specific cytotoxic effects of immune cells in CCA organoids. Our work is also the first to demonstrate both cellular contact-based cytotoxicity and soluble factors-mediated cytotoxicity of tumor organoids induced by immune cells.

CCA organoids were cultured with mismatched PBMC which resulted in a variable cytotoxic effect. Addition of IL-2 to the cultures enhanced organoid cell death, demonstrating that immune cell function can be modulated in the newly developed co-culture system. The number of CD4⁺ and CD8⁺ T cells far exceeded the number of NK cells in these cultures. We suspected that T cells might be responsible for the majority of the cytotoxic effect, despite different expression levels of MHC class 1 molecules on the three organoid lines. Therefore, CCA organoids were combined with purified CD3⁺ T cells to analyze their specific effect. This confirmed that T cells have potent cytotoxic effects on most, but not all CCA organoid lines. The stronger killing effect of T cells compared to PBMC was probably caused by higher actual effector cell (T cell)/target cell ratios.

In addition to conventionally used flow cytometric and time-lapse confocal analysis to quantify cell death, we aimed to find an easy, quick and scalable readout by employing a CYFRA quantification assay. The increase in CYFRA determined in the co-culture supernatant of CCA2 with T cells indicates organoid cell death in concordance with flow cytometry and confocal imaging. However, even though similar levels of cell death were found for CCA3 by flow cytometry analysis, there was no clear increase in CYFRA concentration. A possible explanation could be that the number of CCA3 organoid cells in (co-)culture on day seven was too low, which could be attributed to the lower proliferation rate of these organoids or efficient killing by immune cells at an earlier stage. Consequently, the amount of CYFRA released into the supernatant was too low to measure a significant increase.

Besides the effect that immune cells have on cell viability when cultured in direct cellular contact with tumor organoids, we also demonstrated that soluble factors produced by immune cells have an effect on CCA organoid growth. In detail, one of the organoid lines was susceptible to cell death by soluble factors, while the other two organoid lines displayed induced proliferation by TIL conditioned medium. CD8⁺ cytotoxic T cells are known to produce granzymes and perforins to induce apoptosis in cancer cells³⁶, which could explain the cytotoxic effects seen in the organoids. In addition to this, T cells produce a range of cytokines supported by CD4⁺ T helper cells, including TNF- α , IFN- γ and IL-2.³⁷ These cytokines could play a part in the inhibition or stimulation of CCA organoids. It would be

interesting to further investigate what soluble factors specifically cause cell death in some CCA organoids and what soluble factors cause the acceleration of growth in others.

In general, both direct cellular contact with immune cells and soluble factors produced by immune cells seem to induce a marked heterogeneity in CCA patient organoid responses. CCA tumors are known to be notoriously heterogeneous, displaying a wide range of genomic and epigenetic abnormalities and molecular patterns⁴. Therefore, their biological behavior is diverse, and variation in immune cell interactions is to be expected. Studies in which rectal cancer organoids were co-cultured with TIL also showed patient-specific differences in immune killing.²¹ The factors determining effectivity of immune cell-based killing and immunotherapy in patients are complex and poorly understood. To identify contributing factors to the differences in susceptibility to killing of organoids in our co-culture system, we analyzed the protein expression levels of immune co-stimulatory and co-inhibitory molecules and differences in transcriptomes. Although considerable variation in protein expression of immune molecules and response to IFN- γ stimulation was found among the CCA organoid lines, we could not find a direct link to the diversity in response. Gene set enrichment analysis of genes that were expressed in higher levels in CCA1 identified three cell adhesion processes. (Proto)cadherins were the most abundant adhesion genes enriched in these processes. E-cadherin is the best studied cadherin, and is known to interact with dendritic cells, macrophages, NK cells and T cells.³⁸ However, e-cadherin was not found to be overexpressed here and it remains unclear if the identified (proto)cadherins are able to modify immune cells, and, if so, whether they would be stimulatory or inhibitory. This does not provide further evidence helping to explain the described differences in susceptibility to immune cell-related cytotoxicity specifically. Thus, further studies are needed using more patient-derived organoid lines to elucidate mechanisms adopted by CCA organoid cells to evade immune cell killing.

The implementation of immune cells in CCA organoid cultures, which consist of epithelial cancer cells only, has provided an important step towards a more complex representation of the tumor microenvironment. The combination of patient-derived CCA organoids and autologous tumor-infiltrating immune cells potentially provides a patient-specific model to determine which ICI could benefit the patient. Acquisition of matched CCA organoids and PBMC or TIL from large patient cohorts remains challenging. CCA organoid research is still at an early stage, and establishment of confirmed CCA cultures is not successful for all patients, with a reported establishment rate of approximately 36%.³⁹ Moreover, the number of TIL required for the current co-culture protocol demands larger pieces of tumor tissue for isolation, limiting TIL co-cultures to the relatively small subset of CCA patients undergoing surgical resection. Nonetheless, the feasibility of autologous cancer organoid and TIL co-culture has been demonstrated for rectal cancer organoids. In this study, three co-cultures of rectal cancer organoids with TIL were treated with PD-1 antibody pembrolizumab and marked differences in effectivity were observed. No effect was found in one organoid line, temporary improvement was shown for the second, and improved cytotoxicity was only detected in the third organoid line.²¹ This study also revealed that organoids established from patients with a complete pathological response to neo-adjuvant chemoradiotherapy

showed higher sensitivity to TIL-mediated killing *in vitro*, showing evidence of clinical relevance of organoid immune cell co-cultures. Subsequently, studies need to be designed to investigate the predictive value of this *in vitro* model by comparing patient response to ICI to the effect of these ICI in co-cultures of CCA organoids and autologous TIL.

In conclusion, this study provides an optimized and innovative *in vitro* 3D co-culture method in which patient-derived CCA organoids are cultured with immune cells. Assessing cell death using this method demonstrated quantifiable direct and indirect anti-tumor organoid immune responses that vary between CCA organoid lines. As proof of principle, and likely supplemented with patient-specific immune cells, the co-culture method presented in this study could serve as a useful tool to examine the efficacy of new ICI and to predict which, if any, ICI would be most effective in individual patients.

REFERENCES

1. Patel T. Cholangiocarcinoma--controversies and challenges. *Nat Rev Gastroenterol Hepatol*, 2011. 8(4):189-200.
2. Rizvi S, Gores GJ. Pathogenesis, diagnosis, and management of cholangiocarcinoma. *Gastroenterology*, 2013. 145(6):1215-29.
3. Banales JM, Cardinale V, et al. Expert consensus document: Cholangiocarcinoma: current knowledge and future perspectives consensus statement from the European Network for the Study of Cholangiocarcinoma (ENS-CCA). *Nat Rev Gastroenterol Hepatol*, 2016. 13(5):261-80.
4. Banales JM, Marin JGG, et al. Cholangiocarcinoma 2020: the next horizon in mechanisms and management. *Nat Rev Gastroenterol Hepatol*, 2020. 17(9):557-88.
5. Razumilava N, Gores GJ. Cholangiocarcinoma. *Lancet*, 2014. 383(9935):2168-79.
6. Larkin J, Chiarion-Sileni V, et al. Five-Year Survival with Combined Nivolumab and Ipilimumab in Advanced Melanoma. *N Engl J Med*, 2019. 381(16):1535-46.
7. Reck M, Rodriguez-Abreu D, et al. Pembrolizumab versus Chemotherapy for PD-L1-Positive Non-Small-Cell Lung Cancer. *N Engl J Med*, 2016. 375(19):1823-33.
8. Kim RD, Chung V, et al. A Phase 2 Multi-institutional Study of Nivolumab for Patients With Advanced Refractory Biliary Tract Cancer. *JAMA Oncol*, 2020. 6(6):888-94.
9. Klein O, Kee D, et al. Evaluation of Combination Nivolumab and Ipilimumab Immunotherapy in Patients With Advanced Biliary Tract Cancers: Subgroup Analysis of a Phase 2 Nonrandomized Clinical Trial. *JAMA Oncol*, 2020. 6(9):1405-9.
10. Boj SF, Hwang CI, et al. Organoid models of human and mouse ductal pancreatic cancer. *Cell*, 2015. 160(1-2):324-38.
11. Broutier L, Mastrogianni G, et al. Human primary liver cancer-derived organoid cultures for disease modeling and drug screening. *Nat Med*, 2017. 23(12):1424-35.
12. Fujii M, Shimokawa M, et al. A Colorectal Tumor Organoid Library Demonstrates Progressive Loss of Niche Factor Requirements during Tumorigenesis. *Cell Stem Cell*, 2016. 18(6):827-38.
13. Li X, Francies HE, et al. Organoid cultures recapitulate esophageal adenocarcinoma heterogeneity providing a model for clonality studies and precision therapeutics. *Nat Commun*, 2018. 9(1):2983.
14. Sachs N, de Ligt J, et al. A Living Biobank of Breast Cancer Organoids Captures Disease Heterogeneity. *Cell*, 2018. 172(1-2):373-86 e10.
15. van de Wetering M, Francies HE, et al. Prospective derivation of a living organoid biobank of colorectal cancer patients. *Cell*, 2015. 161(4):933-45.
16. Yan HHN, Siu HC, et al. A Comprehensive Human Gastric Cancer Organoid Biobank Captures Tumor Subtype Heterogeneity and Enables Therapeutic Screening. *Cell Stem Cell*, 2018. 23(6):882-97 e11.
17. Koh V, Chakrabarti J, et al. Hedgehog transcriptional effector GLI mediates mTOR-Induced PD-L1 expression in gastric cancer organoids. *Cancer Lett*, 2021. 518:59-71.
18. Tsai S, McOlash L, et al. Development of primary human pancreatic cancer organoids, matched stromal and immune cells and 3D tumor microenvironment models. *BMC Cancer*, 2018. 18(1):335.
19. Marcon F, Zuo J, et al. NK cells in pancreatic cancer demonstrate impaired cytotoxicity and a regulatory IL-10 phenotype. *Oncoimmunology*, 2020. 9(1):1845424.
20. Holokai L, Chakrabarti J, et al. Murine- and Human-Derived Autologous Organoid/Immune Cell Co-Cultures as Pre-Clinical Models of Pancreatic Ductal Adenocarcinoma. *Cancers (Basel)*, 2020. 12(12).
21. Kong JCH, Guerra GR, et al. Tumor-infiltrating lymphocyte function predicts response to neoadjuvant chemoradiotherapy in locally advanced rectal cancer. *JCO Precision oncology*, 2018. 2:1-15.
22. Dijkstra KK, Cattaneo CM, et al. Generation of Tumor-Reactive T Cells by Co-culture of Peripheral Blood Lymphocytes and Tumor Organoids. *Cell*, 2018. 174(6):1586-98 e12.

23. Saito Y, Muramatsu T, *et al.* Establishment of Patient-Derived Organoids and Drug Screening for Biliary Tract Carcinoma. *Cell Rep*, 2019. 27(4):1265-76 e4.
24. Li L, Knutsdottir H, *et al.* Human primary liver cancer organoids reveal intratumor and interpatient drug response heterogeneity. *JCI insight*, 2019. 4(2).
25. Maier CF, Zhu L, *et al.* Patient-Derived Organoids of Cholangiocarcinoma. *Int J Mol Sci*, 2021. 22(16).
26. Nuciforo S, Fofana I, *et al.* Organoid Models of Human Liver Cancers Derived from Tumor Needle Biopsies. *Cell Rep*, 2018. 24(5):1363-76.
27. Lampis A, Carotenuto P, *et al.* MIR21 Drives Resistance to Heat Shock Protein 90 Inhibition in Cholangiocarcinoma. *Gastroenterology*, 2018. 154(4):1066-79 e5.
28. Zhou G, Sprengers D, *et al.* Antibodies Against Immune Checkpoint Molecules Restore Functions of Tumor-Infiltrating T Cells in Hepatocellular Carcinomas. *Gastroenterology*, 2017. 153(4):1107-19 e10.
29. Xu Y, Carrascosa LC, *et al.* An Engineered IL15 Cytokine Mutein Fused to an Anti-PD1 Improves Intratumoral T-cell Function and Antitumor Immunity. *Cancer Immunol Res*, 2021. 9(10):1141-57.
30. Huang da W, Sherman BT, *et al.* Systematic and integrative analysis of large gene lists using DAVID bioinformatics resources. *Nat Protoc*, 2009. 4(1):44-57.
31. Huang da W, Sherman BT, *et al.* Bioinformatics enrichment tools: paths toward the comprehensive functional analysis of large gene lists. *Nucleic Acids Res*, 2009. 37(1):1-13.
32. Chapman MH, Sandanayake NS, *et al.* Circulating CYFRA 21-1 is a Specific Diagnostic and Prognostic Biomarker in Biliary Tract Cancer. *J Clin Exp Hepatol*, 2011. 1(1):6-12.
33. Huang L, Chen W, *et al.* Serum CYFRA 21-1 in Biliary Tract Cancers: A Reliable Biomarker for Gallbladder Carcinoma and Intrahepatic Cholangiocarcinoma. *Dig Dis Sci*, 2015. 60(5):1273-83.
34. Ku NO, Strnad P, *et al.* Keratins: Biomarkers and modulators of apoptotic and necrotic cell death in the liver. *Hepatology*, 2016. 64(3):966-76.
35. Alam A, Cohen LY, *et al.* Early activation of caspases during T lymphocyte stimulation results in selective substrate cleavage in nonapoptotic cells. *J Exp Med*, 1999. 190(12):1879-90.
36. Farhood B, Najafi M, *et al.* CD8(+) cytotoxic T lymphocytes in cancer immunotherapy: A review. *J Cell Physiol*, 2019. 234(6):8509-21.
37. Borst J, Ahrends T, *et al.* CD4(+) T cell help in cancer immunology and immunotherapy. *Nat Rev Immunol*, 2018. 18(10):635-47.
38. Yu W, Yang L, *et al.* Cadherin Signaling in Cancer: Its Functions and Role as a Therapeutic Target. *Front Oncol*, 2019. 9:989.
39. van Tienderen GS, Li L, *et al.* Hepatobiliary tumor organoids for personalized medicine: a multicenter view on establishment, limitations, and future directions. *Cancer Cell*, 2022.

SUPPLEMENTARY INFORMATION

SUPPLEMENTARY MATERIALS AND METHODS

Organoid culture

In short, biopsies were washed in Advanced DMEM/F12 (Gibco), minced, and digested using a 2.5 mg/ml collagenase A solution (Sigma Aldrich). The cell suspension was strained through a 70 µm strainer, cells were washed in Advanced DMEM/F12 and plated in 75% BME (Cultrex, diluted in Advanced DMEM/F12). Until splitting, organoids were maintained in classical organoid initiation medium as described by Huch *et al.*¹ After the first split, culture was continued in organoid expansion medium (OM) which was refreshed twice a week. Organoids were passaged in 1:3 to 1:10 split ratios once a week. Exact medium composition can be found in Supplementary Table S2.

Co-culture assay for immune cell analysis

PBMC were thawed 2-3 days in advance at 37°C, then resuspended and cultured in TM either with or without anti-human CD3/CD28 dynabeads at a 1:20 bead:cell ratio, in the presence of 20 IU/ml (4 ng/ml) IL-2. On the day of co-culture, organoids were harvested, mechanically broken, and dissociated into single cells by TrypLE Express incubation (3-5 cycles of 5 minutes at 37°C). PBMC were harvested, counted, and either cultured alone or combined with organoid single cells at a 50000:25000 = 2:1 ratio. They were resuspended in 200 µL OM-nic with 10% human serum and plated in a 96-well round-bottom plate. 100 IU/ml (20 ng/ml) IL-2 was added to some conditions, and 5 µg/mL brefeldin (Sigma) and 1:1000 monensin (eBioscience Invitrogen) were added to all conditions. After 19 hours, cells were washed, stained with fixable viability dye eFluor 506 first and then anti-EpCAM, anti-CD45, anti-CD3, anti-CD8 and anti-CD4, followed by intra-cellular staining of IFN-γ and TNF-α using the Foxp3 staining buffer set.

Effect of BME on T cells

PBMC from healthy donors were thawed at 37°C, then resuspended and cultured in TM with anti-human CD3/CD28 dynabeads at a 1:100 bead:cell ratio, in the presence of 20 IU/ml (4 ng/ml) IL-2. After three days, PBMC were harvested, counted and resuspended in 200 µL OM-nic with 10% human serum, in the presence or absence of 10% BME. They were plated in a 96-well flat-bottom suspension plate. After three and seven days, respectively, PBMC were harvested and stained with fixable viability dye eFluor 506. Cell surface staining was then performed with anti-CD45, anti-CD8, anti-CD4, anti-CD3, anti-HLA-DR and anti-CD137 antibodies (Suppl. Table S3). For Ki-67 staining, cells were fixed and permeabilized using the Foxp3 staining buffer set. PBMC were measured using a FACSCanto II flow cytometer and analyzed using FlowJo software.

Confocal time-lapse imaging settings and analysis

The blue nuclear Hoechst 33342 staining, green caspase 3/7 probe and CellTrace Far Red were sequentially imaged using 405, 488 and 640 nm solid state lasers for excitation and detected at 435-480, 500-550 and 650-760 nm, respectively. An additional bright field

channel was included. For 180 hours, every 6 hours 9 z-stacks of 7 planes with 7.4 μm interval were imaged covering 9 times 1284550 μm^2 and 44.4 μm in height.

Maximum projections of the z-stacks were analyzed with a custom analysis pipeline in the Opera Phenix Harmony PhenoLOGIC software (Perkin Elmer). In short, organoids were segmented based on the combined Hoechst and green caspase signals. Within the segmented organoid area, the percentage surface area of dead cells was determined using the green caspase 3/7 probe channel, reflecting the level of cell death within the individual organoids. T cells were detected using the far-red signal.

TIL isolation

Single cell suspensions from tumors and tumor-free liver tissues were obtained by tissue digestion as described previously.² Briefly, fresh tissues were first cut into small pieces, and then digested with 0.125 mg/mL collagenase IV (Sigma-Aldrich), 0.2 mg/mL DNase I (Roche), 1000 IU/ml hyaluronidase (Sigma), and 0.05% FCS in Hanks' Balanced Salt solution with Ca^{2+} and Mg^{2+} (Sigma) for 30-60 minutes at 37 °C with continuous stirring. Cell suspensions were filtered through 100 μm pore cell strainers (BD Biosciences) and mononuclear immune cells were obtained by Ficoll density gradient centrifugation. Viability, cell count and purity were determined by trypan blue exclusion and MacsQuant (Miltenyi).

Preparation of conditioned media from PBMC and TIL

PBMC from healthy donors or TIL from CCA or hepatocellular carcinoma patients were thawed at 37°C, then resuspended and cultured in the presence or absence of anti-human CD3/CD28 dynabeads at a 1:100 bead:cell ratio at a concentration of $0.5\text{-}1 \times 10^6$ cells/ml OM-nic with 10% human serum. OM-nic with 10% human serum without cells was used as control medium. Conditioned medium was collected on day six and stored at 4°C until the next day or frozen at -20°C until later use. On the day of use, the conditioned medium and control medium were concentrated 10-fold by centrifugation at 3100-3200 g for 30-40 minutes at 20°C using 3KDa centrifugal filters (Amicon Ultra 3K device-3000MWCO).

RNA sequencing

RNA from three CCA organoid lines was collected in Qiazol lysis buffer (Qiagen) and isolated using the miRNeasy mini kit (Qiagen) according to manufacturer's instructions. Subsequently, RNA sequencing was performed by Novogene, which resulted in approximately 20-30 million, paired-end reads. The sequencing data were uploaded to the Galaxy Web platform public server usegalaxy.org.³ Next, the data were trimmed for adapters using Trim Galore! (version 0.4.3.1), and mapped using RNA STAR (version 2.6.8a) against the human reference genome GRCh38. By applying the built-in hg38 genome annotation file, mapped reads were translated into raw counts using FeatureCounts (version 2.0.1).

TABLES

Supplementary Table S1. Patient characteristics

	CCA1	CCA2	CCA3
Type of CCA	Perihilar	Intrahepatic	Intrahepatic
Sex	Female	Female	Male
Age	34	77	60
Pre-treatment	None	None	None
Etiology	PSC	Unknown	Unknown
Tumor stage (TNM)	T2N2M0	T3N1M0	T1NXM0
Tumor differentiation	Moderate	Moderate to poor	Well to moderate
Fibrosis/Cirrhosis	No	No	No
Gamma-GT ^a	546	68	93
AP ^a	1831	73	74
Bilirubin ^a	13	8	5
CA19.9 ^b	42	18	64
AFP ^b	5	4	-
CEA ^b	-	45.8	-

^aDetermined 2-4 weeks before surgery. ^bDetermined 4-6 weeks before surgery. Gamma-GT = gamma-glutamyltransferase; AP = alkaline phosphatase; CA19.9 = cancer antigen 19.9; AFP = alpha fetoprotein; CEA = carcinoembryonic antigen.

Supplementary Table S2. Organoid media compositions

Medium component	Manufacturer	Initiation medium	Expansion medium (OM)
Advanced DMEM/F12	Gibco		
HEPES	Life Technologies	10 mM	10 mM
Ultraglutamine	Lonza	2 mM	2 mM
Pen/strep	Life Technologies	100 U/ml	100 U/ml
Primocin	InvivoGen	0.5 mg/ml	0.5 mg/ml
N2 supplement	Gibco	1%	1%
B27 supplement (without vitamin A)	Gibco	2%	2%
Gastrin I	Sigma-Aldrich	10 nM	10 nM
FGF10	Peptotech	100 ng/ml	100 ng/ml
HGF	Peptotech	25 ng/ml	25 ng/ml
EGF	Peptotech	50 ng/ml	50 ng/ml
A8301	Tocris	5 μM	5 μM
Nicotinamide	Sigma-Aldrich	10 nM	10 nM
Forskolin	Tocris	10 μM	10 μM
N-Acetyl Cystein	Sigma-Aldrich	1 mM	1 mM
R-spondin-1 conditioned medium	Self-produced	10%	10%
Noggin conditioned medium	Self-produced	10%	
Wnt3a conditioned medium	Self-produced	30%	
Y27632	Tocris	10 μM	
hES cell cloning recovery solution	Stemgent	2 μM	

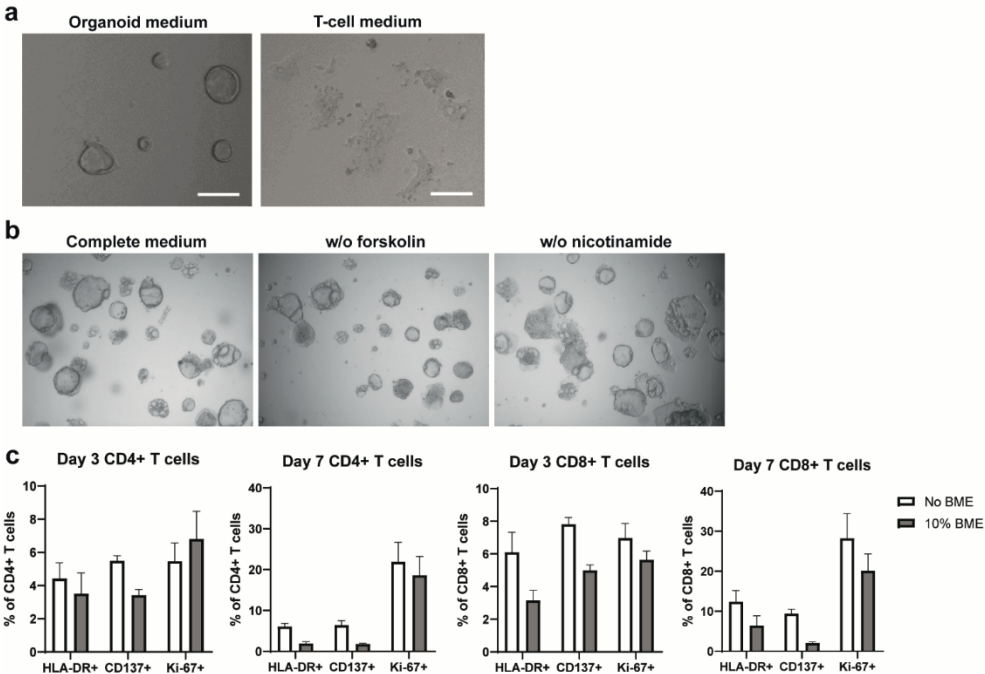
Supplementary Table S3. Anti-human antibodies and reagents used for flow cytometry staining

Antibody / Reagent	Clone	Isotype	Supplier
CD56-FITC	TULY56	mlgG1	eBioscience-Thermo Fisher Scientific
CD8-PE	RPA-T8	mlgG1, k	Biolegend
CD326 (EpCAM)-PerCP-eF710	1B7	mlgG1	eBioscience-Thermo Fisher Scientific
CD45-APC-Fire750	HI30	mlgG1,k	Biolegend
CD14-BV510	M5E2	mlgG2a,k	Biolegend
CD3 PE-Cy7	UCHT1	mlgG1,k	eBioscience-Thermo Fisher Scientific
CD45-APC-eFluor780	HI30	mlgG1,k	eBioscience-Thermo Fisher Scientific
CD8a-PE	OKT8	mlgG2a	eBioscience-Thermo Fisher Scientific
CD4-APC-eFluor780	OKT4	mlgG2b,k	eBioscience-Thermo Fisher Scientific
CD45-APC	HI30	mlgG1,k	Biolegend
CD4-FITC	Oct-04	mlgG2b,k	Biolegend
CD4 PE	13B8.2	mlgG1	Beckman
HLA-DR-PerCP-Cy5.5	LN3	mlgG2b	eBioscience-Thermo Fisher Scientific
CD137 (4-1BB)-APC	4B4-1	mlgG1,k	BD Pharmingen
CD8-eFluor450	RPA-T8	mlgG1,k	eBioscience-Thermo Fisher Scientific
CD45-APC-eFluor780	HI30	mlgG1,k	eBioscience-Thermo Fisher Scientific
Ki67-FITC	B56	mlgG1,k	BD pharmingen
CD4 PerCP-Cy5.5	SK3	mlgG1	B&D
HLA-DR-PE	LN3	mlgG2b	eBioscience-Thermo Fisher Scientific
Ki67-FITC	20Raj1	mlgG1,k	eBioscience-Thermo Fisher Scientific
CD273 (B7-DC)-PE	MIH18	mlgG1	eBioscience-Thermo Fisher Scientific
HLA-A,B,C-FITC	W6/32	mlgG2a,k	Biolegend
CD274(B7-H1)-PE-Cy7	MIH1	mlgG1	eBioscience-Thermo Fisher Scientific
CD276(B7-H3)-APC	7-517	mlgG1,k	eBioscience-Thermo Fisher Scientific
HLA-DR, DP, DQ-FITC	Tü39	miGG2a,k	Biolegend
CD155-PE	2H7CD155	mlgG1	eBioscience-Thermo Fisher Scientific
CD112-PECy7	TX31	mlgG1	Biolegend
CD274 (B7-H1)-APC	MIH1	mlgG1	eBioscience-Thermo Fisher Scientific
Vista(B7-H5)-AlexaFluor488	#730804	mlgG2b	R&D systems
Galectin-9 PE	9M1-3	mlgG1,k	Biolegend
CD80-PE-Cy7	2D10	mgG1,k	Biolegend
CD86 APC	IT2.2	mlgG2b,k	Biolegend
IFN-gamma-APC-R700	B27	mlgG1,k	BD Biosciences
TNFa-FITC	MAB11	mlgG1,k	eBioscience-Thermo Fisher Scientific
Human Fc block			BD Biosciences
Annexin V apoptosis detection kit APC			eBioscience -Thermo Fisher Scientific
DAPI			Biolegend
Fixable viability dye eFluor 506			eBioscience-Thermo Fisher Scientific

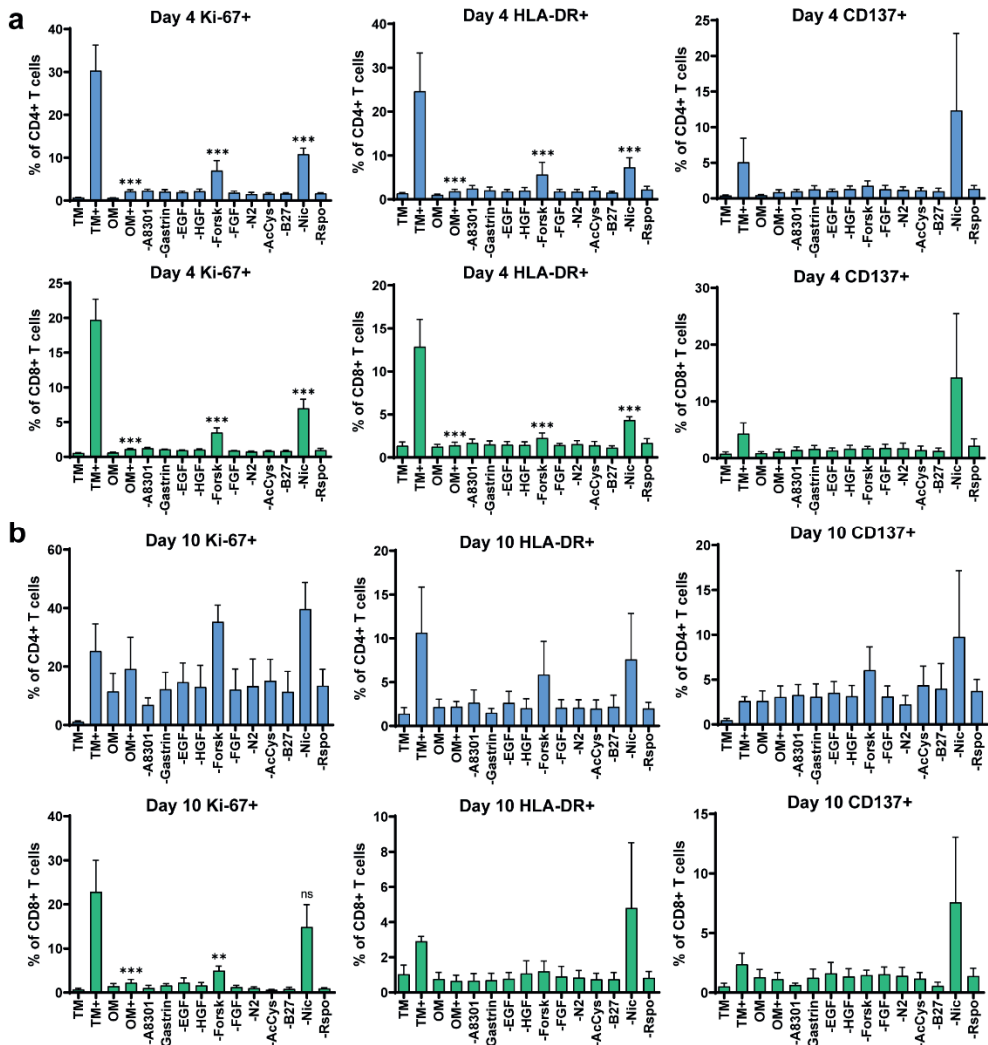
Supplementary Table S4. Genes identified in the set of 1000 upregulated genes in CCA1 that are part of the cell adhesion-related biological processes

GO:0007156	GO:0007155	GO:0016339
RET	FBLN7	NLGN1
PCDHGB7	SRPX	PCDHGB4
TENM3	NLGN1	PCDHB16
PCDHGB5	COL16A1	PCDHB6
PCDHGB4	PCDHGB4	PCDHB5
PCDH10	PCDH10	PCDHB13
PCDH17	TGFB11	PCDHB3
ROBO1	ITGB2	CDH16
CDH7	NID2	PCDHB11
PCDHA1	THBS4	
PCDHA3	PCDH17	
PCDHA2	ROBO1	
PCDH9	PCDHA1	
PCDHGA3	CHST10	
PCDHGA2	PCDHA3	
PCDH20	CTNNA3	
PCDHGA1	PCDHA2	
PCDHB15	MPDZ	
PCDHB13	EDIL3	
PCDHB11	IL32	
PCDHGA10	MYBPC1	
PCDHGA11	CD72	
PCDHGA12	AMBP	
PCDHB16	PCDHB15	
PCDHB6	PCDHB11	
PCDHB5	CLDN10	
PCDHB3	BCAM	
FAT4	MMRN1	
CDH16	PTK7	
PCDHB8	ADGRB1	
	PCDHB6	
	CASS4	
	CERCAM	
	ANOS1	
	CNTN1	
	CNTN3	
	SPACA4	
	PCDHB3	
	ITGA5	
	CDH16	
	EPHA3	
	ITGA9	

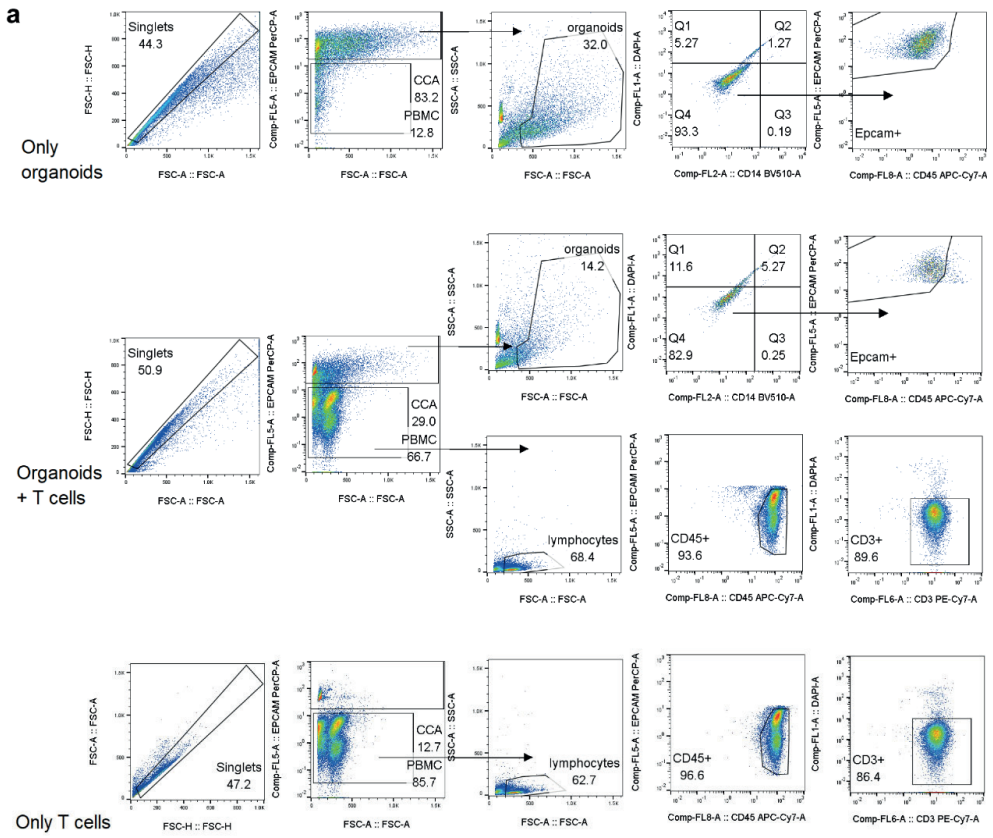
SUPPLEMENTARY FIGURES



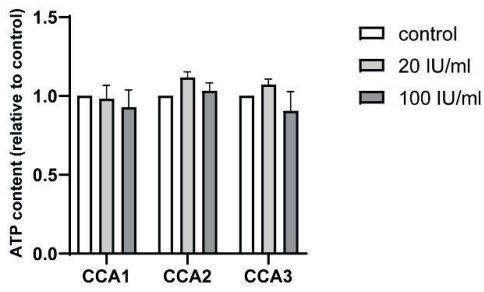
Suppl. Figure S1. Additional evaluation of the effect of different medium compositions on CCA organoids. (a) Bright field images demonstrate that CCA organoids cultured in T cell medium (TM) don't retain the morphology they have in organoid medium (OM). (b) CCA organoids were not affected by the removal of either forskolin or nicotinamide from the organoid medium as shown by bright field images. (c) PBMC were pre-activated for three days, then cultured in OM without nicotinamide with 10% human serum, in the presence or absence of 10% BME. Flow cytometric analysis for HLA-DR, CD137 and Ki-67 expression in CD4⁺ and CD8⁺ T cells at day three and day seven of PBMC culture (n=3 biological replicates from different PBMC donors). Scalebar: 100 μm (a), 500 μm (b). All values with error bars represent mean with SEM.



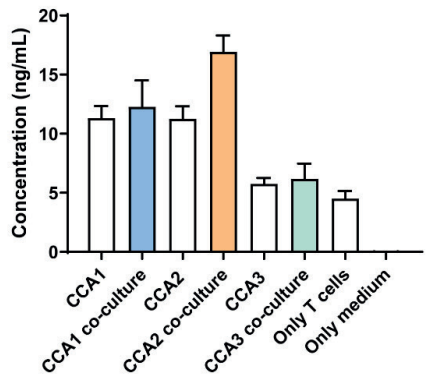
Supplementary Figure S2. Effect of organoid medium components on T cells. (a, b) Flow cytometric analysis shown for Ki-67, HLA-DR and CD137 expression in CD4⁺ and CD8⁺ T-cells at day four (a) and day ten (b) of culture in T cell medium without and with anti-CD3/CD28 coated beads (TM, TM+), organoid medium without and with anti-CD3/CD28 coated beads (OM, OM+), and organoid medium without specified components in the presence of anti-CD3/CD28 coated beads (n=3 biological replicates from different PBMC donors). Statistical significance is depicted for OM+, -Forsk and -Nic compared to TM+. Removal of forskolin or nicotinamide is less effective in reversing the inhibition caused by OM+ compared to TM+ on day four compared to day seven (Fig. 1D). All values with error bars represent mean with SEM. ** p < 0.01, *** p < 0.001.



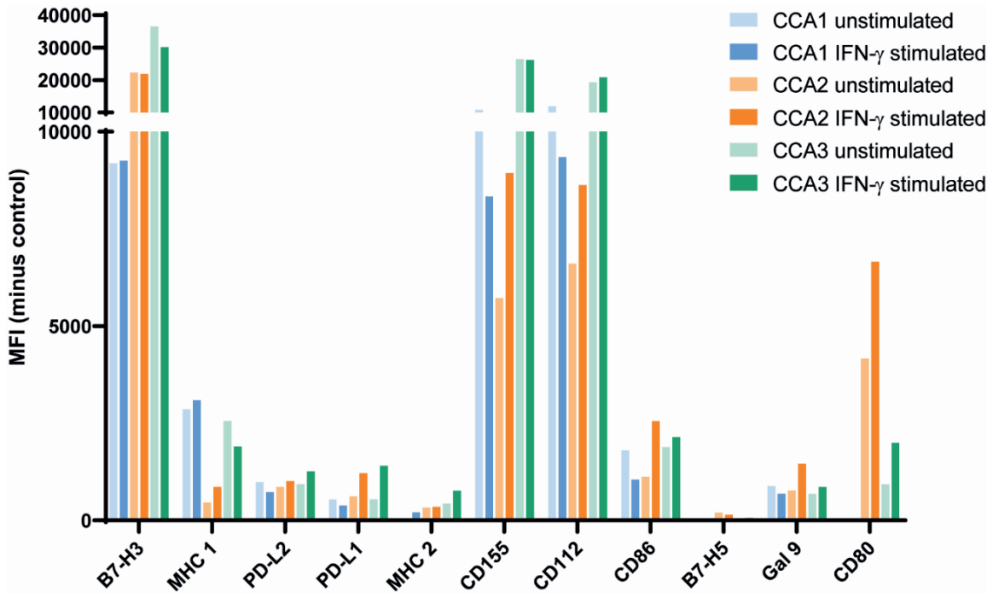
b IL-2 effect on organoids



c CYFRA



Supplementary Figure S3. Analysis pipeline for co-culture flow cytometry data and effect of IL-2 on CCA organoid viability. (a) Flow cytometry dot plots show the gating strategy of co-culture experiments. Live organoid cells were gated on single cells, EpCAM⁺, DAPI⁻, CD14⁻ and CD45⁻, and live T cells were gated on single cells, EpCAM⁺, CD45⁺, DAPI⁻ and CD3⁺. **(b)** ATP quantification of CCA organoids cultured in organoid medium supplemented with 0, 20 IU/ml (4 ng/ml) or 100 IU/ml (20 ng/ml) IL-2 (n=3 technical replicates) demonstrates IL-2 has no effect on organoid viability. **(c)** Quantification of CYFRA in supernatant after seven days of CCA organoid and T cell co-culture. All values with error bars represent mean with SEM.



Supplementary Figure S4. Differences in expression of co-inhibitory and co-stimulatory immune molecules in CCA organoids. Flow cytometry for the expression of co-inhibitory and co-stimulatory molecules in CCA organoid lines without and with IFN- γ stimulation. Depicted as median fluorescence intensity (MFI) after subtraction of the control values.

SUPPLEMENTARY INFORMATION REFERENCES

1. Huch M, Gehart H, *et al.* Long-term culture of genome-stable bipotent stem cells from adult human liver. *Cell*, 2015. 160(1-2):299-312.
2. Zhou G, Sprengers D, *et al.* Reduction of immunosuppressive tumor microenvironment in cholangiocarcinoma by ex vivo targeting immune checkpoint molecules. *J Hepatol*, 2019. 71(4):753-62.
3. Afgan E, Baker D, *et al.* The Galaxy platform for accessible, reproducible and collaborative biomedical analyses: 2016 update. *Nucleic Acids Res*, 2016. 44(W1):W3-W10.

CHAPTER

6

Extracellular matrix drives tumor organoids toward desmoplastic matrix deposition and mesenchymal transition

Gilles S. van Tienderen¹, Ruby Lieshout^{1*}, Oskar Rosmark^{2*}, Jorke Willemse¹, Floor de Weijer¹, Linda Elowsson Rendin², Gunilla Westergren-Thorsson², Michael Doukas³, Bas Groot Koerkamp¹, Martin E. van Royen³, Luc J.W. van der Laan¹, and Monique M.A. Verstegen¹

**These authors contributed equally*

¹Erasmus MC Transplant Institute, Department of Surgery, Erasmus University Medical Center, Rotterdam, The Netherlands

²Lung Biology, Department of Experimental Medical Science, Lund University, Lund, Sweden

³Department of Pathology, Erasmus MC Cancer Institute, Erasmus University Medical Center, Rotterdam, The Netherlands

ABSTRACT

Patient-derived tumor organoids have been established as promising tools for *in vitro* modelling of multiple tumors, including cholangiocarcinoma (CCA). However, organoids are commonly cultured in basement membrane extract (BME) which does not recapitulate the intricacies of the extracellular matrix (ECM). We combined CCA organoids (CCAOs) with native tumor and liver scaffolds, obtained by decellularization, to effectuate a model to study the interaction between epithelial tumor cells and their surrounding ECM. Decellularization resulted in removal of cells while preserving ECM structure and retaining important characteristics of the tissue origin, including stiffness and presence of desmoplasia. The transcriptome of CCAOs in a tumor scaffold much more resembled that of patient-paired CCA tissue *in vivo* compared to CCAOs cultured in BME or liver scaffolds. This was accompanied by an increase in chemoresistance to clinically-relevant chemotherapeutics. CCAOs in decellularized scaffolds revealed environment-dependent proliferation dynamics, driven by the occurrence of epithelial-mesenchymal transition. Furthermore, CCAOs initiated an environment-specific desmoplastic reaction by increasing production of multiple collagen types. In conclusion, convergence of organoid-based models with native ECM scaffolds will lead to better understanding of the *in vivo* tumor environment.

INTRODUCTION

Cholangiocarcinoma (CCA) is a highly aggressive tumor which arises from the biliary duct epithelium. It is associated with a low 5-year survival rate, due to its biological complexity, late-stage diagnosis, and limited treatment options.¹ This malignant phenotype is related to the complex interplay between cells, both primary and stromal/immune, and extracellular matrix. Particularly in CCA, the dysregulation of the extracellular environment through extracellular matrix (ECM) remodeling, characterized by desmoplasia, is a vital aspect of cancer progression.² Understanding the biology behind the interaction of primary tumor cells with their tissue microenvironment may lead to more effective targeted therapies for cancer patients.

However, clinical translation of basic research on this topic is hindered by several obstacles. An intrinsic limitation often found in experimental systems is the lack of faithful recapitulation of interpatient cellular heterogeneity, a particularly important issue in CCA.³ Thus, to capture the underlying mechanisms at play, it is crucial to use primary patient-modelling cancer cells and ECM. CCA organoids (CCAO) have been successfully established and have demonstrated to be promising *in vitro* patient-specific tumor models.⁴ Until now, organoid-based research has focused on expanding the possibilities of obtaining CCAOs, performing high throughput drug screening, and identifying cancer gene functionality.^{5, 6} However, these organoids have an inherent limitation since they consist solely of epithelial-sourced cells. More recently, multiple studies have combined tumor organoids with components of their tumor micro-environment, including immune and stromal cells.^{7, 8} Although very useful, these models lack native tissue structures and ECM components that are typically associated with CCA. The chemical and mechanical cues from the ECM are key drivers in various crucial aspects of cancer, including initiation, progression, and metastasis.⁹ Decellularization techniques have allowed for the isolation of native patient-derived extracellular matrix with preserved tissue architecture^{10, 11}, providing a source for more physiologically accurate scaffolds. Several studies using decellularized material have primarily used cancer cell lines to model cellular behavior, limiting applicability.¹²⁻¹⁴ Thus, combining tumor organoids with ECM could elucidate more about the role of primary epithelial cells in the remodeling of ECM within CCA.

Here, we describe an *in vitro* model using patient-derived CCAOs in combination with decellularized CCA matrix (CCA-M) and tumor-free liver matrix (TFL-M) to study the interaction of tumor cells with their surrounding ECM. The scaffolds retain many of the physiological environmental cues of the (tumor) microenvironment. Our results show that CCA-M induces a transcriptome profile closely resembling *in vivo* patient tumor tissue with an accompanying chemo resistance in CCAOs. Furthermore, migration and proliferation dynamics are environment-specific, and related to the induction of epithelial-mesenchymal transition (EMT). Lastly, primary epithelial tumor cells can, in the absence of desmoplasia, initiate a desmoplastic reaction through increased collagen production (e.g. COL1A1, COL3A1, COL6A3), while, in the presence of desmoplasia, produce a distinct ECM-related protein signature linked to patient survival.

MATERIALS AND METHODS

Sample procurement for decellularization and organoid initiation

Cholangiocarcinoma (CCA) tumor specimens (n=9 in total, of which n=3 for CCAOs, including n=2 intrahepatic CCA and n=1 perihilar CCA) were obtained from patients who underwent a curative-intent surgical resection. All resections were performed at the Erasmus MC in Rotterdam. Use of tissue for research purposes was approved by the Medical Ethical Council of the Erasmus MC and written informed consent was given by all patients (MEC-2013-143). Tumor-free liver (TFL) specimens were obtained from patients who underwent liver transplantation (MEC-2014-060) or from postmortem liver donations that were unsuitable for transplantation, but with consent for research (MEC-2012-090). Samples were confirmed to be tumor or non-tumorous with histopathological assessment. All samples were stored at 4°C in Belzer UW cold storage solution (UW, Bridge to Life) and processed within 24 hours after collection when used for organoid initiation, or at a later stage when used for decellularization.

Initiation and propagation of cholangiocarcinoma organoids (CCAOs)

Organoid initiation was as previously described.⁴ In short, biopsies were minced and digested in 2.5 mg/ml collagenase type A (Sigma) for 30-120 min at 37°C. The duration of digestion depended on the amount of desmoplasia and/or fibrosis present in the biopsy. Digestion was continued until no visible pieces of tissue remained. Subsequently, the cell suspension was strained (100 µm cell strainer) and washed in cold Advanced DMEM/F12. After centrifugation (453g, 5 min, 4°C), the cell pellet was resuspended in basement membrane extract (BME, Cultrex). The mixture of cells and BME was plated in droplets in 24- or 48-well suspension culture plates (Greiner). BME was allowed to solidify at 37°C for 30–45 min before addition of startup medium (SEM, Table S1). Medium was refreshed every 3 to 4 days. After the first passaging, SEM was replaced by expansion medium (EM, Table S2). Organoids were passaged in 1:3 to 1:6 ratios approximately every 7 days depending on their rate of proliferation. Passaging was done with mechanical dissociation of organoid fragments and BME and subsequent re-plating of organoid fragments in fresh BME. CCA organoids were confirmed to be tumorigenic by xenografting and mutational analysis (Table S5).

Decellularization procedure of human patient-derived tissue

Both CCA and TFL tissue were washed with dH₂O to remove traces of blood or debris. Subsequently, tissue samples underwent a freeze-thaw cycle to disrupt cell membranes through formation of intra-cellular ice crystals. Uniform sized tissue samples were made using a 6 mm diameter biopsy punch resulting in small cylinders of approximately 2-10 mm in height. All tissue samples, regardless of origin or method of retrieval, were decellularized with a solution consisting of 4% Triton-X-100 and 1% NH₃ (hereafter referred to as TX-100 solution) and subsequent DNase treatment. Cylindrical tissue samples were placed on a magnetic stirrer (1500 RPM) at room temperature (RT). TX-100 solution was replaced every 1h for a total of 10 cycles, which resulted in the tissues showing a translucent, white

appearance. TX-100 solution was washed out of the cylindrical tissue samples with dH₂O for a minimum of 1h. Lastly, tissues were incubated with DNase solution (10mg/ml DNase type I (Sigma) in 0.9% NaCl + 100mM CaCl₂ + 100mM MgCl₂) for 4h at 37°C. Alternatively, whole liver decellularization (only in case of research livers) with TX-100 solution and subsequent DNase treatment occurred according to previously published protocol.¹⁵ Biopsy samples were taken before and after decellularization for histological and DNA content analysis.

Confirmation of decellularization procedure

Biopsies were fixed in 4% paraformaldehyde (PFA, Fresenius Kabi), and subsequently embedded in paraffin, sectioned at 4 μm, and stained with 4',6-diamidino-2-phenylindole (DAPI, Vectashield, Vectorlabs) or Hematoxylin-Eosin (H&E) according to standard procedures. Slides were imaged with a Zeiss Axioskop 20 microscope and captured with a Nikon DS-U1 camera or, if stained with DAPI, analyzed using an EVOS microscope (Thermo Fisher Scientific). Additionally, DNA extraction from patient tissue samples, before and after decellularization, was done using a QIAamp DNA Mini Kit (Qiagen) according to manufacturer's instructions. Subsequently, total DNA yield was measured using a NanoDrop spectrophotometer (Thermo Fisher Scientific). Lastly, the quality and length of base pairs for DNA was measured using a 2100 BioAnalyzer (Agilent technologies) with a DNA-1000 kit (Agilent Technologies).

Biochemical characterization of decellularized matrices

Total collagen was measured using a total collagen kit (QuickZyme biosciences) according to manufacturer's protocol. An infinite M nano plate reader (TECAN) was used to measure absorbance at 570 nm. For glycosaminoglycan (GAG) content, a GAG assay kit (Bicolor) was used according to manufacturer's protocol. Before the assay, samples were digested at 65C with a papain solution (10mg/ml, Sigma) for 8h. In this case, absorbance was measured with a Model 680 XR Microplate Reader (Bio-Rad) at 680 nm.

Mechanical characterization of decellularized matrices

The stiffness of CCA-M and TFL-M tissue before and after decellularization was assessed with nanoindentation measurements using a PIUMA Nanoindenter (Optics11). Tissue slices (approx. 2mm height) were cut and kept in PBS at -20°C until further analysis. To start, cyanoacrylate adhesive was used to attach the CCA-M and TFL-M slices to a petri dish, after which the slices were submerged in PBS. Each sample was measured at 3 different locations, with each location being measured in a 3x3 grid with a distance between measuring points of 100 μm. An indentation speed of 2.5 μm/s was used with a total indentation depth of 10 μm. Each indentation was measured in triplicate. Measurements for which no point of contact could be determined or were discarded. The analysis was performed in the Dataviewer software (Piuma) which used the Hertzian contact model to calculate the elastic moduli from the force-distance curves. Comparison between groups was made by Mann-Whitney U Test.

Preparation of decellularized matrices for organoid culture

Decellularized tissues were embedded in optical cutting temperature (OCT) compound, mounted on a metal holder, and cut with a cryotome (Leica) at -15°C into $200\ \mu\text{m}$ thick scaffolds that were collected in a 50mL tube and kept frozen until further use. One day before recellularization, scaffolds were washed with sterile PBS three times at RT. This was followed by an additional wash with Advanced DMEM/F12 and incubated overnight at 37°C in Advanced DMEM/F12 supplemented with 10x concentration of Penicillin, streptomycin, and Primocin to minimize infections occurring from pathogens that may have been present in the tissue. Next, CCA matrix (CCA-M) and TFL matrix (TFL-M) scaffolds were washed in Advanced DMEM/F12 three times before CCAO addition.

Recellularization

CCAOs ($n=3$) grown in BME droplets were washed in ice cold advanced DMEM/F12 to separate the cells from the BME. Next, they were dissociated to single cells and small aggregates of cells with TrypLE (Thermo Fisher Scientific) for 15 minutes at 37°C while applying mechanical disruption thrice during the 15 minutes. TrypLE was inactivated by adding cold AdvDMEM/F12 and cells were centrifuged for 5 minutes (4°C at 453g) before being counted using TrypanBlue (Thermo Fisher Scientific). The resulting cell pellet was resuspended in EM supplemented with $10\ \mu\text{M}$ Y27632 at a concentration of 1.5×10^5 cells/ $5\ \mu\text{l}$. The small volume ($5\ \mu\text{l}$) per scaffold ensures relatively high cell adherence due to the scaffold absorbing the medium containing the cells. The source of scaffolds and organoids used for each experiment can be found in the corresponding figure legend. The samples were incubated at 37°C for 2 h before $300\ \mu\text{l}$ EM supplemented with $10\ \mu\text{M}$ Y27632 was added to the wells. EM+Y27632 was replaced with EM after 3 days and medium was refreshed every 3 or 4 days. Standard organoid cultures in BME served as a control.

Cell metabolic activity assessment

To assess metabolic activity of CCAOs in the different environments, Presto Blue Cell Viability Reagent (Thermo Fisher Scientific) was used at multiple time points for the same sample. Day 1 was measured at 24 hours after seeding. Presto Blue compound was diluted 1:10 in EM. The scaffolds were incubated in the dark at 37°C , 5% CO_2 for 4 hours. After incubation, the medium was plated in triplicate in a 96 wells plate. The absorbance was recorded with excitation of 530nm and emission of 590nm using an Omega POLARstar Microplate reader (BMG labtech). Empty scaffolds without cells were used for calculating background absorbance. Background was subtracted and data was normalized to day 1.

GFP-tagging of CCAOs

CCAOs were transduced using lentivirus produced from a 3th generation single constitutive promoter (EF1) lentivector for the dual expression of CRed2 and copGFP (SBI, Sanbio).¹⁶ Organoids were harvested and dissociated to smaller fragments by vigorous pipetting in cold advanced DMEM/F12. Organoid fragments were transferred to a 24-wells plate for stable transduction using $500\ \mu\text{l}$ of virus supernatant, supplemented with polyethylenimine (PEI, 1:1000, Invitrogen) and $500\ \mu\text{l}$ EM. The organoid fragments were spinoculated at 32°C , for

60 min at 800 rpm. After this, the plate was transferred to 37°C for 6 hours after which the fragments were re-plated in BME to form organoids. Transduction efficiency was determined by GFP detection using a fluorescence microscope and subsequently sorted based on copGFP positivity to create a homogenous population.

Immunofluorescent staining

To evaluate localization of protein abundance, immunofluorescent staining was performed combined with whole mount confocal microscopy. All samples were fixed for 10 minutes using 4% PFA and permeabilized with 0.1% Triton X-100 diluted in PBS for 15 minutes. Subsequently, samples were exposed to 10% serum diluted in 1% BSA-PBS to prevent nonspecific antibody binding. Primary antibodies (Vimentin 1:100, Bio-connect; Zonula Occludens-1 (ZO-1) 1:100, ProteinTech; Keratin 7 (KRT7) 1:100, Dako; Ki67 ready to use, gift from the Department of Pathology, Erasmus MC University Medical Center Rotterdam) were added to the organoids and incubated overnight at 4°C. Incubation with secondary antibody Alexa 488 (1:100, Fisher Scientific) took place for 60 minutes at RT. Cytoskeletal staining with Phalloidin Alexa Fluor™ 488 (1:200, Fisher Scientific) and nuclear staining with DAPI were incubated for 2h at RT before confocal imaging.

Confocal imaging of immunofluorescence

All samples, both stained and GFP-tagged, were analyzed using confocal imaging. Samples were imaged using a Leica 20X (NA 1.0) water dipping lens on Leica DM6000 CFS microscope with a LEICA TCS SP5 II confocal system or an Opera Phenix HCS system (PerkinElmer) equipped with a 20x air objective (NA 0.4) and 40x water immersion objective (NA 1.1). For detection on the Opera Phenix High-Content Screening System (PerkinElmer). Stained images were processed using ImageJ/Fiji. Alternatively, GFP-tagged organoid proliferation and migration was analyzed using the Opera Phenix Harmony PhenoLOGIC software (v4.9, Perkin Elmer). Specifically, Alexa 488 positive cells (or cell clusters) were segmented as 3D volumes using a local threshold (0.6) to compensate for loss of signal and allow efficient detection of cells that are deeper in the matrix. 3D volumes smaller than 20000 μm^3 were excluded to eliminate small fragments and debris. Automated segmentation is next confirmed by visual inspection of the raw images. To probe the adherence to Gompertz growth model, least squares regression was used as a fitting method (Prism 8), and a non-linear fit curve was established. The starting population was constrained to >0 and no constraint was placed on maximum population (YM).

To visualize collagen, Second Harmonic Generation (SHG) microscopy was used.¹⁷ In short, the Leica water dipping lens (20x) with numerical aperture of 1.00 was used to deliver the excitation signal and to collect the emission signal. The SHG signal was collected using 880 nm excitation. The SHG signal was collected using PMT detectors with emission filter of 435-445 nm, the DAPI signal with 415-495 nm, and the Fluor 488 signal using 500-550 nm. Averaging was performed over 4 lines to reduce the effect of background noise.

Stable Isotope Labeling with Amino acids in Cell culture (SILAC)

SILAC-R-Spondin medium was produced by replacing conventional L-lysine with $^{13}\text{C}_6$ L-lysine-2HCL ('heavy'; Thermo Fischer Scientific, Waltham, MA, USA). SILAC-R-Spondin was harvested, filtered and stored at -20°C until use. SILAC-EM was prepared by replacing advanced DMEM/F12 and R-spondin with their SILAC counterparts containing the heavier amino acids. All CCAOs were cultured for a minimum of 21 days in total in 'heavy' medium before use within the experiment. Organoids with surrounding ECM substrates were harvested by removal of medium and subsequently snap-frozen in liquid nitrogen and stored at -80°C . Before analysis, samples were lyophilized (Zirbus Technology Sublimator 400).

Sample preparation for SILAC mass spectrometry

Lyophilized samples were rehydrated in 100-200 μl extraction buffer with 100 mM ammonium bicarbonate with 8 M urea, and homogenized using a Bioruptor®Plus (Diagenode SA, Seraing, Belgium) at 4°C for 40 cycles, 15 s ON/OFF. Samples were centrifuged (14000 g, 15 min) and the protein content of supernatants was determined using Pierce BCA Protein Assay Kit (Thermo Fisher Scientific). 30 μg of this urea soluble protein fraction was processed further by reduction with 5 mM tris-2-carboxyethyl phosphine (TCEP) for 30 min at 37°C , alkylated with 10 mM iodoacetamide for 45 min at room temperature, followed by overnight trypsin digestion at 37°C . Digestion was stopped by addition of trifluoroacetic (TFA) acid to a pH < 3. Samples were desalted using C18 reversed-phase spin columns (UltraMicro Spin Column, Nest group, Ipswich, MA, USA) according to manufacturer's instructions. After desalting, samples were resuspended in 2% acetonitrile (ACN), 0.1% TFA and the peptide concentrations were determined using a NanoDrop 2000c Spectrophotometer (Thermo Fisher Scientific).

LC MS/MS analysis

The LC MS/MS analysis was performed on a Tribrid mass spectrometer (MS) Orbitrap Fusion equipped with a Nanospray source and coupled with an EASY-nLC 1000 ultrahigh pressure liquid chromatography (UHPLC) pump (Thermo Fischer Scientific, San Jose, CA). One μg of peptides was loaded and concentrated on an Acclaim PepMap 100 C18 precolumn (75 μm x 2 cm, Thermo Scientific) and then separated on an Acclaim PepMap RSLC column (75 μm x 25 cm, nanoViper, C18, 2 μm , 100 \AA) with a column temperature of 45°C . Peptides were eluted by a nonlinear 2h gradient at a flow rate of 300 nL/min from 2% solvent B (0.1% formic acid (FA)/ACN, Merck)/98% Solvent A (0.1% FA in water, Merck) to 40% solvent B.

The Orbitrap Fusion was operated in the positive data-dependent acquisition (DDA) mode. Full MS survey scans from m/z 375-1500 with a resolution 120,000 were performed in the Orbitrap detector. The automatic gain control (AGC) target was set to 4×10^5 with an injection time of 50 ms. The most intense ions (up to 20) with charge states 2-7 from the full MS scan were selected for fragmentation. MS2 precursors were isolated with a quadrupole mass filter set to a width of 1.2 m/z. Precursors were fragmented by Higher Energy Collision Dissociation (HCD) and detected in Orbitrap detector with a resolution of 30,000. The normalized collision energy (NCE) in HCD cell was set 30%. The values for the AGC target and

injection time were 5×10^4 and 54 ms, respectively. The duration of dynamic exclusion was set to 45 s and the mass tolerance window to 10 ppm.

Data analysis for SILAC

Analysis of raw files was performed with MaxQuant (version 1.6.17.0). The resulting peak lists were searched in Andromeda against a reviewed human UniProtKB database (release 2020_04), complemented with the standard MaxQuant contaminant database. Enzyme specificity was set to trypsin/P with a maximum of two missed cleavages. Precursor mass tolerance was set to 4.5 ppm and fragment ion mass tolerance to 20 ppm. Carbamidomethylation of cysteine was used as fixed modification, oxidation (Methionine), deamination (Asparagine), hydroxyproline and acetylation were considered as variable modifications. The false discovery rate (FDR) was set to 0.01 for both peptides and proteins. Additional data analysis on protein comparisons was done with R (version 4.0.3). Proteins identified are divided into cellular, core matrisome, and matrisome-associated. Furthermore, the identified matrisome proteins are subdivided into ECM-affiliated proteins, secreted factors, collagens, ECM regulators, ECM glycoproteins, and proteoglycans as determined by MatrisomeDB.¹⁸ For analysis of differential abundance, EdgeR (version 3.32.1) and Limma (version 3.46.0) R packages were used. We classified proteins as 'exclusive' if they are present in all samples ($n=2$ biological replicates) of one condition, while absent in all others ($n=4$). The mass spectrometry proteomics data have been deposited to the ProteomeXchange Consortium via the PRIDE partner repository¹⁹ with the dataset identifier PXD028408.

Bulk RNA-sequencing

RNA from CCA primary tissue and CCAOs cultured in CCA-M ($n=9$), TFL-M ($n=6$), and BME ($n=3$) was collected in lysis buffer at day 14 (QIAzol lysing reagent, Qiagen) and isolated using the miRNeasy mini kit (Qiagen) according to the manufacturer's protocol. Bulk RNA-sequencing was performed by Novogene (Beijing, China) resulting in 20-30 million, 150 nucleotides long, paired-end reads (accession number GSE188527). Sequencing data were uploaded to the Galaxy Web platform public server usegalaxy.org.²⁰ Sequences were trimmed for adapters using Trim Galore! (version 0.4.3.1), and mapped using RNA STAR (version 2.6.8a) against the human reference genome GRCh38. Mapped reads were translated to counts using FeatureCounts (version 2.0.1) applying the built-in hg38 genome annotation file. CCA primary tissue bulk RNA-sequencing data from patient CCAO1 was retrieved from our previously published manuscript⁴ (accession number GSE84073) and incorporated into this dataset. We previously sequenced data from CCAOs cultured in basement membrane extract (BME) and expansion medium (accession number GSE179601). All raw counts were batch corrected using ComBat-seq (available via sva package version 3.36.0) using a negative binomial regression model. After filtering for genes with low expression, we could compare the expression profiles of 16,637 genes. Analysis of differential expression was performed using edgeR (version 3.32.1) and Limma (version 3.46.0) R packages. Genes were considered differentially expressed when the adjusted p-value was <0.05 (Benjamini Hochberg FDR corrected). Subsequent gene set enrichment

analysis (GSEA) on the log₂ fold change values was done using fgsea (version 1.16.0) and gage (version 2.40.1) R packages. To increase specificity for gene set enrichment, fgsea results were combined with gage results. Thus, only pathways which are significantly enriched in both analysis methods are retained.

To assess similarity between *in vivo* tissue and our *in vitro* model, we filtered overall gene expression to only include top 100 DE genes between CCA-M and TFL-M, as well as between CCA-M and BME. These gene sets were used to create a Pearson's correlation matrix as a comparative method to *in vivo* CCA tissue transcriptome.

***In vitro* drug assay**

CCAOs (n=3) were dissociated to single cells or small clumps with TrypLE (Thermo Fisher Scientific) for 3 x 5 minutes at 37°C while applying mechanical disruption through pipetting. TrypLE was inactivated by adding cold AdvDMEM/F12, centrifuged for 5 minutes (4°C at 1500RPM) and counted for plating out at a concentration of 5000 cells per decellularized matrix in 96 well plates. EM was added for 3 days. Subsequently, a concentration dilution series of gemcitabine, cisplatin, or a combination of both compounds was added, and cell viability was measured using RealTime-Glo (Promega) at multiple time points for a total duration of 72h according to manufacturer's instructions. The same scaffold was measured at multiple time points, allowing for quantitative analysis of cell viability over time.

Live/Dead staining

Recellularized scaffolds were incubated in EM containing 100 µg/ml Hoechst 33342, 12.5 µg/ml propidium iodide (PI, Sigma-Aldrich), 1 µM calcein acetoxymethyl ester (Calcein AM, Thermo Fisher Scientific) for 30 minutes at 37 °C in the dark. Images were captured with an EVOS fluorescent microscope or with the Leica SP5 inverted confocal microscope.

Cancer Genome Atlas (TCGA) survival analysis

Exclusively identified matrisome-related proteins in CCA-M, TFL-M, or BME were probed for their influence on patient survival within the TCGA CCA cohort. Both protein and gene expression was determined. 36 patients from the TCGA-CCA cohort were included for gene expression analysis, and 30 patients for protein analysis. Only patient data which included survival data were included in the analysis. Data for gene expression linked to survival was accessed through GEPIA²¹, and data for protein expression through TRGAted.^{21, 22} Group cut-offs for gene expression was at the median, and the hazard ratio was determined from the Cox Proportional Hazard regression model. For protein expression, optimal cutoff points are based on finding the lowest log-rank p-value, and the hazard ratio was also determined from the Cox Proportional Hazard regression model. Progression free survival and overall survival were plotted through GEPIA and TRGAted.

Statistical analyses

All statistical analyses were conducted using GraphPad Prism (version 8, GraphPad Software) or R (version 4.0.3, R Core Team). Qualitative data were analyzed with the χ^2 or Fisher exacts tests and were presented with numbers and percentages. Continuous variables were tested

using a Mann-Whitney-U test and presented graphically as means with standard deviation or standard error of mean. Multi-variate analysis was done with 2-way ANOVA with multiple comparison testing for different time points and Bonferroni correction. In all tests, a p value of <0.05 is considered significant.

RESULTS

Culturing cholangiocarcinoma organoids in native CCA tumor ECM induces tumor-specific characteristics

Patient-derived *in vitro* models were created by combining CCAOs with decellularized matrix (Fig. 1A), collected from resected material (Table S3). H&E staining showed a dense extracellular matrix in the CCA tissue surrounding the tumor cells, which was retained after decellularization (Fig. 1B, black arrows point at desmoplastic area). This desmoplastic area mainly consists of high-density collagen bundles (Fig. 1C). TFL-M also maintained its original tissue structure, but, as expected, no fibrosis was present. Quantitative analysis of collagen showed a 2.3-fold higher amount of collagen in decellularized CCA compared to decellularized TFL, congruent with the dense extracellular matrix visible in histochemical stainings (Fig. 1B-D1). The increase in collagen content after decellularization is related to the relative shift in weight of collagen compared to the total weight. sGAG content of CCA tissue before decellularization was approximately 1.5-fold higher compared to TFL, and this difference was retained after decellularization (Fig. 1E). Similarly, mechanical analysis showed a significantly stiffer extracellular matrix in CCA compared to TFL, that was maintained after decellularization (T=0: $p=0.013$, T=decell: $p<0.0001$, Fig. 1F). Analysis of DNA content showed a decrease from an average concentration of 970.7 ng/mg wet tissue to 17.5 ng/mg wet tissue for CCA and a decrease from 1272.0 ng/mg wet tissue to 22.2 ng/mg wet tissue in TFL (Fig. 1G, H). This equals a significant reduction of 98.2% ($p=0.008$) and 98.3% ($p=0.008$), respectively. DAPI staining revealed the absence of nuclei in decellularized CCA-M and TFL-M (Fig. S1A). No fragments of dsDNA could be detected after decellularization (Fig. S1B), confirming complete decellularization according to well-defined criteria.^{23, 24} Cell aggregates derived from three patient-derived CCAOs were directly seeded on decellularized CCA-matrix (CCA-M) and decellularized TFL-matrix (TFL-M). Quantification of DNA content at day 14 after recellularization showed significant restoration of DNA levels in both environments (CCA-M: 953 ng/mg wet tissue, $p=0.036$, TFL-M: 775 ng/mg wet tissue, $p=0.036$, Fig. 1G, H), to similar levels as seen in native tissue. Microscopic analysis confirmed the presence of cells in tightly packed cystic structures that were located on the scaffold, similar to standard culture conditions in BME (Fig. 2A). Bulk RNA sequencing was performed on CCAOs grown in CCA-M, TFL-M, and BME. Importantly, Principal Component Analysis (PCA) revealed segregations of different clusters, with the locations of the samples correlated with both the culture environment as well as patient source of the CCAOs (Fig. 2B). Thus, using decellularization, scaffolds can be produced that retain important characteristics of the tumor extracellular environment, including desmoplasia and increased stiffness, which influences overall cellular behavior as displayed by the different transcriptomes.

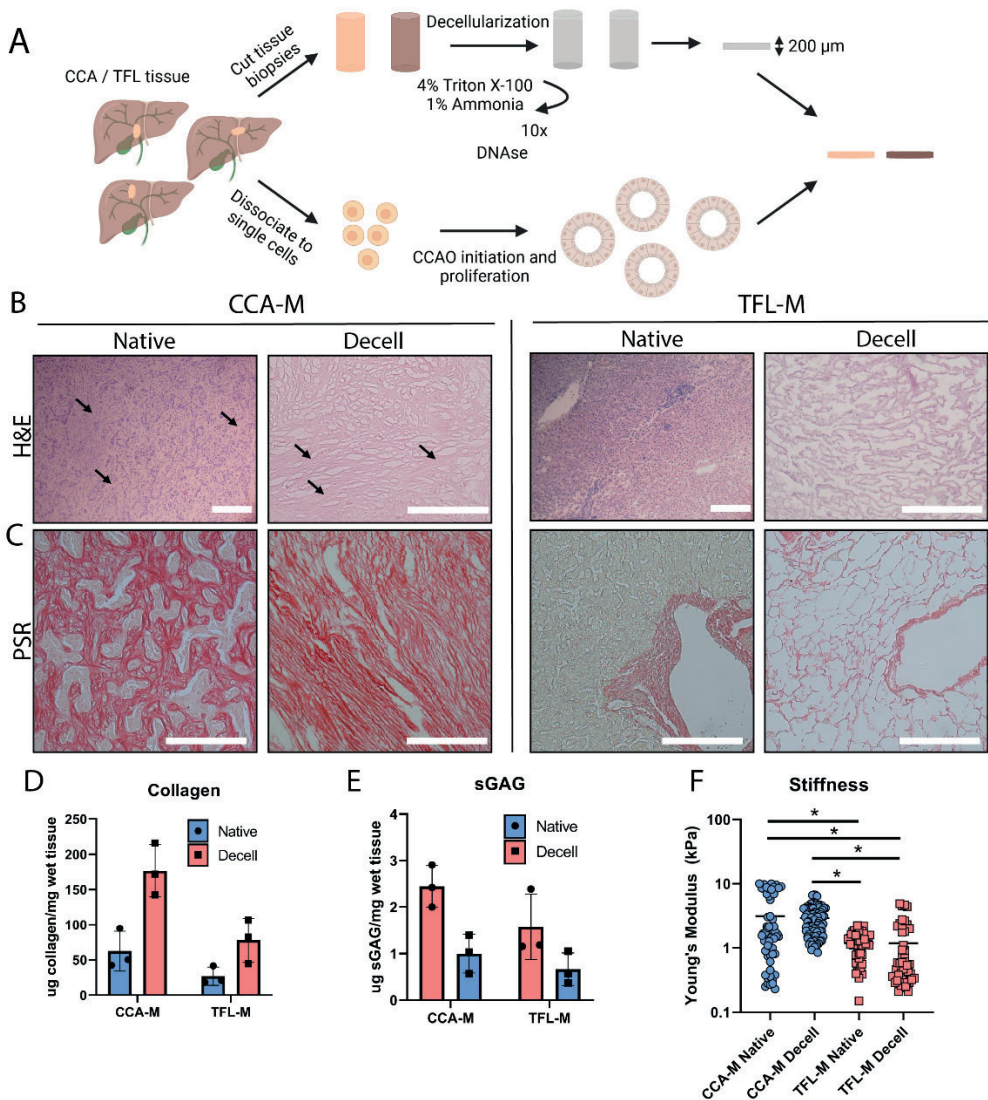


Figure 1A-F. Decellularization and recellularization of cholangiocarcinoma (CCA) and tumor-free liver (TFL) tissue. (a) Schematic overview of utilizing resected tissue specimens of cholangiocarcinoma (CCA) and tumor-free liver tissue (TFL) for both decellularization and organoid initiation to create a comprehensive tumor model. (b, c) Histological characterization of CCA extracellular matrix (CCA-M) and TFL-M sections before and after decellularization, stained with hematoxylin and eosin (H&E, B) and Picosirius Red (PSR, C). Scale bars indicate 200 μm. Arrows indicate desmoplasia in the tumor environment. (d) Total collagen content before (Native) and after (Decell) decellularization for CCA and TFL tissue. Error bars indicate ± SD. (e) Sulfated glycosaminoglycan (sGAG) content before (Native) and after (Decell) decellularization of CCA and TFL tissue. Error bars indicate ± SD. (f) Stiffness measurements performed through nano-indentations on CCA tissue before decellularization ($n=57$), after decellularization ($n=81$), TFL before decellularization ($n=56$), and after decellularization ($n=47$). * p -value < 0.05. Error bars indicate ± SEM. Analysis for panel B-C was done with CCA-M1 and TFL-M1; panel D-F with CCA-M1-3, TFL-M 1-3.

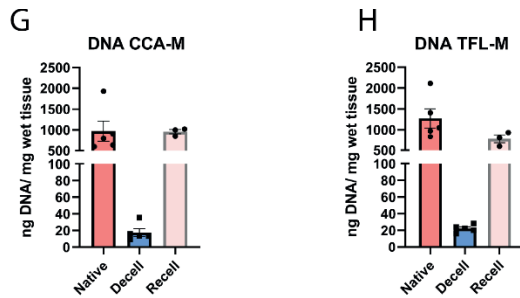


Figure 1G-H. Decellularization and recellularization of cholangiocarcinoma (CCA) and tumor-free liver (TFL) tissue. (g, h) DNA quantification of CCA (D) and TFL (E) before decellularization (Native, n=5), after decellularization (Decell, n=5), and after recellularization (Recell, n=3). * p-value < 0.05. Error bars indicate \pm SEM. Figure panel G, H used CCA-M1-5, TFL-M1-5 and CCAO1-3.

CCAOs in CCA-M have a more tumor-specific transcriptome comparable to CCA tumor tissue *in vivo*

To probe the different culture environments, molecular profiles were further analyzed and differentially expressed genes (DEG) were identified for CCAOs grown in CCA-M compared to TFL-M or BME (Suppl. File 1, 2). CCA-M cultured CCAOs lose their stem-cell phenotype to a certain extent, as seen by downregulation of stem cell markers *LGR5* ($p=0.008$) and *CD44* ($p=0.03$) and Wnt target gene *CLDN2* ($p=0.01$) when comparing to CCAOs cultured in BME (Fig. 2C). On the other hand, various transporters, including *AQP7P1* ($p=0.01$), *TCIM* ($p=0.02$), and *ASIC4* ($p=0.008$) are upregulated in CCA-M. Comparing CCA-M and TFL-M cultured CCAOs, clustering was observed based on ECM-related genes, including various collagens, MMPs, and integrin's (Fig. S2A). Important ECM adherens junction molecules were differentially expressed, including *ITGB2-AS1*, *ITGB8* (both $p=0.02$), and *ITGB1* ($p=0.0502$), showing the role of cell-ECM interactions in directing cellular behavior (Fig. 2D). Furthermore, increased integrin expression (i.e. *ITGB8* and *ITGB1* upregulation in CCA-M) has been linked extensively to the induction of EMT.²⁵ This is corroborated by the upregulation of *SNAI1* ($p=0.005$), an inducer of EMT in CCA²⁶, and *TWISTNB* ($p=0.02$), another EMT marker²⁷, in CCA-M (Fig. 2D). This was further explored through gene set enrichment analysis (GSEA) for DEG between CCA-M and TFL-M cultured CCAOs. GSEA showed significant upregulation of EMT (Normalized Enrichment Score (NES) 2.60) in CCA-M, with scaffold and patient-dependent clustering of EMT-related genes (Fig 2E, Fig. S2C). Furthermore, CCA-M also induced TNF-alpha signaling (NES 4.03), which, particularly in combination with NF-kB, provides cell survival signals important for cancer survival and progression *in vivo*.^{28, 29} TFL-M mainly induces upregulation of genes related to cellular proliferation pathways, including G2M checkpoint (NES 3.28) and E2F targets (NES 3.19) (Fig. 2E, Fig. S2B). GSEA on biological processes revealed a similar phenotype, with complex processes related to cytokine production, intracellular signaling transduction, and cell activation upregulated in CCA-M (Fig. 2F), while more cellular proliferation-related pathways are dominant in TFL-M (Fig. S2B, bottom). Comparing CCA-M and BME cultured CCAOs showed similar results in regards to gene set enrichment differences (Fig. S3A, B).

We hypothesized that CCA-M resembles *in vivo* CCA tissue more closely due to mimicking the native microenvironment. To this extent, bulk RNA sequencing data of patient-paired CCAOs and CCA tumor tissue were batch-corrected and filtered based on differential gene expression. As expected, CCA-M and TFL-M gene expression profiles were highly similar within each group (correlation coefficient (CC) > 0.95). Importantly, CCA-M showed a significantly larger average correlation to CCA tissue gene signatures compared to TFL-M (CC $0.83 \pm SD0.03$ vs CC $0.70 \pm SD0.03$, $p=0.004$, Fig. 2G). Similarly, when comparing gene expression profiles of CCA-M to BME, a more pronounced difference in correlation to *in vivo* CCA tissue was found (CCA-M CC $0.88 \pm SD0.04$ vs BME CC $0.63 \pm SD0.06$, $p<0.0001$, Fig. S3C). This large difference provides strong evidence that CCAOs in CCA-M exhibit a more representative phenotype for *in vivo* patient CCA tissue compared to CCAOs in TFL-M or BME.

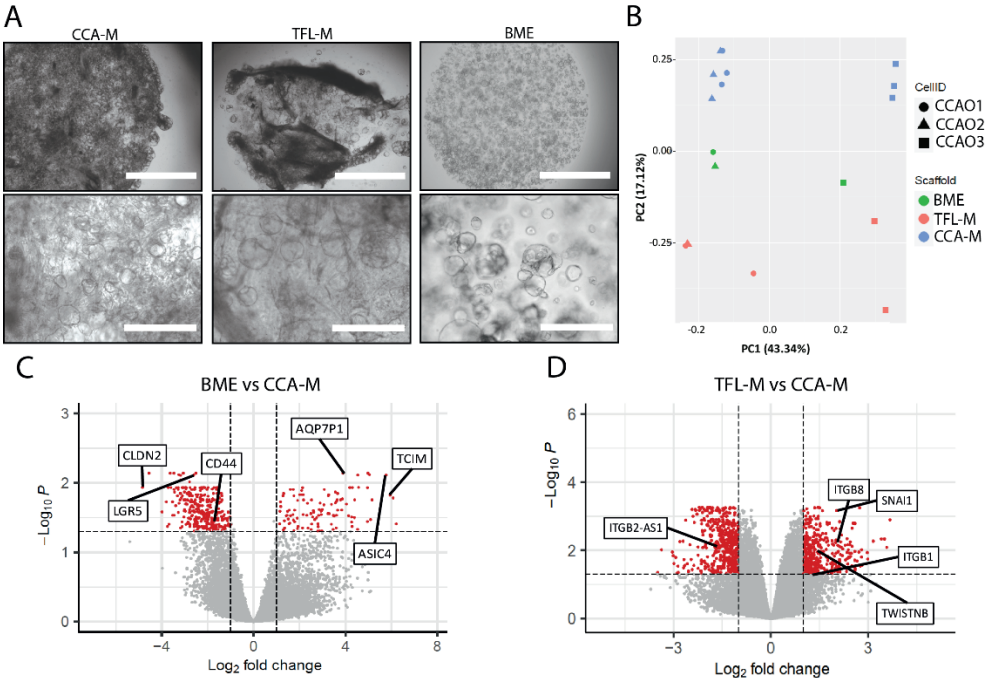


Figure 2A-D. Transcriptome analysis of CCAOs cultured in decellularized matrix. (a) Representative bright-field microscopy images of CCAOs cultured in CCA-M, TFL-M, or BME at day 7. Top row scale bars 2000 μ m, bottom row scale bars 400 μ m. **(b)** Principal Component Analysis (PCA) plot displaying the transcriptome differences of CCAOs cultured in CCA-M, TFL-M, and Basement Membrane Extract (BME). **(c, d)** Volcano scatter plots of statistical significance (adj. p-value) versus magnitude of change (Log_2FC) showing differentially expressed genes (DEG) between CCAOs grown in CCA-M and BME (A), and CCA-M and TFL-M (B). Highlighted are DEG of specific interest. Red dots represent an adjusted p-value of <0.05 and a log_2 fold change of $>|1|$. Analysis for panel A was done with CCA01, CCA-M1, and TFL-M2; panel B with CCA01-3, CCA-M1-3, and TFL-M1,2; panel C with CCA01-3 and CCA-M1-3; and panel D with CCA01-3, CCA-M1-3 and TFL-M1,2.

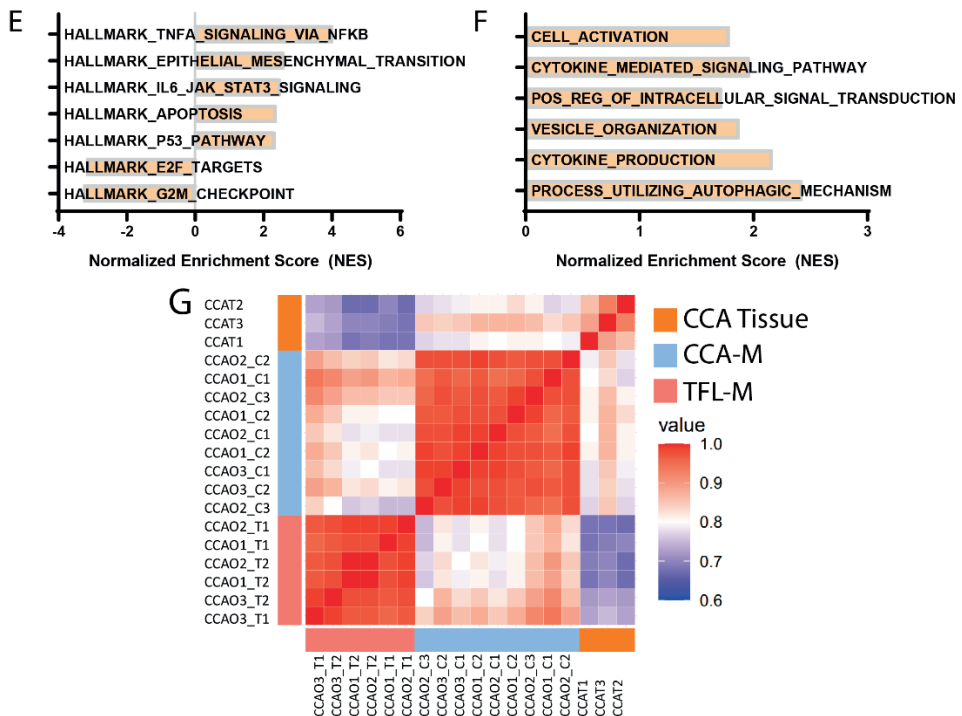


Figure 2E-G. Transcriptome analysis of CCAOs cultured in decellularized matrix. (e, f) GSEA analysis incorporating DEG comparing CCA-M and TFL-M for Hallmark gene sets (e) and Gene Ontology: Biological Processes (GO:BP) (f). Positive NES indicates upregulation of the particular gene set in CCA-M. Negative NES scores for GO:BP are shown in Suppl. Fig. S2B. All NES scores presented are significantly enriched (adj. p val. < 0.05). The most enriched pathways, based on NES score, are represented in the figure. (g) Correlation matrix incorporating CCA tumor tissue (CCAT), and CCAO in CCA-M and TFL-M transcriptome profiles. Top 100 DEG comparing CCA-M and TFL-M were used for the comparison matrix. A value of 1 represents complete correlation, and a value of 0 indicates no correlation. Analysis for panel E-G was done with CCAO1-3, CCA-M1-3 and TFL-M1,2.

The extracellular environment induces chemoresistance in CCAOs

To probe the role of the extracellular environment in drug resistance, the response of CCAOs to chemotherapeutics was assessed. The standard of care treatment for CCA patients is a combination of gemcitabine and cisplatin. Therefore, CCA-M and TFL-M cultured CCAOs were exposed to different concentrations of gemcitabine and a fixed concentration of cisplatin (10 μM) as a combinational therapy (Fig. 3A). Similar to previously published results⁵, response to cisplatin monotherapy was absent at physiologically relevant concentrations (data not shown). CCAOs exhibited a dose-dependent response to chemotherapeutics in CCA-M, TFL-M, and BME, with an initial resistance during the first 24 hours and a subsequent sharper decrease in cell viability (Fig. 3B). Interestingly, patient-specific differences in response to chemotherapeutics were present in CCA-M (Fig. 3C). The chemotherapeutic killing of CCAOs was also visible via live/dead stainings (Fig. 3D). When comparing the response of CCAOs in CCA-M and TFL directly at different concentrations, a significant

difference in chemo response was observed at different dosages of gemcitabine (1 μM $p=0.023$, 10 μM $p=0.0438$, 100 μM $p=0.018$, Fig. 3E). Thus, at both low and high gemcitabine concentrations there was a protective effect of the extracellular tumor environment on cellular viability. Comparing CCAOs in decellularized matrices and BME directly in regards to drug response is potentially flawed, due to the cell location as a consequence of different seeding strategies, 2D vs 3D culture, and potential effect of drug diffusion through BME.³⁰

Together this data shows that CCAOs in a CCA-M environment are able to mimic *in vivo* CCA tumor tissue on a transcriptional level more closely, which coincides with an increased resistance to chemotherapeutics. Combinational therapy with gemcitabine and cisplatin is only able to provide a relatively modest benefit to overall survival in patients³¹, and this data suggests that this effect is, to a certain extent, due to the desmoplastic environment.

ECM-specific differences in growth dynamics mimic cancer-related proliferative and migratory patterns

In vivo, cancer progression is grounded in two fundamental processes of growth: cell invasion and expansive growth of tumor cells.^{32, 33} Cancer cell invasive behavior can be further divided into two main patterns: collective cell migration and individual cell migration.³⁴ As invasion is inherently linked to the surrounding environment of the tumor, we sought to determine the growth dynamics of CCAOs within CCA-M and TFL-M. To this extent, CCAOs were genetically labeled with a GFP-tag and imaged in real time via live-cell confocal microscopy for a duration of 14 days.

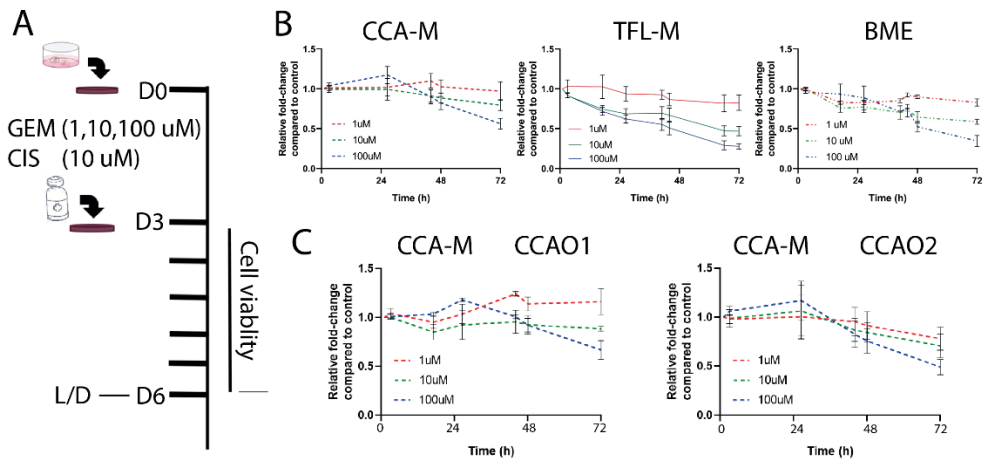


Figure 3A-C. Chemotherapy treatment response of CCAOs. (a) Schematic overview of chemotherapy response measurements comparing CCA-M, TFL-M, and BME. GEM = gemcitabine, CIS = cisplatin, L/D = Live/Dead staining (b) Cell viability measurements with RealTime-Glo in response to combinational therapy with gemcitabine (1, 10, 100 μM) and constant cisplatin (10 μM) ($n=6$). Each condition was measured at multiple time points during the 72h. (c) Cell viability measurements for two different patient-derived organoid lines (CCAO1, CCAO2, $n=3$ per organoid line) on CCA-M with varying concentrations of gemcitabine (1, 10, 100 μM) and constant cisplatin (10 μM). Error bars indicate \pm S.D. Analysis for Figure 3 was done with CCAO1,2, CCA-M1-3, and TFL-M1-3.

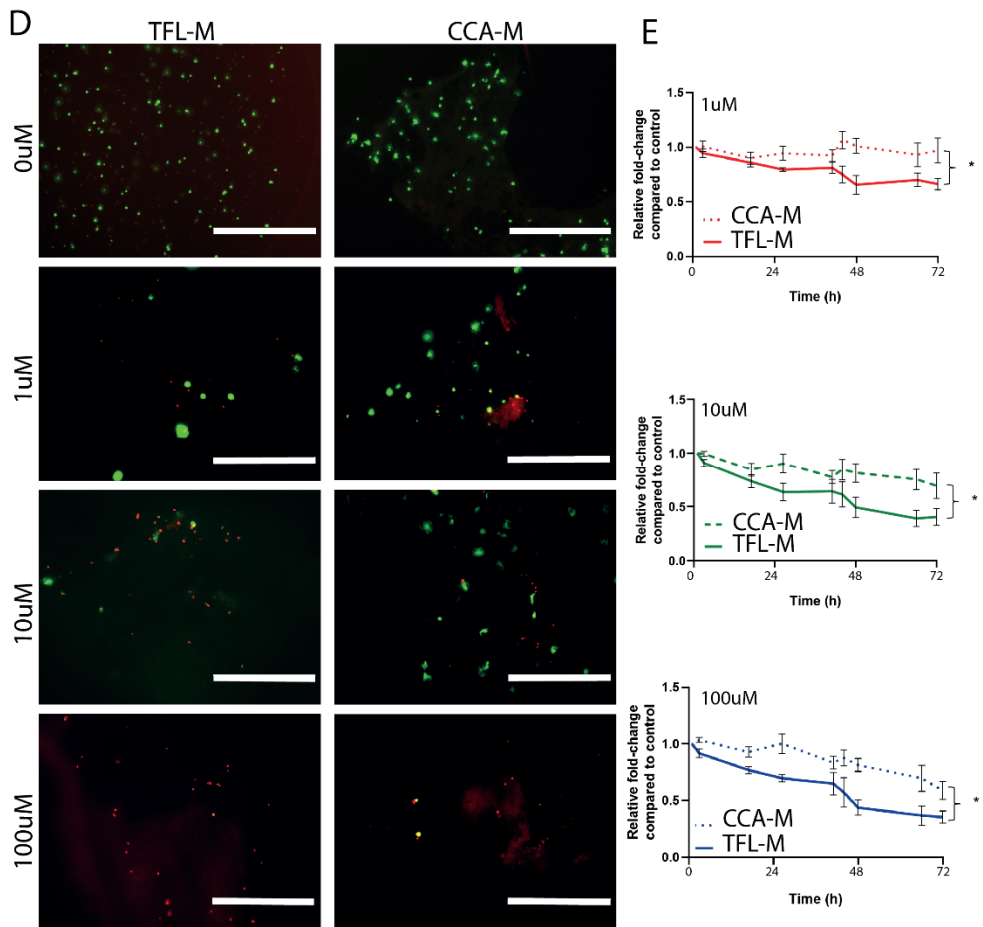


Figure 3D-E. Chemotherapy treatment response of CCAOs. (d) Representative images of CCAOs in CCA-M and TFL-M at 72h after treatment with gemcitabine and cisplatin. CalceinAM (green) and PI (red) are markers for alive and dead cells, respectively. (e) Cell viability measurements directly comparing different concentrations of gemcitabine (top: 1uM, middle: 10uM, bottom: 100 uM) with a constant 10 uM concentration of cisplatin. * p-value < 0.05. Error bars indicate \pm S.D. Analysis for Figure 3 was done with CCAO1,2, CCA-M1-3, and TFL-M1-3.

The amount of GFP-signal was quantified over time through total surface area and volume, to discern formation of large cell aggregates (ratio surface area/volume is lower) and small aggregates/single cells (ratio surface area/volume is higher). Additionally, the average height of GFP-signal was measured to provide an up/downwards directionality to the proliferation.

CCAOs were able to proliferate in CCA-M and TFL-M, demonstrated by the overall increase in GFP-signal over time (Fig. 4A, Fig. S4A, Suppl. Video 1 and 2). In addition, a difference in cell proliferative behavior can be observed in the two environments. CCAOs grown in TFL-M form a collective invasive front, whereas a more spread out inducement of growth throughout the whole matrix, more reminiscent of individual cell migration and proliferation, was observed in CCA-M (Fig. 4A). Cellular surface area shows a 3.4-fold

increase over time (compared to day 1) in CCA-M and 2.5-fold increase in TFL-M after 14 days ($p=0.014$, Fig. 4B). GFP-signal tracking of this increase showed that CCAOs in TFL-M are proliferating partly in an upward trajectory, possibly through a nutrient gradient caused by the culture conditions (Fig. 4C). CCA-M induces an initial upward movement, followed by a slight decrease from day 9 onward. This suggests different behavior occurring, with an increase in cellular growth within the matrix through the aforementioned individual cell migration and subsequent proliferation of these cells in CCA-M.

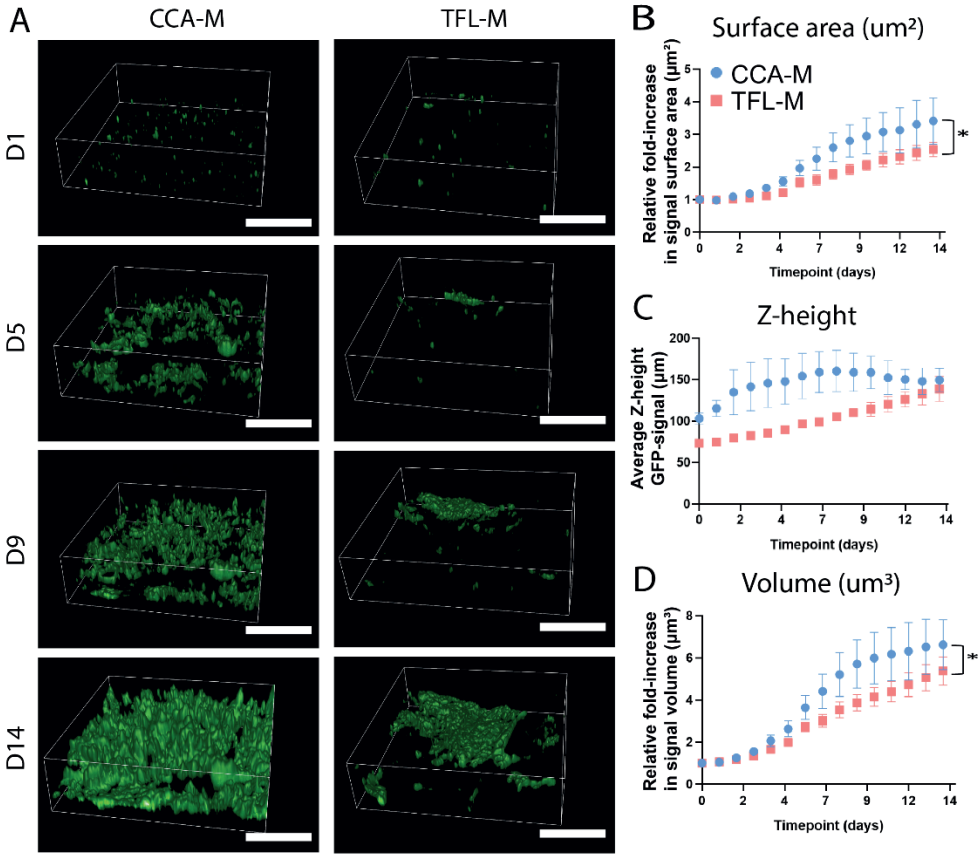


Figure 4A-D. CCAO growth and migration dynamics are extracellular matrix-dependent. (a) Representative 3D live cell confocal images of GFP-tagged CCAOs on CCA-M and TFL-M at day 1, day 5, day 9, and day 14 are shown. Scale bars indicate 400 μm . (b) Analysis of GFP-positive surface area (μm^2) measurements relative to day 0. Live-cell confocal images ($n=4$ for both CCA-M and TFL-M) were obtained for 14 days. (c) Analysis of the average Z-height of GFP-positive signal over time on CCA-M and TFL-M. The average Z-height is calculated from the bottom of the plate, which is taken as 0 μm . (d) Analysis of GFP-positive volume (μm^3) measurements relative to day 0 representing cellular growth. All error bars within this figure indicate \pm S.D. Analysis for panel A-D was done with CCAO1,2, CCA-M2,3, and TFL-M2,3.

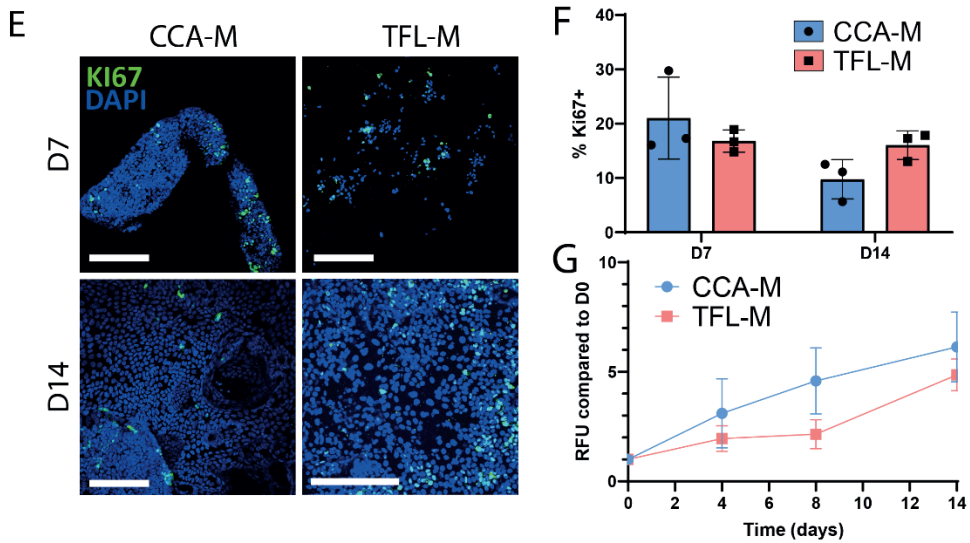


Figure 4E-G. CCAO growth and migration dynamics are extracellular matrix-dependent. (e) Representative immunofluorescent images of Ki67 (green), a marker for proliferation, at day 7 and 14. Nuclei were stained with DAPI (blue). Scale bar indicates 200 μ m. (f) Analysis of immunofluorescent images ($n=3$) of Ki67 staining for each time point and condition. Independent samples were analyzed for day 7 and day 14. (g) Quantitative PrestoBlue measurements showing metabolic activity of CCAOs as represented by absorbance relative to D0 ($n=3$ per time point). All error bars within this figure indicate \pm S.D. Analysis for panel E-G was done with CCAO1-3 on CCA-M1, TFL-M1.

GFP-signal volume measurements, representative of total cellular volume and displayed as a fold change from day 1, showed a significant difference in cellular volume, particularly around day 6-10, which levels off near day 14 (Day 9: 5.70 (CCA-M) vs 3.87 (TFL-M); Day 14: CCA-M 6.62 (CCA-M) vs 5.38 (TFL-M), $p=0.019$, Fig. 4D). The larger increase in volume compared to surface area indicates the formation of larger clusters of cells forming over time (increase in ratio volume to surface area). CCAOs grown in both CCA-M and TFL-M, adhere to the laws of Gompertz growth dynamics to a certain degree ($R^2 =$ CCA-M 0.79, TFL-M 0.95, Fig. S4B).³⁵

Expression of proliferation marker KI67 confirmed partly the observed growth rates at the gene level (Fig. S4C). At the protein level, cell proliferation at both day 7 and day 14 in CCA-M and TFL-M was observed, however without significant differences (Fig. 4E, F). Further quantitative analysis through metabolic activity measurements of CCAOs adhere to the same observed trends, namely the induction of a higher initial proliferation rate in CCAOs when cultured in their native (CCA-M) environment (Fig. 4G), although this difference was not significant ($p=0.15$). These results give insight into the complex growth behavior of CCA tumors likely induced by the microenvironment, mimicking defined cancer cell migration patterns.

The observed growth dynamics are related to the formation of morphological structures associated with the induction of EMT

To further dissect these macro-scale observations of collective cell behavior, detailed morphological and proteome analyses were performed. Actin filament staining after 7 days showed the formation of organoid-like morphology, showing densely packed structures composed of multiple cells, in CCA-M and TFL-M, confirming previous bright field images (Fig. 5A, left panel, Fig. 1F). Additionally, the use of Second-Harmonic Generation (SHG) microscopy enabled visualization of collagen bundles, which confirmed the difference in collagen content and structure, caused by the presence (CCA-M) and absence (TFL-M) of the desmoplastic environment (Fig. 5A, middle panel). After 14 days, a dysregulated cellular layer has formed through rearrangement of actin filaments, with visible tightly attached focal adhesions, suggesting the presence of partially, but not complete, polarized cancer cells (Fig. 5B). This was corroborated by the lack of pronounced localization of zonula occludens (ZO-1) in the cell membrane (Fig. S5A). Moreover, KRT7, a well-established marker for CCA³⁶, showed localized expression in both environments (Fig. S5A). CCAOs cultured in BME show limited transformation of cellular morphology, and exhibited similar structures to scaffold cultures at day 7 (Fig. S5B).

To determine the biomechanical cues driving the observed complex structures and growth dynamics, a comprehensive proteomic analysis was performed, with proteins classified according to MatrisomeDB.¹⁸ SILAC was utilized to discriminate between pre-existing proteins present and soluble proteins that are produced by the CCAOs. A total of 1640, 1604, and 1357 produced proteins were identified while being cultured in CCA-M, TFL-M, and BME, respectively. The relative division of protein abundance was similar between all conditions, except for an increased production of core matrisome proteins in TFL-M (Fig. 5C).

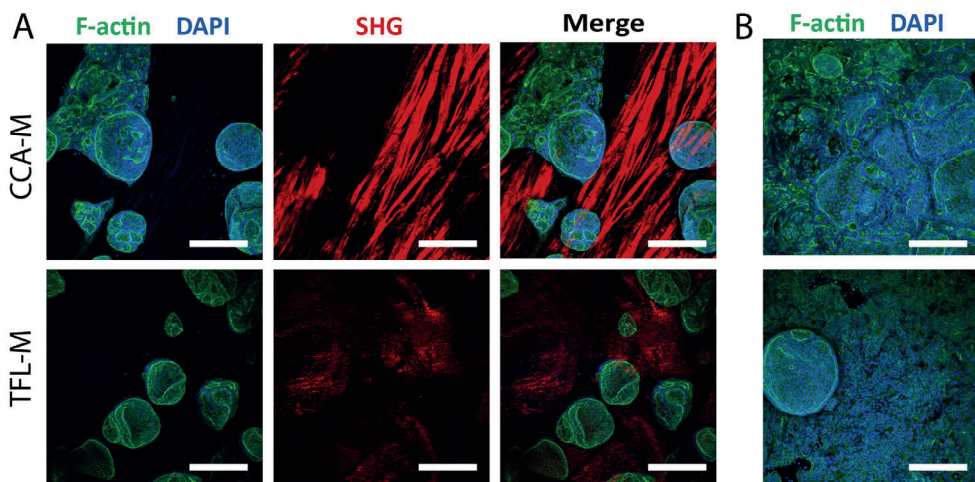


Figure 5A-B. Phenotypic comparison between CCAOs cultured in CCA-M and TFL-M. (a, b) Whole mount imaging of F-actin (Phalloidin, green), DAPI (blue), and second-harmonic generation (SHG, red) of CCAOs in CCA-M and TFL-M at day 7 (**a**) and 14 (**b**). Scale bars indicate 200 μ m. Analysis for panel A-B was done with CCAO1,2, CCA-M5, and TFL-M6.

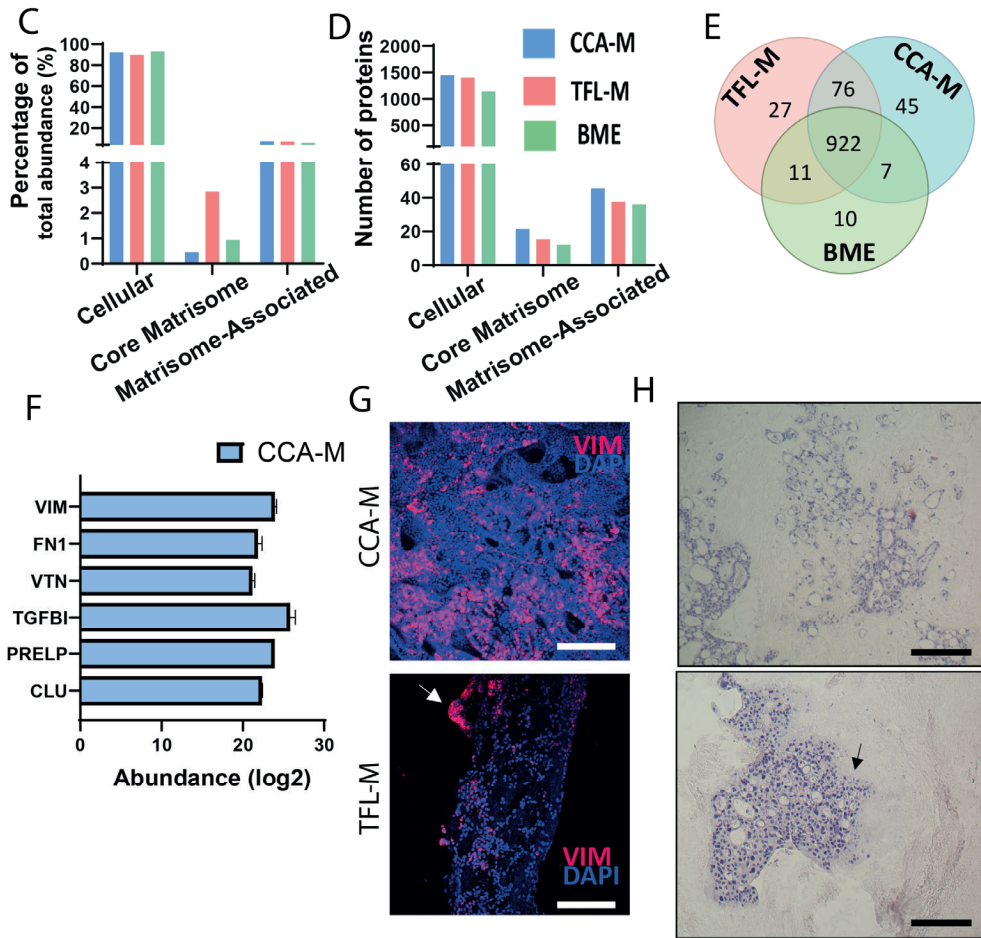


Figure 5C-H. Phenotypic comparison between CCAOs cultured in CCA-M and TFL-M. (c, d) Interleaved bar plot of relative percentage (c) and total number of proteins (d) produced. Proteins are subdivided into cellular, core matrisome, and matrisome-associated. (e) Venn diagram showing exclusive and overlapping protein production in CCA-M, TFL-M, or BME. Proteins are deemed exclusive if they are present in all samples of one condition, and absent in all other samples. (f) Bar plot of selected exclusively identified proteins in CCA-M. Values are log₂ transformed. (g) Whole mount confocal imaging of Vimentin (red) and DAPI (blue) of CCAOs in CCA-M and TFL-M. Scale bars indicate 200 μ m. (h) Representative Hematoxylin and Eosin (H&E) staining of the cross-section located within the scaffold. Arrows highlight the invasive front-like phenotype. Scale bars indicate 200 μ m. Analysis for panel C-E was done with CCAO1,2 on CCA-M2, TFL-M2; panels F-G with CCAO2 on CCA-M2 and TFL-M1.

To determine the biomechanical cues driving the observed complex structures and growth dynamics, a comprehensive proteomic analyses was performed, with proteins classified according to MatrisomeDB.¹⁸ SILAC was utilized to discriminate between pre-existing proteins present and soluble proteins that are produced by the CCAOs. A total of 1640, 1604, and 1357 produced proteins were identified while being cultured in CCA-M, TFL-M, and BME, respectively. The relative division of protein abundance was similar between all

6

conditions, except for an increased production of core matrisome proteins in TFL-M (Fig. 5C). However, the highest number of proteins produced was identified in CCA-M in all three MatrisomeDB categories, showing that culture of CCAOs in their native microenvironment results in an increased diversity of proteins (Fig. 5D). The same trend can be seen when looking at exclusively produced proteins (Fig. 5E). To determine if the migratory dynamics, phenotypic morphology, and difference in protein productions are related, we performed gene set enrichment analysis (GSEA) on the exclusively produced proteins of CCA-M (Fig. 55C). The Gene Ontology (GO) term Extracellular exosomes, involved in a multitude of processes, including (but not limited to) EMT³⁷, was significantly associated with this protein signature. To metastasize from a primary tumor site, cancer cells often undergo the process of EMT to obtain invasive and migratory properties.³⁸ Classical EMT markers such as VIM, TGFBI, and FN1 are among proteins exclusively produced in CCA-M (Fig. 5F). Additionally, other molecules that have been shown to regulate and mediate EMT induction, such as VTN³⁹ and CLU⁴⁰, or associated with CCA development, such as PRELP⁴¹, were also exclusively produced by CCAOs cultured in CCA-M. This data is in line with the transcriptome enrichment of EMT-related markers in CCA-M (Fig. 2C, D) and known evidence about EMT occurrence in CCA.³⁸ Furthermore, presence of VIM was confirmed by immunofluorescence staining, showing spread out positivity in CCA-M, similar to the tumor cell growth pattern observed (Fig. 5G, Fig. 4A). VIM expression was also observed in TFL-M, localized more regionally, suggesting high expression at the invasive front (Fig. 5G). These findings are in agreement with previous publications that demonstrated the relationship between high VIM expression and invasive phenotype of cancer cells.^{42,43} The disparity between SILAC and immunofluorescence staining of VIM is likely due to a difference in sensitivity. Cross sectional imaging of H&E stained CCAOs on CCA-M and TFL-M confirmed the different invasive characteristics: the invasive front (TFL-M) and more widespread invasion of single or multi-cellular structures (CCA-M) (Fig. 5H, Fig. S4A).

To conclude, both CCA-M and TFL-M induce organoid-like morphologies, with distinct cellular behavior related to EMT and invasive capabilities mimicking known cancer migratory patterns. Furthermore, we show that ECM permissiveness for the occurrence of invasion is environment dependent.

The cell-ECM feedback loop is dependent on the extracellular environment

To further compare proteomes in different environments, proteome profiles of proteins that were present in all samples (total 922 proteins) were analyzed (Suppl. File 3). Correlation analysis indicates a clear clustering separating CCAOs cultured in BME and CCAOs in decellularized matrix, as well as clustering CCA-M and TFL-M (Fig. 6A). When comparing proteins produced by CCAOs in CCA-M or BME, two important proteins in CCA-M stand out: Growth/Differentiation Factor 15 (GDF15), related to EMT and metastasis in cancer⁴⁴, and heparan sulfate proteoglycan (HSPG), which also has enhanced expression in CCA tumor stroma *in vivo* (Fig. 6B).⁴⁵ BME upregulated proteins, compared to CCA-M or TFL-M, included Nucleolin, a multi-functional protein which is related to Wnt signaling^{46,47}, and ribosomal-related proteins ribosomal protein L4 (RPL4) and nucleophosmin 1 (NPM1). Differentially

expressed proteins in TFL-M compared to BME included phosphoglucomutase 1 (PGM1) and kinectin 1 (KTN1), both promoters of cancer progression (Fig. 6C).^{48, 49} Limited differentially expressed proteins were present when comparing CCA-M to TFL-M, with notably GDF15 consistently overproduced in CCA-M (Fig. S6A). This, combined with the exclusive protein profile (Fig. S5C), confirmed that CCA-M was able to induce cellular functioning that differentiates itself from BME and TFL-M. To expand on previous GSEA analysis, a decellularized matrix signature, combining CCA-M and TFL-M, consisted of pathway upregulation primarily related to the interaction between ECM and cells, including extracellular matrix, collagen fibril organization, and extracellular exosomes (Fig. 6D). On the other hand, a BME induced protein signature showed a focus on extracellular matrix specifically related to the basement membrane and laminin-1 complex (Fig. S6C). All taken together, these data unveil significantly regulated proteins depending on the environment. This indicates that the interaction between CCAOs and environment is bi-directional, with CCAOs being influenced by the extracellular matrix components already present, but also suggesting that CCAOs can modify their environment.

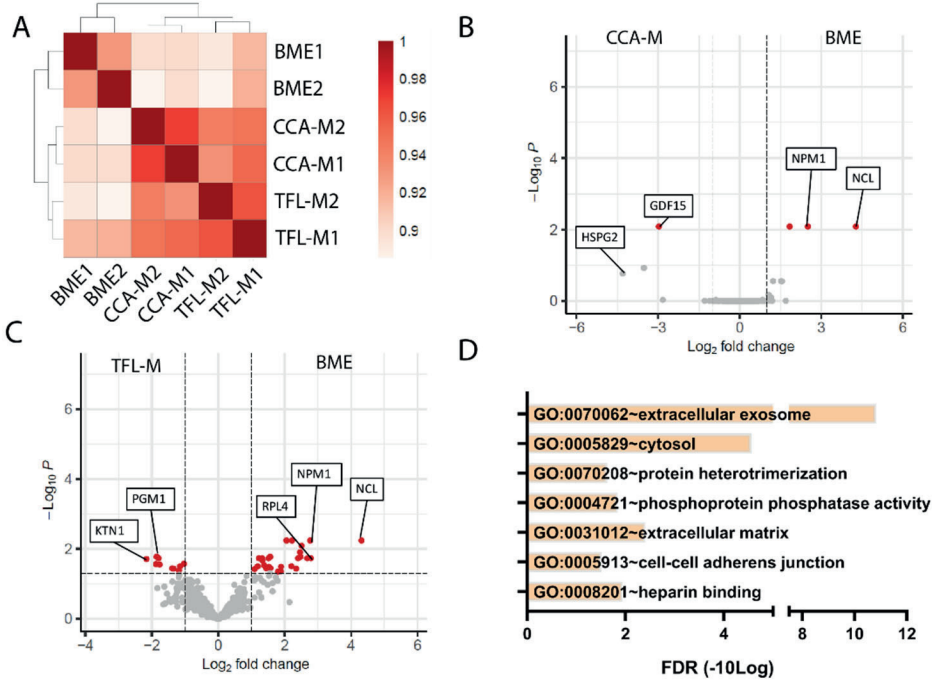


Figure 6A-D. Proteome analysis of CCAOs cultured in CCA-M, TFL-M, and BME. (a) Heatmap of hierarchical clustering based on Spearman correlation of CCAOs in CCA-M, TFL-M, and BME. Only proteins present in all samples are used for clustering. Protein abundance values are log₂ transformed before analysis. (b, c) A volcano scatter plot of statistical significance (adj. p-value) versus magnitude of change (Log₂FC) showing DE proteins between CCA-M (b) or TFL-M (c) and BME culture. Positive log₂ fold change indicates increased abundance in a BME environment. (d) GSEA of proteins exclusively present in decellularized matrix (CCA-M and TFL-M) compared to BME. Results were obtained by using the DAVID database^{50, 51}, and filtered for GO:BP, GO:MF, and GO:CC. Analysis for panel A-D was done with CCAO1,2, CCA-M2, and TFL-M2.

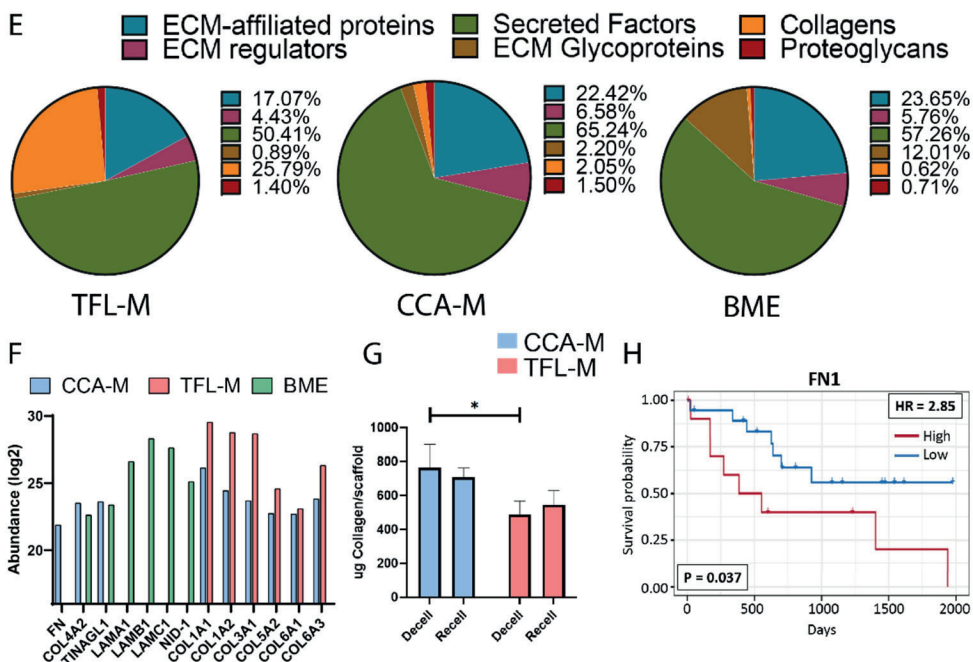


Figure 6E-H. Proteome analysis of CCAOs cultured in CCA-M, TFL-M, and BME. (e) Pie charts showing relative abundance (%) of matrisome proteins. **(f)** ²Log transformed abundance values of selected exclusive and shared proteins related to the matrisome. **(g)** Collagen quantification of CCA-M (left) and TFL-M (right) before and after recellularization. $n=3$, * p -value < 0.05. Error bars indicate \pm S.D. **(h)** Overall survival plot for groups with high and low protein expression of FN1 in the TCGA-CHOL cohort. Optimal cutoff points are based on finding the lowest log-rank p -value. Hazard ratio (HR) is determined from the Cox Proportional Hazard regression model.²² Analysis for panel E-F was done with CCAO1,2, CCA-M2, and TFL-M2; panel G decellularization values with CCAM4-6, TFL-M4-6, recellularization values with CCAO1 on CCA-M4-6 and TFL-M4-6.

CCAOs are able to induce a desmoplastic reaction directly through increased collagen production

CCA and extracellular matrix are inherently linked *in vivo*, and research on the role of the desmoplastic environment in tumor progression show the complexity of this interaction.² Thus, we hypothesized that utilizing native ECM *in vitro* would enable more accurate modelling of the initiation and progression of desmoplasia *in vivo*. In all environments (CCA-M, TFL-M, and BME) the majority of the produced proteins consisted of secreted factors (Fig. 6E, Fig. S6D). CCAOs in BME had at least 5.5x (12.01% vs 2.20-0.89%) as much relative production of glycoproteins, which are the main components of the basement membrane.⁵² *In vivo*, the desmoplastic extracellular environment in CCA consists mainly of a dense network of different types of collagens and fibronectin.^{53, 54} Looking at overall relative collagen production, CCAOs in TFL-M produced approximately 12x (25.79% vs 2.05-0.62%) as much collagens compared to CCA-M or BME (Fig. 6E). Furthermore, collagens produced in both a CCA-M and TFL-M setting were consistently more produced in the latter (Fig. 6F). This data was confirmed by quantifying the amount of collagen present per scaffold through

hydrolysis, which showed a significant higher amount of collagen in decellularized CCA compared to TFL ($p=0.03$), owing to the desmoplasia present (Fig. 6G). After recellularization, no significant difference was observed, indicating that there was a relative increase in collagen production within TFL-M. On the other hand, CCA-M induced production of more unique matrisome-related proteins, including the production of collagen (COL4A2) and fibronectin (FN1) (Fig. 6F, Fig. S6E). Survival-outcome analysis showed that in the TCGA-CHOL cohort of CCA patients ($n=30$), a high expression of FN1 was associated with a worse overall survival and progression free survival (Fig. 6H, Fig. S6F). For BME, the bulk of glycoproteins produced are related to the basement membrane, including LAMA1, LAMB1, LAMC1, NID-1, and NID-2 (Fig. 6F), and this matrisome signature was not associated with any clinical response (Fig. S6G, H). Taken together, CCAOs recapitulate the initiation of a desmoplastic response when grown in TFL-M, illustrated by the high amount of collagen deposition. On the other hand, the CCA-M environment is already desmoplastic, and results in progression, rather than initiation, of desmoplasia through production of clinically relevant extracellular matrix proteins.

DISCUSSION

Herein, we demonstrate that patient-derived cholangiocarcinoma organoids can be cultured on tumor (CCA-M) and tumor-free liver (TFL-M) decellularized matrix to create a model encompassing both cellular and extracellular aspects of CCA. The transcriptomic profile of CCAOs cultured in a CCA environment are able to mimic the gene expression profile of patient-paired *in vivo* CCA better than CCAOs in TFL-M or BME, validating the relevance of the improved model. This is accompanied by an increase in resistance to gemcitabine with cisplatin, the standard regimen for CCA. Furthermore, CCAOs show distinct growth and proliferation dynamics depending on their environment (i.e. CCA-M or TFL-M), which is linked to different patterns of invasion and an ECM-dependent induction of EMT. Lastly, primary epithelial cells, cultured as CCAOs, can aid in the shaping of a desmoplastic environment directly through increased collagen production.

The successful initiation of CCAOs, as first described by Broutier *et al.*⁴, allowed for studying various aspects of tumor biology, including biomarker discovery and drug response studies, due to their ability to recapitulate patient-specific transcriptome profiles.⁵ We show that CCAOs in CCA-M better mimic *in vivo* patient CCA tissue on a transcriptome level, while also upregulating tumor-related pathways, such as EMT and TNF-alpha signaling. Epithelial CCA cells exhibit high single cell inter-tumor heterogeneity *in vivo*⁵⁵, and to what extent our model is able to model this phenomenon remains elusive. Recently, single cell (sc)RNA sequencing of hepatobiliary tumor organoids showed heterogeneity recapitulation⁵⁶, albeit slightly limited, and extending scRNA sequencing to this model could provide more granularity on the existence of subpopulations and representation of the *in vivo* tumor tissue. Additionally, the difference found in overall transcriptome is linked to the observed increased chemo resistance in a tumor environment. The true prognostic value of the tumor desmoplastic environment in CCA is complicated, also dependent on other stromal

components⁵⁷, including cancer-associated fibroblasts (CAFs), which are not included within the model described here. Nevertheless, our findings open up avenues to find ECM-targeting therapeutics that could affect the desmoplastic environment. To note, the current set-up does not provide a patient-specific model encompassing organoids and ECM material from the same patient. Instead, the model is used to comprehensively cover the relationship between cells and ECM within the context of CCA, finding common denominators that can be applied to the overall CCA patient population. Increasing the patient pool for CCAOs would provide further validation of the various findings related to tumor cell-ECM interactions discussed herein.

Other methods for organoid culture have primarily focused on creating a more defined hydrogel, to probe aspects that are relevant for the maintenance of organoids.⁵⁸ These alternatives are complementary, as decellularized matrices are able to provide a model that encompasses the extracellular matrix of the tumor comprehensively, but importantly, does not allow isolation and investigation of singular features (e.g. separating the effect of stiffness and matrix composition). Thus, it is clear that modelling tumor behavior is multifaceted, with no 'one model fits all' philosophy.

Live-cell imaging and tracking analysis indicated that CCAOs are able to proliferate and migrate in distinct patterns depending on their environment, while adhering to the growth model as postulated by Gompertz.⁵⁹ Similarly, *in vivo*, Gompertz's growth model allowed for tracking the growth trajectory of liver cancer in mice up to 100 days.⁶⁰ Albeit with a shorter time-frame, which possibly could be extended by creating larger scaffolds, a similar adherence to this model could be observed. This allows for applications in basic research on growth and proliferation and potentially more in-depth observations on growth-inhibiting preclinical drug testing.

Additionally, these distinct growth patterns are linked to different migration patterns: collective cell migration and individual cell migration.^{61, 62} Collective cell migration is often associated with high expression of *CDH1* and various integrin's, while individual cell migration is usually marked by EMT and predominates in a stiff environment.^{63, 64} These findings are in alignment with our data, where collective cell migration occurs within an invasive-mimicking environment (TFL-M), with gene expression upregulation of *ITGB2-AS1*, and an invasive front phenotype. Individual cell migration in our system occurs within the stiffer tumor environment (CCA-M), with induction of vimentin on a protein level and gene set enrichment of EMT. Recently, single-cell analysis of CCA tissue revealed a sub-cluster of malignant epithelial cells with an EMT-dominant signature⁵⁵, with high expression of *FN1*, congruent with our CCA-M model. The combination of CCAOs and decellularized matrix described in this study is very well suited to serve as a pathophysiological relevant *in vitro* system that integrates cancer cell proliferation, invasion, migration and EMT occurrence thoroughly. Particularly, the duality of our findings, both modelling a tumor environment and outgrowth into liver tissue, facilitates insight into different patterns of CCA behavior.

In this study, epithelial CCA cells are shown to produce soluble components of their extracellular environment, mimicking the environment already present. In BME, this

consists of LAMA1, LAMB1, NID-1, and NID-2, important components of the basement membrane, but not representative of the tumor extracellular environment of CCA.⁶⁵ CAFs are known to be important in the production of various desmoplasia-related components including various collagens, fibronectin, and periostin.^{2, 66} Here, primary epithelial tumor cells, possibly by undergoing EMT, are also able to produce some of these components (COL1A1, COL3A1, FN1) in the presence of an established desmoplastic tumor environment and in the absence of CAFs. If no established desmoplastic environment is present, a pronounced increase in collagen production is observed, suggesting the initiation of a desmoplastic environment by the cells themselves, in alignment with the proposed hypothesis of the formation of stroma in CCA as a response to malignant growth.⁶⁷ Primary tumor cells could thus circumvent the effectiveness of CAF-targeting drugs focused on desmoplasia reduction.⁶⁸ Patient survival in CCA is inherently linked to the extracellular environment⁶⁹⁻⁷¹, and this mechanistic insight of production by epithelial cells could provide new opportunities for therapeutic targeting.

In conclusion, this study demonstrates that combining tumor organoids and decellularized matrix provides a complex *in vitro* model that can recapitulate key components of CCA tumor biology, including EMT, desmoplasia, and overall transcriptome profiles. The increased production of extracellular matrix proteins, primarily collagens, indicates that epithelial tumor cells are able to contribute to their own desmoplastic environment. Complementing organoid-based cell culture models with tumor decellularized matrix is applicable to a variety of tumors and could result in overall better recapitulation of tumor behavior *in vivo*.

REFERENCES

1. Wellner UF, Shen Y, *et al.* The survival outcome and prognostic factors for distal cholangiocarcinoma following surgical resection: a meta-analysis for the 5-year survival. *Surgery today*, 2017. 47(3):271-9.
2. Sirica AE, Gores GJ. Desmoplastic stroma and cholangiocarcinoma: clinical implications and therapeutic targeting. *Hepatology*, 2014. 59(6):2397-402.
3. Brandi G, Farioli A, *et al.* Genetic heterogeneity in cholangiocarcinoma: a major challenge for targeted therapies. *Oncotarget*, 2015. 6(17):14744.
4. Broutier L, Mastrogianni G, *et al.* Human primary liver cancer–derived organoid cultures for disease modeling and drug screening. *Nat Med*, 2017. 23(12):1424.
5. Li L, Knutsdottir H, *et al.* Human primary liver cancer organoids reveal intratumor and interpatient drug response heterogeneity. *JCI insight*, 2019. 4(2).
6. Artegiani B, van Voorthuysen L, *et al.* Probing the tumor suppressor function of BAP1 in CRISPR-engineered human liver organoids. *Cell Stem Cell*, 2019. 24(6):927-43. e6.
7. Dijkstra KK, Cattaneo CM, *et al.* Generation of tumor-reactive T cells by co-culture of peripheral blood lymphocytes and tumor organoids. *Cell*, 2018. 174(6):1586-98. e12.
8. Liu J, Li P, *et al.* Cancer-associated fibroblasts provide a stromal niche for liver cancer organoids that confers trophic effects and therapy resistance. *Cell Mol Gastroenterol Hepatol*, 2021. 11(2):407-31.
9. Winkler J, Abisoye-Ogunniyan A, *et al.* Concepts of extracellular matrix remodelling in tumour progression and metastasis. *Nature communications*, 2020. 11(1):1-19.
10. Crapo PM, Gilbert TW, *et al.* An overview of tissue and whole organ decellularization processes. *Biomaterials*, 2011. 32(12):3233-43.
11. Verstegen MMA, Willemsse J, *et al.* Decellularization of whole human liver grafts using controlled perfusion for transplantable organ bioscaffolds. *Stem cells and development*, 2017. 26(18):1304-15.
12. Parkinson GT, Salerno S, *et al.* Patient-derived scaffolds as a model of colorectal cancer. *Cancer medicine*, 2021. 10(3):867-82.
13. Landberg G, Fitzpatrick P, *et al.* Patient-derived scaffolds uncover breast cancer promoting properties of the microenvironment. *Biomaterials*, 2020. 235:119705.
14. Sensi F, D'Angelo E, *et al.* Recellularized colorectal cancer patient-derived scaffolds as in vitro pre-clinical 3D model for drug screening. *Cancers (Basel)*, 2020. 12(3):681.
15. Willemsse J, Verstegen MMA, *et al.* Fast, robust and effective decellularization of whole human livers using mild detergents and pressure controlled perfusion. *Materials Science and Engineering: C*, 2020. 108:110200.
16. Hall MP, Woodroffe CC, *et al.* Click beetle luciferase mutant and near infrared naphthyl-luciferins for improved bioluminescence imaging. *Nature communications*, 2018. 9(1):1-12.
17. Chen X, Nadiarynk O, *et al.* Second harmonic generation microscopy for quantitative analysis of collagen fibrillar structure. *Nature protocols*, 2012. 7(4):654-69.
18. Shao X, Taha IN, *et al.* MatrisomeDB: the ECM-protein knowledge database. *Nucleic Acids Res*, 2020. 48(D1):D1136-D44.
19. Vizcaino JA, Deutsch EW, *et al.* ProteomeXchange provides globally coordinated proteomics data submission and dissemination. *Nat Biotechnol*, 2014. 32(3):223-6.
20. Afgan E, Baker D, *et al.* The Galaxy platform for accessible, reproducible and collaborative biomedical analyses: 2016 update. *Nucleic acids research*, 2016. 44(W1):W3-W10.
21. Tang Z, Li C, *et al.* GEPIA: a web server for cancer and normal gene expression profiling and interactive analyses. *Nucleic acids research*, 2017. 45(W1):W98-W102.
22. Borcharding N, Bormann NL, *et al.* TRGAted: A web tool for survival analysis using protein data in the Cancer Genome Atlas. *F1000Research*, 2018. 7.
23. Badylak SF, Gilbert TW: Immune response to biologic scaffold materials *Seminars in immunology* 2008; 20:109-16.

24. Gilbert TW, Sellaro TL, *et al.* Decellularization of tissues and organs. *Biomaterials*, 2006. 27(19):3675-83.
25. Hamidi H, Ivaska J. Every step of the way: integrins in cancer progression and metastasis. *Nature Reviews Cancer*, 2018. 18(9):533-48.
26. Qian Y, Yao W, *et al.* aPKC- ζ /P-Sp1/Snail signaling induces epithelial–mesenchymal transition and immunosuppression in cholangiocarcinoma. *Hepatology*, 2017. 66(4):1165-82.
27. Li S, Li Q. Cancer stem cells, lymphangiogenesis, and lymphatic metastasis. *Cancer Lett*, 2015. 357(2):438-47.
28. Wang X, Lin Y. Tumor necrosis factor and cancer, buddies or foes? 1. *Acta Pharmacol Sin*, 2008. 29(11):1275-88.
29. Escarcega RO, Fuentes-Alexandro S, *et al.* The transcription factor nuclear factor-kappa B and cancer. *Clin Oncol*, 2007. 19(2):154-61.
30. Shin W, Wu A, *et al.* Spatiotemporal gradient and instability of Wnt induce heterogeneous growth and differentiation of human intestinal organoids. *Iscience*, 2020. 23(8):101372.
31. Valle J, Wasan H, *et al.* Cisplatin plus gemcitabine versus gemcitabine for biliary tract cancer. *New England Journal of Medicine*, 2010. 362(14):1273-81.
32. Zhang L, Lu L, *et al.* Convolutional invasion and expansion networks for tumor growth prediction. *IEEE Trans Med Imaging*, 2017. 37(2):638-48.
33. Hood JD, Cheresh DA. Role of integrins in cell invasion and migration. *Nature Reviews Cancer*, 2002. 2(2):91-100.
34. Krakhmal NV, Zavyalova MV, *et al.* Cancer invasion: patterns and mechanisms. *Acta Naturae (англоязычная версия)*, 2015. 7(2 (25)).
35. West J, Newton PK. Cellular interactions constrain tumor growth. *Proceedings of the National Academy of Sciences*, 2019. 116(6):1918-23.
36. Banales JM, Cardinale V, *et al.* Cholangiocarcinoma: current knowledge and future perspectives consensus statement from the European Network for the Study of Cholangiocarcinoma (ENSCCA). *Nature Reviews Gastroenterology & Hepatology*, 2016. 13(5):261-80.
37. Ruivo CF, Adem B, *et al.* The biology of cancer exosomes: insights and new perspectives. *Cancer Res*, 2017. 77(23):6480-8.
38. Vaquero J, Guedj N, *et al.* Epithelial-mesenchymal transition in cholangiocarcinoma: from clinical evidence to regulatory networks. *J Hepatol*, 2017. 66(2):424-41.
39. Taliana L, Evans MD, *et al.* Vitronectin is present in epithelial cells of the intact lens and promotes epithelial mesenchymal transition in lens epithelial explants. *Mol Vis*, 2006. 12:1233-42.
40. Shiota M, Zardan A, *et al.* Clusterin mediates TGF- β -induced epithelial–mesenchymal transition and metastasis via Twist1 in prostate cancer cells. *Cancer Res*, 2012. 72(20):5261-72.
41. Wang C, Maass T, *et al.* A systems biology perspective on cholangiocellular carcinoma development: focus on MAPK-signaling and the extracellular environment. *J Hepatol*, 2009. 50(6):1122-31.
42. Hu L, Lau SH, *et al.* Association of Vimentin overexpression and hepatocellular carcinoma metastasis. *Oncogene*, 2004. 23(1):298-302.
43. Singh S, Sadacharan S, *et al.* Overexpression of vimentin: role in the invasive phenotype in an androgen-independent model of prostate cancer. *Cancer Res*, 2003. 63(9):2306-11.
44. Li C, Wang J, *et al.* GDF15 promotes EMT and metastasis in colorectal cancer. *Oncotarget*, 2016. 7(1):860.
45. Sabit H, Tsuneyama K, *et al.* Enhanced expression of basement-membrane-type heparan sulfate proteoglycan in tumor fibro-myxoid stroma of intrahepatic cholangiocarcinoma. *Pathol Int*, 2001. 51(4):248-56.
46. Reister S, Mahotka C, *et al.* Nucleolin promotes Wnt signaling in human hematopoietic stem/progenitor cells. *Leukemia*, 2019. 33(4):1052-4.
47. Ugrinova I, Petrova M, *et al.* Multifaceted nucleolin protein and its molecular partners in oncogenesis. *Adv Protein Chem Struct Biol*, 2018. 111:133-64.

48. Li Y, Liang R, *et al.* AMPK-dependent phosphorylation of HDAC8 triggers PGM1 expression to promote lung cancer cell survival under glucose starvation. *Cancer Lett*, 2020. 478:82-92.
49. Gao L, Chen S, *et al.* Kinectin 1 promotes the growth of triple-negative breast cancer via directly co-activating NF-kappaB/p65 and enhancing its transcriptional activity. *Signal Transduction and Targeted Therapy*, 2021. 6(1):1-12.
50. Huang DW, Sherman BT, *et al.* Bioinformatics enrichment tools: paths toward the comprehensive functional analysis of large gene lists. *Nucleic acids research*, 2009. 37(1):1-13.
51. Sherman BT, Lempicki RA. Systematic and integrative analysis of large gene lists using DAVID bioinformatics resources. *Nature protocols*, 2009. 4(1):44-57.
52. Sekiguchi R, Yamada KM. Basement membranes in development and disease. *Curr Top Dev Biol*, 2018. 130:143-91.
53. Sirica AE. The role of cancer-associated myofibroblasts in intrahepatic cholangiocarcinoma. *Nature reviews Gastroenterology & hepatology*, 2012. 9(1):44-54.
54. Høgdall D, Lewinska M, *et al.* Desmoplastic tumor microenvironment and immunotherapy in cholangiocarcinoma. *Trends in cancer*, 2018. 4(3):239-55.
55. Zhang M, Yang H, *et al.* Single-cell transcriptomic architecture and intercellular crosstalk of human intrahepatic cholangiocarcinoma. *J Hepatol*, 2020. 73(5):1118-30.
56. Zhao Y, Li ZX, *et al.* Single-Cell Transcriptome Analysis Uncovers Intratumoral Heterogeneity and Underlying Mechanisms for Drug Resistance in Hepatobiliary Tumor Organoids. *Advanced Science*, 2021.2003897.
57. Guedj N, Blaise L, *et al.* Prognostic value of desmoplastic stroma in intrahepatic cholangiocarcinoma. *Modern Pathology*, 2021. 34(2):408-16.
58. Ng S, Tan WJ, *et al.* Mechanically and chemically defined hydrogel matrices for patient-derived colorectal tumor organoid culture. *Biomaterials*, 2019. 219:119400.
59. Rodriguez-Brenes IA, Komarova NL, *et al.* Tumor growth dynamics: insights into evolutionary processes. *Trends in ecology & evolution*, 2013. 28(10):597-604.
60. Yang D, Gao P, *et al.* Gompertz tracking of the growth trajectories of the human-liver-cancer xenograft-tumors in nude mice. *Comput Methods Programs Biomed*, 2020. 191:105412.
61. Friedl P, Hegerfeldt Y, *et al.* Collective cell migration in morphogenesis and cancer. *Int J Dev Biol*, 2004. 48(5-6):441-9.
62. Friedl P, Locker J, *et al.* Classifying collective cancer cell invasion. *Nat Cell Biol*, 2012. 14(8):777-83.
63. Ehrbar M, Sala A, *et al.* Elucidating the role of matrix stiffness in 3D cell migration and remodeling. *Biophys J*, 2011. 100(2):284-93.
64. Khalil AA, Friedl P. Determinants of leader cells in collective cell migration. *Integrative biology*, 2010. 2(11-12):568-74.
65. Carpino G, Overi D, *et al.* Matrisome analysis of intrahepatic cholangiocarcinoma unveils a peculiar cancer-associated extracellular matrix structure. *Clin Proteomics*, 2019. 16(1):1-12.
66. Utispan K, Thuwajit P, *et al.* Gene expression profiling of cholangiocarcinoma-derived fibroblast reveals alterations related to tumor progression and indicates periostin as a poor prognostic marker. *Molecular cancer*, 2010. 9(1):1-20.
67. Lee JI, Campbell JS. Role of desmoplasia in cholangiocarcinoma and hepatocellular carcinoma. *J Hepatol*, 2014. 61(2):432-4.
68. Mertens JC, Fingas CD, *et al.* Therapeutic effects of deleting cancer-associated fibroblasts in cholangiocarcinoma. *Cancer Res*, 2013. 73(2):897-907.
69. Thuwajit C, Thuwajit P, *et al.* Clustering of patients with intrahepatic cholangiocarcinoma based on serum periostin may be predictive of prognosis. *Oncology letters*, 2017. 14(1):623-34.
70. Aishima S-i, Taguchi K-i, *et al.* Tenascin expression at the invasive front is associated with poor prognosis in intrahepatic cholangiocarcinoma. *Modern pathology*, 2003. 16(10):1019.
71. Hirashita T, Iwashita Y, *et al.* Expression of matrix metalloproteinase-7 is an unfavorable prognostic factor in intrahepatic cholangiocarcinoma. *J Gastrointest Surg*, 2012. 16(4):842-8.

SUPPLEMENTARY INFORMATION

TABLES

Supplementary Table S1. Medium components for Starting Expansion Medium (SEM)

Component	Concentration	Brand
Adv+		Gibco
N2	1%	Gibco
B27	2%	Gibco
N-Acetylcystein	1mM	Sigma-Aldrich
gastrin	10 nM	Sigma-Aldrich
EGF	50 ng/ml	Peprotech
FGF10	100 ng/ml	Peprotech
HGF	25 ng/ml	Peprotech
nicotinamide	10nM	Sigma-Aldrich
A83.01	5 μ M	Tocris
Forskolin	10 μ M	Tocris
R-Spondin	10%	Conditioned medium
WNT	30% Wnt	Conditioned medium
Noggin	25 ng/ml	Conditioned medium
Y27632	10 μ M	Tocris
hES cell cloning recovery solution	1:1000 dilution	Stemgent

Supplementary Table S2. Medium components for Expansion Medium (EM)

Component	Concentration	Brand
Adv+		Gibco
N2	1%	Gibco
B27	2%	Gibco
N-Acetylcystein	1mM	Sigma-Aldrich
gastrin	10 nM	Sigma-Aldrich
EGF	50 ng/ml	Peprotech
FGF10	100 ng/ml	Peprotech
HGF	25 ng/ml	Peprotech
nicotinamide	10nM	Sigma-Aldrich
A83.01	5 μ M	Tocris
Forskolin	10 μ M	Tocris
R-Spondin	10%	Conditioned medium

Supplementary Table S3. Patient information and characteristics

Sample	Gender	Age	Localisation	Histological grade
CCAO1	F	34	Perihilar	Moderate-well differentiated
CCAO2	M	60	intrahepatic (segment 4)	Moderate-well differentiated
CCAO3	F	77	intrahepatic (segment 4)	Poor-moderate differentiated
CCAM1	F	75	intrahepatic (segment 7-8)	Moderate differentiated
CCAM2	F	72	intrahepatic (segment 4a-7-8)	Moderate differentiated
CCAM3	F	57	intrahepatic (segment 1)	Moderate differentiated
CCAM4	F	58	Intrahepatic (segment 2-3)	Moderate differentiated
CCAM5	F	59	Intrahepatic (segment 6)	Poor-moderate differentiated
CCAM6	M	64	Intrahepatic (segment 4)	moderate differentiated
TFLM1	M	65	n.a.	n.a.
TFLM2	M	66	n.a.	n.a.
TFLM3	M	68	n.a.	n.a.
TFLM4	F	58	n.a.	n.a.
TFLM5	F	59	n.a.	n.a.
TFLM6	M	64	n.a.	n.a.

Supplementary Table S4. Patient characteristics of CCAOs

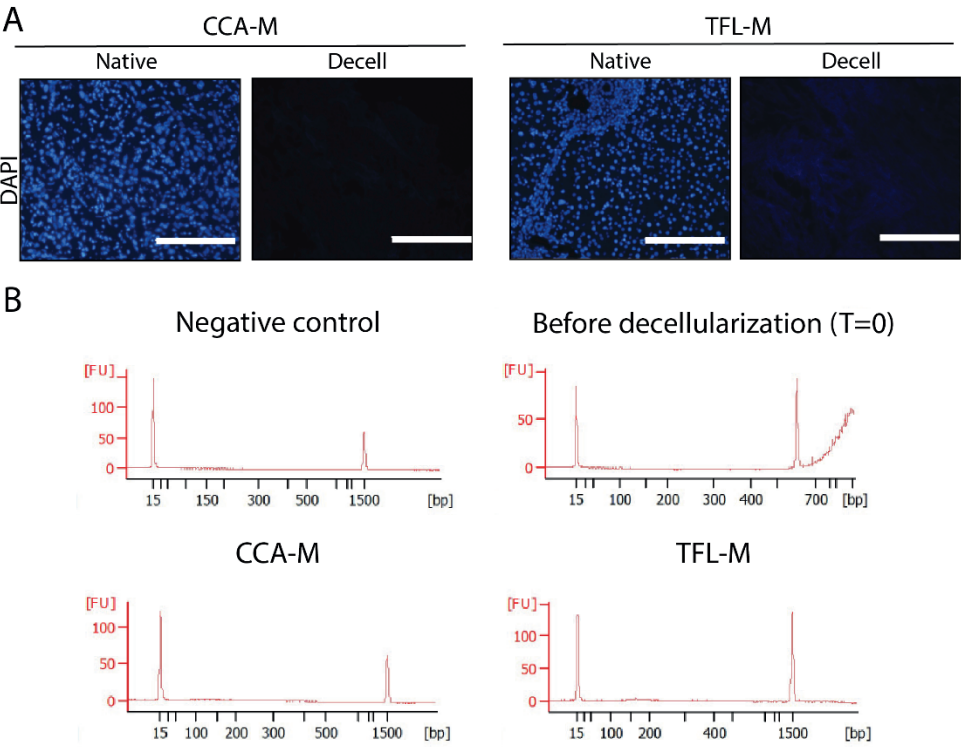
	CCAO1	CCAO2	CCAO3
Pre-treatment	None	None	None
Etiology	PSC	Unknown	Unknown
Tumor stage (TNM)	T2N2M0	T1NXM0	T3N1M0
Fibrosis/Cirrhosis	No	No	No
Bilirubin^a	13	5	8
CA19.9^b	42	64	18
AFP^b	5	-	4
CEA^b	-	-	45.8
Gamma-GT^a	546	93	68
AP^a	1831	74	73

^aDetermined 2-4 weeks before surgery. ^bDetermined 4-6 weeks before surgery. Gamma-GT = gamma-glutamyltransferase; AP = alkaline phosphatase; CA19.9 = cancer antigen 19.9; AFP = alpha fetoprotein; CEA = carcinoembryonic antigen.

Supplementary Table S5. Analysis of mutations present in CCAO1, 2, and 3.

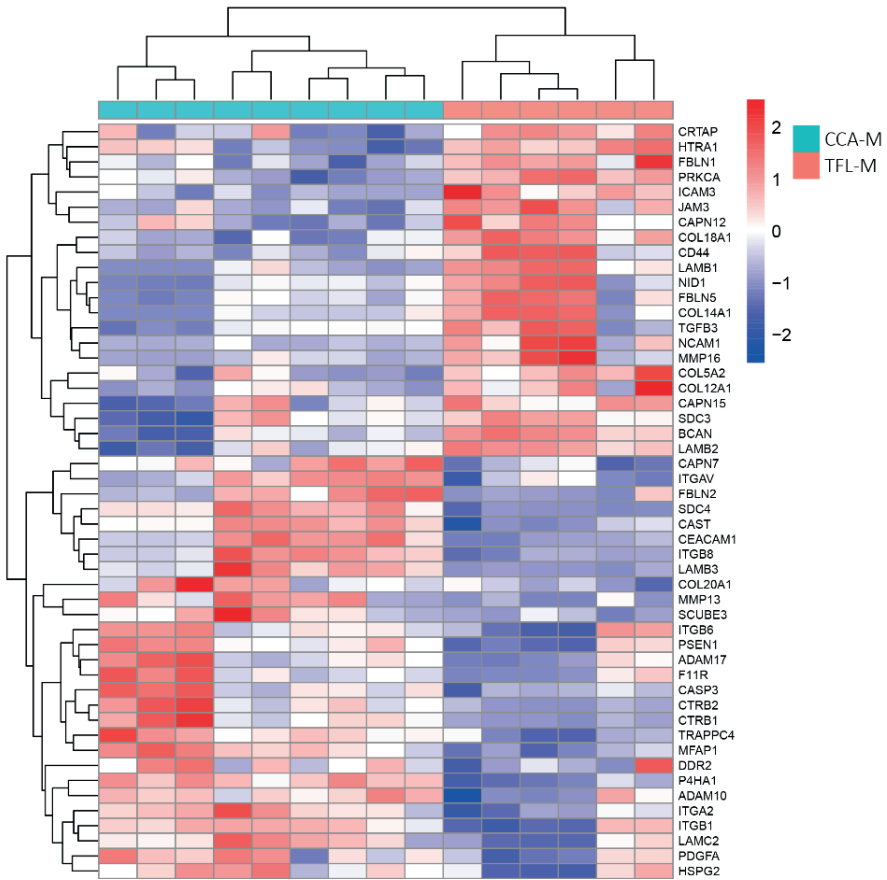
Organoid	Mutations		Chromosomal imbalance	
			Loss	Gain
CCAO1	ARID1A	p.Arg1989Ter	CDKN2A (homozygous)	
	IGF1R	Splicing		
	KRAS	p.Gly12Asp		
CCAO2	KRAS	p.Gly12Asp	ARID1A	DDR2
	TP53	p.Ala347Thr	VHL	MYC
			CTNNB1	IGF1R
			BAP1	
			FHIT	
			PIK3R1	
			ROS1	
			FGFR1	
			CDKN2A	
			TP53	
			SMAD4	
CCAO3	BAP1	p.Pro190Thr	MTOR	MYC
			ARID1A	PTEN
			NRAS	IGF1R
			CTNNB1	ERBB2
			BAP1	RNF43
			CDKN2A(homozygous)	

SUPPLEMENTARY FIGURES

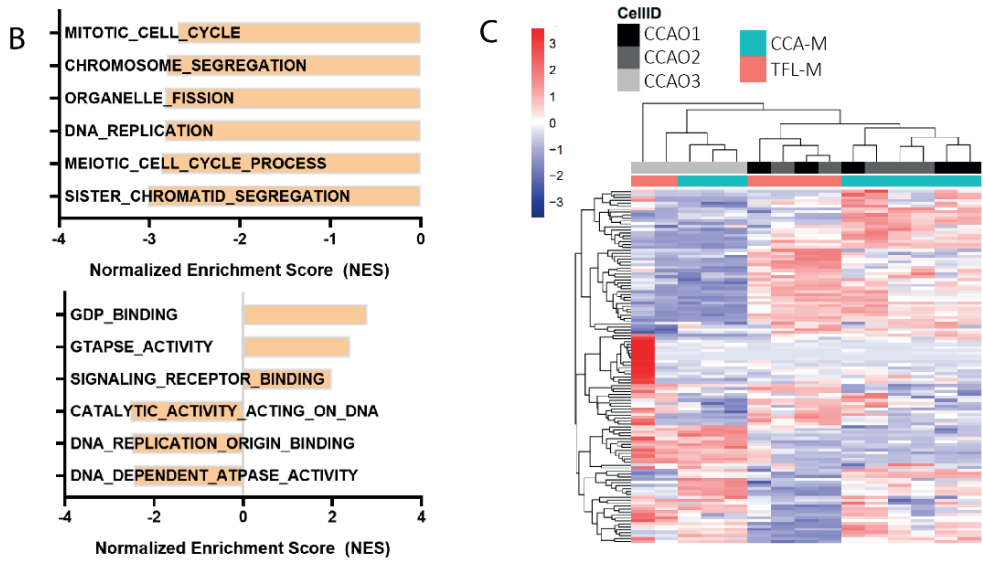


Suppl. Figure S1. Characterization of decellularized CCA and TFL tissue. (a) immunocytochemical characterization of CCA-M and TFL-M sections before and after decellularization stained with 4',6-diamidino-2-phenylindole (DAPI). Scale bars indicate 200 μ m. **(b)** Representative dsDNA curves of samples created by the Bioanalyzer. The T=0 samples show a clear rise in [FU] from around 700 bp on forwards. No dsDNA was detected in CCA-M and TFL-M samples, similar to the negative control.

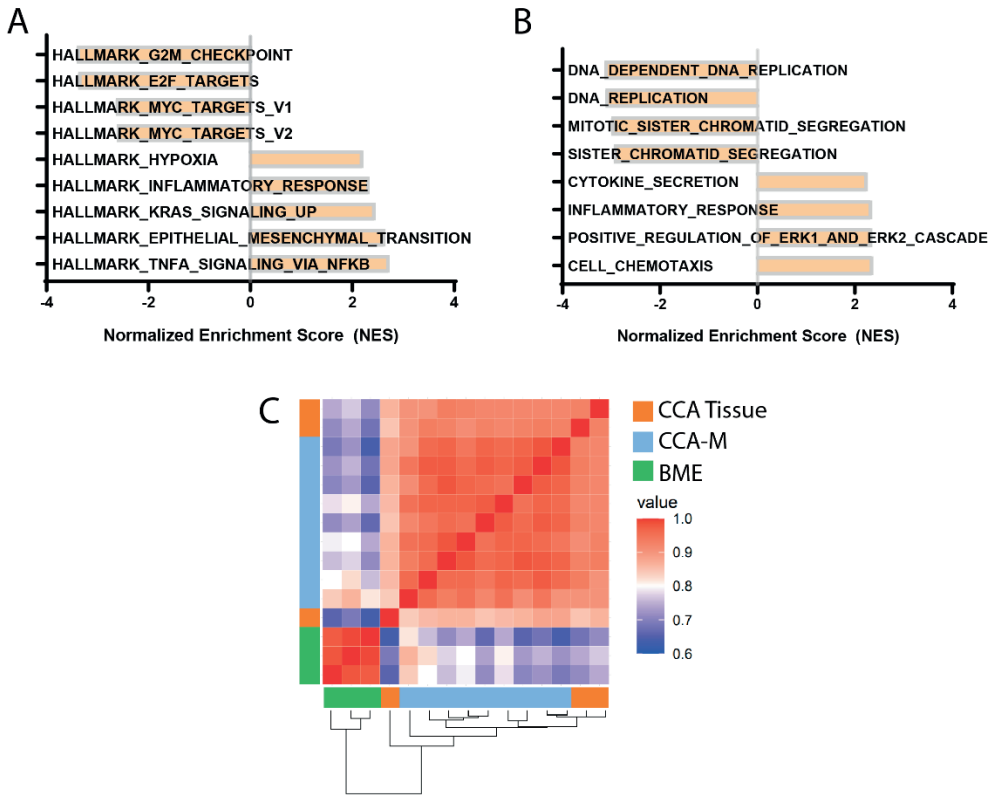
A



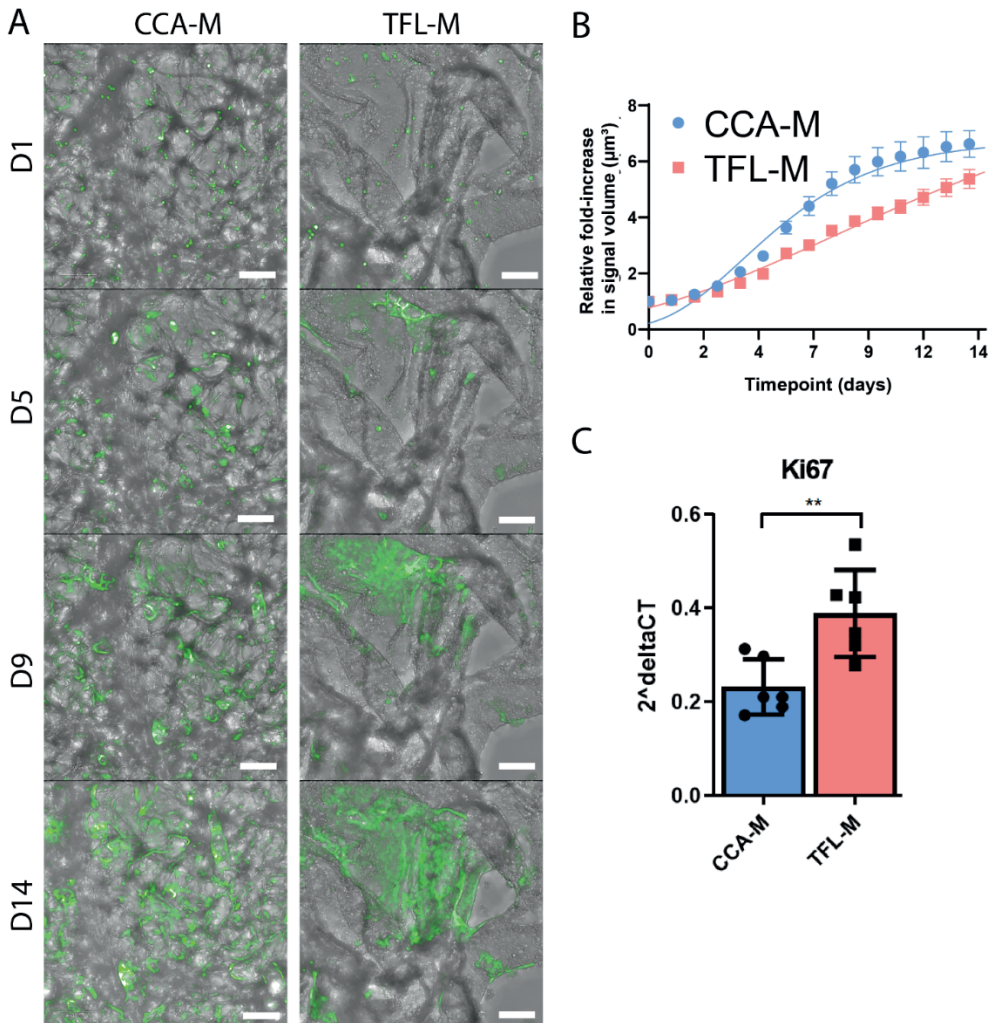
Suppl. Figure S2A. Transcriptome differences between CCA-M and TFL-M show extracellular matrix influences tumor-related pathways. (a) Heatmap showing the top 50 genes defining extracellular matrix organization and remodeling (R-HAS-1474244) ordered according to DE between CCA-M and TFL-M. The color map corresponds to the Z-scored Log_2 normalized counts. Important ECM remodeling-related genes, such as collagens, MMPs, and integrin's, show pronounced clustering.



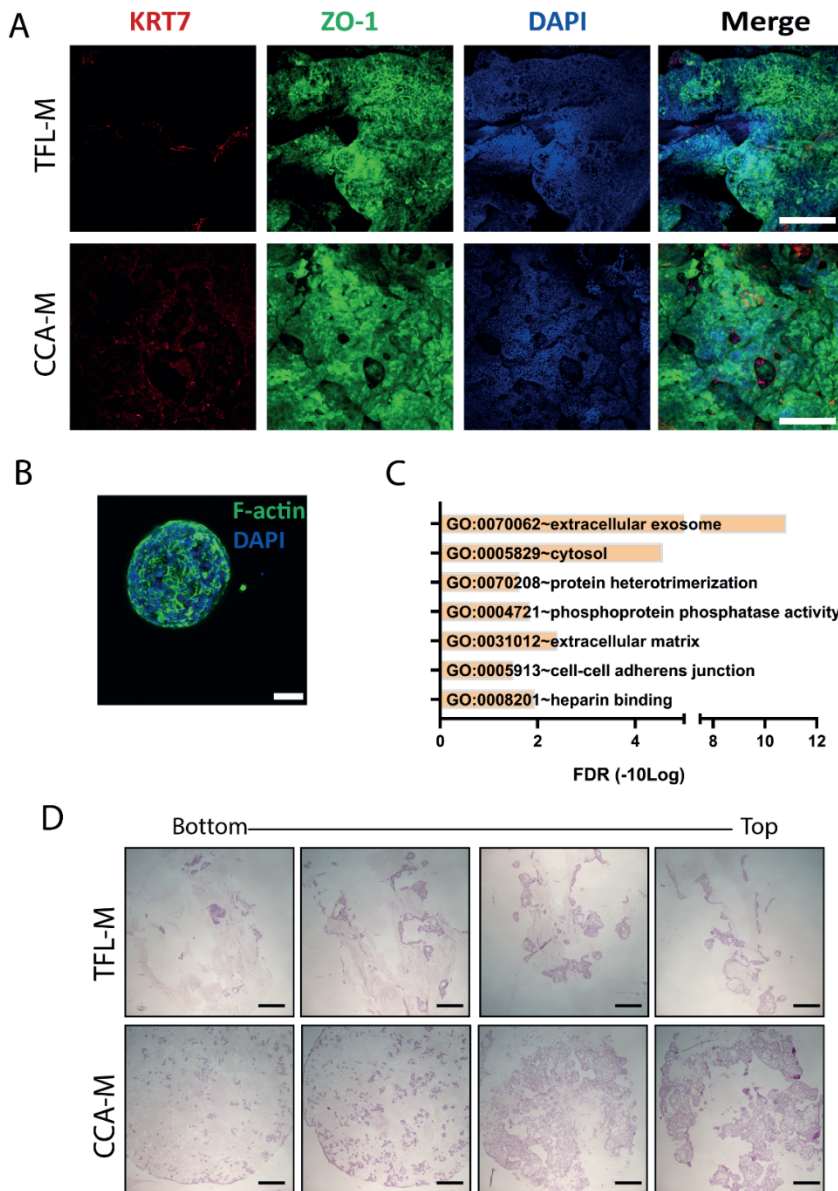
Suppl. Figure S2B-C. Transcriptome differences between CCA-M and TFL-M show extracellular matrix influences tumor-related pathways. (b) GSEA analysis integrating DEG between CCA-M and TFL-M based on gene sets derived from Gene Ontology: Biological Processes and Gene ontology: Molecular Function. Biological processes are mostly related to cellular proliferation and division. DNA division-related functions are enriched in TFL-M, while CCA-M shows more prominent cellular activity including signaling receptor binding. **(c)** Heatmap showing expression of genes defining epithelial-mesenchymal transition (Hallmark_EMT, M5930), with patient- and scaffold-dependent clustering present. The color scale corresponds to the Z-scored Log_2 normalized counts.



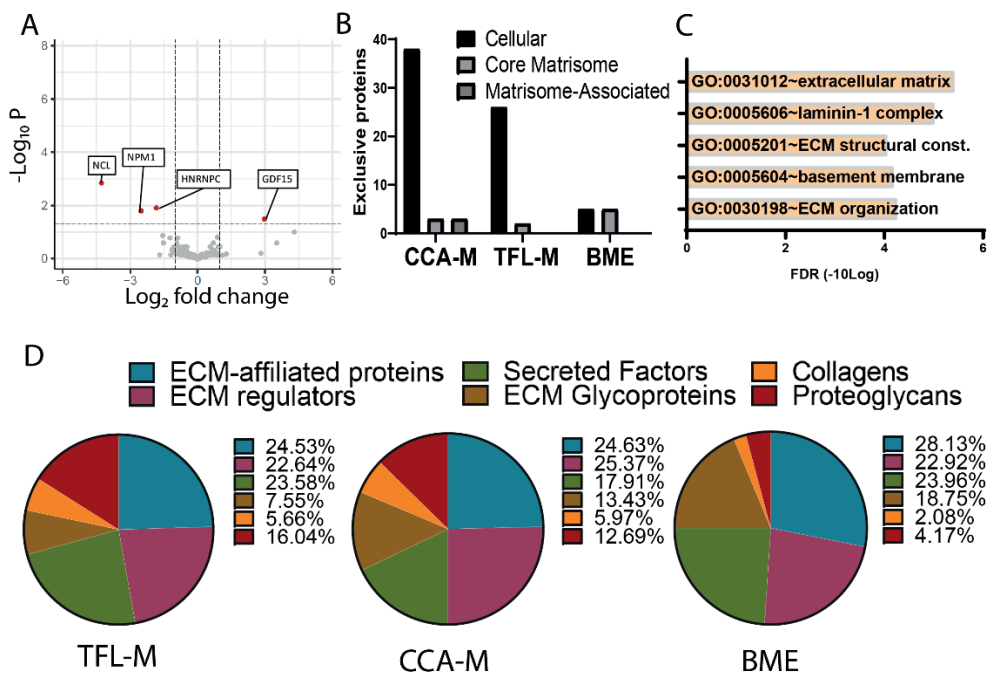
Suppl. Figure S3. Transcriptome differences between CCA-M and BME. (a, b) GSEA analysis for Hallmark gene sets (a) and Gene Ontology: Biological Processes (b) incorporating DEG comparing CCA-M and BME. Positive NES indicates upregulation of the particular gene set in CCA-M, negative NES indicates upregulation in BME. All NES scores presented are significantly enriched (adj. p val. < 0.05). (c) Correlation matrix between CCA tumor tissue, CCA-M, and BME transcriptome profiles. Top 100 DEG comparing CCA-M and BME were used for the comparison matrix. A value of 1 shows complete correlation, and a value of 0 shows no correlation.



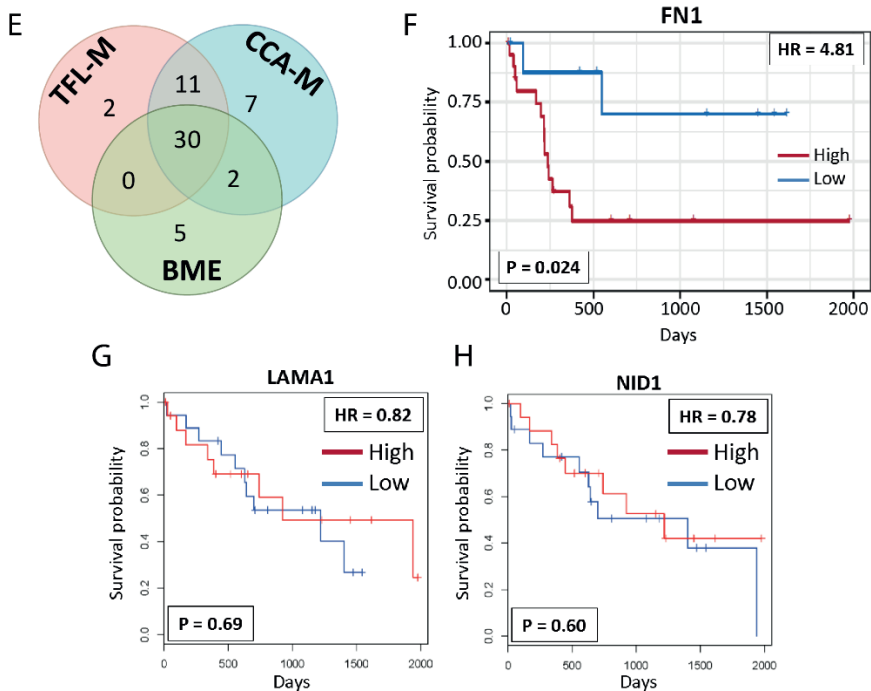
Suppl. Figure S4. Additional characterization of cell proliferation and migration of CCAOs on CCA-M and TFL-M. (a) Representative overlaid confocal and brightfield images of recellularized CCA-M and TFL-M with GFP-tagged CCAOs shows cell proliferation on both types of scaffold which is directed along the scaffold morphology. Scale bars indicate 200 μm. (b) Volume of GFP-tagged CCAOs over time plotted with a non-linear fit curve (Gompertz growth model). Least squares regression was used for fitting method. (c) RT-PCR shows upregulation of Ki67, a marker for proliferation, on a gene expression level in TFL-M scaffolds after 14 days in culture.



Suppl. Figure S5. Additional characterization of CCAOs shows distinct phenotypes induced by decellularized matrix compared to BME. (a) Whole-mount confocal imaging of KRT7 (red), ZO-1 (green), and DAPI (blue) of CCA-M and TFL-M cultured CCAOs after 14 days of culture. Scale bar indicates 200 μ m. **(b)** Whole-mount confocal imaging of F-actin (Phalloidin, green) and DAPI (blue) of CCAOs in BME culture 7 days after splitting. F-actin is located mostly in the cell membrane, similar to day 7 decellularized matrix cultures. Scale bar indicates 50 μ m. **(c)** GSEA of proteins exclusively present in CCA-M. Results were obtained using the DAVID database.¹ **(d)** Representative H&E stainings of CCA-M and TFL-M sectioned at multiple intervals from top to bottom. In TFL-M, the formation of large clusters of tumor cells forming at the top can be observed. In CCA-M, more widespread cellular presence is observed throughout the scaffold. Scale bars indicate 500 μ m. Higher magnification images can be found in Fig. 5H.



Suppl. Figure S6A-D. In-depth characterization of matrisome unveils a distinct tumor environment protein signature. (a) A volcano scatter plot of statistical significance (p -value) versus magnitude of change (Log_2 fold change) showing DE proteins between CCA-M and TFL-M. Positive log_2 fold change indicates increased abundance in CCA-M. (b) A bar graph of exclusive protein production separated for MatrisomeDB categories. (c) GSEA analysis of proteins exclusively present in a BME environment. BME culture limits CCAOs to producing extracellular matrix proteins that are related to the basement membrane. (d) Pie charts showing relative proportion of number of different matrisome proteins present. A more diverse set of collagens and proteoglycans are produced by CCAOs in decellularized scaffolds, both CCA-M and TFL-M, compared to BME.



Suppl. Figure S6E-H. In-depth characterization of matrisome unveils a distinct tumor environment protein signature. (e) Venn diagram of exclusively produced matrisome-related proteins. Proteins are deemed exclusive if they are present in all samples of one condition, and absent in all other samples. (f) Progression Free Survival (PFS) plot for groups with high and low protein expression of FN1 in the TCGA-CHOL cohort. Optimal cutoff points are based on finding the lowest log-rank p-value. Hazard ratio (HR) is determined from the Cox Proportional Hazard regression model.² (g) Overall survival plot for groups with high and low gene expression of LAMA1 in the TCGA-CHOL cohort. Group cut-offs for gene expression are at the median. Hazard ratio (HR) is determined from the Cox Proportional Hazard regression model.³ (h) Overall survival plot for groups with high and low gene expression of NID1 in the TCGA-CHOL cohort. Group cut-offs for gene expression are at the median. Hazard ratio (HR) is determined from the Cox Proportional Hazard regression model.³

SUPPLEMENTARY INFORMATION REFERENCES

1. Sherman BT, Lempicki RA. Systematic and integrative analysis of large gene lists using DAVID bioinformatics resources. *Nat Protoc*, 2009. 4(1):44-57.
2. Borchering N, Bormann NL, *et al.* TRGAted: A web tool for survival analysis using protein data in the Cancer Genome Atlas. *F1000Research*, 2018. 7.
3. Tang Z, Li C, *et al.* GEPIA: a web server for cancer and normal gene expression profiling and interactive analyses. *Nucleic Acids Res*, 2017. 45(W1):W98-W102.

CHAPTER

**General discussion &
Summary**

7

Cholangiocarcinoma (CCA) is a heterogeneous malignancy of the biliary tract. It is rare, occurring in 0.3-6 people per 100,000, but has a dismal prognosis with 5-year survival rates reported at 7-20%.¹ One of the factors responsible for this bleak outlook is the long non-symptomatic phase during CCA development. This leads to late discovery, often at locally advanced or metastasized stages, when patients are ineligible for curative surgical intervention. Moreover, CCA is notoriously heterogeneous, both inter- and intra-tumorally, and is remarkably resistant to (chemo)therapeutics, making it challenging to treat with systemic therapies. The development of targeted therapeutics and immunotherapy have changed the paradigm of cancer treatment over the last decades. Targeted therapeutics successfully treat cancer based on their molecular aberrations instead of their cell of origin, while immunotherapy harnesses the patient's own immune system to kill the tumor. Both of these approaches have shown promise in CCA treatment, although stratification of patients based on tumor characteristics is pivotal.²⁻⁴ Evaluating the plethora of putative CCA therapeutics in clinical trials is very expensive and time-consuming, and limited by the rarity of the disease, especially when stratification is necessary.

Patient-derived CCA organoids were established recently from resected tumor tissue and core needle biopsies.^{5, 6} They are an innovative scalable 3D preclinical model system that resembles to a large extent the histopathology, mutations and gene expression profiles of the epithelial cancer cell compartment of the patient tumor.⁵⁻⁹ In addition, they are amenable to drug screening and biomarker identification for therapy sensitivity.^{5, 8, 10} However, the CCA organoid model field is still in its infancy, and many applications of CCA organoids are still unexplored. For example, they could have value in studying drug resistances, cancer progression, dissecting intra- and inter-tumor heterogeneity, or identification of new therapeutic targets and stratification approaches. Moreover, CCA organoids only include the epithelial cancer cell compartment of the tumor, while CCA usually contains a complex tumor microenvironment (TME) that includes cancer-associated fibroblasts, immune cells, endothelial cells, and an extensive desmoplastic stroma.¹¹⁻¹³ Therefore, the aim of this thesis was to explore new applications of the CCA organoid model to discover therapeutic targets and to extend the current CCA organoid model to include the immune cell and tumor-specific stroma components of the TME to facilitate research of a broader range of therapeutics.

Bile as a potential source of cholangiocarcinoma organoids

The first step to acquire patient-derived organoids, is to obtain a patient sample containing live tumor cells. As only a minority of patients is eligible for surgical resection, CCA organoid derivation is currently reliant on core needle biopsies for most patients, which has inherent risks of bleeding and needle tract seeding leading to metastases.^{6, 14, 15} (Suspected) CCA patients regularly undergo diagnostic or therapeutic endoscopic interventions of the biliary tree, which provides access to bile. It is known that cancer cells are present in bile of CCA patients.¹⁶⁻¹⁸ Thus, bile could be an alternative minimally invasive source for CCA cell acquisition for organoid culture.

Soroka *et al.* were the first to report cholangiocyte organoids initiated from bile of PSC patients obtained during endoscopic retrograde cholangiopancreatography (ERCP).¹⁹ In **chapter 2**, we established organoids from bile obtained via ERCP and percutaneous transhepatic cholangiopathy (PTC) in patients with a variety of diseases, and from gallbladders of healthy organ donors. These organoids express genes specific for the extrahepatic biliary tree and have limited hepatocyte-fate differentiation potential, indicating they are likely initiated from cells shed by the local extrahepatic environment. This suggests CCA bile organoid culture would be best suited for extrahepatic tumors. Bile cholangiocyte organoid functionality was demonstrated by their ability to repopulate decellularized extrahepatic bile duct scaffolds in a monolayer of cholangiocyte-like cells. We also established several bile organoid cultures from patients with CCA, although we did not find any proof that these organoids were of tumor origin, but rather derived from local extrahepatic cholangiocytes. Some of these patients had intrahepatic tumors, which could complicate CCA cell acquisition via bile. Furthermore, non-tumorous organoid overgrowth is a known problem of tumor organoid establishment.^{5, 20, 21} Cell sorting or selection by medium composition adjustments may restrain this.^{20, 22} Even though this overgrowth is a challenge, CCA organoid establishment from bile holds promise, especially for extrahepatic tumors. This could allow tumor follow-up over time by multi-sampling, creating an opportunity for longitudinal examination of CCA biology and therapy sensitivity.

New applications of the cholangiocarcinoma organoid model to discover therapeutic targets

Patient stratification and identification of druggable targets by kinome profiling

Current stratification strategies for CCA are based on molecular profiling, which have led to successful clinical trials and concurrent FDA approval of IDH1 inhibitor ivosidenib and FGFR inhibitor pemigatinib in CCA patients with the appropriate genetic aberrations.^{2, 3, 23-25} However, even in pre-selected patient populations, these compounds are only effective in about one third of patients, while other drugs demonstrate even more selective effects. Improving the stratification of patients will lead to more effective treatment of CCA and will result in approval of more (targeted) therapeutics in specific CCA patient groups.

In **chapter 3**, we hypothesized that kinase activity more directly predicts kinase inhibitor efficacy, as kinase activity is the result of the complex interplay of genetic aberrations, with concurrent transcriptome and proteome changes, combined with the influence of extracellular signals. Kinome profiling was performed for CCA organoids to determine the activity of a broad range of kinases, combined with drug screening of targeted therapeutics. Kinase activity patterns in CCA are highly individual, reflecting the heterogeneous nature of the disease, and identifying potentially interesting personalized therapeutic targets (e.g. JAK). In contrast, MAPK, Src and EGFR family kinases were identified as putative druggable targets in CCA in general. In an exploratory correlation analysis, sensitivity for several kinase inhibitors was linked to their target kinase activity, while other drugs were correlated with unexpected kinase targets.

Our study demonstrates kinome profiling is feasible in CCA organoids and holds promise as a method to identify druggable targets and biomarkers for therapy stratification. However, this needs validation in a larger study including more patient-derived CCA organoid lines, and eventually in clinical trials. Additionally, one limitation is that this study only included FDA-approved compounds, which are often multi-kinase inhibitors affecting many kinase pathways. It would be interesting to include more specific compounds against the therapeutic targets identified by kinome profiling to confirm their potential in CCA therapy, and to apply patient-specific drug libraries based on their kinome profiles. Furthermore, kinome profiling before and after treatment could define which kinases are the most important targets of used compounds in CCA and could elucidate which kinase pathways are activated to escape kinase inhibitors.

Dissecting the role of inflammatory cytokines

Chronic fibrotic inflammatory disease primary sclerosing cholangitis (PSC) leads to the development of CCA in 9-20% of patients.^{26,27} PSC patients are ~20 years younger than other patients when they are diagnosed with CCA, but have a comparably dismal prognosis.^{27, 28} With the development of modern molecular characterization techniques and the increasing collaborative efforts in the field, biological differences between PSC-related CCA (PSC-CCA) and sporadic CCA have recently gained attention.²⁹ Understanding these could identify new treatment options for PSC-CCA patients.

In **chapter 4**, we demonstrated that PSC-CCA cancer cells have a higher proliferative index than sporadic CCA. Screening of PSC-related inflammatory cytokines in CCA organoids proved that IL-17A has a direct proliferation inducing effect, and IL-17A was locally expressed in PSC-CCA tumor tissue. This indicates IL-17A might contribute to the higher proliferative index in PSC-CCA and could potentially be a therapeutic target, especially in highly proliferative CCAs. In line with that, IL-17A has been shown to contribute to tumorigenesis and cancer progression in a range of malignancies, including colon, pancreas, liver and lung.³⁰⁻³⁴ Inhibition of IL-17A or its producing cells has been demonstrated to constrain cancer progression in mouse models of breast and colon cancer.^{31, 35} Moreover, IL-17A was shown to induce resistance to chemotherapy, VEGFR inhibitors and immune checkpoint inhibitors in preclinical models.^{31, 36, 37} The clinical value of IL-17A inhibition in cancer patients is yet to be discovered.

One of the limitations of this study is that the effect of IL-17A was evaluated in organoids initiated from sporadic CCA instead of PSC-CCA. PSC-CCA is a very rare disease, so sample acquisition is challenging, and the relatively low establishment efficiency of CCA organoids further dilutes the pool of potential PSC-CCA organoid cultures.²⁰ In future experiments, the proliferation inducing effect of IL-17A should be examined side by side in PSC-CCA and sporadic CCA organoid lines, to investigate if sensitivity is similar and confirm the effect in a larger number of patient-derived cultures. IL-17A inhibition in CCA organoids could confirm its potential as a therapeutic target in CCA, either as a monotherapy or combination therapy regimen to abrogate resistance.

This study demonstrated that it is feasible to study the effect of inflammatory cytokines, and likely other biological factors, in CCA organoids to identify new potential therapeutic targets. The organoid model is particularly suited to show the direct effect of these factors on the epithelial cancer cell compartment of the tumor. Even though this provides important insight into the biological processes involved in cancer, the cells and stromal compartment of the TME modulate the effect of biological factors on cancer cells in the patient. Therefore, a modifiable CCA organoid model system with the option to add components of the TME, e.g. cancer-associated fibroblasts, immune cells, and the extracellular matrix, could have an immense value in CCA research, as it allows the determination of the effects of endogenous substances and therapeutics on isolated components of the tumor and on the tumor as a whole.

Extending the cholangiocarcinoma organoid model with tumor microenvironment components

Adding immune cells to the CCA organoid model

Modeling the interaction between immune cells and cancer cells *in vitro* could facilitate preclinical research of anti-tumor immunity and immunotherapy in CCA. In **chapter 5**, proof-of-concept is shown of an innovative and optimized co-culture method for CCA organoids and human blood-derived immune cells. Anti-organoid immune responses were quantifiable in co-cultures and in organoids exposed to soluble factors produced by immune cells, with variable responses between CCA organoid lines. Diversity in immune cell interactions with CCAs are to be expected, as CCAs are known to be heterogeneous, which leads to a variety of biological behavior.¹

A limitation of this study is that co-cultures were established using allogeneic immune cells from healthy donors or other liver cancer patients, which induces allogeneic immune activation due to mismatched human leukocyte antigens (HLAs) that activate T cells. Currently, co-culture of CCA organoids and patient-specific immune cells from large patient cohorts remains challenging. CCA organoid establishment is only successful in about one third of patients and the number of tumor-infiltrating lymphocytes (TILs) required for co-cultures demands the use of resected specimen to obtain enough tumor tissue.²⁰ Nonetheless, feasibility of autologous TIL co-culture has been reported for rectal cancer organoids.³⁸ Therefore, a follow-up study should combine CCA organoids and autologous immune cells, preferably TIL, to examine patient-specific anti-tumor immune responses. The TIL population contains both effector T and B lymphocytes and immunosuppressive regulatory T cells.³⁹ As the regulatory T cells are able to dampen the anti-cancer cytotoxic T cell activity in the patient^{12, 39}, it is likely that anti-CCA organoid responses in an autologous co-culture model with TILs are dampened too. This would provide an accurate model to test the ability of immune checkpoint inhibitors to overcome the immunosuppressive conditions. Subsequently, a clinical trial comparing patient response and autologous co-culture response to immune checkpoint inhibitors is necessary to determine the clinical predictive value of the model. Then, the autologous co-culture model could provide a

platform to test immune checkpoint inhibitors and to determine factors that influence immunotherapy sensitivity, which could lead to better patient stratification.

Adding the extracellular matrix to the CCA organoid model

Thus far, CCA organoids were cultured in a basement membrane hydrogel that does not reflect the physical properties nor the matrix components of the CCA extracellular matrix (ECM).⁵⁻¹⁰ In **chapter 6**, we explored the interaction between CCA cells and the surrounding ECM by establishing a culture model for CCA organoids in decellularized CCA ECM and tumor-free liver ECM. Decellularization of resected CCA and tumor-free liver tissue biopsies effectively removed cells while maintaining the structural integrity of the ECM. The decellularized ECM supports CCA organoid growth, similar to how decellularized bile duct tissue supports bile derived organoid growth in **chapter 2**. In fact, CCA organoids cultured in the decellularized CCA ECM more closely resembled the gene expression patterns of the original tumor tissue compared to the traditional culture methods, indicating the model more faithfully represents the patient tumor. Organoid culture in CCA ECM increases chemotherapy resistance, which demonstrates the value of a relevant ECM in drug efficacy research. In line with these results, a CCA xenograft model demonstrated that inhibition of ECM-producing cancer associated fibroblasts (CAFs) counteracts resistance and can restore chemotherapy response.⁴⁰ In the tumor-free ECM, CCA organoids initiated deposition of collagens, creating their own desmoplastic environment in which CCA thrives. These results indicate that in the absence of CAFs, the most important ECM modulators in the CCA TME, CCA cells themselves are able to modify the ECM to its advantage.

A question that remains for future research is to what extent the CCA ECM is heterogeneous between patients, and the importance of providing a patient-specific ECM to CCA organoids. Furthermore, the important ECM-modulating role of CAFs should be explored in the decellularized ECM, with and without the presence of CCA organoids. A co-culture model of CCA organoids and CAFs has been established recently, demonstrating that CAFs stimulate CCA organoid growth and induce therapy resistance, both *in vitro* and upon xenografting *in vivo*.⁴¹ Addition of the more biologically relevant decellularized ECM could solidify these findings. In turn, this combined model system could be used to test therapeutics that target CAFs or the components of the ECM as a new therapeutic strategy for CCA treatment.

Future outlook: Extending cholangiocarcinoma organoid models to overcome current limitations

It is clear that the CCA organoid model holds promise as a preclinical model for therapy discovery and identification of stratification strategies. They mirror the epithelial cancer cell compartment of the patient tumor to a large extent and are amenable to many downstream applications. Moreover, organoids can be combined with other components of the TME to create a more well-rounded tumor model.

However, current studies have all been performed with a small number of patient-derived organoid lines, demonstrating feasibility of diverse CCA organoid applications, but hampering the translation of these findings to the clinic. Causal factors could be the rarity of CCA, especially when research groups are dependent on resected specimen, the

suboptimal organoid establishment efficiency, and the time and effort needed to initiate, confirm and characterize a new patient-derived CCA organoid culture. Therefore, in the ideal world, a shared CCA organoid biobank would be established that contains CCA organoids from the whole spectrum of clinical CCA phenotypes, including all anatomical sites, histological subtypes, and underlying diseases. Every organoid line would be fully characterized by multi-omics approaches, ensuring the biobank covers the broad range of molecular aberrations relevant in CCA, and enabling analyses of the correlations between research findings and the molecular characteristics of the organoids. Although this might sound far off, living organoid biobanks have been developed for other cancer types consisting of up to 100 patient-derived organoid cultures.⁴²⁻⁴⁵ Ideally, a prospective CCA organoid biobank would also collect matching patient-derived TME components, including CAFs, tumor-infiltrating and circulating immune cells, and tumor-derived ECM. This would allow researchers to request CCA organoids of their pheno- and genotype of interest, together with TME building blocks that would cater best to their research question. Such a well characterized tailor-made CCA model could advance our knowledge of cancer biology, facilitate therapy discovery and development, and allow for identification of biomarkers for therapy stratification.

Yet, there are several challenges to overcome before a living organoid biobank of CCA organoids is feasible and valuable to its full potential. First, to generate an organoid library of the full spectrum of CCA phenotypes and genotypes, including rare subtypes such as PSC-related CCA, a high establishment rate is important. For potential personalized medicine applications, it is even more crucial to be able to cater to the majority of CCA patients. Sample acquisition also inevitably provides patient risk that has to be justified by a high chance of clinical benefit. This challenge can be approached twofold, increasing patient inclusion on the one hand, and improving establishment efficiency from samples on the other hand. An obvious way to increase inclusion is involving more centers in CCA organoid research. On top of that, CCA organoid derivation from bile could expand the patient pool by providing a less invasive method to gain access to CCA cells. Once samples are acquired, approximately 36% of resected tissue and core needle biopsies results in successful CCA organoid culture.²⁰ A multi-center evaluation could not identify patient or tumor characteristics correlated to successful organoid derivation.^{20, 46} However, genetic aberrations and underlying disease were not taken into account, and could be important factors in successful organoid establishment. Thus, they require further attention. In addition, standardization of sample acquisition and culture initiation protocols could increase the success rate. Likewise, selection for cancer organoids over non-malignant organoids by handpicking or medium composition adjustments could improve establishment efficiencies.²⁰

Second, there are logistical and financial aspects to consider. The relative rarity of CCA necessitates extensive international collaborative efforts to create a biobank containing the full spectrum of the disease. Furthermore, establishment and maintenance of living organoid biobanks requires a research environment focused on this purpose. Non-profit companies like HUB Organoid Technology show that it is logistically and financially feasible

to establish and manage these biobanks in a centralized and specialized institute, and to make them available to academic and industry partners upon request and ethical approval.^{43, 47}

Third, there are biological aspects of the CCA organoid model that are still to be explored. One of those is the preservation of intratumor heterogeneity, a key characteristic of CCA that contributes to high therapy resistance. Nuciforo *et al.* addressed this by comparing the cancer cell fraction that harbors identified mutations in 3 CCA organoid cultures and the corresponding patient tissue samples, which suggests that intratumor heterogeneity was partially retained.⁶ Sequencing of single cell-derived clonal organoids, combined with modern single cell analysis methods could shed further light on the preservation of intratumor heterogeneity in CCA organoids.^{48, 49} In addition, it is important to realize that organoids can only recapitulate intratumor heterogeneity from the specific biopsy site. Li *et al.* demonstrated that multiple CCA organoid lines from distinct regions within the same tumor can respond differently to therapeutics, and molecular profiling of multiple lines from one patient revealed heterogeneous mutational patterns and transcriptomic variation.¹⁰ In many cancer types, sequencing studies have revealed that multi-sampling is vital to gain complete coverage of the heterogeneous genetic aberrations in a tumor.⁵⁰⁻⁵³ Thus, to capture the complete extent of a tumor in organoid culture, multi-sampling is necessary.

Another interesting question is if CCA organoids could mimic disease progression. Cancer is remarkably capable of adaptation and genomic instability combined with changing environmental cues causes tumor evolution over time. A regrettable clinical implication of this phenomenon is the adaptation to treatment, leading to the development of therapy resistance and disease progression.⁵⁰ Ideally, CCA organoids would mirror these temporal developments that occur in the patient when exposed to the same therapeutics. Otherwise, sequential biopsies as the disease evolves in the patient could ensure the CCA organoid models remain clinically relevant.

This closely relates to the final challenge to be addressed, which is the determination of the translational value of CCA organoids. Even though they resemble many aspects of the original tumors, their clinical predictive value can only be determined in clinical trials that match patient and patient-derived organoid treatment to compare outcomes. 17 studies predicting patient treatment response based on *in vitro* cancer organoid drug sensitivity were recently reviewed.⁵⁴ Collectively, they achieved a sensitivity of 81% and a specificity of 74%, although the number of patients included in several of the studies was limited. Nonetheless, organoid-directed therapy selection is clearly feasible in cancer patients, providing confidence that this could be replicated with CCA organoids.

Once these challenges have been overcome, a living CCA organoid biobank could come to its full potential and facilitate an abundance of preclinical applications to advance the field of CCA research.

Conclusion

Cholangiocarcinoma is a heterogeneous cancer with a dismal prognosis due to late diagnosis and limited treatment options. CCA organoid culture has provided the field with an innovative patient-derived preclinical CCA model with the potential to further our understanding of the disease and improve CCA treatment. In my thesis, I have explored new applications of the CCA organoid model and extended this model with the addition of TME components and a potential new source of organoids. It was shown that bile is a minimally invasive source of healthy extrahepatic cholangiocyte organoids, which could be extended to CCA patients in future research. Moreover, kinome profiling of CCA organoids was a feasible and promising technique to identify druggable targets in tumor cells and, combined with drug screening, to provide biomarkers for therapy stratification. The effect of inflammatory cytokines could be studied in the CCA organoid model and identified IL-17A as a proliferation inducing factor and potential druggable target. CCA organoids were combined with immune cells and decellularized ECM to create new model systems that more faithfully represent the patient tumor and could provide a platform to test immunotherapy and ECM-targeted therapeutics. Thus, CCA organoids are a promising model for the discovery of new therapies and stratification strategies, that can be modified based on the research question by addition of TME components.

REFERENCES

1. Banales JM, Marin JGG, *et al.* Cholangiocarcinoma 2020: the next horizon in mechanisms and management. *Nat Rev Gastroenterol Hepatol*, 2020. 17(9):557-88.
2. Abou-Alfa GK, Sahai V, *et al.* Pemigatinib for previously treated, locally advanced or metastatic cholangiocarcinoma: a multicentre, open-label, phase 2 study. *The Lancet Oncology*, 2020. 21(5):671-84.
3. Abou-Alfa GK, Macarulla T, *et al.* Ivosidenib in IDH1-mutant, chemotherapy-refractory cholangiocarcinoma (ClarIDHy): a multicentre, randomised, double-blind, placebo-controlled, phase 3 study. *Lancet Oncol*, 2020. 21(6):796-807.
4. Rizvi S, Khan SA, *et al.* Cholangiocarcinoma—evolving concepts and therapeutic strategies. *Nature reviews Clinical oncology*, 2018. 15(2):95-111.
5. Broutier L, Mastrogianni G, *et al.* Human primary liver cancer-derived organoid cultures for disease modeling and drug screening. *Nat Med*, 2017. 23(12):1424-35.
6. Nuciforo S, Fofana I, *et al.* Organoid Models of Human Liver Cancers Derived from Tumor Needle Biopsies. *Cell Rep*, 2018. 24(5):1363-76.
7. Lampis A, Carotenuto P, *et al.* MIR21 drives resistance to heat shock protein 90 inhibition in cholangiocarcinoma. *Gastroenterology*, 2018. 154(4):1066-79. e5.
8. Saito Y, Muramatsu T, *et al.* Establishment of Patient-Derived Organoids and Drug Screening for Biliary Tract Carcinoma. *Cell Rep*, 2019. 27(4):1265-76 e4.
9. Maier CF, Zhu L, *et al.* Patient-Derived Organoids of Cholangiocarcinoma. *Int J Mol Sci*, 2021. 22(16).
10. Li L, Knutsdottir H, *et al.* Human primary liver cancer organoids reveal intratumor and interpatient drug response heterogeneity. *JCI insight*, 2019. 4(2).
11. Sirica AE, Gores GJ. Desmoplastic stroma and cholangiocarcinoma: clinical implications and therapeutic targeting. *Hepatology*, 2014. 59(6):2397-402.
12. Fabris L, Sato K, *et al.* The Tumor Microenvironment in Cholangiocarcinoma Progression. *Hepatology*, 2021. 73 Suppl 1:75-85.
13. Zhang M, Yang H, *et al.* Single-cell transcriptomic architecture and intercellular crosstalk of human intrahepatic cholangiocarcinoma. *J Hepatol*, 2020. 73(5):1118-30.
14. Robertson EG, Baxter G. Tumour seeding following percutaneous needle biopsy: the real story! *Clin Radiol*, 2011. 66(11):1007-14.
15. Singh A, Siddiqui UD. The Role of Endoscopy in the Diagnosis and Management of Cholangiocarcinoma. *J Clin Gastroenterol*, 2015. 49(9):725-37.
16. Kurzawinski TR, Deery A, *et al.* A prospective study of biliary cytology in 100 patients with bile duct strictures. *Hepatology*, 1993. 18(6):1399-403.
17. Hung LY, Chiang NJ, *et al.* A Microfluidic Chip for Detecting Cholangiocarcinoma Cells in Human Bile. *Sci Rep*, 2017. 7(1):4248.
18. Sugimoto S, Matsubayashi H, *et al.* Diagnosis of bile duct cancer by bile cytology: usefulness of post-brushing biliary lavage fluid. *Endosc Int Open*, 2015. 3(4):E323-8.
19. Soroka CJ, Assis DN, *et al.* Bile-Derived Organoids From Patients With Primary Sclerosing Cholangitis Recapitulate Their Inflammatory Immune Profile. *Hepatology*, 2019. 70(3):871-82.
20. van Tienderen GS, Li L, *et al.* Hepatobiliary tumor organoids for personalized medicine: a multicenter view on establishment, limitations, and future directions. *Cancer Cell*, 2022. 40(3):226-30.
21. Dijkstra KK, Monkhorst K, *et al.* Challenges in Establishing Pure Lung Cancer Organoids Limit Their Utility for Personalized Medicine. *Cell Reports*, 2020. 31(5):107588.
22. Drost J, Clevers H. Organoids in cancer research. *Nature Reviews Cancer*, 2018. 18(7):407-18.
23. Zhu AX, Macarulla T, *et al.* Final Overall Survival Efficacy Results of Ivosidenib for Patients With Advanced Cholangiocarcinoma With IDH1 Mutation: The Phase 3 Randomized Clinical ClarIDHy Trial. *JAMA Oncol*, 2021. 7(11):1669-77.

24. FDA. FDA approves ivosidenib for advanced or metastatic cholangiocarcinoma. <https://www.fda.gov/drugs/resources-information-approved-drugs/fda-approves-ivosidenib-advanced-or-metastatic-cholangiocarcinoma> 2022.
25. FDA. FDA grants accelerated approval to pemigatinib for cholangiocarcinoma with an FGFR2 rearrangement or fusion. <https://www.fda.gov/drugs/resources-information-approved-drugs/fda-grants-accelerated-approval-pemigatinib-cholangiocarcinoma-fgfr2-rearrangement-or-fusion> 2022.
26. Karlsen TH, Folseraas T, *et al.* Primary sclerosing cholangitis - a comprehensive review. *J Hepatol*, 2017. 67(6):1298-323.
27. Song J, Li Y, *et al.* Cholangiocarcinoma in Patients with Primary Sclerosing Cholangitis (PSC): a Comprehensive Review. *Clin Rev Allergy Immunol*, 2020. 58(1):134-49.
28. Jansson H, Olthof PB, *et al.* Outcome after resection for perihilar cholangiocarcinoma in patients with primary sclerosing cholangitis: an international multicentre study. *HPB*, 2021. 23(11):1751-8.
29. Goepfert B, Folseraas T, *et al.* Genomic Characterization of Cholangiocarcinoma in Primary Sclerosing Cholangitis Reveals Therapeutic Opportunities. *Hepatology*, 2020. 72(4):1253-66.
30. Li X, Bechara R, *et al.* IL-17 receptor-based signaling and implications for disease. *Nat Immunol*, 2019. 20(12):1594-602.
31. Wang K, Kim MK, *et al.* Interleukin-17 receptor a signaling in transformed enterocytes promotes early colorectal tumorigenesis. *Immunity*, 2014. 41(6):1052-63.
32. Zhang Y, Zoltan M, *et al.* Immune cell production of interleukin 17 induces stem cell features of pancreatic intraepithelial neoplasia cells. *Gastroenterology*, 2018. 155(1):210-23. e3.
33. Sun C, Kono H, *et al.* Interleukin-17A plays a pivotal role in chemically induced hepatocellular carcinoma in mice. *Digestive diseases and sciences*, 2016. 61(2):474-88.
34. Jin C, Lagoudas GK, *et al.* Commensal microbiota promote lung cancer development via $\gamma\delta$ T cells. *Cell*, 2019. 176(5):998-1013. e16.
35. Coffelt SB, Kersten K, *et al.* IL-17-producing $\gamma\delta$ T cells and neutrophils conspire to promote breast cancer metastasis. *Nature*, 2015. 522(7556):345-8.
36. Chung AS, Wu X, *et al.* An interleukin-17-mediated paracrine network promotes tumor resistance to anti-angiogenic therapy. *Nature Medicine*, 2013. 19(9):1114-23.
37. Zhang Y, Chandra V, *et al.* Interleukin-17-induced neutrophil extracellular traps mediate resistance to checkpoint blockade in pancreatic cancer. *J Exp Med*, 2020. 217(12).
38. Kong JCH, Guerra GR, *et al.* Tumor-Infiltrating Lymphocyte Function Predicts Response to Neoadjuvant Chemoradiotherapy in Locally Advanced Rectal Cancer. *JCO Precis Oncol*, 2018. 2:1-15.
39. Zhou G, Sprengers D, *et al.* Reduction of immunosuppressive tumor microenvironment in cholangiocarcinoma by ex vivo targeting immune checkpoint molecules. *J Hepatol*, 2019. 71(4):753-62.
40. Yamanaka T, Harimoto N, *et al.* Nintedanib inhibits intrahepatic cholangiocarcinoma aggressiveness via suppression of cytokines extracted from activated cancer-associated fibroblasts. *British Journal of Cancer*, 2020. 122(7):986-94.
41. Liu J, Li P, *et al.* Cancer-Associated Fibroblasts Provide a Stromal Niche for Liver Cancer Organoids That Confers Trophic Effects and Therapy Resistance. *Cell Mol Gastroenterol Hepatol*, 2021. 11(2):407-31.
42. Jacob F, Salinas RD, *et al.* A Patient-Derived Glioblastoma Organoid Model and Biobank Recapitulates Inter- and Intra-tumoral Heterogeneity. *Cell*, 2020. 180(1):188-204.e22.
43. Sachs N, de Ligt J, *et al.* A Living Biobank of Breast Cancer Organoids Captures Disease Heterogeneity. *Cell*, 2018. 172(1):373-86.e10.
44. Calandrini C, Schutgens F, *et al.* An organoid biobank for childhood kidney cancers that captures disease and tissue heterogeneity. *Nature Communications*, 2020. 11(1):1310.

45. Yao Y, Xu X, *et al.* Patient-Derived Organoids Predict Chemoradiation Responses of Locally Advanced Rectal Cancer. *Cell Stem Cell*, 2020. 26(1):17-26.e6.
46. van Tienderen GS, Li L, *et al.* Hepatobiliary tumor organoids for personalized medicine: a multicenter view on establishment, limitations, and future directions. *Cancer Cell*, 2022.
47. Hub Organoid Technology. www.huborganoids.nl 2022.
48. Jager M, Blokzijl F, *et al.* Measuring mutation accumulation in single human adult stem cells by whole-genome sequencing of organoid cultures. *Nat Protoc*, 2018. 13(1):59-78.
49. Roerink SF, Sasaki N, *et al.* Intra-tumour diversification in colorectal cancer at the single-cell level. *Nature*, 2018. 556(7702):457-62.
50. Dagogo-Jack I, Shaw AT. Tumour heterogeneity and resistance to cancer therapies. *Nature Reviews Clinical Oncology*, 2018. 15(2):81-94.
51. Gerlinger M, Rowan AJ, *et al.* Intratumor heterogeneity and branched evolution revealed by multiregion sequencing. *N Engl J Med*, 2012. 366:883-92.
52. Yates LR, Gerstung M, *et al.* Subclonal diversification of primary breast cancer revealed by multiregion sequencing. *Nature medicine*, 2015. 21(7):751-9.
53. Zhang J, Fujimoto J, *et al.* Intratumor heterogeneity in localized lung adenocarcinomas delineated by multiregion sequencing. *Science*, 2014. 346(6206):256-9.
54. Wensink GE, Elias SG, *et al.* Patient-derived organoids as a predictive biomarker for treatment response in cancer patients. *NPJ Precis Oncol*, 2021. 5(1):30.

CHAPTER

Nederlandse samenvatting

8

Cholangiocarcinoom (CCA) is een heterogene maligniteit van de galwegen. Het is een zeldzame vorm van kanker, met een incidentie van 0,3-6 per 100.000 personen wereldwijd, en heeft een zeer slechte prognose waarbij slechts 7-20% van de patiënten 5 jaar na diagnose nog in leven is. Eén van de factoren die leidt tot dit sombere vooruitzicht is de snelle tumoruitbreiding van de ziekte. Op het moment van diagnose is de ziekte vaak al uitgebreid, hetzij lokaal (in de intra- of extrahepatische galwegen) of op afstand, waardoor curatieve chirurgische interventie niet meer mogelijk is. Naast beperkingen door de anatomische presentatie speelt de inter- en intra-tumor heterogeniteit een belangrijke rol. De heterogene samenstelling van de tumor en aanzienlijke chemoresistentie zorgen ervoor dat systemische behandeling vaak niet effectief is.

De ontwikkeling van doelgerichte therapie en de introductie van immunotherapie hebben gezorgd voor verbeteringen in de behandeling van kanker in de afgelopen decennia. Doelgerichte systemische therapie richt zich op het doden van kankercellen op basis van hun moleculaire afwijkingen en immunotherapie is erop gericht het immuunsysteem van de patiënt zelf te activeren om de kankercellen te doden. Beide methoden zijn veelbelovend voor de behandeling van CCA. Voor succesvolle toepassing in de kliniek is accurate patiënt stratificatie essentieel gebleken. Bij dit proces wordt een bepaalde behandeling gekozen gebaseerd op de specifieke karakteristieken van de tumor bij de patiënt. Het testen van het complete spectrum van veelbelovende nieuwe medicijnen in klinische studies is zeer kostbaar en tijdrovend, en wordt beperkt door de zeldzaamheid van de ziekte, zeker wanneer stratificatie nodig is. Een patiënt-specifiek, tumor-representatief en schaalbaar *in vitro* model is nodig om dit proces te versnellen. Hierdoor zal het mogelijk worden in het laboratorium het effect van verschillende medicijnen te testen alvorens de patiënt bloot te stellen aan een behandeling.

Patiënt-specifieke CCA organoïden gekweekt uit tumorweefsel zijn recent ontwikkeld en bieden een innovatief CCA *in vitro* model. Deze organoïden zijn schaalbaar en 3-dimensionaal (3D), en representeren in belangrijke mate de histopathologie, mutaties en genexpressie profielen van het epitheliale kankercel compartiment van de patiënttumor. CCA organoïden zijn geschikt voor het screenen van medicijnen en het identificeren van biomarkers voor therapiegevoeligheid. Het CCA organoïd model staat echter nog in de kinderschoenen. Met de huidige techniek is het slechts mogelijk om voor ongeveer een derde van de CCA patiënten organoïden te initiëren. Ook zijn veel toepassingen nog niet onderzocht. Het model zou bijvoorbeeld gebruikt kunnen worden bij het bestuderen van therapie resistentie, en inter- en intra-tumor heterogeniteit. Belangrijk is om op te merken dat CCA organoïden enkel de epitheliale kankercel component van de tumor presenteren, terwijl het CCA in de patiënt een complexe en uitgebreide tumor micro-omgeving heeft, onder meer bestaande uit kanker-geassocieerde fibroblasten, immuuncellen, endotheelcellen en een collageenrijke stromale omgeving. Het doel van het onderzoek in dit proefschrift is daarom om nieuwe toepassingen van het CCA organoïden model te ontwikkelen in de zoektocht naar therapeutische aanknopingspunten, en het CCA organoïd model uit te breiden met de immuuncel en tumor-specifieke stroma componenten van de tumor micro-omgeving.

Gal als bron van CCA organoïden

CCA organoïden kunnen momenteel worden gecreëerd uit chirurgisch verwijderd tumorweefsel of tumorbipten. Aangezien slechts 20-30% van de CCA patiënten een resectie ondergaat, en een histologisch biopt een invasieve techniek is met bijbehorende risico's, zou een alternatieve bron voor CCA organoïden waardevol zijn. In **hoofdstuk 2** wordt beschreven hoe organoïden kunnen worden gemaakt uit cellen in gal verkregen uit de galwegen tijdens diagnostische en therapeutische ingrepen en uit de galblaas. Deze organoïden vertonen karakteristieken passend bij een oorsprong uit de galwegen buiten de lever. Aangezien eerder aangetoond is dat CCA cellen ook in gal detecteerbaar zijn, zou deze methode in de toekomst een veelbelovend alternatief kunnen zijn als bron voor CCA organoïden, in het bijzonder voor tumoren in de galwegen buiten de lever. Deze vorm van monstername is minimaal invasief, waardoor CCA organoïden eenvoudig op meerdere tijdstippen zouden kunnen worden gekweekt om de tumor en zijn therapiegevoeligheid zo gedurende het ziekteproces te volgen.

Nieuwe toepassingen van CCA organoïden voor het ontdekken van nieuwe therapeutische aanknopingspunten

De uitgebreide heterogeniteit in moleculaire afwijkingen van het CCA vraagt om stratificatie van patiënten bij het bepalen van de meest effectieve therapie. Stratificatie is momenteel alleen gebaseerd op genetische afwijkingen in de tumor. Dit heeft geleid tot de ontwikkeling van succesvolle doelgerichte therapieën, maar zelfs na preselectie van patiënten op basis van mutaties, zijn deze middelen slechts effectief in ongeveer een derde van de patiënten. In **hoofdstuk 3** wordt kinoom profilering toegepast om de activiteit van een grote groep kinases te bepalen, met als doel de stratificatie van patiënten te verbeteren en nieuwe therapeutische aanknopingspunten te vinden. Kinase activiteitspatronen in CCA organoïden zijn divers, waardoor zowel individuele als meer algemene kinases als potentiële behandelopties worden geïdentificeerd. Correlatie analyse tussen kinase activiteit en gevoeligheid voor de kinase remmer, toont aan dat sommige remmers verbonden zijn met de activiteit van de kinase die zij remmen, en anderen juist correleren met onverwachte kinases. Kinoom profilering is een veelbelovende techniek voor stratificatie die in toekomstige studies gevalideerd dient te worden.

Primaire scleroserende cholangitis (PSC) is een chronische fibrotische inflammatoire aandoening die in 9-20% van de patiënten leidt tot de ontwikkeling van CCA. In **hoofdstuk 4** worden CCA organoïden gebruikt om de invloed van PSC-gerelateerde inflammatoire cytokines op de proliferatie van CCA tumorcellen te onderzoeken. Het blijkt namelijk dat tumorcellen in PSC-CCA sneller prolifereren dan in sporadische CCA. IL-17A heeft een direct proliferatie-inducerend effect op de CCA organoïden. Eerdere studies tonen aan dat deze cytokine bijdraagt aan tumor progressie en therapie resistentie. IL-17A zou daarmee een interessant doelwit kunnen zijn voor de behandeling van CCA.

Verbeteren van het CCA organoïd model door toevoeging van tumor micro-omgeving componenten

Het huidige CCA organoïd model bevat enkel de epitheliale tumorcel component. Hoewel dit onderzoek naar het directe effect van factoren op tumorcellen faciliteert, missen er belangrijke componenten van de tumor micro-omgeving die de respons kunnen moduleren. In **hoofdstuk 5** wordt een co-cultuur methode beschreven voor CCA organoïden en immuuncellen die zijn geïsoleerd uit humaan bloed. Zowel directe cel-cel interactie, als indirecte effecten via oplosbare factoren geproduceerd door de immuuncellen, zijn kwantificeerbaar en tonen variatie tussen verschillende CCA organoïd lijnen. Dit model van de interactie tussen immuuncellen en tumorcellen kan preklinisch onderzoek naar anti-tumor immuniteit en immunotherapie in CCA faciliteren.

In **hoofdstuk 6** staat het samenspel tussen de extracellulaire matrix (ECM) en de CCA cellen centraal. Tot nu toe werden CCA organoïden gekweekt in een algemeen gebruikte basaal membraan hydrogel die noch de fysieke eigenschappen, noch de matrix componenten van de ECM in een CCA reflecteert. Daarom worden CCA organoïden in dit hoofdstuk gekweekt in gedecellulariseerde CCA en tumor-vrije lever ECM. Hierbij zien we dat gen expressie patronen van CCA organoïden in de CCA ECM meer overeen komen met de tumor in de patiënt dan organoïden die gekweekt worden in de traditionele kweekmethode. Ook induceert kweek in de CCA ECM meer chemoresistentie voor het in CCA patiënten gebruikte middel gemcitabine. Wanneer de CCA organoïden in de tumor-vrije lever ECM worden gekweekt, produceren zij collagenen, waarmee ze zelf de stijve fibreuze omgeving creëren waarin CCA tumorcellen floreren.

Conclusie

In het onderzoek beschreven in dit proefschrift heb ik nieuwe toepassingen van het CCA organoïd model onderzocht en heb ik het model aangevuld met componenten uit de tumor micro-omgeving. Gal is een minimaal invasieve bron voor gezonde organoïden van de galwegen buiten de lever, die uitgebreid kan worden naar CCA patiënten in toekomstig onderzoek. Kinoom profilering van CCA organoïden is een veelbelovende techniek om therapeutische aanknopingspunten te identificeren en om, gecombineerd met het screenen van medicijnen, nieuwe biomarkers voor therapie stratificatie te vinden. Ook kan het effect van inflammatoire cytokines bestudeerd worden in CCA organoïden. Dit heeft geresulteerd in de observatie dat het cytokine IL-17A een proliferatie-inducerende factor is en een mogelijk nieuw therapeutisch aanknopingspunt. Voor de uitbreiding van het tumor model, heb ik CCA organoïden succesvol gecombineerd met immuuncellen en gekweekt in gedecellulariseerde ECM om nieuwe modelsystemen te creëren die de patiënt tumor beter representeren en een platform vormen om immunotherapie en ECM-gerichte therapie te onderzoeken. Kortom, CCA organoïden zijn in hun huidige vorm, of uitgebreid met andere tumorcomponenten, een veelbelovend model voor de ontdekking van nieuwe therapieën en tumor stratificatie strategieën. Er is echter nog veel extra onderzoek nodig om deze organoïden technologie ook echt toe te passen in de kliniek en nuttig te maken voor de individuele patiënt.

APPENDICES

List of publications

PhD Portfolio

Curriculum Vitae

Dankwoord

LIST OF PUBLICATIONS

Publications in this thesis

Lieshout R.*, Willemse J.*, van der Laan L.J.W., Verstegen M.M.A. From organoids to organs: Bioengineering liver grafts from hepatic stem cells and matrix. *Best Practice and Research in Clinical Gastroenterology*, 2017. 31(2):151-9.

*These authors contributed equally

Vicent S., **Lieshout R.**, Saborowski A., Verstegen M.M.A., Raggi C., Recalcati S., Invernizzi P., van der Laan L.J.W., Alvaro D., Calvisi D.F., Cardinale V. Experimental models to unravel the molecular pathogenesis, cell of origin and stem cell properties of cholangiocarcinoma. *Liver International*, 2019. 39 Suppl 1:79-97.

Roos F.J.M.* , Wu H.* , **Lieshout R.#**, Willemse J.#, Albarinos L.A.M., Kan Y.Y., Poley J.W., Bruno M.J., de Jonge J., Bartfai R., Marks H., IJzermans J.N.M., Verstegen M.M.A.‡, van der Laan L.J.W.‡ Cholangiocyte organoids from human bile retain a local phenotype and can repopulate bile ducts in vitro. *Clinical and Translational Medicine*, 2021. 11(12):e566.

*These authors contributed equally

#These authors contributed equally

‡These authors contributed equally

Lieshout R.*, Zhou G.* , van Tienderen G.S., de Ruiter V., van Royen M.E., Boor P.P.C., Magré L., Desai J., Köten K., Kan Y.Y., Ge Z., Carrascosa L.C., Geuijen C., Sprengers D., van der Laan L.J.W., Verstegen M.M.A., Kwekkeboom J. Modelling immune cytotoxicity for cholangiocarcinoma with tumor-derived organoids and effector T cells. *British Journal of Cancer*, 2022. 127(4):649-60.

*These authors contributed equally

Lieshout R.*, Faria A.V.S.* , Peppelenbosch M.P., van der Laan L.J.W., Verstegen M.M.A., Fuhler G.M. Kinome profiling of cholangiocarcinoma organoids reveals potential druggable targets that hold promise for treatment stratification. *Molecular Medicine*, 2022. 28(1):74.

*These authors contributed equally

Lieshout R.*, Kamp E.J.C.A.* , Verstegen M.M.A., Doukas M., Dinjens W.N.M., Köten K., IJzermans J.N.M., Bruno M.J., Peppelenbosch M.P., van der Laan L.J.W.#, de Vries A.C.# Cholangiocarcinoma cell proliferation is enhanced in primary sclerosing cholangitis: A role for IL-17A. *International Journal of Cancer*, 2022. Accepted.

*These authors contributed equally

#These authors contributed equally

Van Tienderen G.S., **Lieshout R.***, Rosmark O.* , Willemse J., de Weijer F., Elowsson Rendin L., Westergren-Thorsson G., Doukas M., Groot Koerkamp B., van Royen M.E., van der Laan L.J.W., Verstegen M.M.A. Extracellular matrix drives tumor organoids toward desmoplastic matrix deposition and mesenchymal transition. *Under review*.

*These authors contributed equally

Other publications

Broutier L., Mastrogiovanni G.* , Verstegen M.M.A.* , Francies H.E., Gavarro L.M., Bradshaw C.R., Allen G.E., Arnes-Benito R., Sidorova O., Gaspersz M.P., Georgakopoulos N., Koo B.K., Dietmann S., Davies S.E., Praseedom R.K., **Lieshout R.**, IJzermans J.N.M., Wigmore S.J., Saeb-Parsy K., Garnett M.J., van der Laan L.J.W., Huch M. Human primary liver cancer-derived organoid cultures for disease modeling and drug screening. *Nature Medicine*, 2017. 23(12):1424-35.

Schneeberger K., Sánchez-Romero N., Ye S., van Steenbeek F.G., Oosterhoff L.A., Pla Palacin I., Chen C., van Wolferen M.E., van Tienderen G., **Lieshout R.**, Colemonts-Vroninks H., Schene I., Hoekstra R., Verstegen M.M.A., van der Laan L.J.W., Penning L.C., Fuchs S.A., Clevers H., De Kock J., Baptista P.M.* , Spee B.* Large-Scale Production of LGR5-Positive Bipotential Human Liver Stem Cells. *Hepatology*, 2020. 72(1):257-70.

**These authors contributed equally*

Li M., Wang L., Wang Y., Zhang S., Zhou G., **Lieshout R.**, Ma B., Liu J., Qu C., Verstegen M.M.A., Sprengers D., Kwekkeboom J., van der Laan L.J.W., Cao W., Peppelenbosch M.P., Pan Q. Mitochondrial Fusion Via OPA1 and MFN1 Supports Liver Tumor Cell Metabolism and Growth. *Cells*, 2020. 9(1):121.

Liu J., Li P., Wang L., Li M., Ge Z., Noordam L., **Lieshout R.**, Verstegen M.M.A., Ma B., Su J., Yang Q., Zhang R., Zhou G., Carrascosa L.C., Sprengers D., IJzermans J.N.M., Smits R., Kwekkeboom J., van der Laan L.J.W., Peppelenbosch M.P., Pan Q., Cao W. Cancer-Associated Fibroblasts Provide a Stromal Niche for Liver Cancer Organoids That Confers Trophic Effects and Therapy Resistance. *Cellular and Molecular Gastroenterology and Hepatology*, 2021. 11(2):407-31.

Nguyen L.* , Jager M.* , **Lieshout R.**, de Ruiter P.E., Locati M.D., Besselink N., van der Roest B., Janssen R., Boymans S., de Jonge J., IJzermans J.N.M., Doukas M., Verstegen M.M.A., van Boxtel R., van der Laan L.J.W., Cuppen E., Kuijk E. Precancerous liver diseases do not cause increased mutagenesis in liver stem cells. *Communications Biology*, 2021. 4(1):1301.

**These authors contributed equally*

PHD PORTFOLIO

Name PhD student: Ruby Lieshout
Department: Surgery
Research period: June 2016 – May 2020
Promotors: Prof. dr. Luc. J. W. van der Laan
Prof. dr. Jan N.M. IJzermans
Co-promotor: Dr. Monique. M.A. Verstegen

General courses

2016	Systematic Literature Research	1.0 ECTS
2016	Basic and Translational Oncology	1.8 ECTS
2016	Workshop Ingenuity Pathway Analysis (IPA)	0.4 ECTS
2017	Microscopic Image Analysis: From Theory to Practice	0.8 ECTS
2017	Research Management Training for PhD Students and Post Docs	1.0 ECTS
2017	Research Integrity	0.3 ECTS
2018	NCBI, Pubmed & Other Open Source Software	1.0 ECTS
2020	Photoshop and Illustrator Workshop	0.3 ECTS

Conferences

2016	Cell Press LabLinks Symposium: The Organoid Revolution: Organs in a Dish
2016	7 th Dutch Liver Retreat Including oral presentation
2017	Annual Science Day of the Department of Surgery Including oral presentation
2017	5 nd International Liver Congress of the EASL
2017	Erasmus MC Cancer Institute Research Day
2018	8 th Dutch Liver Retreat
2018	Erasmus MC Molecular Medicine Research Day
2018	Erasmus MC Cancer Institute Research Day Including oral presentation
2019	Annual Science Day of the Department of Surgery Including oral presentation
2019	9 th Dutch Liver Retreat Including oral presentation
2019	ISSCR Symposium on Stem Cells & Organoids in Development & Disease Including poster presentation
2019	Erasmus MC Molecular Medicine Research Day Including poster presentation and pitch, awarded with Best Poster Award
2019	54 th International Liver Congress of the EASL Including poster presentation

Seminar and meeting attendance

2016-2018	Weekly Gastrointestinal Oncology Meeting
2016-2020	Weekly Experimental Gastroenterology and Hepatology Seminar
2018-2020	(Bi-)weekly Organoid meeting

Teaching activities

2017	Supervision of master graduation project of Terry Jorna, Biomedical Sciences, Radboud University (six months)
2017-2018	Supervision of master internship of Demy van Gilst, Molecular Medicine, Erasmus University Medical Center (eight months)
2018	Lecture and student supervision during an interfaculty case study, bachelor students of Nanotechnology, Clinical Technology and Medicine (one evening)
2018-2019	Supervision of master graduation project of Kirti Krishnamurthy, Molecular Genetics & Biotechnology, Leiden University (8 months)

ABOUT THE AUTHOR

Ruby Lieshout was born on October 7th 1992 in Hoorn, the Netherlands. She grew up in Heerhugowaard and graduated from high school at the Trinitas College in her hometown in 2010. After a gap year, she started her bachelor in Veterinary Medicine at the University of Utrecht in 2011. In 2012 she was selected for the two year interdisciplinary honours programme Descartes College, which she successfully completed in 2014. In the same year, she obtained her bachelor's degree and was selected for the master's honours programme in Veterinary Medicine at the University of Utrecht. During this 12 month research internship, she studied liver cancer in dogs using organoid technology under supervision of prof. dr. Alain de Bruin, dr. B.A. Schotanus, dr. B. Spee, and dr. ir. M.J.M. Toussaint. In that year, she established and characterized organoid cultures of canine hepatocellular carcinoma, and found a passion for basic and translational cancer research. At that time, she also met prof. dr. Luc van der Laan who was working on the establishment of organoids from human liver cancer at the time. A few days before starting her master's in Veterinary Medicine, she was invited by prof. dr. Luc van der Laan to talk about a PhD position at the Erasmus University Medical Center in Rotterdam. In 2016, she started her PhD research on liver cancer organoids under supervision of prof. dr. Luc van der Laan, prof. dr. Jan IJzermans, and dr. Monique Verstegen. In the course of the project, the focus shifted to cholangiocarcinoma organoids and their use in therapy improvement, which resulted in the thesis in front of you today.



